Compositional tuning of Zn- based semiconducting nanoparticles by Atmospheric Pressure Plasmas and study of their optoelectronic properties

Gunisha Jain

B.Tech. (Hons), M.Tech. (Hons)

Faculty of Computing, Engineering and the Built Environment, Ulster University

Thesis submitted for the degree of Doctor of Philosophy

January 2019

(I confirm that word count for the thesis is less than 100,000 words.)

Content

Acknowledgement

I would like to take the opportunity to thank all the people who have motivated and supported me during my PhD.

First off, I would like to express my sincere gratitude and appreciations to my research supervisor Prof. Davide Mariotti for the continued guidance, feedback, encouragement and exceptional support throughout my research. It has been tremendous honour to have had the opportunity to learn and develop my research skills under your supervision. I would also like to acknowledge my second supervisor Prof. Paul Maguire for his excellent help and advice during my PhD research.

I am also grateful to my colleagues, Dr. Somak Mitra, Dr. Janish Patel, Dr. Sadegh Askari, Dr. Manuel-Macias-Montero, Dr. Tamilselvan Velusamy, Dr. Conor Rocks, Dr. Calum McDonald, Dr. Atta Ul Haq, Dr. Darragh Carolan, Dr. David Ratherford, Dr. Charles Mahony, Dr. Mark Tweedie, Ruari McGlynn, Bruno Alessi, Dilli Babu, Hussain Hussain and Tahereh. Further, I would like to appreciate the academic and technical support of the NIBE staff specially Brian, Ann, Damian, and also Research Office of the University of Ulster. I would like to acknowledge the sources of funding, Vice Canceller Research Scholarship (VCRS), that made this PhD possible.

Further, I would like to thank my friends, Dr. Garima Mittal, Anuj Bisht, Monali Dahale, Dr. Preetam kumar Sharma, Amit kumar Singhal and Anukriti Singh for their constant support and encouragement over the duration to my work.

Finally, I would like to give a big thank to my mom Usha Jain for being my strongest support system, my father Jainendra Jain and my brother Lohit Jain for constant encouragement. It would not have been possible without their support.

Publications

A. Published peer-reviewed journal article

1. Liguari, A.; Gallingani, T.; Padmanaban, D.B.; Laurita, R.; Velusamy, T.; **Jain, G.;** Macias-Montero, M.; Mariotti, D.; Gherardi, M.; Synthesis of Copper-Based Nanostructures in Liquid Environments by Means of a Non-equilibrium Atmospheric Pressure Nanopulsed Plasma Jet. *Plasma chemistry and plasma processing* **2018,** 38 (6), 1209-22.
2. **Jain, G.;** Macias-Montero, M.; Velusamy, T.; Maguire, P.; Mariotti, D.; Porous zinc oxide nanocrystalline film deposition by atmospheric pressure plasma: Fabrication and energy band estimation. *Plasma, processes and polymer* **2017**, 14 (12),1-8.
3. Chengsheng, Ni.; Hedley, G.; Payne, J.; Svrcek,V.; McDonald,C.; Jagadamma, L. K.; Edwards, P.; Martin, R.; **Jain, G.;** Carolan, G.; Mariotti, D.; Maguire, P.; Samuel, I.; Irvine, J.; Charge carrier localized in zero-dimensional (CH3NH3)3Bi2I9 clusters. *Nature Communication*, **2017**, 8:170
4. Mariotti, D.; Belmonte, T.; Benedikt , J.; Velusamy, T.; **Jain**, **G.;** Svrcek, V.; Low-Temperature Atmospheric Pressure Plasma Processes for "Green" Third Generation Photovoltaics. *Plasma Processes and Polymer,* **2016**, 13, 70–90. (Review article)

B. Manuscripts submitted or in preparation

1. Liguori, A.; Gallingani, T.; Padmanaban, D.B.; Laurita, R.; Velusamy, T.; **Jain, G.;** Macias-Montero, M.; Mariotti, D.; Gherardi, M.; Synthesis of copper-based nanostructures in liquid environments by means of a non-equilibrium atmospheric pressure nanopulsed plasma jet. (to be submitted to Plasma Chemistry and Plasma Processing)
2. **Jain, G.;** Roxy, C.; Maguire, P.; Mariotti, D.; One-step synthesis of air-stable, defect-free and hydroxy-terminated ZnO Quantum Dots. (to be submitted to Advanced Functional Materials)
3. **Jain, G.;** Roxy, C.; Maguire, P.; Mariotti, D.; Dopant site identification in doped ZnO and its impact on electrochemical properties. (in preparation)

C. Conference presentations

1. **Jain, G.;** Roxy, C.; Maguire, P.; Mariotti, D.; Ethylene-di-amine as a dopant in N doped ZnO by atmospheric pressure plasma, ***Oral Presentation***, Materials Research Society (MRS) Fall, Boston, 2017.
2. **Jain, G.;** Macias-Montero, M.; Velusamy, T.; Maguire, P.; Mariotti, D.; Deposition of porous zinc oxide nanocrystalline film by rf atmospheric pressure plasma and estimation of band alignment, ***Poster Presentation***, Plasma Processing, Gordon Conference, Andover, 2016.
3. Padmanaban, D. B.; Carolan, D.; Velusamy, T.; Rocks, C.; **Jain, G.;** Maguire, P.; Mariotti, D.; Simple and Single-Step Synthesis of Metal Oxides for Photovoltaics. ***Oral Presentation,*** E-MRS, Strasbourg, 2017.

Summary

The main objective of this work is to study the impact of compositional variation on the material property of zinc-based semiconductors. Non-thermal atmospheric pressure plasma systems are used to synthesise these nanosized semiconductors. Relevant applications are explored, specifically photovoltaics and supercapacitors.

In this context, porous zinc oxide (ZnO) film, ZnO quantum dots (QDs) and zinc nitride (Zn_2N_3) nanoparticles (NPs) are synthesised with gas-phase atmospheric pressure plasma. Further, doped ZnO and zinc peroxide (ZnO_2) NPs are synthesised with liquid-phase non-thermal atmospheric pressure plasma. This work also includes extensive material characterization of synthesised nanomaterials to analyse their properties.

Firstly, porous ZnO is synthesised and directly deposited from the gas phase plasma system. Detailed material characterization has validated the purity of the synthesised material. Further, analysis of band alignment has shown the intactness of electronic properties of ZnO. This synthesised porous ZnO is used as an electron transport layer in photovoltaics. Initial results have shown that porous ZnO is not an appropriate choice for perovskite based solar cells. More specifically, control over the device fabrication is difficult task in ZnO/ perovskite solar cells. In another solar cell configuration, N doped carbon quantum dots are used as an active material. Preliminary results have shown promising results in using porous ZnO as electron transport layer with quantum dots active solar cells.

The second important finding of this work is the formation of defect-free self-hydroxyl passivated ultra-small ZnO QDs (~1.9 nm) from gas phase plasma system. This passivation happens because of the high surface energy of the small size QDs. Hydroxyl passivation of the ZnO QDs has shown the surface defect termination. This defect-termination has led to the very stable ultra-violet emission of ZnO QDs without any visible emission.

Later, ZnO_2 is produced with a hybrid liquid-plasma system. Impact of synthesis current is analysed on intrinsic crystal defects. The results have shown that intrinsic defects in the lattice has reduced with increasing synthesis current. Analysis of ZnO_2 formation mechanism has revealed that ionized oxygen species plays a major role in

the final synthesis of ZnO_2.

Further, doped ZnO is also synthesised successfully with a hybrid liquid-plasma system. Detailed characterization has revealed many interesting outcomes of doping. With doping, the absorption edge is extended in the visible region and bandgap is reduced to 2.98 eV. The dopant position in the lattice was analysed with the help of many characterization techniques. Results have indicated that at a lower dopant concentration, substitutional doping plays a major role. Later, an in-built constraint towards the substitutional occupation site is observed and interstitial dopant concentration dominates over substitutional with increase in doping concentration. Also, initial experiments have shown pseudocapacitive nature in N-doped and C-N doped ZnO for the first time. Highest areal capacitance (1.6 F/ cm^2) was observed for C-N doped ZnO. Collectively, these results have also indicated the positive impact of substitution doping on the visible absorption and storage capacity of the ZnO.

Finally, for very first time, the synthesis of Zn_2N_3 nanoparticle in gas-phase atmospheric pressure plasma is studied. The complexity of producing Zn_2N_3 at atmospheric pressure is demonstrated with the help of different nitrogen precursor. At first, pure nitrogen gas was used as a nitrogen precursor where zinc, zinc oxide and zinc nitride mixed phase were synthesised. However, a great degree of difficulty was observed in identifying the chemical composition of synthesised material. In another attempt, ammonia gas was used as a nitrogen precursor. Synthesis of pure a phase Zn_2N_3 was observed with ammonia. Also, surface oxidation was observed after atmospheric exposure of synthesised Zn_2N_3.

Abbreviations

APμP	Atmospheric Pressure Microplasma
BE	Binding Energy
CBM	Conduction Band Minimum
CPD	Contact Potential Difference
DMF	Dimethylformamide
EBD	Energy Band Diagram
EDX	Energy Dispersive X-ray Spectroscopy
E_f	Fermi Level
E_g	Bandgap Energy
ETL	Electron Transport Layer
FF	Fill Factor
FTIR	Fourier Transform Infrared
FWHM	Full Width Half Maximum
HRTEM	High Resolution Transmission Electron Microscopy
I_{sc}	Short Circuit Current
I-V	Current-Voltage
KE	Kinetic Energy
LED	Light Emitting Diode
$MAPbI_3$	Methylammonium Lead Halide
MOCVD	Metal Organic Chemical Vapour Deposition
NP	NP Nanoparticle
PECVD	Plasma Enhanced Chemical Vapour Deposition
PL	Photoluminescence
QD	Quantum Dot
RF	Radio Frequency
Sccm	Standard Cubic Centimetre Per Minute

TEM	Transmission Electron Microscopy
UV-Vis	Ultra Violet Visible
VBM	Valence Band Maximum
V_{oc}	Open Circuit Voltage
XPS	X-ray Photoelectron Spectroscopy
XRD	X-ray Diffraction

NOTE ON ACCESS TO CONTENTS

I hereby declare that with effect from the date on which the thesis is deposited in the Research Student Administration of Ulster University, I permit

1. The Librarian of the University to allow the thesis to be copied in the whole or in part without reference to me on the understanding that such authority applies to the provision of single copies made for study purposes or for the inclusion within the stock of another library.

2. The thesis to be made available through the Ulster Institutional Respiratory and/or EThOS under the terms of the Ulster eTheses Deposit Agreement which I have signed.

IT IS A CONDITION OF USE OF THIS THESIS THAT ANYONE WHO CONSULTS IT MUST RECOGNISE THAT THE COPYRIGHT RESTS WITH THE AUTHOR AND THAT NO QUOTATION FROM THE THESIS AND NO INFORMATION DERIVED FROM IT MAY BE PUBLISHED UNLESS THE SOURCE IS PROPERLY ACKNOLOWLEDHED."

Chapter 1: Introduction

1.1 Background

Research in nanotechnology and nanomaterials is very prominent since last century. Nanomaterials applications have been explored in many fields e.g. energy, medicine, information technology, environmental science etc. Particularly, meeting the world energy demand with clean, affordable, efficient and renewable resources is one of the main drivers for today's research endeavours. Nanotechnology can make a significant contribution in this context. Altering the materials characteristics at the atomic, molecular, and macro-molecular scale can lead to diverse physical properties such as electrical conductivity, magnetic properties, fluorescence, hardness, or strength and can contribute to meet demanding application requirements.[1] One of the aspects in the deployment of nanotechnologies for various applications is represented by production cost and throughput of nanomaterials. Therefore, both nanomaterials that can meet the application requirements as well as synthesis processes that can lead to large-scale and low-cost production should be considered.

Semiconductor nanoparticles (NPs) are for instance a particular class of nanomaterials, which offer great promise for a range of applications but also present synthetic challenges. Semiconducting NPs have acquired much interest because of their wide range of applications including photovoltaic cells,[2] light emitting devices,[3] electronic devices[4] and fluorescent tags for biomedical applications.[5] While the bandgap of bulk semiconductors cannot be altered easily, the bandgap of semiconductor NPs depends on their size, due to quantum confinement effect. This size-tunable property is quite useful in many applications like energy storage, energy conversion, optoelectronics etc.

Significant research has been carried out on the study of nanocrystals (NCs) of group II-VI material such as cadmium sulfide (CdS) and cadmium selenide (CdSe) and group IV-VI material such as lead sulfide (PbS) and lead selenide (PbSe). Extensive effort have been devoted to integrate these materials in devices such as light-emitting diodes,[6] photovoltaic cells[7,8] and other applications such as fluorescent tags for biomedical applications.[9,10] Solution-based synthesis methods for these semiconductors are now well-established and excellent control over their properties such as NPs size has been achieved.[11,12] In spite of the significant progress, these

materials confront a number of non-trivial challenges which favour the choice of exploring other materials; group II and VI compounds can present application obstacles as they are often toxic, not stable in ambient air or have very limited reserves in the earth's crust. These limitations represent challenges to their applicability in large-scale industrial applications. Therefore, non-toxic more viable materials should be explored. In this direction, Si NCs can be a possible solution to solve these problems and extensive research has been done on silicon.[13–16] However, silicon NCs are not generally stable in ambient air and synthesis process can have signification effect on the surface of NCs, and that can change optoelectronic properties of NCs. Therefore, further research is needed to manipulate the properties of Si NCs (e.g. strain engineering and composition tuning).

In the context of number of different applications, while silicon may offer some opportunities ahead, obstacles imposed by the nature of Pb and other toxic or expensive materials motivates investigation of alternative materials. Other potential candidates should be explored. Of course, many options and directions are indeed possible. This work is focused on Zn-based semiconducting NCs. More specifically, Zn combined with oxygen and nitrogen has provided an interesting synthetic platform to investigate oxides and nitrides with various stoichiometry and degree of doping also leading to key and important materials properties such as direct bandgap, air stability, low-cost and environmentally friendly.

Atmospheric pressure microplasmas (APμPs) based approach is used in this work to produce Zn-based semiconducting NCs. Because of the unique characteristic of having high electron temperature and low neutral gas temperature, APμPs systems are very useful in synthesis of nanomaterials and surface properties tailoring of the materials. With all of unique characteristics, it also displays a good amount of reliability in scalability of these systems.

1.2 Aims and Objectives

The aim of this work is to investigate opportunities to manipulate the electronic structure and achieve desired optoelectronic properties by modifying the stoichiometric content of Zn-based semiconductors. Synthesis of Zn-O-N based nanomaterials with different APμPs will be achieved. Detail characterization will be performed to study the effect of composition tailoring on the materials properties.

The work in this thesis can be divided in three main parts.

- Firstly, synthesis of different zinc oxide (ZnO) nanostructures and impact of quantum confinement on ZnO properties is investigated.
- Secondly, doped (e.g. N & C) ZnO is synthesised to study the impact of doping and different composition on the ZnO properties. Also, effect of composition on electrochemical properties of ZnO is also studied.
- Finally, Synthesis of Zinc Nitride (Zn_2N_3) nanoparticles.

Importantly, the simplest form of Zn precursors was used throughout this project and limited to solid Zn in the form of a wire or a foil. A range of characterization techniques have been used to collect relevant information about morphology, chemical composition and optical properties of NPs.

Overall, the main objectives of this PhD study were the following:

- Developing the suitable atmospheric pressure plasma reactors for the synthesis of Zn based semiconductors NPs.
- NPs properties study with different characterization techniques.
- Effect of different ZnO structures (porous and QDs) on material's properties.
- Investigating the quantum confinement and compositional effect on Zn-N-O system.
- Study of electrochemical and photovoltaic effect of synthesised NPs.

1.3 Thesis structure

The thesis chapters are organized as follows:

Chapter 2 is a literature review that starts with the basic mechanism of nanoparticle formation, fundamentals of non-thermal microplasmas, details about APμPs reactors and their applications for the synthesis of nanoparticles. A brief background about properties of ZnO, doped-ZnO and Zn_2N_3 nanostructures will be discussed and their possible applications will be explored.

Chapter 3 Basic working principles of material characterization techniques which have been used in this project to analyse materials properties will be explained.

Chapter 4 is focused on the synthesis of Zn based NPs by direct current liquid-plasma interaction. This chapter contains two parts:

1) Synthesis of ZnO_2 using ethanol as an electrolyte in the reactor. A detailed analysis of ZnO_2 synthesis will be discussed supported by results from different characterization techniques. Possible synthesis mechanisms will be discussed.
2) Synthesis of ZnO and N-doped ZnO using deionized (DI) water and DI-ethylenediamine (EDA) electrolyte, respectively. The effect of electrolyte composition on the doping in ZnO will be evaluated. A detailed characterization is performed to understand the dopant nature. Electrochemical studies are performed to analyse material energy storage properties. An interpretation will be discussed about dopant site in the ZnO lattice.

Chapter 5 is focused on the synthesis of Zn based NPs by gas-phase radio frequency plasma with a solid Zn wire precursor. This chapter also contains two parts:

1) Synthesis of porous ZnO nanocrystalline films and the band energy diagram is studied. The porous ZnO nanocrystalline film is used in photovoltaics as an electron transport layer with perovskite and N-doped carbon QDs as active materials.
2) Synthesis of hydroxyl passivated ZnO quantum dots. A detailed analysis will be given including photoluminescence properties that emphasize the highly UV emitting nature without any visible emission contribution.

Chapter 6 is focused on the synthesis of Zinc nitride (Zn_2N_3) NPs by gas-phase radio frequency plasma with Zn wire precursor. This chapter also contains two parts:

1) An attempt to synthesis Zn_2N_3 NPs with pure nitrogen gas as a nitrogen precursor. A range of characterization analyses are performed; a conclusion of this work is that the use of molecular nitrogen gas as precursor presents synthetic challenges to produce Zn_2N_3, particularly in this configuration reactor.
2) Synthesis of Zn_2N_3 NPs with 10% NH_3-Ar gas as a nitrogen precursor. A range of characterization is performed to confirm the Zn_2N_3 NPs production.

Chapter 7 includes the concluding remarks and suggestions for future work.

1.4 References

1. Joachim, C. To be nano or not to be nano? *Nat. Mater.* **4,** 107–109 (2005).
2. Sargent, E. H. Colloidal quantum dot solar cells. *Nat. Photonics* **6,** 133–135 (2012).
3. Shirasaki, Y., Supran, G. J., Bawendi, M. G. & Bulović, V. Emergence of colloidal quantum-dot light-emitting technologies. *Nat. Photonics* **7,** 933 (2013).
4. Kim, D. K., Lai, Y., Diroll, B. T., Murray, C. B. & Kagan, C. R. Flexible and low-voltage integrated circuits constructed from high-performance nanocrystal transistors. *Nat. Commun.* **3,** 1–6 (2012).
5. Fan, J. & Chu, P. K. Group IV nanoparticles: Synthesis, properties, and biological applications. *Small* **6,** 2080–2098 (2010).
6. Colvin, V. L., Schlamp, M. C. & Alivisatos, A. P. Light-emitting diodes made from cadmium selenide nanocrystals and a semiconducting polymer. *Nature* **370,** 354–357 (1994).
7. Chuang, C.-H. M., Brown, P. R., Bulović, V. & Bawendi, M. G. Improved performance and stability in quantum dot solar cells through band alignment engineering. *Nat. Mater.* **13,** 796–801 (2014).
8. Lan, X., Masala, S. & Sargent, E. H. Charge-extraction strategies for colloidal quantum dot photovoltaics. *Nat. Mater.* **13,** 233–240 (2014).
9. Kumar Bhunia, A., Kanti Samanta, P., Saha, S. & Kamilya, T. Safety concerns towards the biomedical application of PbS nanoparticles: An approach through protein-PbS interaction and corona formation. *Appl. Phys. Lett.* **104,** (2014).
10. Dubertret, B. *et al.* In vivo imaging of quantum dots encapsulated in phospholipid micelles. *Science (80-.).* **298,** 1759–1762 (2002).
11. Chang, J. & Waclawik, E. R. Colloidal semiconductor nanocrystals: controlled synthesis and surface chemistry in organic media. *RSC Adv.* **4,** 23505–23527 (2014).
12. Li, H. *et al.* Size- and shape-controlled synthesis of PbSe and PbS nanocrystalsvia a facile method. *CrystEngComm* **12,** 1127–1133 (2010).
13. Ji, X., Wang, H., Song, B., Chu, B. & He, Y. Silicon Nanomaterials for Biosensing and Bioimaging Analysis. *Front. Chem.* **6,** 1–9 (2018).
14. Su, X. *et al.* 1-s2.0-S0039914013005584-main.pdf. *Adv. Energy Mater.* **4,** n/a-

n/a (2014).

15. Romero, J. J. *et al.* Photoluminescent 1-2 nm sized silicon nanoparticles: A surface-dependent system. *Chem. Mater.* **25,** 3488–3498 (2013).
16. Tang, W. *et al.* Formation and photoluminescence of ‘cauliflower’ silicon nanoparticles. *J. Phys. Chem. C* **119,** 11042–11047 (2015).

Chapter 2: Literature Review and Background

2.1 Introduction to nanotechnology

Since thousands of years, nanomaterials have been used in many fields unconsciously. For example, gold (Au) nanoparticles has been used as an inorganic dye in ceramic porcelains[1] from thousands of years or use of colloidal gold in the treatment of arthritis[2]. Over the years, advancement in technology has enabled researchers to see and modify materials at nanoscale and understanding of atomic interactions. Understanding of materials physical properties and phenomenon at nanoscale leads to the design, fabrication and applications of nanomaterials in many fields, this branch of technology is called as nanotechnology. Miniaturization of materials at the nanoscale enables us to shrink semiconductor devices or create nanoscale and targeted diagnostic and therapeutic tools. At the nanoscale, materials exhibit remarkable properties, for example lower melting point, reduced lattice constant, surface energy etc. which are very different than those of their bulk counterpart.

The main challenge in nanotechnology is to integrate these materials into or with macroscopic systems that can provide an interface with users. Moreover, precise control on fabrication and processing of nanomaterials is required to produce desired material properties. For example, doping in bulk semiconductor is a very well executed process, however control of dopants at the nanoscale is much more challenging because even a slight fluctuation in doping concentration can greatly impact the overall properties of the nanomaterials. Furthermore, it is hard to control the location of dopants within nanoscale materials where surface atoms behave differently than core atoms. It follows that reproducibility and a uniform distribution of dopants in the lattice is very challenging. On many occasions, overcoming the energy requirements to maintain a high surface energy can be challenging, e.g. to prevent Ostwald ripening or agglomeration of nanomaterials. Overall, the controls over size, uniform size distribution, morphology, crystallinity, chemical composition are all important to achieve desired physical properties. Synthesis methods therefore play a very important role in fabricating nanomaterials. In broad terms, two types of fabrication approaches can be considered: top-down and bottom-up as shown in figure 2.1.

There are several advantages and disadvantages for both approaches which often depend on the material that needs to be fabricated. One of the problems in top-down approaches is the lack of control over surface characteristics and resulting properties, for instance conductivity at the interface can be reduced due to inelastic surface scattering and generate excessive heat. Materials are built atom-by-atom, molecule-by-molecule or cluster-by cluster, in a bottom-up approach. This approach provides more control where many of the nanomaterial characteristics can be designed to a high accuracy. The drawback of bottom-up methods is often the scalability of the fabrication process with limitation over its throughput. In this thesis work, plasma-based synthesis methods are used to produce desired nanomaterials following bottom-up strategies.

In this chapter, basic mechanism behind nanoparticle formation will be discussed. Later, plasmas will be introduced, and various plasma-based methods reviewed. The focus will then shift on the materials relevant for this thesis and in particular the synthesis, properties and application Zn-based nanomaterials will be discussed.

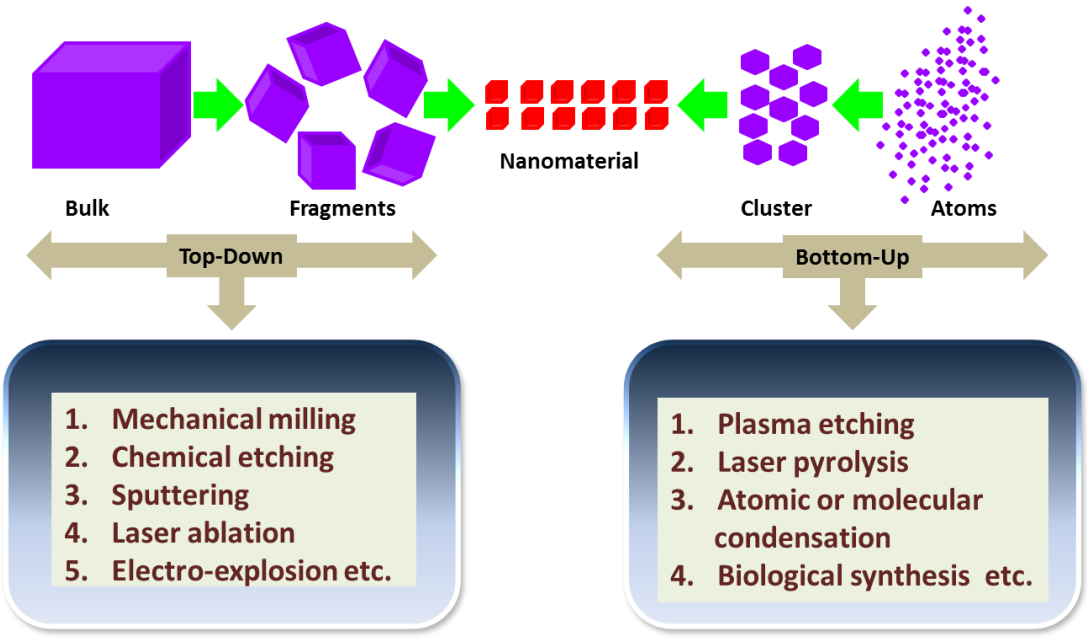

Figure 2.1: Two types of approaches to fabricate nanomaterials, top-down and bottom-up and corresponding examples of synthesis based on the concept.

2.2 Nanoparticle formation mechanism

2.2.1 Fundamental of nucleation and growth of nanoparticles

For most applications, the most important requirements for nanoparticles can be summarized as follows: (i) uniform size distribution, (ii) identical shape and morphology, (iii) identical chemical composition and crystal structure and (iv) no agglomeration. These strongly depend on the synthesis approach and and overall control on synthesis conditions, which are in turn determined and often limited by basic mechanism of nanoparticle formation of each process.

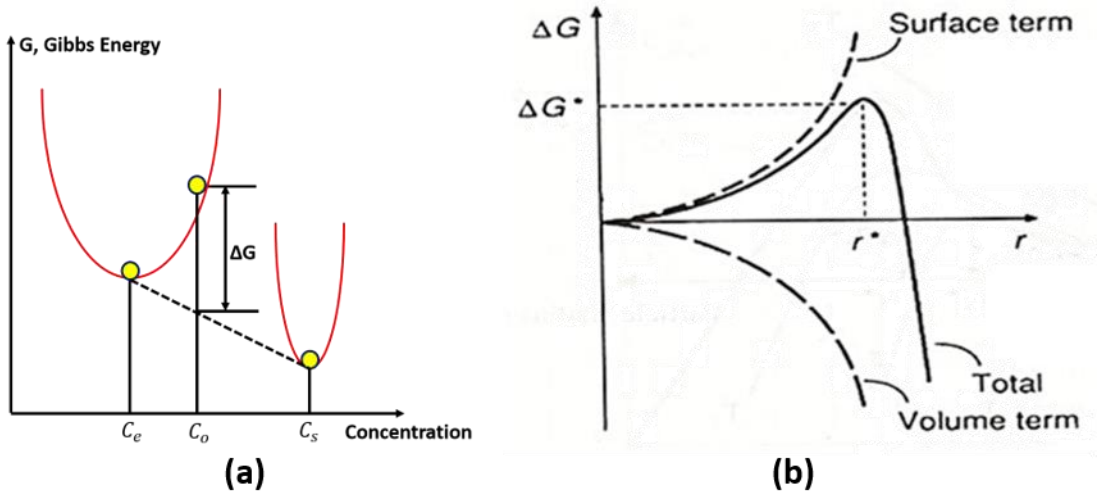

Figure 2.2: (a) Schematic representation of reduction of Gibbs free energy in saturated solution by forming solid phase (C_s) and maintaining equilibrium concentration (C_e) (b) Representation of surface Gibbs energy and Volume Gibbs energy as a function of nucleus radius.[2]

Nanoparticles can be synthesised by homogeneous nucleation from vapour or liquid or by heterogeneous nucleation on substrate. The new phase is formed when the solution has a solute concentration that is higher than the equilibrium solubility (supersaturation) or when a temperature decreases below the phase transformation point.

Supersaturated solution possesses high Gibbs free energy and tends to reduce it by segregating salute from the solution as shown in figure 2.2a. The nucleation happens when the solute concentration C in solution is greater than C_o ($C > C_o$). Gibbs free energy ΔG is the driving force for the nucleation and growth of the nanoparticles. The change in Gibbs energy is a function of both the change in volume energy and surface

energy. When the initial nucleation takes place with the formation of a new solid, both volume and surface energy compete, figure 2.2b. A new nucleus is only stable if the radius exceeds the critical size, *r**. A nucleus with radius smaller than the critical size will dissolve into the solution to reduce the overall energy. Nucleus that have a radius bigger than *r** are stable and will continue to grow.

In the synthesis of nanoparticles or quantum dots, the critical radius limits the minimum size of the particles in the supersaturated solution or vapour. By increasing the change in the Gibbs free energy ΔG and reducing the surface energy of new phase, this critical size and free energy can be reduced further. The critical size and

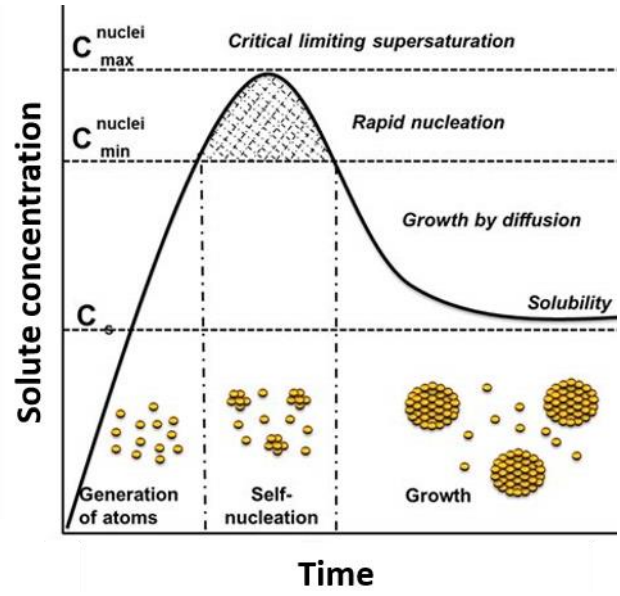

Figure 2.3: Schematic representation of process of nucleation and growth.[3,4]

free energy reduction can be achieved by increasing supersaturation of the solution. Overall, supersaturation, low viscosity and low critical energy barrier (i.e. energy barrier that must be overcome to start nucleation process) is required to create a high number of nuclei. That means, for a given concentration of the solute, smaller size nuclei will be created by creating large number of nuclei. The nucleation and growth process of the nanoparticle or nanostructure formation can be understood by figure 2.3 as a function of time.

As the concentration of the solute increases, there is no nucleation even above the equilibrium concentration (figure 2.3). Nucleation occurs only after the solute concentration reaches the minimum required supersaturation concentration (C_{min}^{nuclei})

according to a defined energy barrier for the system. The concentration of species decrease after the initial nucleation and the change in Gibbs free energy reduces. When the concentration of the solute decreases below this concentration, nucleation stops but growth will proceed till the equilibrium concentration or solubility. On this basis, in order to obtain uniform size distributions, it is necessary that all the nuclei are formed at the same time under the same condition. The nucleation time should be very short where species concentration should increase abruptly to very high concentration and quickly brought to a minimum concentration.

The growth from the nuclei includes various steps from the generation of precursor species, diffusion to the growth surface, adsorption and irreversible incorporation onto the solid surface. The growth process can be determined by the diffusion process and the surface process. When the growth process is controlled by the diffusion of growth species from the bulk solution to the particle surface, the growth rate is determined by the diffusion rate. Later, when the concentration of growth species on the particle surface is same as that in the bulk, the growth rate is controlled by surface processes.

2.2.2 Nanoparticle formation in non-thermal plasma

In non-thermal plasma, the formation of nanoparticles also happens in three steps: nucleation, cluster formation and growth. However, the process is not similar as described in 2.2.1.

In nucleation process, initial nuclei, either neutral or singly negatively charged, are formed at a large concentration. However, often, chemical reactions tend to dominate in cluster growth than physical condensation. In this type of plasma, ion-neutral clustering seems to be a more robust mechanism than neutral-neutral clustering because of confined anions in plasma. Other neutral and cation species will diffuse out of bulk plasma and may not have enough time into plasma for nucleation. The nucleation process has been studied mostly on silane gas containing plasma to form silicon nanocrystals. According to experimental and modelling, it is suggested that nucleation is an outcome of reaction between silicon hydride anion and neutral species containing only single Si atom.[5–8] The kinetic data for reactions in silane plasma suggested that reaction between anion-molecules and anion-radicals involving Si addition and H_2 elimination.[8] Other simulation reports also support anion-neutral clustering mechanisms for nucleation in silane plasmas but the quantitative accuracy

of these simulations is limited.[6,9] Another system that has gained attention is carbon containing plasmas. A detailed experimental and theoretical analysis was performed by Mao *et al.* where they concluded that at smaller size, neutral acetylene molecule reacts with anion and at larger size anion reacts with radicals.[10] Altogether most studies on nucleation in silane and hydrocarbon plasma supports anion-neutral reaction as a key for cluster growth. In other studies of Ni and Cu nanoparticle formation, it was found that initial clustering may involve chemical reactions, which are more complicated than the simple condensation of metal vapour onto metal clusters.[11] It is also possible that both condensation and chemical reaction are present concurrently. Moreover, the nucleation process is strongly dependent on the material, precursor type and other operating conditions.

After nucleation, coagulation among particles can take place as generally observed in neutral-gas aerosol. However, in non-thermal plasmas, particles are negatively charged and because of that coulombic repulsive force strongly oppose the coagulation or aggregation of particles. That can lead to monodisperse size of the particles.[12,13] In some cases coagulation of particles can occur.[14,15] This is possible when particles are very small, in which case they may not have a charge.

Growth of nanoparticles onto their surface can follow two mechanisms, physical vapour growth (PVG) and chemical vapour growth (CVG). In PVG, in a supersaturated vapour, molecule collides and sticks together. This type of growth mechanism is more common in metals. In non-thermal plasmas, gas temperature is typically low enough to form saturated vapour and to lead condensation on cluster surface. While in the CVD growth mechanism, where chemical reaction happens on nanoparticle surface because of molecules, radicals or ions collision with nanoparticle. Anions are ruled out as growth species because of their key role in nucleation. This kind of growth mechanism happens mostly where precursor exists in the gas phase mainly chemically dissociated compounds. For example, silane plasmas where growth mechanism happens because of neutral species such as SiH_4, SiH_2 and SiH_3 etc and cations like SiH_3^+. The reaction between nanoparticle with these species adds Si to the particle and releases H_2 back to the plasma.[16] In this kind of process, vapour supersaturation is not required but overall system should be out of equilibrium with respect to condensed phase.

2.3 Atmospheric pressure microplasmas for nanomaterials synthesis

2.3.1 Introduction to atmospheric pressure plasmas and microplasmas

Plasma is a highly ionized gas and in principle can be formed from any state of matter. Most often, and for technological applications, plasmas are produced via gas electric discharges where the energy to sustain the ionization rate is initially transferred to electrons and following to gaseous molecule/atoms creating ions, radicals photons etc. Figure 2.4 represents the plasma constituent species and corresponding mass and time of species in the plasma.[17] Plasma can be classified in two categories according to the operating gas pressure: low-pressure plasma (LPP) and atmospheric pressure plasma (APP). LPP have been widely used for material processing applications and represent well established processes in industry, from electronics to medicine.

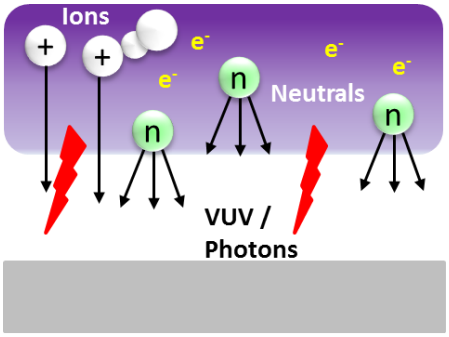

Species	Mass (g)	Gas Phase reaction (s)	Surface reaction(s)
Electrons	10^{-28}	10^{-9}	10^{-16} -10^{-15}
Ions	10^{-16} - 10^{-15}		10^{-12}
Photons		10^{-9} - 10^{-8}	
Neutrals	10^{-24} -10^{-22}	10^{-3} -10^{-1}	10^{-12}
Radicals	10^{-24} -10^{-22}	10^{-5} -10^{-4}	10^{-3} -10^{-2}

Figure 2.4: Showing plasma constituent species and mass and time scales for various plasma species.[17]

Although this does not and has not represented a challenge for the widespread utilization of LPP processes, low-pressure operation does require vacuum equipment that adds up to the overall process costs. APPs therefore have been seen as an alternative where high pressure working conditions would significantly lower the processing cost. However, at higher pressure, plasma properties change significantly and generally lead to arc discharges, which are characterised by high collision rates and elevated gas temperatures. High gas temperature is not desirable for many materials applications. Therefore, the possibility of low-temperature APPs is important. Low-temperature APPs can be more broadly termed as non-equilibrium APP because of the high electron temperature vs. a low gas temperature.

Table 1: Different aspects of microplasma and conventional plasma.[11]

Aspects	Microplasma	Conventional Plasma
Operating pressure	Atmospheric pressure	Always needs low pressure
Gas temperature	Can be as low as room temperature	Always needs temperature above 1000 °C
Particle size and distribution	Fine size, narrow size distribution	Relative larger size and wider size distribution
Setup and its investment	Quite small, easily moved, low cost	Always large, fixed, high cost

On a first approximation, in order to maintain non-equilibrium behaviour , it is necessary to maintain *pD* scaling, where *p* and *D* stands for pressure and for the smallest dimension of plasma volume, respectively.[18–20] At atmospheric pressure, this implies that at least one dimension of the plasma volume should be reduced to less than 1 mm. In these cases, APPs are referred to atmospheric pressure microplasmas (APμPs). Table 1 shows the different aspects of the microplasma and conventional plasma.

Microplasmas have unique characteristics such as non-equilibrium thermodynamics,[21,22] non-Maxwellian electron energy,[23] excimer generation[24–26] and new sheath dynamics.[27] APμPs offer distinctive features such as: [28]

(1) High-pressure chemistry: the collision rate is significantly high at high pressure and lead to favourable conditions for particle formation.[29] Higher radical density leads to efficient particle nucleation.
(2) Continuous-flow: in APμPs plasma residence time is short, which can help to prevent agglomeration.
(3) Microreactor geometry: Because of the nanoliters reactor volume with the normally used gas flow rate ($\geq$ 100 sccm) reduces residence time distribution significantly.

2.3.2 Basic concepts of microplasma

When the plasma volume is confined into small dimensions, the properties and physical behaviour of the plasma changes. The surface to volume ratio increases as the plasma size decreases which leads to enhanced plasma stability. According to Paschen's law, the gas breakdown voltage used to initiate a direct-current discharge increase at high pressure. Breakdown voltage can be reduced back by decreasing the electrode gap, which however impacts the overall electric field distribution, charge distribution, energy distribution of different species (electrons, ions, radicals, neutrals) and overall plasma neutrality. Traditional properties and scaling laws of plasma do not apply at these scales and justify a different regime of operation sometime called microplasma regime (MPR).

At steady-state, the power transferred to plasma should be equal to power lost. Because of the volumetric confinement, electron temperature and density tend to increase.[21,30] Also, electrons gain energy through strong electric fields and exchange it with other species, i.e. neutrals, ions, etc.[31] Overall the plasma energy balance is determined by the electron density and the energy exchange rate through inelastic collision (e.g. vibrational and rotational energy exchange). This energy balance analysis can be used to understand non-equilibrium. A basic relationship holds:[28]

$$p \propto \frac{T_g^{\frac{3}{2}}}{D^2 \varepsilon n_e K_e} \qquad (1)$$

where, p is the pressure, D is a characteristic dimension of the plasma, T_g is the gas temperature, ε is the average energy exchanged in each collision, n_e is the electron density and K_e is the collision rate. Figure 2.5 represents the relation between pressure (p) to the dimension of plasma (D). Thermal equilibrium is shown by a solid curve where temperature of heavy species (ions and neutrals) is the same as the electron temperature ($T_g = T_e$). Molecules and ions in plasma are effectively heated by electron collision. The grey area in figure 2.5 represents the non-equilibrium regime where electron collision does not heat the gas effectively and the gas temperature is kept below the electron temperature ($T_g < 0.1\ T_e$). This gray area regime allows enough energetic gas chemistry to synthesize materials without increasing the T_g. T_g can be as low as room temperature in this regime. In the region between $T_g = 0.1T_e$ to $T_e = T_g$, plasmas are likely to be thermally unstable.

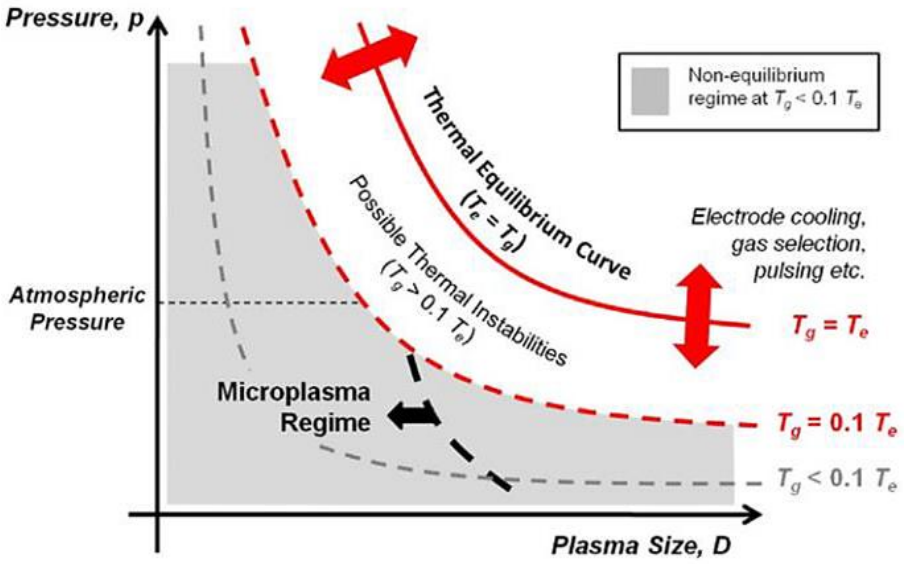

Figure 2.5: Shows the transition from thermal equilibrium to non-equilibrium as a function of pressure (p) and plasma size (D). It shows the MPR where gas temperature is considerably lower than electron temperature. T_g and T_e stand for gas and electron temperature, respectively.[28]

This plot is sensitive to input power, electrode geometry, gas composition, gas flow rate etc. A change in the configuration or operating conditions can shift the thermal equilibrium curve so that non-equilibrium behaviour can be achieved in a somewhat wider range of volume-pressure combinations. For example, if input power increases, the thermal curve shifts downwards to the left and decreases the non-equilibrium region. Another aspect is if the heat removal can be increased by applying a cooling system, this would shift the thermal curve upwards and non-equilibrium region will enlarge. Further, if pressure increases in region right to the MPR, this plasma approaches thermal equilibrium. But by decreasing plasma dimensions, it can be shifted into the region where non-equilibrium behaviour as well as working at atmospheric pressure can be achieved.

In summary, the wide range of plasma parameters allows for a range of possibilities to work within a non-equilibrium regime and figure 2.5 above highlight the opportunity of non-equilibrium APμPs.

2.3.3 APµPs reactor configurations

Various microplasma configurations with different electrode geometries have been developed, which can use various methods of power supply, including direct-current (DC) and radio frequency (RF) ranging from kHz to GHz. While originally most microplasma systems relied on the synthesis of nanoparticles in gas-phase, recently synthesis in the liquid phase by coupling microplasma to a solution have found widespread investigation.

a) *Gas- phase* APµPs reactor

Here, the nanoparticle formation happens in the gas phase. Various gas-based system configurations can be used in the production of nanoparticles as described below.

(i) Hollow-electrode microplasmas

In this design, generally two hollow metal capillary tubes are separated by 1-2 mm, connected to a power supply. These two hollow tubes act like cathode and anode and as a precursor transporter as shown in figure 2.6. The precursor is introduced in vapour form with a carrier inert gas such as Ar/He and dissociation take place in the plasma volume between the two electrodes. The voltage and current are in the range of hundreds volt and several mA, which are suitable conditions to prepare nanomaterials and too small to ionize electrodes. Synthesised materials have been collected by an electrostatic precipitator or by a filter placed next to the reactor.

Chiang and Sankaran[32] used this design to synthesize iron nanoparticles. Particle size and distribution was measured by a cylindrical differential mobility analyser and an ultrafine condensation particle counter attached to the reactor. They also used these nanoparticles as a catalyst for the growth of carbon nanotubes. They studied catalytic properties of different compositional-tuned Ni_xFe_{1-x} nanoparticles. A similar reactor was used to produce multi-metallic nanoparticles.[33] Different organometallic compounds were used, such as Ni(Cp)2, Fe(Cp)2, Cu(acac)2, Pt(acac)2 (Cp= cyclopentadienyl and acac = acetylacetonate), to produce multi-metallic particles with various composition by varying precursor flow rates. Hollow-electrode geometry was also used in nanodiamonds[34] formation.

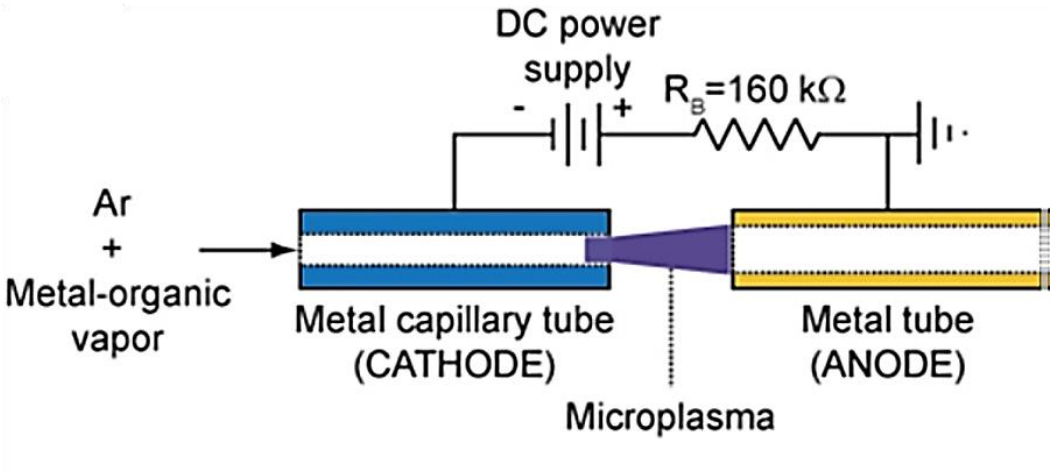

Figure 2.6: Schematic diagram of hollow-electrode microcharges.[32]

(ii) Microplasma jets

Various microplasma jet configurations with different type of power supplies (DC, RF or microwave) have been used for nanomaterial fabrication. Three parameters should be considered carefully in microplasma jets:[35] (1) location control of deposition area by regulating precursor flow by using capillaries etc. (2) managing consumable wire in case of wire precursor microplasma jet system (3) power supply coupling to the plasma system.

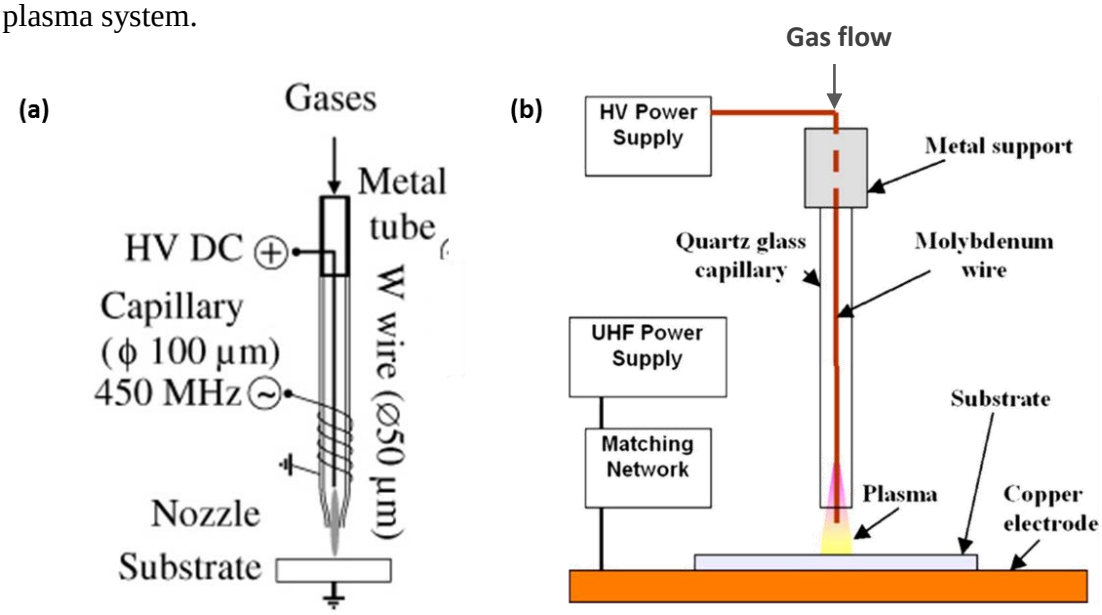

Figure 2.7: Different arrangements electrodes for microplasma jets.[36–38]

Figure 2.7 shows different examples of microplasma jets. In figure 2.7a, the microplasma generator consists of a capillary (100–500 µm inner diameter) made of quartz or alumina joined to a metal tube where the gases are injected, and a tungsten wire (50 µm in diameter) inserted into the capillary. This capillary is wound around by

a 5-turn coil whose end is connected to a 450 MHz UHF generator (5–30 W) via a matching circuit, while the other end is grounded. Plasma ignition was ensured by 15 kV DC power source.[36] Tungsten oxide nanoparticles were formed in the process. Figure 2.7b, a Mo wire was used as precursor and electrode and connected to high voltage power source. Ar/O_2 mixtures were used to produce plasma. Synthesized material was collected onto Si substrate connected to copper electrode. Microplasma was ignited between Mo wire and Si substrate and MoO_x nanomaterial was obtained.[37] Different metal wires have also been used, such as Mo,[39] Au,[40] Cu[41] etc., to produce nanomaterials with microplasma jets. Various gases Ar, He, N_2, H_2, O_2 or their mixtures injected into the capillary to form plasma. Different nanomaterial structures can be formed by controlling gas flow, gas composition, substrate distance and input power.

(iii) Nanostructure growth on substrate by microplasma

Figure 2.8b shows another type of microplasma where a hollow tungsten carbide (WC) tube cathode, Ar carrier gas and RF power supply was used. The WC tube is connected directly to the Fe-coated Si substrate. The distance between cathode and the substrate was 3 mm. The plasma was formed between the substrate and the cathode. A methane gas line was introduced into the microplasma afterglow and different parameters, i.e. plasma exposure time, plasma power and gas flow rate/composition was studied. A mixture of carbon nanotubes and Si nanowires/nanocones were formed via $FeSi_x$ catalytic growth, Si diffusion and oxidation.[38]

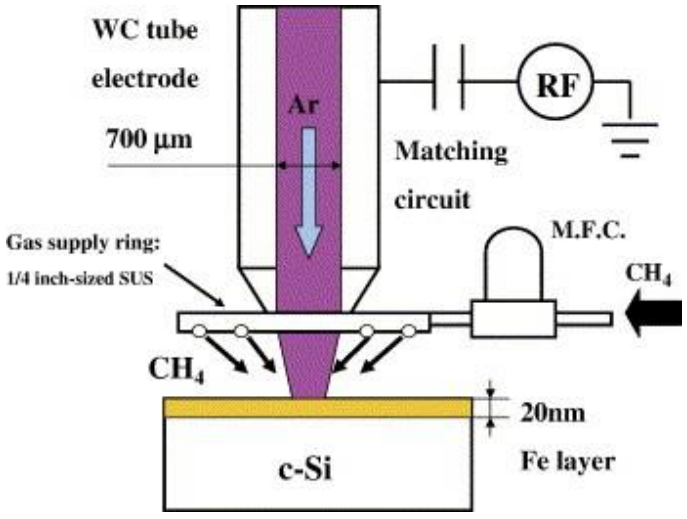

Figure 2.8: Microplasma system to produce Si-CNT mixture on the Fe-coated Si substrate. [38]

b) *Liquid-phase* APµPs reactor

Here, the nanoparticle formation happens in the liquid phase. Various liquid based system configurations can be used in the production of nanoparticles as described below. Microplasma coupled to liquids represents a new approach to form colloidal nanoparticles in solution where the bulk liquid is at ambient condition. More than nanoparticle synthesis, liquid phase microplasma can be a potential guidance for various application e.g. surface engineering,[42] flame electrochemistry,[43] spectrochemical analysis,[44] wastewater remediation[45] etc. Several hybrid plasma-liquid systems have been developed. Mainly, one where plasma is produced at the surface of liquid (figure 2.9a) and another where plasma is inside the liquid (figure 2.9b).

Figure 2.9a shows plasma generated at the surface of liquid, used for the synthesis of Au nanoparticles from $HAuCl_4$. In this case, a stainless steel (SS) capillary tube is used as cathode and a Pt foil as anode; He was used as gas plasma. Au NPs were formed near the solution surface where plasma interacted with the liquid. It was found that particle size very much depends onto the process parameters such as solution temperature, current, starring rate etc.[46] The same method was used to synthesise several other nanoparticles (Fe_3O_4,[47] Ag,[48] Cu_2O[49] etc).

By moving plasma inside liquid allows increase in pressure more significantly because of high density of liquid.[50] Due to this, many highly reactive species are created in the liquid phase (e.g. $OH^{\cdot}$, $H^{\cdot}$, $O^{\cdot}$, H_2O_2, O_3 etc.), which can be effectively utilized to promote various reactions leading to surface engineering of materials. In the gas phase, plasma energy coupling to the electrons can heat up bulk gas while in liquid phase, solution can act as a heat sink and dissipate the heat quickly and maintain non-equilibrium state.[50]

Figure 2.9b shows a setup where microplasma is inside the liquid, for preparing water-soluble CNTs. To enhance the discharge between electrodes, O_2, N_2 and Ar bubbling gases were used. Microplasma was generated by high pulsed voltage. In this experiment, commercially available CNTs were used with deionized water. This solution was treated with microplasma. They showed that because of excitation and ionization of H_2O molecule generate $H^{\cdot}$ and $O^{\cdot}$ radicals. Because of strong oxidative nature of $O^{\cdot}$ produced $OH^{\cdot}$ by reacting with $H^{\cdot}$. This hydrophilic $OH^{\cdot}$ Groups attached

to the CNT surface and water solubility was achieved.[51] With surface modification, this method can be used in producing other nanoparticles e.g. Au[52] etc.

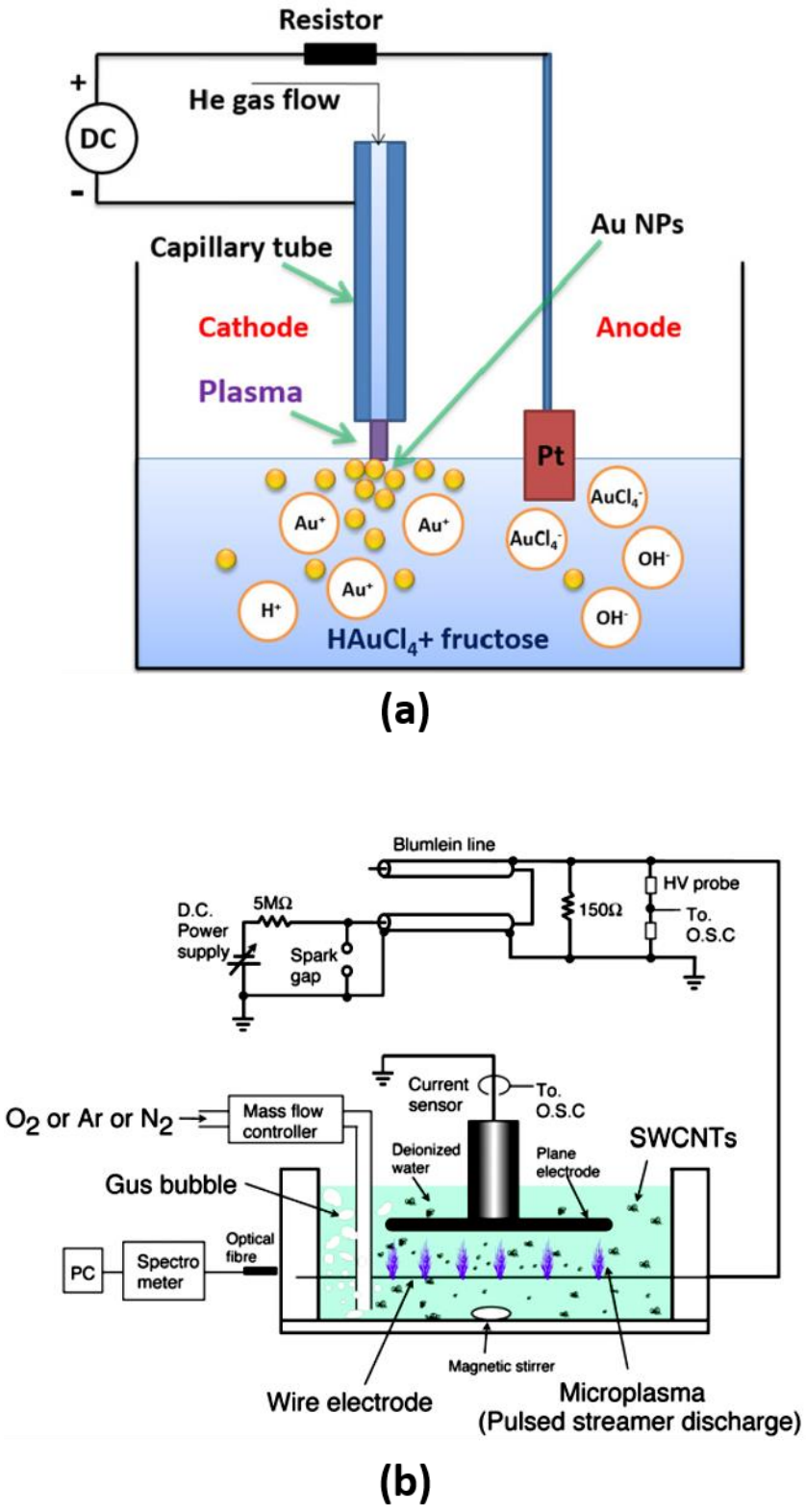

Figure 2.9: Schematic of hybrid plasma-liquid where (a)plasma is produced at the surface of liquid [46] and (b) plasma produced inside the liquid.[51]

2.3.4 Formation of nanoparticles in the microplasma

(i) Nanoparticle formation in the *gas-phase* microplasma

Nucleation and growth of nanoparticles in APμP is not fully understood and very few reports are present. The ability of microplasma to form nanoparticles of high-melting point materials in comparatively lower gas temperature makes it more interesting to understand the growth process.

According to fewer studies, surface heating of particle is considered to be the main mechanism for growth of nanoparticles in the APμP.[53,54] APμP has shown the ability of heating particle to temperature above the crystalline threshold. Because of high electron density, electron interaction with the charged species, e.g. recombination of ions with electron etc., considered to be the main source of the particle heating. Therefore, nucleation and particle growth in APμP requires higher radical densities for nanoparticle formation.

(ii) Nanoparticle formation in the *liquid-phase* microplasma

In the liquid-phase microplasma, nanoparticle formation and processing can be very complicated. This liquid-phase based microplasam systems are not understood completely to understand nanoparticle formation in the process.

A purposed mechanism is discussed here where, similarly to the synthesis in gas phase, radicals, ions, neutrals and photons are generated but these species now interact with a liquid phase and initiate cascaded reaction in the liquid including electrons. Figure 2.10a shows schematic diagram of plasma interaction with liquid where electrons from the plasma can initiate non-equilibrium cascaded reactions at plasma-liquid interface (figure 2.10b) and in the volume below the plasma-liquid interface (figure 2.10c). This cascaded chemistry mainly depends on molecular potentials and reaction activation energies.[42] Electron reaches in the liquid volume in the form of transient species (e.g. hydrated electrons, partially solvated electron etc.) and have only potential energy. Therefore, behaviour of these electrons described within the electrochemical or physical chemistry laws. The travel path of these electrons in the liquid depends on binding state of the electron, the solvent and electron density.

This hybrid plasma-liquid approach is different than electrochemistry-based approaches. Here, reduction can be controlled without reducing agent and without any undesired product formation. The most studied system is the production of gold nanoparticles where aqueous solution of $HAuCl_4$ is used. Electrons induce the reduction of the Au-salt to form Au^0 atoms.[42] Nucleation happens by collision of Au atoms and grows in large NPs. Nanoparticles growth continues until the precursor is present in the solution. At higher precursor concentration, larger particles are formed because of reduced length between Au^0 atoms.

Overall, APµPs have proved to be a powerful technique to synthesize nanomaterials with wide variety of reactor configuration and parameter controls. One of the major drawback of APµPs still remains the low yield and low throughput of the process; while this has not been solved completely, viable engineering solutions are being investigated (e.g. reactors in parallel arrangement).[55]

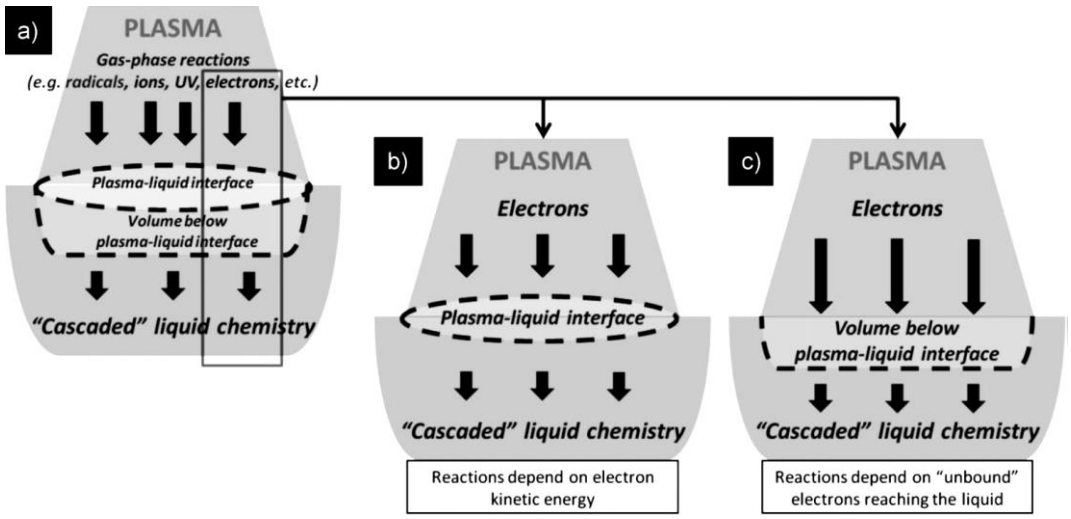

Figure 2.10: Schematic diagram presenting three different type of reaction happens in plasma-induced liquid reaction (a) gas-phase species and plasma induces liquid reactions where electrons initial non-equilibrium reactions on the plasma-liquid interface, electron energy distribution (b) and electron density plays important role (c).[42]

2.4 Zinc (Zn) nanostructure compounds

2.4.1 Introduction to zinc-based compounds

Zinc (Zn) is an important element in the periodic table because of its use in a wide variety of applications. Zinc is used in galvanising other metals to prevent rusting and for instance galvanised steel is used in car bodies, street lamps, safety barriers,

suspension bridge etc. to prevent them from environmental damage. Zinc is also used in die-casting in automobile, electrical and hardware industry and is a key component in preparing alloys such as brass. Even in biological systems, zinc is found as an active site for many enzymes. In nature, zinc is present in zinc sulphide and calamine ores.

Zinc compounds, such as ZnO, doped ZnO, ZnS are also used in many applications. ZnO is the most used compound of Zn and it has been used in electronics, as a transparent electrodes and light-emitting diodes, rubber industry, paints, cosmetics, pharmaceuticals, batteries etc. Zinc sulphide is used in luminous paints, fluorescent lights and x-ray screens.

2.4.2 Zinc oxide (ZnO)

ZnO has a wurtzite hexagonal structure (space group *p*6*mc*) with lattice parameters *a* =0.3296 nm and *c* = 0.52 nm. Basic properties of ZnO are given in the table 2. The ZnO structure is composed of several alternating planes composed of tetrahedrally coordinated O^{2-} and Zn^{2+} ions stacked alternatively along the *c*-axis as shown in figure 2.11. This non-central symmetric structure is responsible for piezoelectric and pyroelectric behaviour of ZnO, which can be used in sensors, converters, energy generators and photocatalysts for hydrogen production. ZnO hardness, rigidity and piezoelectric constant make it also interesting for the ceramic industry while low toxicity, biodegradability makes it suitable in biomedical applications.

ZnO is a wide bandgap (3.37 eV) semiconductor with high excitonic binding energy (60 meV), high chemical, thermal and mechanical stability at room temperature makes it useful candidate in electronics, optoelectronics and laser technology. Transparent nature of ZnO is used in many industries for transparent electrodes in flat panel displays, low emissivity coatings, touch screens, thin film solar cells etc.[56] Another use of ZnO is in electronic devices like photocatalyst, photo detectors, light emitting diodes or power devices.[57–59] Various morphologies such as nanoparticles, nanoballs, nanoflowers etc. have attracted attention in photocatalytic degradation of organic dyes.[60–63] This is because of their high photocatalytic efficiency, non-toxic nature and low cost.[64]

One important feature of ZnO is the polar character of its surfaces. Because of the positively charged Zn-(0001) plane and negatively charged O-$(000\bar{1})$ plane, surfaces

result in a dipole moment and polarization along the c-axis as well as a divergence in surface energy. ZnO favours faster growth in the three directions $< 2\bar{1}\bar{1}0 >$, $< 01\bar{1}0 >$ and $< 0001 >$ which have polar surfaces and tuning the growth rate it is possible to achieve various novel morphologies. ZnO nanostructures include nanorods,[66,67] needles,[68,69] ribbons,[70] nanowires,[71] nanosheets,[72,73] nanoflowers,[74] tetrapods[75], porous

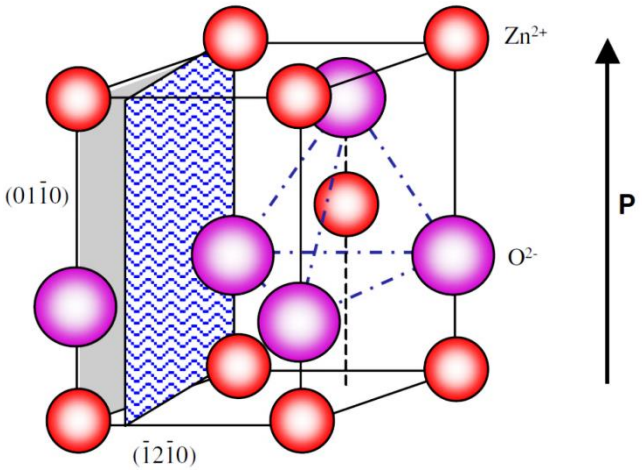

Figure 2.11: The wurtzite structure of ZnO with tetrahedral coordination of Zn-O.[65]

Table 2: Basic properties of Zinc Oxide (ZnO).

Property	Value
Lattice parameters at 300 K:	
a_0	0.32495 nm
c_0	0.52069 nm
a_0/c_0	1.602 (1.633 for ideal
u	0.345
Density	5.606 g/cm^3
Stable phase at 300 K	wurtzite
Melting point	1975°C
Thermal conductivity	0.6, 1-1.2
Linear expansion coefficient	a_0: 6.5 × 10^{-6},
Static dielectric constant	8.656
Refractive index	2.008, 2.029
Energy gap	3.4 eV (direct)
Intrinsic carrier concentration	<10^6/cm^3
Exciton binding energy	60 meV
Electron effective mass	0.24
Electron Hall mobility at 300	200 cm^2/V·s
Hole effective mass	0.59
Hole Hall mobility at 300 K	5-50 cm^2/V·s

ZnO[76] etc. Different synthesis methods have been used to synthesise ZnO nanostructures, e.g. mechanochemical process,[77] precipitation,[78] precipitation in the presence of surfactant,[79] sol-gel,[80] solvothermal,[81] hydrothermal,[82] microwave technique,[83] emulsion and microemulsion technique,[84] atmospheric pressure plasma[76,85,86] etc.

Nanowires are probably the most studied nanostructures of ZnO. Their outstanding electronic, photonic and piezoelectric properties makes it useful the solar cells,[87] sensors,[88] UV lasers,[89] nanogenerators,[90] LED[91] etc. However, a range of factors can play crucial roles in determining application device performance, such as vertical alignment of the nanowires, distribution density, defect-free crystallinity etc. The control over these properties during the synthesis process is therefore very important to improve the device performance.

Borah *et al.* synthesized highly dense NWs on graphene foam to construct an ultraviolet (UV) detector.[92] This UV detector showed fast response and recovery times at 9.5 s and 38 s with external quantum efficiency of 2490.8 % at low illumination power density of 1.3 mW/cm^2. A pressure sensitive Si/ZnO nanowire heterostructure matrix LED array was also developed.[93] A piezo-phototropic effect was observed where strain induced piezo-polarization charges efficiently modulate the LED emission intensity. As the external strain increases, the emission intensity increases and then decreases with a maximum value at a compressive strain of 0.15-0.2%.

Many other ZnO nanostructures have been used in many different applications. Porous ZnO is successfully used in the fabrication of photoanodes for dye sensitised solar cells,[94–96] in the photocatalytic degradation of various dye molecules,[97,98] for gas sensors[99–101] etc. A porous ZnO thin film combines the following features: (1) interesting ZnO properties such as antibacterial activity, piezoelectricity, biocompatibility etc. (2) high surface area because of porous nature and (3) thin film area allows preparation of large-area substrate materials in a controllable and repeatable way. Physical vapour deposition methods are found to be most successful methods. In this process, adsorption of atoms/molecules on a substrate surface is driven by physisorption, i.e. Van der Waal forces or chemisorption. Nucleation and coalescence take place after adsorption. Porous ZnO structure were prepared by template based solution-dipping method as shown in figure 2.12.[102]

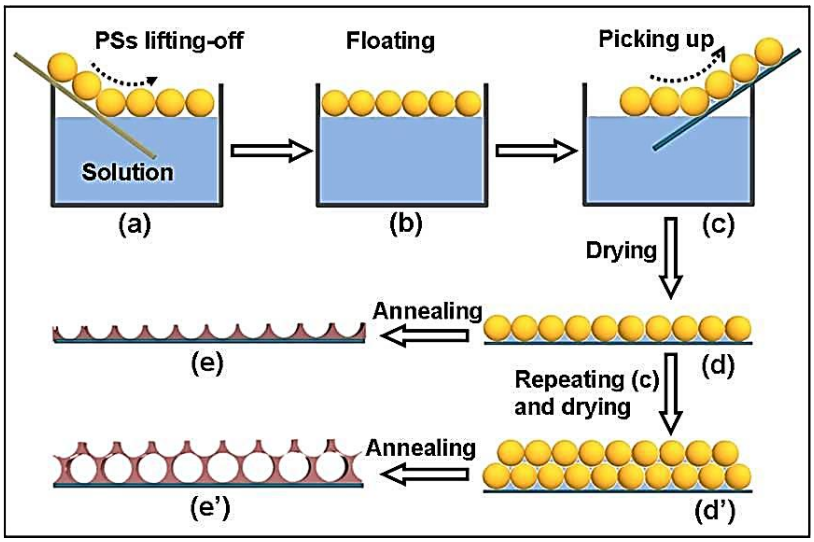

Figure 2.12: Schematic illustrate fabrication of multi-layer ZnO ordered porous films. (a) The PS monolayer colloidal template on a glass slide is dipped into the prepared precursor solution [0.02 mol/L Zn(O2CCH3)2]. (b) The PS template lifts off the glass substrate, due to surface tension of the solution, and floats on the solution surface. (c) The floating PS template is transferred, by picking it up, onto an Al_2O_3 flat ceramic substrate installed with two Pt electrodes or silicon wafer or quartz glass substrate. The picked-up PS template also contains the solution in the interstitials among PSs due to the capillarity. (d) The solution-dipped monolayer PS template is covering on the substrate after drying. (d') The solution dipped bilayer PS template is covering on the substrate after repeating (c) and drying. (e) The monolayer ZnO ordered porous film is fabricated on the substrate after annealing at 450 0C for 2 hours to remove PS template, (e') The bilayer ZnO ordered porous film is fabricated on the substrate after annealing at 450 0C for 2 hours to remove PS template.[102]

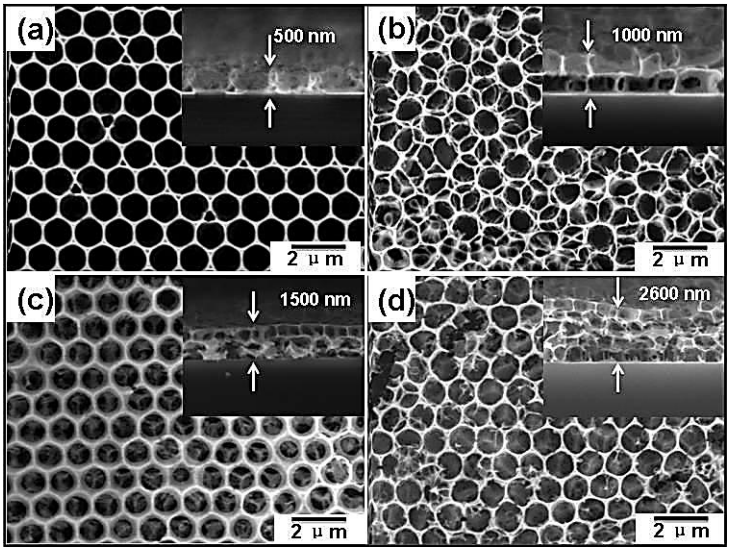

Figure 2.13: FESEM images of the ZnO porous thin films with different thicknesses on the silicon wafer substrate, prepared by the layer-by-layer strategy based on solution-dipping of monolayer PS template and transfer (Fig. 19). (a)Monolayer, (b)Bilayer, (c) Trilayer, and(d) Tetralayer. The insets are the corresponding cross-sectional images.[102]

Polystyrene (PS) was used as template and dipped into 0.02 mol/L $Zn(O_2CCH_3)_2$ zinc precursor solution. After annealing, porous ZnO structure was constructed (figure 2.13), where repetition of the process led to the formation of four layers as shown in figure 2.13d. Light illuminated NO_2 sensing was performed with this porous structure. The results showed that a high concentration of NO_2 increased the response of the thin film. Film thickness also increased the sensitivity towards NO_2 detection, but the response rate was reduced for thicker films. Porous ZnO are also used as photoanodes in dye sensitized solar cells. These high surface area porous layers allow optimal dye load and resulting into solar conversion efficiency of 4.58%.[96] Chen *et al.* prepared a porous ZnO electrode by cathodic electrodeposition using aqueous zinc nitride precursor and polyvinylpyrrolidone surfactant. The porous structure was made up of hexagonal wurtzite crystalline grains of 20-40 nm. The final photoanode of an optimized 8 μm thickness showed conversion efficiency of 5.08%.[103] In another report, squarine-sensitized mesoporous ZnO showed larger photocurrent and solar to energy conversion efficiencies than standard TiO_2-based electrodes sensitized with the same dye.[104] Porous ZnO matrix also showed suitable applicability for energy storage and for instance stable specific high capacity of 50μA.h.cm^{-2} and high Coulombic efficiencies were produced when tested in lithium cells for prolonged time.[105] Porous ZnO also showed superior piezoelectric properties[105] than conventional dense microstructure films.[106] Finally, porous ZnO structures were also used for dye degradation. The photo-degradation rate of pollutant, mainly methylene blue (MB) and Congo red, was higher for large-diameter pore containing ZnO than narrower pores (8 nm).[97]

Among the different ZnO nanostructures (e.g. nanowire, nanoneedles, nanoflowers), zero-dimensional ZnO quantum dots (QDs) have higher stability and resistivity toward oxygen and water with bandgap tunability.[107]QDs are manmade semiconductors with diameter close to or below the Bohr radius. At these dimensions, material optical and electronic properties drastically change. The emission properties of QDs can be controlled by their shape and size and the emission energy show an inverse nature with particle size (figure 2.14a). Electrons can be excited to the conduction band from the valence band by absorbing light and creating a hole in the valence band. This electron-hole pair can recombine by emitting a longer wavelength photon. Generally, as the particle size decreases, the bandgap increases (figure 21b). Because of these tunable

properties, ZnO QDs have been studied for various applications such as QD-based LEDs,[108] narrow-band width QD photodetectors,[109] single-electron transistors[110] etc.

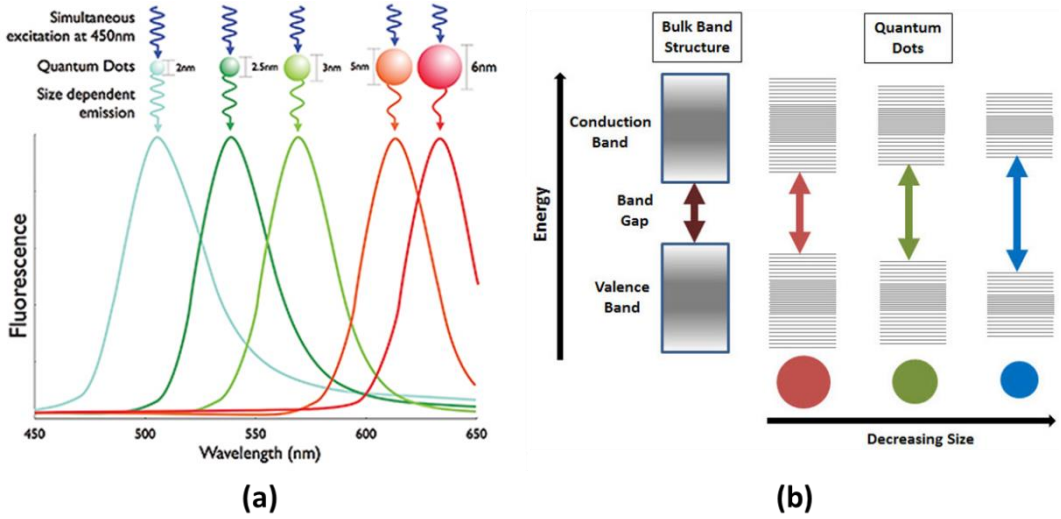

Figure 2.14: (a) Blue shift in the emission wavelength as the particle size decreases, (b) Increase in band gap with decrease in size and change in the electronic structure.[111]

Three-dimensional quantum confinement of carriers can improve the optoelectronic properties of ZnO QDs by increasing carrier life-time and enhancing photoluminescence. However, controlling these properties is challenging because these are determined by defects such as oxygen/zinc vacancies and oxygen/zinc interstitials.[112] QDs are unique in this respect because are less prone to deeper structural defects and tend to segregate defects at the surface. However, at the same time, the impact of surface defects is stronger than in bulk and the understanding of the resulting more complex optoelectronic properties can be difficult. It has been observed for instance that quantum confined systems can enhance excitonic emission from ZnO but still have surface defects related emissions.[113] Because defects are at the surface, they can be easily accessed, and passivation strategies can offer opportunities for controlling as well as tuning these properties, particularly emission properties.[114,115]

When the particle size of ZnO is below 7 nm, quantum confinement effects start to dominate.[116] Nevertheless, QDs are prone to surface defects more than defects in the core of QDs. ZnO photoluminescence is observed from both the UV and the visible region, the first related to excitonic emission and the latter corresponding to defect related emission. Because of the higher probability of surface defects in QDs, a stronger excitonic emission is generally observed.[113] However, surface dangling bonds

and active surface energy makes ZnO QDs prone to agglomeration. As a result, when agglomerated quantum confinement effect may be reduced and lead a red shift in the emission spectra.[117] Stable long-term PL of QDs can only be observed with the passivating of surface defects (see section 5.2). ZnO QDs also showed strong visible luminescence due to the small size of ZnO QDs. A size-dependent study showed that the change in the emission properties are more related to the size than to oxygen vacancies.[118] Such tunable emission properties in QDs are attractive for many applications. However, size and surface states are strongly determined by the synthesis process.

ZnO QDs have also been used in combination with other materials to create high performance sensors and ultraviolet detectors.[56,119] A heterojunction high-performance ultraviolet photodetector was fabricated with ZnO QDs decorated on Zn_2SnO_4 NWs.[119] In comparison to pristine Zn_2SnO_4 NWs, ZnO QDs-Zn_2SnO_4 NWs showed 10 times higher responsivity (figure 2.15a) and photocurrent (figure 2.15b).

The electron concentration and lifetime were increased in the NWs conduction channel because of the hole migration in the ZnO QDs, which improved the photo-response. In another report a ZnO QD/graphene heterojunction showed extraordinary quantum efficiency in visible-blind ultraviolet (UV) detection because of strong quantum confinement in ZnO QDs and high charge mobility of graphene.[56] These hybrid systems are more efficient than conventional materials because of (1) strong quantum confinement effects (e.g. higher light absorption, charge mobility and spectral tunability, (2) efficient photo-carrier generation because of superior exciton dissociation and charge transfer at the interface and (3) high photoconductive gain.

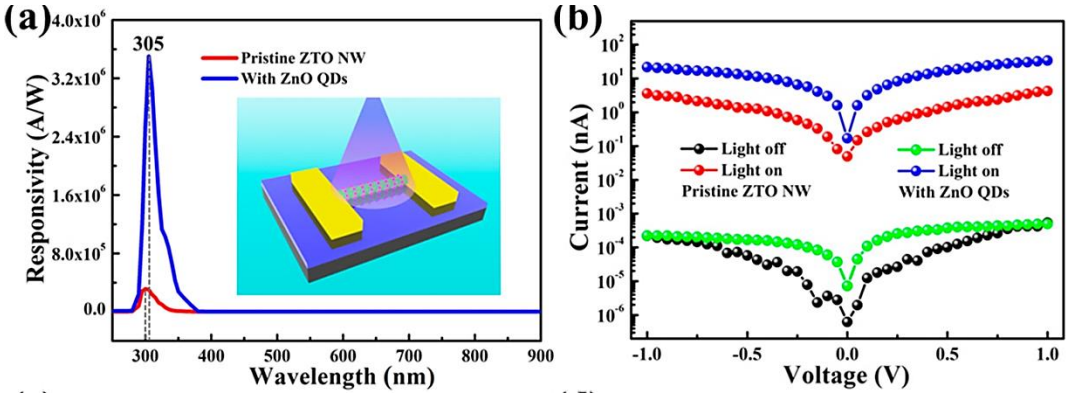

Figure 2.15: Performance characterization of the photodetectors. (a) Spectral responsivity of photodetectors made of a pristine ZTO NW and a ZnO QD decorated ZTO NW at different wavelengths ranging from 250 to 900 nm at a bias voltage of 1 V. The inset is the schematic illustration of the as-fabricated photodetector on a SiO2/Si

substrate. (b) I−V curves of two kinds of photodetectors under dark and 300 nm UV illumination with a light intensity of 0.67 μW/cm2.[119]

2.4.3 Doped ZnO

As described above, ZnO nanostructures have shown attractive properties for a vast variety of applications. In order to improve further some of the properties of ZnO nanomaterials, compositional modification can be introduced, e.g. by doping ZnO.[120] Using a transition metal as dopant (e.g. Co, Cu), photocatalytic properties can be improved because the dopant metal create a trap site for electron or hole from ZnO and restrain their recombination.[64,121,122]

In next generation of inorganic LED and laser, ZnO is a potential substitute for GaN and its derivatives which are costly and energy consuming. In this context, , there has been much effort in trying to produce p-type conductivity in ZnO.[58] However, ZnO is an n-type conductor because of intrinsic doping of hidden hydrogen atoms in ZnO lattice which are responsible for shallow donor levels.[123] The most challenging hurdle here is to produce stable p-type conductivity in ZnO by over-compensating the n-donor contribution. Doping in compound semiconductors is more complex than elemental semiconductors (e.g. Si, Ge) and there is the possibility of forming oxidic phase of the dopant, for example in Al-doped ZnO for instance $ZnAl_2O_4$ and Al_2O_3. Most common dopants used to generate p-type conductivity are Li, P, As and N. Nitrogen and oxygen have strong similarities in terms of ionic radius and energy positioning of their 2p-orbitals. Many reports have been presented to prepare N-doped ZnO with no success in achieving the p-type character.[124–128] However, photocatalytic properties can be improvd with N-doped ZnO.[129–132] Because of nitrogen doping, the particle size was oseen to decrease, and the absorbance in visible light increased.[132] Nitrogen doping also improved the emission properties.[133] Altogether, ZnO properties can be tuned and can change drastically with doping. Doping concentration and intrinsic defect compensation play an important role in overall property change.

2.4.4 Zinc peroxide (ZnO_2)

ZnO_2 is known for and historically used as surgical antiseptic; however it is used also in several other technologies and processes such as in the rubber industry where ZnO_2 is applied to accelerate vulcanization of nitril-carboxyl rubber to produce attrition resistant rubber,[134,135] photocatalysis,[136] for the synthesis of ZnO,[137] for H_2O_2

production,[138] cosmetic and pharmaceutical industries and for therapeutic applications.[139,140]

Many processes have been used to synthesize ZnO_2: from organometallic precursors,[141,142] hydrothermal process,[143,144] laser ablation of solids in liquids (LASL),[139,145] sol-gel[140] and many more.[136,146,147] Kim *et al.*[141] used zinc (II) isobutylcarbamate ($Zn(OCONHC_4H_9)_2$ with H_2O_2 at 60 ^oC to produce ZnO_2 while Chen *et al.*[142] used another metal-organic precursor such as $Mg(C_6H_{11})Cl$ to complete the reaction for the synthesis of ZnO_2 with $ZnCl_2$. In hydrothermal processes, the hydrothermal decomposition of zinc acetate aqueous solution with H_2O_2 produces ZnO_2.[144] Alternatively, hydrothermal reaction of zinc oxide and H_2O_2 at 80-140 ^oC for 20 h produces ZnO_2. Drmosh *et al.*[145] obtained nanoparticles through the irradiation of a Zn plate through an Nd–YAG laser, with a wavelength of 355 nm, which resulted in nanoparticle with diameters ranging from 3 nm to 4 nm. They used various surfactants such as sodium dodecyl sulfate (SDS), cetyltrimethylammonium bromide (CTAB) and glycol monododecyl ether (OGM) to understand the effect on size and morphology. Sun *et al.* used a 35 W Xenon lamp to irradiate an aqueous solution of zinc acetate dihydrate and 30% hydrogen peroxide to start ZnO_2 formation through a sol-gel process. The lamp spectral irradiance was similar to that of sunlight, which was required to form zinc peroxide from the precursor zinc acetate. The solution irradiation time was 6 h under continuous stirring to obtain a ZnO_2 precursor sol. After two days aging, the sol was baked at 40 ^oC overnight which resulted into ZnO_2 nanoparticles synthesis. The reaction temperature and reaction time were of great influence to obtain either sol or gel. Additionally, they observed that a temperature over 200 ^oC leads to the zinc peroxide transformation into pure zinc oxide with high crystallinity. Overall, most of the techniques that have been used for ZnO_2 are complex processes in terms of required chemical precursors, reaction time (like sol-gel more than 2 days) and control on size by surfactant etc. Here, we will present a very simple process for the synthesis of ZnO_2.

2.4.5 Zinc Nitride

Zinc nitride (Zn_2N_3) is another semiconducting compound of zinc. It has the anti-bixbyite structure as shown in figure 2.16a. In anti-bixbyite structure, metal atoms are in the tetrahedral sites of an approximately cubic close packed array of N atoms. N

atoms occupy the two positions in the lattice which are 8b (¼ , ¼, ¼ etc.) and 24d (x, 0, ¼ etc.) as shown in figure 2.16b.[148] Basic properties of Zn_2N_3 can be seen in table 3.

Zn_3N_2 was first synthesized by Juza and Hahn[149] in 1940 but did not find much interest until 1993. Zn_3N_2 is an II-V material blackish-grey in colour and has a cubic crystal structure. Zn_3N_2 has n-type conductivity, low resistivity, high mobility and high carrier concentration. It is a suitable optoelectronic material for infrared sensors, smart windows and energy conversion devices.[150] The low cost of its element makes it an excellent choice for mass production. Various methods have been used to synthesize zinc nitride films, including RF magnetron sputtering, RF plasma-assisted pulsed laser deposition, molten salt electrochemical process, direct reaction between evaporated Zn and NH_3 etc. and a wide range of bandgap values have been reported, from 0.9 eV to 3.2 eV. Different morphologies have been also observed that include nanoneedles,[151] nanowires,[152] empty balls,[153] and hollow structures.[154,155]The different synthesis methods have also produced diverse films with varying crystallinity and with varying degree of vacancy and interstitial defects. In 1993, Kuriyama *et al.*[156] synthesized polycrystalline Zn_3N_2 by reaction between evaporated metallic zinc and NH_3 gas and with high substrate temperature of 683 K.

RF magnetron sputtering[159] was used to prepare polycrystalline Zn_3N_2 using different N_2 concentration. As the N_2 gas concentration was increased from 5% to 100%, pure phase Zn_3N_2 could be produced. The bandgap in this case was from ~1.23 eV to 1.6 eV. In 2005, Zong *et al.*[168] used a nitridation process to produce Zn_3N_2 from zinc powder in the presence of ammonia gas. X-ray diffraction showed the cubic structure and electron microscopic analysis revealed spherical shell morphologies. While details of the bandgap were not provided, this process showed the possibility of Zn_3N_2 synthesis by nitridation from zinc powder. The same nitridation process could be used for the synthesis of Zn_3N_2 nanowires, exhibiting a bandgap of 3.22 eV; this result was in good agreement with the results of Kuriyama *et.al.*[152] but much larger than other reported values, e.g. 2.3 eV[160] and 1.23 eV.[159]

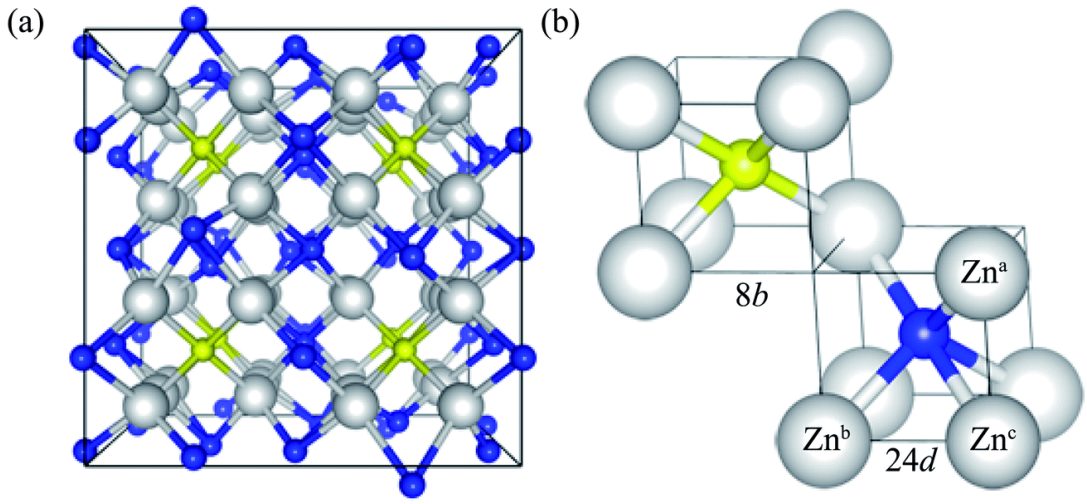

Figure 2.16: (a) shows the atomic structure of Zn_2N_3 and (b) shows the special arrangement of zinc and nitrogen atoms; nitrogen atoms shows two positions (8b and 24d wyckoff position).[157]

Table 3: Basic properties of Zn_2N_3.[158]

Crystal structure	anti-bixbyite (*Ia*3 space group)
Lattice parameter	9.769 Å
Energy bandgap	1.25-3.2 eV
Density	6.22 g/cm3
Mobility	100-350 cm2/V s
Carrier concentrations	1018-1020 cm-3
Refractive index (n)	2.5 (@ 2.0 eV)
Extinction coefficient (k)	0.7 (@ 2.0 eV)
Electron effective mass	0.08 m_e □ □0.03 m_e

It is therefore obvious that the optical bandgap of Zn_3N_2 is a controversial issue and a wide range of values have been measured for zinc nitride produced with different methods, different targets and substrates and different conditions. The synthesis of Zn_3N_2 hollow structures was also demonstrated by nitridation of zinc powder:[154] the synthesis process is represented schematically in figure 2.17. The optical bandgap of these structures was indirect and was measured to be 2.81 eV and in some other cases it was 3.23 eV.[155]

Recently Taylor *et al.*[166] synthesised Zn_3N_2 QDs by a chemical route. Diethylzinc was used as a precursor and reacted with ammonia gas in presence of oleylamine capping agent. The resulting QDs were highly emissive and covered a wide wavelength range. The tunability of the QDs was controlled by the amount of diethylzinc. A summary of Zn_3N_2 synthesis methods and relevant results are given in table 4.

Table 4: Summary table of zinc nitride produced with different techniques.

Morphology	Bandgap (eV)	Bandgap character	Electron Mobility ($cm^2 V^{-1}s^{-1}$)	Type of conduction	Ref
Polycrystalline film	1.23	Direct	100	n-type	[159]
Nanowires	3.22				[152]
Polycrystalline film	2.32	direct			[160]
Polycrystalline thin fim (rf-MBE film) (MOCVD film)	1.06		156 118		[161]
Thin film (Prep. In N_2 plasma) (Prep. In Ar plasma)	3.4		35 0.17	n-type n-type	[162]
Powder	0.90		118		[163]
Thin film (300^0C) (500^0C)	3.20 2.25	Direct Direct		n-type p-type	[164]
Thin film	2.11		0.2	n-type	[165]
Hollow structure	2.81	Indirect			[154]
Hollow structure	3.23				[155]
Thin Film (as-deposited) (annealed 350^0C)	1.37 1.12	Direct Direct			[150]
Quantum dots	1.0-2.0				[166]
Polycrystalline thin film	3.2	Direct			[167]

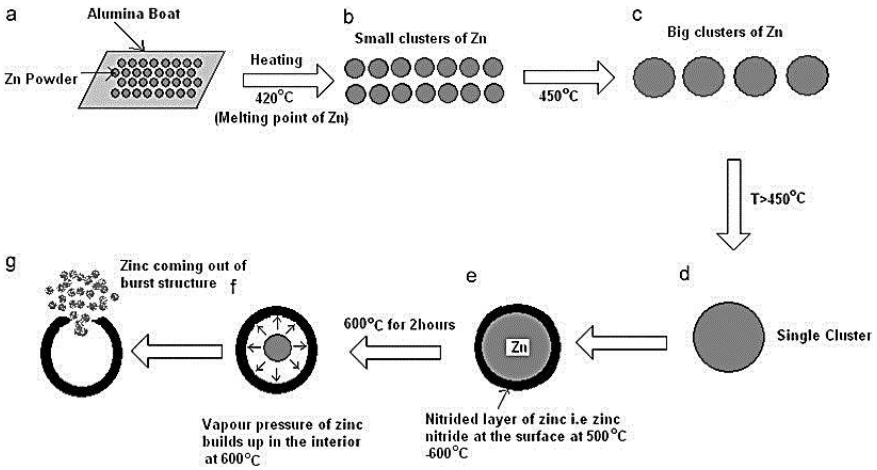

Figure 2.17: Flow chart of hollow Zn3N2 synthesis by nitridation.[154]

2.5 References

1. Camusso, L., Bortone, S. *Ceramics of the World: From 4000 BC to the Present*. (Harry N Abrams Inc, New York, 1992).
2. Cao, G. *Nanostructures & Nanomaterials, Synthesis, Properties and Applications*. (Imperial College Press, 2004).
3. Xia, Y., Xiong, Y., Lim, B. & Skrabalak, S. E. Shape-Controlled Synthesis of Metal Nanocrystals : Simple. *Angewandte Chemie International Edition* **48,** 60–103 (2009).
4. Polte, J. Fundamental growth principles of colloidal metal nanoparticles - a new perspective. *CrystEngComm* **17,** 6809–6830 (2015).
5. Gallagher, A., Howling, A. A., Hollenstein, C. & Gallagher, A. Anion reactions in silane plasma Anion reactions in silane plasma. **5571,** (2002).
6. Jalilpour, P. & Foroutan, G. pressure silane plasma Modelling of silicon hydride clustering in a low-pressure silane plasma. (2000).
7. Fridman, A. A. *et al.* Dusty plasma formation : Physics and critical phenomena . Theoretical approach Dusty plasma formation : Physics and critical phenomena . Theoretical approach. **1303,** (1996).
8. Perrin, J., Bbhm, C., Etemadi, R. & Lloret, A. Possible routes for cluster growth and particle formation in RF silane discharges. (1994).
9. Bordage, M. C., Si, S. H. & Si, S. I. H. Cross-Sections , Rate Constants and Transport Coefficients in Silane Plasma Chemistry ’). **36,** 3–49 (1996).
10. Mao, M., Benedikt, J., Consoli, A. & Bogaerts, A. New pathways for nanoparticle formation in acetylene dusty plasmas : a modelling investigation and comparison with experiments. (2008). doi:10.1088/0022-3727/41/22/225201
11. Lin, L. & Wang, Q. Microplasma: A New Generation of Technology for Functional Nanomaterial Synthesis. *Plasma Chemistry and Plasma Processing* **35,** 925–962 (2015).
12. Mangolini, L., Thimsen, E. & Kortshagen, U. High-Yield Plasma Synthesis of Luminescent Silicon Nanocrystals. *Nano* (2005).
13. Gresback, R., Holman, Z. & Kortshagen, U. Nonthermal plasma synthesis of size-controlled, monodisperse, freestanding germanium nanocrystals. *Applied Physics Letters* **91,** 0–3 (2007).

14. Kawasaki, H. *et al.* Study on growth processes of particles in germane radio frequency discharges using laser light scattering and scanning electron microscopic methods. *Journal of Applied Physics* **83,** 5665–5669 (1998).
15. Shiratani, M. *et al.* Study on growth processes of particulates in helium-diluted silane rf plasmas using scanning electron microscopy. *Applied Physics Letters* **65,** 1900–1902 (1994).
16. Holm, J. & Roberts, J. T. Modifying the composition of hydrogen-terminated silicon nanoparticles synthesized in a nonthermal rf plasma. *Journal of Vacuum Science & Technology A: Vacuum, Surfaces, and Films* **28,** 161–169 (2010).
17. Sankaran, R. M. *Plasma Processing of Nanomaterials*. (CRC Press, 2012).
18. Petrovi??, Z. L. *et al.* Breakdown, scaling and volt-ampere characteristics of low current micro-discharges. *Journal of Physics D: Applied Physics* **41,** (2008).
19. Mariotti, D., McLaughlin, J. A. & Maguire, P. Experimental study of breakdown voltage and effective secondary electron emission coefficient for a micro-plasma device. *Plasma Sources Science and Technology* **13,** 207–212 (2004).
20. Go, D. B. & Pohlman, D. A. A mathematical model of the modified Paschen's curve for breakdown in microscale gaps. *Journal of Applied Physics* **107,** (2010).
21. Kurunczi, P., Abramzon, N., Figus, M. & Becker, K. Measurement of rotational temperatures in high-pressure microhollow cathode (MHC) and capillary plasma electrode (CPE) discharges. *Acta Physica Slovaca* **54,** 115–124 (2004).
22. Penache, C. *et al.* Characterization of a high-pressure microdischarge using diode laser atomic absorption spectroscopy. *Plasma Sources Science and Technology* **11,** 476–483 (2002).
23. Iza, F., Lee, J. K. & Kong, M. G. Electron kinetics in radio-frequency atmospheric-pressure microplasmas. *Physical Review Letters* **99,** 2–5 (2007).
24. El-Habachi, A. & Schoenbach, K. H. Generation of intense excimer radiation from high-pressure hollow cathode discharges. *Applied Physics Letters* **73,** 885–887 (1998).
25. Sankaran, R. M., Giapis, K. P., Moselhy, M. & Schoenbach, K. H. Argon excimer emission from high-pressure microdischarges in metal capillaries. *Applied Physics Letters* **83,** 4728–4730 (2003).

26. Park, S. J., Eden, J. G., Chen, J. & Liu, C. Microdischarge devices with 10 or 30 μm square silicon cathode cavities: Pd scaling and production of the XeO excimer. *Applied Physics Letters* **85,** 4869–4871 (2004).
27. Wagner, A. J., Mariotti, D., Yurchenko, K. J. & Das, T. K. Experimental study of a planar atmospheric-pressure plasma operating in the microplasma regime. *Physical Review E - Statistical, Nonlinear, and Soft Matter Physics* **80,** 1–4 (2009).
28. Mariotti, D. & Sankaran, R. M. Microplasmas for nanomaterials synthesis. *Journal of Physics D: Applied Physics* **43,** (2010).
29. Roca i Cabarrocas, P. Experimental evidence for nanoparticle deposition in continuous argon–silane plasmas: Effects of silicon nanoparticles on film properties. *Journal of Vacuum Science & Technology A: Vacuum, Surfaces, and Films* **14,** 655 (1996).
30. Mariotti, D. Nonequilibrium and effect of gas mixtures in an atmospheric microplasma. *Applied Physics Letters* **92,** 151503–151506 (2008).
31. Foest, R., Schmidt, M. & Becker, K. Microplasmas, an emerging field of low-temperature plasma science and technology. *International Journal of Mass Spectrometry* **248,** 87–102 (2006).
32. Chiang, W. H., Richmonds, C. & Sankaran, R. M. Continuous-flow, atmospheric-pressure microplasmas: A versatile source for metal nanoparticle synthesis in the gas or liquid phase. *Plasma Sources Science and Technology* **19,** (2010).
33. Lin, P. A. & Sankaran, R. M. Plasma-assisted dissociation of organometallic vapors for continuous, gas-phase preparation of multimetallic nanoparticles. *Angewandte Chemie - International Edition* **50,** 10953–10956 (2011).
34. Kumar, A. *et al.* Formation of nanodiamonds at near-ambient conditions via microplasma dissociation of ethanol vapour. *Nature Communications* **4,** 1–8 (2013).
35. Belmonte, T., Arnoult, G., Henrion, G. & Gries, T. Nanoscience with non-equilibrium plasmas at atmospheric pressure. *Journal of Physics D: Applied Physics* **44,** (2011).
36. Shimizu, Y., Sasaki, T., Ito, T., Terashima, K. & Koshizaki, N. Fabrication of spherical carbon via UHF inductively coupled microplasma CVD. *Journal of Physics D: Applied Physics* **36,** 2940–2944 (2003).

37. Mariotti, D., Švrček, V. & Kim, D. G. Self-organized nanostructures on atmospheric microplasma exposed surfaces. *Applied Physics Letters* **91,** 2005–2008 (2007).
38. Yang, Z., Shirai, H., Kobayashi, T. & Hasegawa, Y. Synthesis of Si nanocones using rf microplasma at atmospheric pressure. *Thin Solid Films* **515,** 4153–4158 (2007).
39. Mariotti, D. & Ostrikov, K. Tailoring microplasma nanofabrication: From nanostructures to nanoarchitectures. *Journal of Physics D: Applied Physics* **42,** (2009).
40. Shimizu, Y., Kawaguchi, K., Sasaki, T. & Koshizaki, N. Generation of room-temperature atmospheric H2/Ar microplasma jet driven with pulse-modulated ultrahigh frequency and its application to gold nanoparticle preparation. *Applied Physics Letters* **94,** 2007–2010 (2009).
41. Shimizu, Y., Sasaki, T., Chandra Bose, A., Terashima, K. & Koshizaki, N. Development of wire spraying for direct micro-patterning via an atmospheric-pressure UHF inductively coupled microplasma jet. *Surface and Coatings Technology* **200,** 4251–4256 (2006).
42. Mariotti, D., Patel, J., Švrček, V. & Maguire, P. Plasma-liquid interactions at atmospheric pressure for nanomaterials synthesis and surface engineering. *Plasma Processes and Polymers* **9,** 1074–1085 (2012).
43. Hadzifejzovic, E., Elahi, A. & Caruana, D. J. Control of oxidation state of copper in flame deposited films. *Thin Solid Films* **520,** 5254–5259 (2012).
44. Cserfalvi, T. & Mezei, P. Direct Solution Analysis by Glow-Discharge - Electrolyte-Cathode Discharge Spectrometry. *Journal of Analytical Atomic Spectrometry* **9,** 345–349 (1994).
45. Lukes, P., Appleton, A. T. & Locke, B. R. Hydrogen Peroxide and Ozone Formation in Hybrid Gas-Liquid Electrical Discharge Reactors. *IEEE Transactions on Industry Applications* **40,** 60–67 (2004).
46. Huang, X., Li, Y. & Zhong, X. Effect of experimental conditions on size control of Au nanoparticles synthesized by atmospheric microplasma electrochemistry. *Nanoscale Research Letters* **9,** 1–7 (2014).
47. Wang, R., Zuo, S., Zhu, W., Zhang, J. & Fang, J. Rapid synthesis of aqueous-phase magnetite nanoparticles by atmospheric pressure non-thermal microplasma and their application in magnetic resonance imaging. *Plasma*

Processes and Polymers **11,** 448–454 (2014).

48. Huang, X. Z. *et al.* Plasmonic Ag nanoparticles via environment-benign atmospheric microplasma electrochemistry. *Nanotechnology* **24,** (2013).
49. Du, C. & Xiao, M. Cu2O nanoparticles synthesis by microplasma. *Scientific Reports* **4,** 3–7 (2014).
50. Lu, Y. *et al.* Characterization of a DC-driven microplasma between a capillary tube and water surface. *Epl* **102,** (2013).
51. Imasaka, K., Kato, Y. & Suehiro, J. Enhancement of microplasma-based water-solubilization of single-walled carbon nanotubes using gas bubbling in water. *Nanotechnology* **18,** (2007).
52. Hieda, J., Saito, N. & Takai, O. Exotic shapes of gold nanoparticles synthesized using plasma in aqueous solution. *Journal of Vacuum Science & Technology A: Vacuum, Surfaces, and Films* **26,** 854–856 (2008).
53. Askari, S., Levchenko, I., Ostrikov, K., Maguire, P. & Mariotti, D. Crystalline Si nanoparticles below crystallization threshold: Effects of collisional heating in non-thermal atmospheric-pressure microplasmas. *Applied Physics Letters* **104,** (2014).
54. Kortshagen, U. R. *et al.* Nonthermal plasma synthesis of nanocrystals: Fundamental principles, materials, and applications. *Chemical Reviews* **116,** 11061–11127 (2016).
55. Cao, Z., Walsh, J. L. & Kong, M. G. Atmospheric plasma jet array in parallel electric and gas flow fields for three-dimensional surface treatment. *Applied Physics Letters* **94,** 021501 (2009).
56. Gong, M. *et al.* All-Printable ZnO Quantum Dots/Graphene van der Waals Heterostructures for Ultrasensitive Detection of Ultraviolet Light. *ACS Nano* **11,** 4114–4123 (2017).
57. Janotti, A. & Van De Walle, C. G. Fundamentals of zinc oxide as a semiconductor. *Reports on Progress in Physics* **72,** (2009).
58. Fujita, S. Wide-bandgap semiconductor materials: For their full bloom. *Japanese Journal of Applied Physics* **54,** (2015).
59. Ozgür, M., Hofstetter, D. & Morkoç, H. ZnO Devices and Applications: A Review of Current Status and Future Prospects. *Proceedings of the IEEE* **98,** 1255–1268 (2010).
60. Xu, L. *et al.* ZnO with different morphologies synthesized by solvothermal

methods for enhanced photocatalytic activity. *Chemistry of Materials* **21,** 2875–2885 (2009).

61. Kuriakose, S., Bhardwaj, N., Singh, J., Satpati, B. & Mohapatra, S. Structural, optical and photocatalytic properties of flower-like ZnO nanostructures prepared by a facile wet chemical method. *Beilstein Journal of Nanotechnology* **4,** 763–770 (2013).
62. McLaren, A., Valdes-Solis, T., Li, G. & Shik, C. T. Shape and size effects of ZnO nanocrystals on photocatalytic activity. *Journal of the American Chemical Society* **131,** 12540–12541 (2009).
63. Liu, Z., Zhang, Q., Li, Y. & Wang, H. Solvothermal synthesis, photoluminescence and photocatalytic properties of pencil-like ZnO microrods. *Journal of Physics and Chemistry of Solids* **73,** 651–655 (2012).
64. Kuriakose, S., Satpati, B. & Mohapatra, S. Enhanced photocatalytic activity of Co doped ZnO nanodisks and nanorods prepared by a facile wet chemical method. *Physical Chemistry Chemical Physics* **16,** 12741 (2014).
65. Wang, Z. L. Zinc oxide nanostructures: Growth, properties and applications. *Journal of Physics Condensed Matter* **16,** 829–858 (2004).
66. Yi, G.-C., Wang, C. & Park, W. Il. ZnO nanorods: synthesis, characterization and applications. *Semiconductor Science and Technology* **20,** S22–S34 (2005).
67. Li, Q. *et al.* Fabrication of ZnO nanorods and nanotubes in aqueous solutions. *Chemistry of Materials* **17,** 1001–1006 (2005).
68. Feng, W., Chen, J. & Hou, C. Growth and characterization of ZnO needles. *Applied Nanoscience* **4,** 15–18 (2014).
69. Zhou, Z., Liu, J. & Hu, S. Studies on the kinetics process of tetra-needle-like ZnO whisker growth. *Journal of Crystal Growth* **276,** 317–320 (2005).
70. Leung, Y. H. *et al.* Zinc oxide ribbon and comb structures: Synthesis and optical properties. *Chemical Physics Letters* **394,** 452–457 (2004).
71. Liu, L., Hong, K., Ge, X., Liu, D. & Xu, M. Controllable and Rapid Synthesis of Long ZnO Nanowire Arrays for Dye-Sensitized Solar Cells. *The Journal of Physical Chemistry C* **118,** 15551–15555 (2014).
72. Kim, K. H. *et al.* Piezoelectric two-dimensional nanosheets/anionic layer heterojunction for efficient direct current power generation. *Scientific Reports* **3,** 1–6 (2013).
73. Wang, F. *et al.* Nanometre-thick single-crystalline nanosheets grown at the

water-air interface. *Nature Communications* **7,** 1–7 (2016).

74. Xu, Y. *et al.* Simple synthesis of ZnO nanoflowers and its photocatalytic performances toward the photodegradation of metamitron. *Materials Research Bulletin* **76,** 235–239 (2016).
75. Newton, M. C. & Warburton, P. A. ZnO tetrapod nanocrystals. *Materials Today* **10,** 50–54 (2007).
76. Jain, G. *et al.* Porous zinc oxide nanocrystalline film deposition by atmospheric pressure plasma: Fabrication and energy band estimation; Porous zinc oxide nanocrystalline film deposition by atmospheric pressure plasma: Fabrication and energy band estimation. (2017). doi:10.1002/ppap.201700052
77. Stanković, A., Veselinović, L., Škapin, S. D., Marković, S. & Uskoković, D. Controlled mechanochemically assisted synthesis of ZnO nanopowders in the presence of oxalic acid. *Journal of Materials Science* **46,** 3716–3724 (2011).
78. Lanje, A. S., Sharma, S. J., Ningthoujam, R. S., Ahn, J. S. & Pode, R. B. Low temperature dielectric studies of zinc oxide (ZnO) nanoparticles prepared by precipitation method. *Advanced Powder Technology* **24,** 331–335 (2013).
79. El-Shazly, A. N. *et al.* Nanostructured ZnO photocatalysts prepared via surfactant assisted Co-Precipitation method achieving enhanced photocatalytic activity for the degradation of methylene blue dyes. *Journal of Environmental Chemical Engineering* **4,** 3177–3184 (2016).
80. Li, Y., Xu, L., Li, X., Shen, X. & Wang, A. Effect of aging time of ZnO sol on the structural and optical properties of ZnO thin films prepared by sol-gel method. *Applied Surface Science* **256,** 4543–4547 (2010).
81. Rai, P., Kwak, W.-K. & Yu, Y.-T. Solvothermal Synthesis of ZnO Nanostructures and Their Morphology-Dependent Gas-Sensing Properties. *ACS Applied Materials & Interfaces* **5,** 3026–3032 (2013).
82. Chen, D., Jiao, X. & Cheng, G. Hydrothermal synthesis of zinc oxide powders with different morphologies. *Solid State Communications* **113,** 363–366 (1999).
83. Ul Hassan Sarwar Rana, A., Kang, M. & Kim, H. S. Microwave-assisted Facile and Ultrafast Growth of ZnO Nanostructures and Proposition of Alternative Microwave-assisted Methods to Address Growth Stoppage. *Scientific Reports* **6,** 1–13 (2016).
84. Wang, Y. *et al.* Synthesis of ZnO nanoparticles from microemulsions in a flow type microreactor. *Chemical Engineering Journal* **235,** 191–197 (2014).

85. Hsu, C. M. *et al.* Deposition of transparent and conductive ZnO films by an atmospheric pressure plasma-jet-assisted process. *Thin Solid Films* **570,** 423–428 (2014).
86. Stauss, S., Imanishi, Y., Miyazoe, H. & Terashima, K. High rate deposition of ZnO thin films by a small-scale inductively coupled argon plasma generated in open air. *Journal of Physics D: Applied Physics* **43,** (2010).
87. Law, M., Greene, L. E., Johnson, J. C., Saykally, R. & Yang, P. Nanowire dye-sensitized solar cells. *Nature Materials* **4,** 455–459 (2005).
88. Wan, Q. *et al.* Fabrication and ethanol sensing characteristics of ZnO nanowire gas sensors. *Applied Physics Letters* **84,** 3654–3656 (2004).
89. Chu, S. *et al.* Electrically pumped waveguide lasing from ZnO nanowires. *Nature Nanotechnology* **6,** 506–510 (2011).
90. Wang, Z. L. & Song, J. H. Piezoelectric nanogenerators based on zinc oxide nanowire arrays. *Science* **312,** 242–246 (2006).
91. Shi, Z.-F. *et al.* Epitaxial growth of vertically aligned ZnO nanowires for bidirectional direct-current driven light-emitting diodes applications. *CrystEngComm* **17,** 40–49 (2015).
92. Boruah, B. D., Mukherjee, A., Sridhar, S. & Misra, A. Highly dense ZnO nanowires grown on graphene foam for ultraviolet photodetection. *ACS Applied Materials and Interfaces* **7,** 10606–10611 (2015).
93. Chen, M. *et al.* Tuning Light Emission of a Pressure-Sensitive Silicon/ZnO Nanowires Heterostructure Matrix through Piezo-phototronic Effects. *ACS Nano* **10,** 6074–6079 (2016).
94. Lamberti, A. *et al.* Sponge-like ZnO nanostructures by low temperature water vapor-oxidation method as dye-sensitized solar cell photoanodes. *Journal of Alloys and Compounds* **615,** S487–S490 (2015).
95. Dhamodharan, P., Manoharan, C., Dhanapandian, S. & Venkatachalam, P. Dye-sensitized solar cell using sprayed ZnO nanocrystalline thin films on ITO as photoanode. *Spectrochimica Acta - Part A: Molecular and Biomolecular Spectroscopy* **136,** 1671–1678 (2015).
96. Yalçin, L. & Öztürk, R. Coral-shaped ZnO nanostructures for dye-sensitized solar cell photoanodes. *PROGRESS IN PHOTOVOLTAICS: RESEARCH AND APPLICATIONS* **15,** 326–334 (2013).
97. Pauporté, T. & Rathouský, J. Electrodeposited mesoporous ZnO thin films as

efficient photocatalysts for the degradation of dye pollutants. *Journal of Physical Chemistry C* **111,** 7639–7644 (2007).

98. Lu, H., Zhang, M. & Guo, M. Controllable electrodeposition of ZnO nanorod arrays on flexible stainless steel mesh substrate for photocatalytic degradation of Rhodamine B. *Applied Surface Science* **317,** 672–681 (2014).
99. An, D., Li, Y., Lian, X., Zou, Y. & Deng, G. Synthesis of porous ZnO structure for gas sensor and photocatalytic applications. *Colloids and Surfaces A: Physicochemical and Engineering Aspects* **447,** 81–87 (2014).
100. Li, B. & Wang, Y. Hierarchically assembled porous ZnO microstructures and applications in a gas sensor. *Superlattices and Microstructures* **49,** 433–440 (2011).
101. Wen, W., Wu, J. M. & Wang, Y. De. Large-size porous ZnO flakes with superior gas-sensing performance. *Applied Physics Letters* **100,** 2–6 (2012).
102. Su, X., Duan, G., Xu, Z., Zhou, F. & Cai, W. Structure and thickness-dependent gas sensing responses to NO2under UV irradiation for the multilayered ZnO micro/nanostructured porous thin films. *Journal of Colloid and Interface Science* **503,** 150–158 (2017).
103. Chen, Z., Tang, Y., Zhang, L. & Luo, L. Electrodeposited nanoporous ZnO films exhibiting enhanced performance in dye-sensitized solar cells. *Electrochimica Acta* **51,** 5870–5875 (2006).
104. Venditti, I. *et al.* Electrodeposited ZnO with squaraine sentisizers as photoactive anode of DSCs. *Materials Research Express* **1,** (2014).
105. Garino, N., Lamberti, A., Gazia, R., Chiodoni, A. & Gerbaldi, C. Cycling behaviour of sponge-like nanostructured ZnO as thin-film Li-ion battery anodes. *Journal of Alloys and Compounds* **615,** S454–S458 (2015).
106. Laurenti, M. *et al.* A porous nanobranched structure: an effective way to improve piezoelectricity in sputtered ZnO thin films. *RSC Adv.* **6,** 76996–77004 (2016).
107. Patra, M. K. *et al.* Synthesis of stable dispersion of ZnO quantum dots in aqueous medium showing visible emission from bluish green to yellow. *Journal of Luminescence* **129,** 320–324 (2009).
108. Qiu, Y., Gogna, P., Forouhar, S., Stintz, A. & Lester, L. F. High-performance InAs quantum-dot lasers near 1.3 μm. *Applied Physics Letters* **79,** 3570–3572 (2001).

109. Chen, S. De, Chen, Y. Y. & Lee, S. C. Transverse-electric-field-enhanced response in InAs/AlGaAs/GaAs quantum-dot infrared photodetectors. *Applied Physics Letters* **86,** 1–3 (2005).
110. Schoelkopf, R. J., Wahlgren, P., Kozhevnikov, A. A., Delsing, P. & Prober, D. E. The radio-frequency single-electron transistor (RF-SET): A fast and ultrasensitive electrometer. *Science* **280,** 1238–1242 (1998).
111. No Title. Available at: https://www.cd-bioparticles.com/t/Properties-and-Applications-of-Quantum-Dots_56.html.
112. Johnston, K. *et al.* Identification of donor-related impurities in ZnO using photoluminescence and radiotracer techniques. *Physical Review B - Condensed Matter and Materials Physics* **73,** 1–7 (2006).
113. Fonoberov, V. A., Alim, K. A., Balandin, A. A., Xiu, F. & Liu, J. Photoluminescence investigation of the carrier recombination processes in ZnO quantum dots and nanocrystals. *Physical Review B - Condensed Matter and Materials Physics* **73,** 1–9 (2006).
114. Guo, L. *et al.* Highly monodisperse polymer-capped ZnO nanoparticles: Preparation and optical properties. *Appl. Phys. Lett.* **76,** 2901 (2000).
115. Choy, W. C. H. *et al.* Photoluminescence and Electron Paramagnetic Resonance of ZnO Tetrapod Structures **. *Advanced Functional Materials* 856–864 (2004). doi:10.1002/adfm.200305082
116. Fonoberov, V. A. & Balandin, A. A. Origin of ultraviolet photoluminescence in ZnO quantum dots: Confined excitons versus surface-bound impurity exciton complexes. *Applied Physics Letters* **85,** 5971–5973 (2004).
117. Qiao, B., Zhao, S., Xu, Z. & Xu, X. Synthesis of ZnO quantum dots and their agglomeration mechanisms along with emission spectra based on ageing time and temperature. *Chinese Physics B* **25,** (2016).
118. Zhang, L., Yin, L., Wang, C., Qi, Y. & Xiang, D. Origin of Visible Photoluminescence of ZnO Quantum Dots : Defect-Dependent and Size-Dependent. 9651–9658 (2010).
119. Li, L., Gu, L., Lou, Z., Fan, Z. & Shen, G. ZnO Quantum Dot Decorated Zn2SnO4Nanowire Heterojunction Photodetectors with Drastic Performance Enhancement and Flexible Ultraviolet Image Sensors. *ACS Nano* **11,** 4067–4076 (2017).
120. Barakat, M. A., Schaeffer, H., Hayes, G. & Ismat-Shah, S. Photocatalytic

degradation of 2-chlorophenol by Co-doped TiO2nanoparticles. *Applied Catalysis B: Environmental* **57,** 23–30 (2005).

121. Mohan, R., Krishnamoorthy, K. & Kim, S. J. Enhanced photocatalytic activity of Cu-doped ZnO nanorods. *Solid State Communications* **152,** 375–380 (2012).
122. Hang, D.-R., Sharma, K. H., Chen, C.-H. & Islam, S. E. Enhanced Photocatalytic Performance of ZnO Nanorods Coupled by Two-Dimensional α-MoO_3 Nanoflakes under UV and Visible Light Irradiation. *Chemistry - A European Journal* **22,** 12777–12784 (2016).
123. Van De Walle, C. G. Hydrogen as a cause of doping in zinc oxide. *Physical Review Letters* **85,** 1012–1015 (2000).
124. Herring, N. P., Panchakarla, L. S. & El-shall, M. S. P-Type Nitrogen-Doped ZnO Nanostructures with Controlled Shape and Doping Level by Facile Microwave Synthesis P-Type Nitrogen-Doped ZnO Nanostructures with Controlled Shape and Doping Level by Facile Microwave Synthesis. (2014). doi:10.1021/la404593w
125. Chavillon, B. *et al.* P-type nitrogen-doped ZnO nanoparticles stable under ambient conditions. *Journal of the American Chemical Society* **134,** 464–470 (2012).
126. Cao, P. *et al.* Optical and electrical properties of p-type ZnO fabricated by NH3plasma post-treated ZnO thin films. *Applied Surface Science* **254,** 2900–2904 (2008).
127. Minegishi, K. *et al.* Growth of p-type Zinc Oxide Films by Chemical Vapor Deposition. *Japanese Journal of Applied Physics* **36,** L1453–L1455 (1997).
128. UEKAWA, N., MITANI, Y., KOJIMA, T. & KAKEGAWA, K. Synthesis of nitrogen-doped zinc oxide particles by thermal decomposition of mixture between zinc peroxide aqueous sol and ammonium salts. *Journal of the Ceramic Society of Japan* **117,** 283–288 (2009).
129. Wang, M. *et al.* N Doping to ZnO Nanorods for Photoelectrochemical Water Splitting under Visible Light: Engineered Impurity Distribution and Terraced Band Structure. *Scientific Reports* **5,** (2015).
130. Yang, X. *et al.* Nitrogen-Doped ZnO Nanowire Arrays for Photoelectrochemical Water Splitting 2009. *Nano Letters* 2–7 (2009). doi:10.1021/nl900772q
131. Game, O. *et al.* Concurrent synthetic control of dopant (nitrogen) and defect

complexes to realize broadband (UV–650 nm) absorption in ZnO nanorods for superior photo-electrochemical performance. *Journal of Materials Chemistry* **22,** 17302 (2012).

132. Macías-Sánchez, J. J. *et al.* Synthesis of nitrogen-doped ZnO by sol–gel method: characterization and its application on visible photocatalytic degradation of 2,4-D and picloram herbicides. *Photochem. Photobiol. Sci.* **14,** 536–542 (2015).
133. Ou, Q., Shinji, K., Ogino, A. & Nagatsu, M. Enhanced photoluminescence of nitrogen-doped ZnO nanoparticles fabricated by Nd : YAG laser ablation. *Journal of Physics D: Applied Physics* **41,** (2008).
134. Ibarra, L., Marcos-Fernández, A. & Alzorriz, M. Mechanistic approach to the curing of carboxylated nitrile rubber (XNBR) by zinc peroxide/zinc oxide. *Polymer* **43,** 1649–1655 (2002).
135. Ibarra, L. & Alzorriz, M. Ionic elastomers based on carboxylated nitrile rubber (XNBR) and zinc peroxide: Influence of carboxylic group content on properties. *Journal of Applied Polymer Science* **84,** 605–615 (2002).
136. Hsu, C. C. & Wu, N. L. Synthesis and photocatalytic activity of ZnO/ZnO2 composite. *Journal of Photochemistry and Photobiology A: Chemistry* **172,** 269–274 (2005).
137. Gondal, M. A., Drmosh, Q. A., Yamani, Z. H. & Saleh, T. A. Synthesis of ZnO2 nanoparticles by laser ablation in liquid and their annealing transformation into ZnO nanoparticles. *Applied Surface Science* **256,** 298–304 (2009).
138. Wolanov, Y., Prikhodchenko, P. V, Medvedev, A. G., Pedahzur, R. & Lev, O. Moderate pH. (2013).
139. Palma-Palma, H. E., Camacho-López, M., Camacho-López, M. A. & Vilchis-Néstor, A. R. Preparation of zinc peroxide nanoparticles by laser ablation of solid in liquids. *Superficies y Vacio* **28,** 74–77 (2015).
140. Sun, M., Hao, W., Wang, C. & Wang, T. A simple and green approach for preparation of ZnO2and ZnO under sunlight irradiation. *Chemical Physics Letters* **443,** 342–346 (2007).
141. Kim, K. A., Cha, J. R., Gong, M. S. & Kim, J. G. Preparation of zno2 nanoparticles using organometallic zinc(ii) isobutylcarbamate in organic solvent. *Bulletin of the Korean Chemical Society* **35,** 431–435 (2014).
142. Chen, W. *et al.* Synthesis, Thermal Stability and Properties of ZnO 2

Nanoparticles. *The Journal of Physical Chemistry C* **113,** 1320–1324 (2009).

143. Bai, H. & Liu, X. Green hydrothermal synthesis and photoluminescence property of ZnO2nanoparticles. *Materials Letters* **64,** 341–343 (2010).
144. Escobedo-Morales, A. *et al.* Structural and vibrational properties of hydrothermally grown ZnO2nanoparticles. *Journal of Crystal Growth* **316,** 37–41 (2011).
145. Drmosh, Q. A., Gondal, M. A., Yamani, Z. H. & Saleh, T. A. Spectroscopic characterization approach to study surfactants effect on ZnO2 nanoparticles synthesis by laser ablation process. *Applied Surface Science* **256,** 4661–4666 (2010).
146. Wolanov, Y., Prikhodchenko, P. V, Medvedev, A. G., Pedahzur, R. & Lev, O. Moderate pH. *Environmental Science & Technology* **47,** 8769−8774 (2013).
147. Verma, S. & Jain, S. L. Nanosized zinc peroxide (ZnO_2): a novel inorganic oxidant for the oxidation of aromatic alcohols to carbonyl compounds. *Inorganic Chemistry Frontiers* **1,** 534 (2014).
148. Partin, D. E., Williams, D. J. & O'Keeffe, M. The Crystal Structures of Mg3N2and Zn3N2. *Journal of Solid State Chemistry* **132,** 56–59 (1997).
149. Juza, R. & Hahn, H. Über die Kristallstrukturen von Zn_{3}N_{2}, Cd_{3}N_{2} und Ge_{3}N_{4}. *Z. Anorg. Allg. Chem.* **244,** 125–132 (1940).
150. Jayatissa, A. H., Wen, T. & Gautam, M. Optical properties of zinc nitride films deposited by the rf magnetron sputtering method. *Journal of Physics D: Applied Physics* **45,** (2012).
151. Khan, W. S. *et al.* Optical properties and characterization of zinc nitride nanoneedles prepared from ball-milled Zn powders. *Materials Letters* **65,** 1264–1267 (2011).
152. Zong, F. *et al.* Structural properties and photoluminescence of zinc nitride nanowires. *Applied Physics Letters* **87,** 1–3 (2005).
153. Zong, F. *et al.* Structural properties of zinc nitride empty balls. *Materials Letters* **60,** 905–908 (2006).
154. Khan, W. S. & Cao, C. Synthesis, growth mechanism and optical characterization of zinc nitride hollow structures. *Journal of Crystal Growth* **312,** 1838–1843 (2010).
155. Khan, W. S. *et al.* Solvo-solid preparation of Zn3N2hollow structures; Their PL yellow emission and hydrogen absorption characteristics. *Materials Letters* **65,**

2127–2129 (2011).

156. Kuriyama, K., Takahashi, Y. & Sunohara, F. Optical band gap of Zn 3 N 2 films. *Physical Review B* **48,** 2781–2782 (1993).
157. Yoo, S.-H., Walsh, A., Scanlon, D. O. & Soon, A. Electronic structure and band alignment of zinc nitride, Zn_3N_2. *RSC Adv.* **4,** 3306–3311 (2014).
158. Redondo-Cubero, A. *et al.* Zinc nitride thin films: basic properties and applications. **10105,** 101051B (2017).
159. Futsuhara, M., Yoshioka, K. & Takai, O. Structural, electrical and optical properties of zinc nitride thin films prepared by reactive rf magnetron sputtering. *Thin Solid Films* **322,** 274–281 (1998).
160. Futsuhara, M., Yoshioka, K. & Takai, O. Optical properties of zinc oxynitride thin films. *Thin Solid Films* **317,** 322–325 (1998).
161. Suda, T. & Kakishita, K. Band-gap energy and electron effective mass of polycrystalline Zn 3N2. *Journal of Applied Physics* **99,** 1–4 (2006).
162. Kambilafka, V. *et al.* Thermal oxidation of n-type ZnN films made by r f-sputtering from a zinc nitride target, and their conversion into p-type films. *Superlattices and Microstructures* **42,** 55–61 (2007).
163. Paniconi, G. *et al.* Synthesis, stoichiometry and thermal stability of Zn3N2powders prepared by ammonolysis reactions. *Journal of Solid State Chemistry* **181,** 158–165 (2008).
164. Mohamed, H. A. Structure and optical constants of electron beam deposited zinc nitride films. *Optoelectronics and Advanced Materials, Rapid Communications* **3,** 553–558 (2009).
165. Aperathitis, E., Kambilafka, V. & Modreanu, M. Properties of n-type ZnN thin films as channel for transparent thin film transistors. *Thin Solid Films* **518,** 1036–1039 (2009).
166. Taylor, P. N. *et al.* Synthesis of widely tunable and highly luminescent zinc nitride nanocrystals. *J. Mater. Chem. C* **2,** 4379–4382 (2014).
167. Bhattacharyya, S. R., Ayouchi, R., Pinnisch, M. & Schwarz, R. Transfer characteristic of zinc nitride based thin film transistors. *Physica Status Solidi (C) Current Topics in Solid State Physics* **9,** 469–472 (2012).
168. Zong, F.-J. *et al.* Thermal Decomposition Behaviour of Zn3N2 Powder. *Chinese Physics Letters* **22,** 907–910 (2005).

Chapter 3: Material Characterization Techniques

3.1 Introduction

Several characterization techniques have been used to identify structural, chemical and optical properties of synthesised nanoparticles. All the characterization tools used in this project are listed in table 1 where details of who has carried out the measurements and analyses are provided; author indicates that the PhD candidate was operating the instrument and/or has carried out the analysis and "Collab." stands for collaborator.

Table 3:

Technique	**Equipment**	**Operation Carried out by**	**Analysis Carried out by**
Transmission Electron Microscopy (TEM)	Jeol JEM-2100F	Author	Author
Scanning Electron Microscopy (SEM)	FEI Quanta 200 3D, JEOL JSM-6010PLUS/LV	Author	Author
Energy dispersion X-ray Spectroscopy (EDX)	Attached with TEM	Author	Author
X-ray Photoelectron Spectroscopy (XPS)	Kratos AxisUltra DLD spectrometer	Collab.	Author
X-ray Diffraction (XRD)	Bruker X8 Diffractometer	Author	Author
Raman Spectroscopy	Labram Raman spectroscope (λ = 632.8 nm)	Author	Author
Fourier-transform Infrared Spectroscopy (FTIR)	Thermoscientific Nicolet iS5, model equipped with ATR iD5	Author	Author
Photoluminescence Spectroscopy (PL)	Cary eclipse fluorescence spectrophotometer, Agilent Tech	Author	Author

Uv-Visible Absorption Spectroscopy (UV-Vis)	PerkinElmer LAMDA 365	Author	Author
Kelvin Probe Measurement (KP)	SKP 4.5, KP Technology Ltd.	Collab.	Author
Thermogravimetry Analysis (TGA)	TA instruments	Collab.	Author
Cyclic Voltammetry (CV)	Novacontrol Technologies. Electrochemical interface S/N 602/0	Author	Author
Current-Voltage measurement (I-V)	AM 1.5 irradiation with Keithley 2400	Author	Author

3.2 Material characterization technique

3.2.1 Electron Microscopy

Figure 3.1 shows the interaction of the electron beam with the specimen which can give rise to a number of phenomena and corresponding analysis techniques. According to specimen electron interactions, transmitted electrons, backscattered

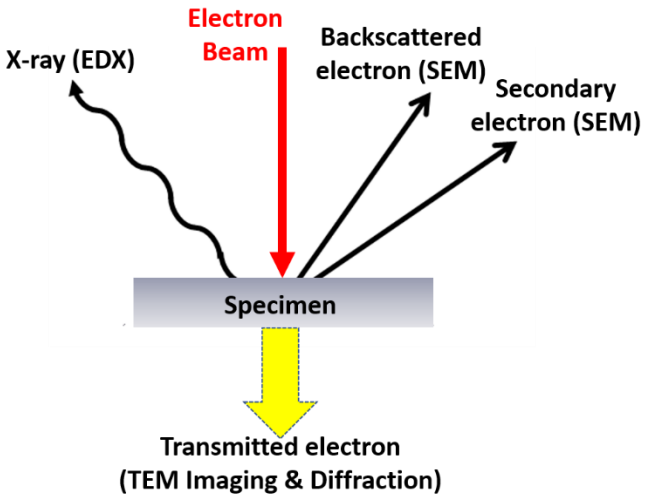

Figure 3.1: Diagram depicting the interaction of an electron beam with a specimen; the transmitted electrons play the main role in transmission electron microscopy. TEM, SEM and EDX are abbreviations for transmission electron microscopy, scanning electron microscopy and energy dispersive x-ray spectroscopy, respectively.

electrons and secondary electrons can be generated (figure 3.1). When the transmitted electrons are accounted in the analysis, this technique is called transmission electron microscopy (TEM). Backscattered and secondary electrons generated via elastic and inelastic scattering are analysed in scanning electron microscopy (SEM). Electron beam interaction with specimen generates characteristics X-ray. This generated characteristic x-ray is used in both TEM and SEM for energy dispersive X-ray spectroscopy (EDX).

(a) Transmission electron microscopy (TEM)

TEM has been used in this project thoroughly to analyse morphology, size and crystalline structure of the NPs. For transmission electron microscopy, the sample should be thin enough so that the electron beam can transmit through the sample.

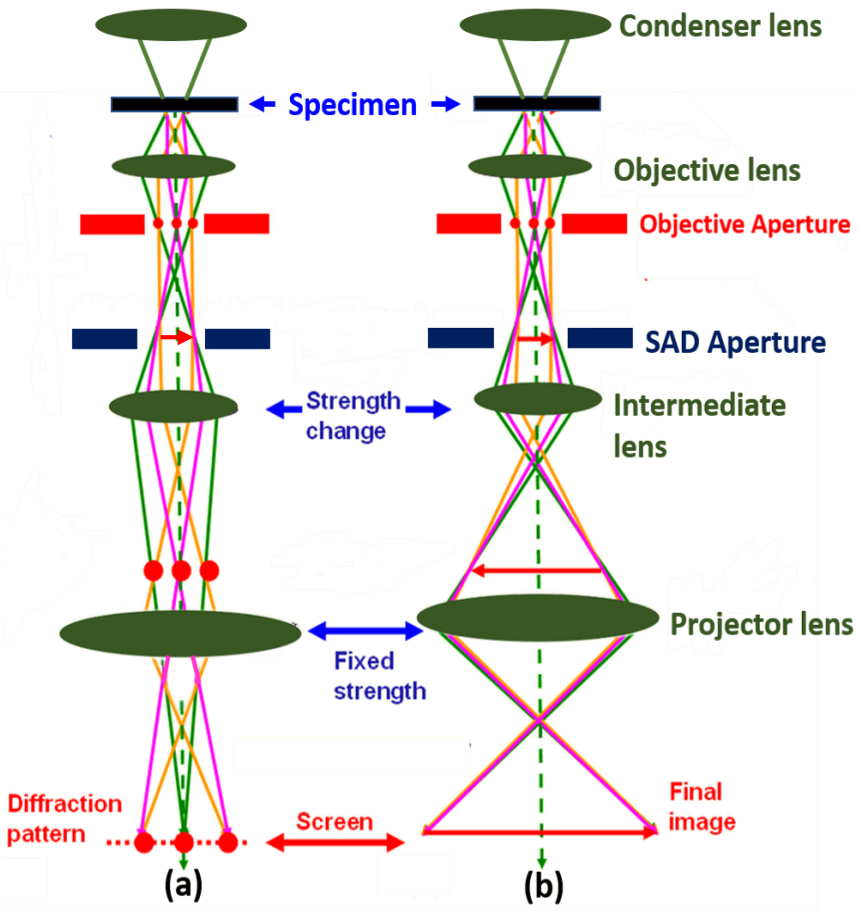

Figure 3.2: Schematic of the electron beam path across the transmission electron microscope in (a) Selective-area diffraction mode and (b) Imaging mode.

In this section, the basic working principles of a will be described. In TEM, an electron is accelerated to few hundreds of kilo-electron volts energy. The voltage used in our

microscope is 200 kV and the wavelength is ~0.0025 nm. This wavelength is smaller than the light wavelength, which is the reason of high resolution in the electron microscope. The theoretical instrumental spatial resolution is proportional to $\lambda^{3/4}$.[1] The working mode of the TEM depends on the collection of the electrons after passing the specimen.

Figure 3.2 shows the path of electron beam in TEM. Accelerated electrons are projected onto a thin specimen (less than 200 nm) by means of the condenser lens. The scattering processes through the specimen determine the kind of information obtained. Inelastic interactions between primary electrons and sample electrons at grain boundaries, dislocations, second-phase particles, defects, density variation etc. lead to complex absorption and scattering effects that change the intensity of transmitted electrons. This is the principle behind imaging shown in figure 3.2b. Elastic scattering does not involve any energy loss and gives rise to diffraction patterns, which are used for SAED working mode (figure 3.2a). SAED has unique capability in determining the crystal structure of materials. In the TEM, changing the strength of the intermediate lenses can be used to switch between imaging and diffraction patterns.

(b) Scanning Electron Microscopy (SEM)

In this project, SEM is used for topographic study of thin films of NPs. Figure 3.3 shows the schematic of the SEM column including electron source, condenser lenses, scan coils, objective lens and detectors. The electron source or gun produces a stable electron beam with high current, small spot size, adjustable energy and small energy dispersion. Different types of electron guns are used in SEMs such as tungsten electron gun, lanthanum hexaboride (LaB_6) gun etc. The beam is focused via a condenser lenses like in a TEM. In contrast to the TEM, in SEMs, the objective lens is placed above the sample that again helps in focusing the beam on the sample. In SEMs, raster scanning is implemented by the help of a scan coil that deflects the beam horizontally and vertically, which helps in scanning a rectangular area of the sample.

In SEM analysis, the image information depends on the acquisition of the signals produced from the electron beam and sample interaction. Elastic and inelastic interactions are two major categories. Elastic scattering results from the deflection of the incident electrons by the specimen atomic nucleus. In this type of interaction, electrons experience no energy loss but a wide-angle directional change of the scattered electrons is observed. When the angle of scattered electrons is more than 90^o, these are called *backscattered electrons* (BSE) and yield a useful signal for the imaging

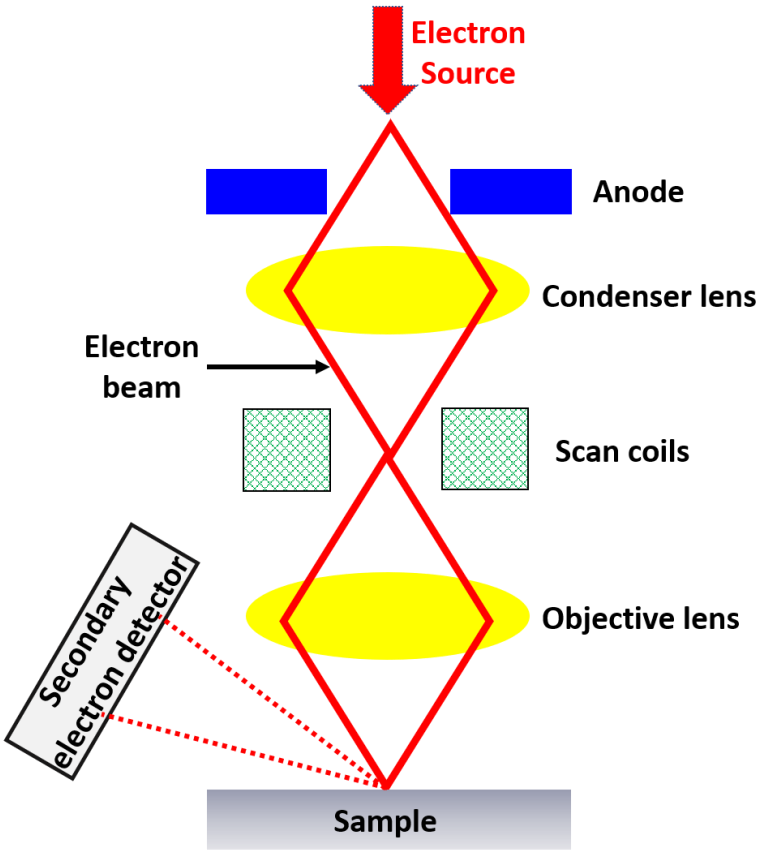

Figure 3.3: Schematic of a scanning electron microscope column.

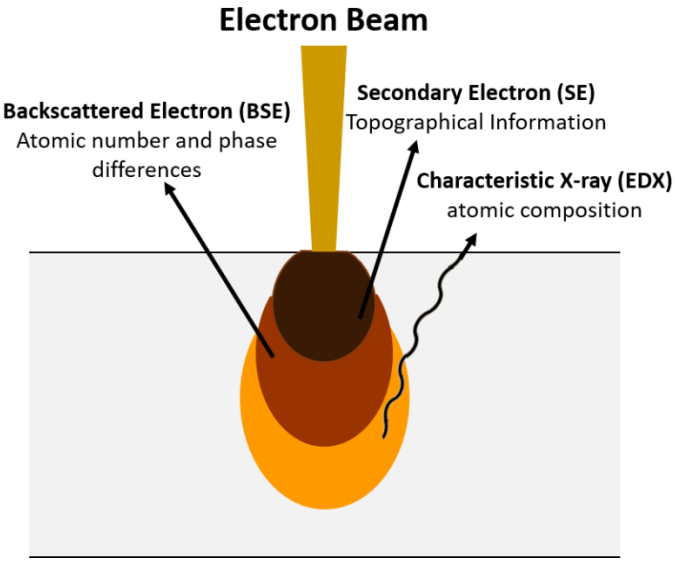

Figure 3.4: Diagram depicting the interaction of the electron beam with the surface of the sample in a scanning electron microscope; the secondary electrons can only pass through a shallow layer of the surface.

of the sample and compositional analysis. Inelastic scattering occurs when substantial energy is transferred to the specimen atoms. The amount of electron energy loss

depends on whether the specimen electrons are excited singly or collectively and also depends on the binding energy of the electron to the atoms. As a result, the excitation of the specimen electrons leads to the generation of *secondary electrons* (SE) that can be used to image or analyse the sample. SEs are specifically used for topographic contrast in the SEM, e.g. visualization of surface texture and roughness. Other signals including the emission of characteristic x-rays, Auger electrons etc. are presented in figure 3.4, showing the area of samples from where they generate and information that can be extracted.

Practically, an important factor that affects the quality of the image is the accelerating voltage. High operating voltages (15-30 keV) result in images with higher resolution at high magnification, although it can lead to damage of the sample surface. Samples with low electric conductivity have a higher chance of damage by the electron beam. Surface charging of the sample by the electron beam can also affect the quality of the image; the sample surface can be connected to the (conductive) sample holder using e.g. copper tape to reduce the effect of charging in non-conductive samples. Although operating at lower voltages reduces the resolution, it has some other advantages; the surface structures are clearer and the sample charge-up or damage is reduced. Another important factor is the distance of the sample from the electron beam; higher resolution and smaller depth of filed is obtained at smaller distances.

(c) Energy dispersion x-ray spectroscopy (EDX)

This technique is used for quantitative elemental analysis of the materials in this project. The collision of an electron from the electron beam with an atom of the sample results in ejecting an electron most likely from an inner shell of the atom. The electron is usually ejected from the K-shell and it leaves a hole behind (figure 3.5). The empty space is filled with an electron from a higher shell and as a result a characteristic x-ray is emitted. The x-ray emitted from the sample after bombarded with the electron beam, is collected by an energy-dispersive spectrometer. The x-ray commonly is K_α in an EDX spectrum which is emitted from an electron transferred from L-shell to the K-shell. It can also be from the other levels; the K_β is from M-shell to K-shell and L_α is from M to L-shell (figure 3.5). The EDX spectrum plots the intensity of the detected x-ray as a function of the energy so that each peak represents characteristic x-ray energy.

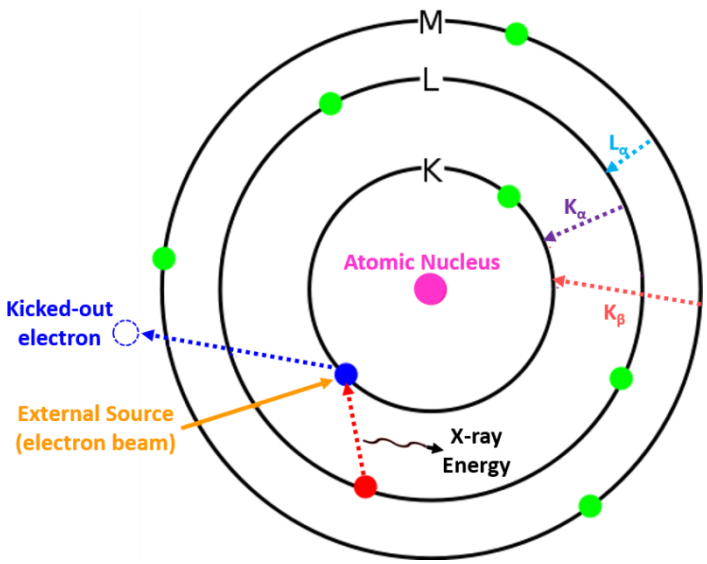

Figure 3.5: The diagram illustrates the basic physics behind energy dispersive x-ray; the electron is knocked-out from the K-shell and created hole is filled from outer shell electron that emits a radiation of a characteristic x-ray.

3.2.2 X-ray photoelectron spectroscopy (XPS)

XPS is one of the most surface-sensitive analytical techniques. In this technique, the sample is irradiated with low energy (~1.5 keV) X-rays to induce the photoelectric effect, where the incident energy is used to knock out electrons from the shell. The kinetic energy (KE) of the photoelectrons is measured by the detector and used for calculating the binding energy (BE) of the electrons via the following relation:

$$BE = h\nu - KE - \varphi \qquad (1)$$

where ν is the frequency of the x-ray, h is the Plank's constant and φ is the spectrometer work-function derived via a calibration process. Figure 3.6 shows the key components of the XPS, the X-ray source, electron transfer lenses, electron energy analyser and detector. All these components are maintained in a stainless-steel chamber under ultra-high vacuum ~ 10^{-10} Torr. This ultr-high vacuum facilitates the transmission of the photoelectrons to the analyser and minimizes the re-contamination rate of a freshly cleaned sample. The x-ray source is commonly an Al source that consists of an Al anode held at potential of 15 kV that is bombarded with emitted electrons from a filament. The generated X-rays are used in combination with a monochromator that provides a narrow (line width < 0.26 eV) Al $K\alpha$ component. The electrostatic lenses collect, focus and accelerate the electron beam into the analyser slit.

The electron energy analyser is a hemispherical energy analyser that consists of two concentric hemispherical electrodes in which the electrons are dispersed while moving along the axis of the analyser. At the end of the analyser, a positive potential position sensitive detector is attached to detect the electrons.

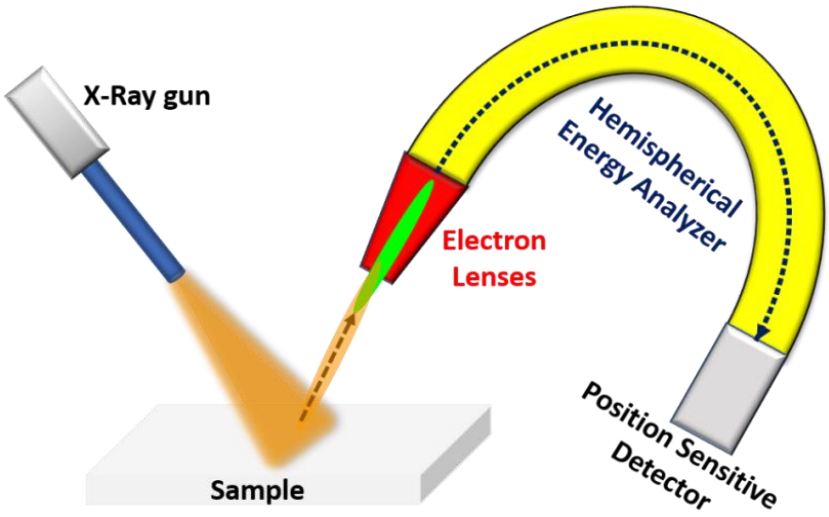

Figure 3.6: Key component representation of XPS setup.

XPS data is presented in terms of graph between binding energy and intensity. The charging of the samples normally causes a shift in the energy of the collected spectra so that the calibration of data is required. The carbon peak C 1s at 284.6 eV is used for calibrating the spectra throughout this thesis. All the XPS measurements were performed by my lab mates Dr. Conor Rocks and Dr. Tamilselvan Velusamy.

3.2.3 X-Ray diffraction (XRD)

X-ray diffraction is a very useful technique for material analysis. XRD gives details on the structural properties of a material. This technique can be used to identify crystal structure, chemical composition and lattice strain.

XRD system uses an x-ray source to create a diffraction peak which is related to the electron distribution in material. The crystal structure of the sample acts as a diffraction grating for x-ray because of comparable spacing of crystal planes in the lattice to the x-ray wavelength, as shown in figure 3.7.

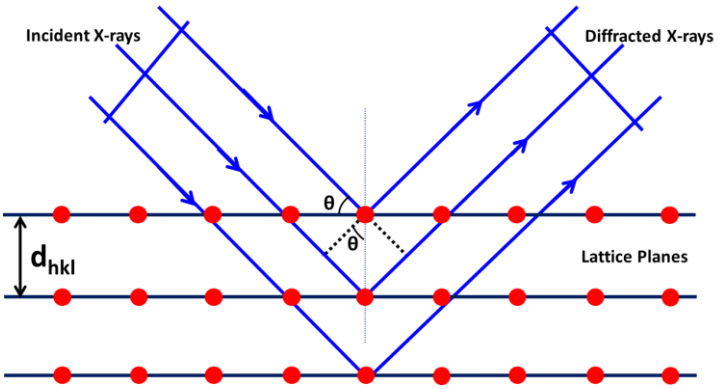

Figure 3.7: Incident x-ray beam interaction with parallel plane of atoms with spacing d_{hkl} to produce diffraction pattern.

The interaction between the incident x-rays and electrons generates elastically scattered waves from many atoms. Constructive interference happens when these waves are in phase. Diffracted beams are in specific direction with the angle θ, also called the Bragg's angle, and this angle is related to wavelength of incident x-rays (λ) and the spacing between atomic planes (d). This is known as Bragg's law and can be represented by equation 2:

$$2d \sin \theta = n \lambda \qquad (2)$$

XRD analysis carried out within this thesis used powder x-ray diffraction, which implies that the x-ray wavelength was fixed (1.54 Å) and θ was variable.

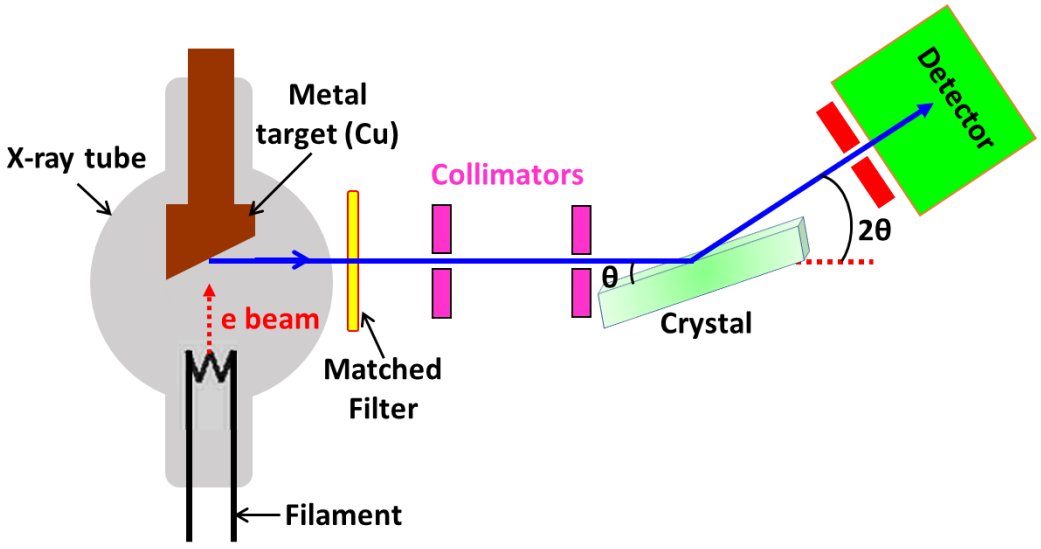

Figure 3.8: Schematic diagram showing XRD setup.

Figure 3.8 shows basic setup of an X-ray diffractometer, which consists of an x-ray tube, a matching filter, collimators and a detector. An x-ray tube is consisting of a filament (Tungsten) and metal target (mainly copper) enclosed in vacuum glass

chamber. When a high voltage is applied on the filament, it emits an electron beam by thermionic emission and this beam hits the metal target to generate x-rays. A matched filter is used to select the characteristic x-ray, here K_{α}. X-rays are aligned by collimators and the resulting narrow x-ray beam strikes on the crystal and diffracted x-rays are detected by the detector. The intensity of the diffraction pattern depends in the arrangement and nature of atoms in the crystal. This technique provides the qualitative identification of crystalline compounds because these diffraction patterns are unique for every crystalline substrate. By comparing experimental data with a database, the exact chemical composition can be inferred.

3.2.4 Raman spectroscopy

Interaction of light with matter results in many phenomena. For example, when the energy of incident photon corresponds to the energy gap between the ground state and excited state, that energy photon can be absorbed, and electrons are promoted to higher energies. This concept is used in absorption spectroscopy that will be described in section 3.2.9; however, if the photon energy doesn't match to the difference of ground state and excited state, in that case photon may interact with a molecule and result in scattering.

If only electron cloud distortion is involved in scattering, there will be no or very less change in the frequency of incident and emitted photon because electrons are comparatively light. This is the elastic scattering. If this happens in the molecules, it is called as Rayleigh scattering as shown in figure 3.9. If nuclear motion is induced during the scattering phenomenon by energy transfer, either from molecule to the incident photon or from photon to molecule, this is termed as Raman scattering or inelastic scattering. In this type of scattering, the light interaction with molecules distorts the electron cloud and induces nuclei motion to form a short-lived virtual state. This state is not stable, and it quickly re-radiates the light photon. If the photon energy absorbed by the molecule in the *m* vibrational state, reach to the virtual state and return to the higher vibrational sates *n*, the emitted frequency of the photon is red shifted. This is called Stokes scattering as shown in figure 3.9.

If the molecules are already in a higher vibrational state *n* because of other factors, such as thermal energy, in that case molecule transfers energy to the scattered photon

by returning to the lower vibrational state *m*. In this case, the phenomenon is named as anti-Stokes scattering (figure 3.9). The difference between frequency of incident and scattered photons corresponds to the vibrational energy level of the molecule and is called the Raman shift.

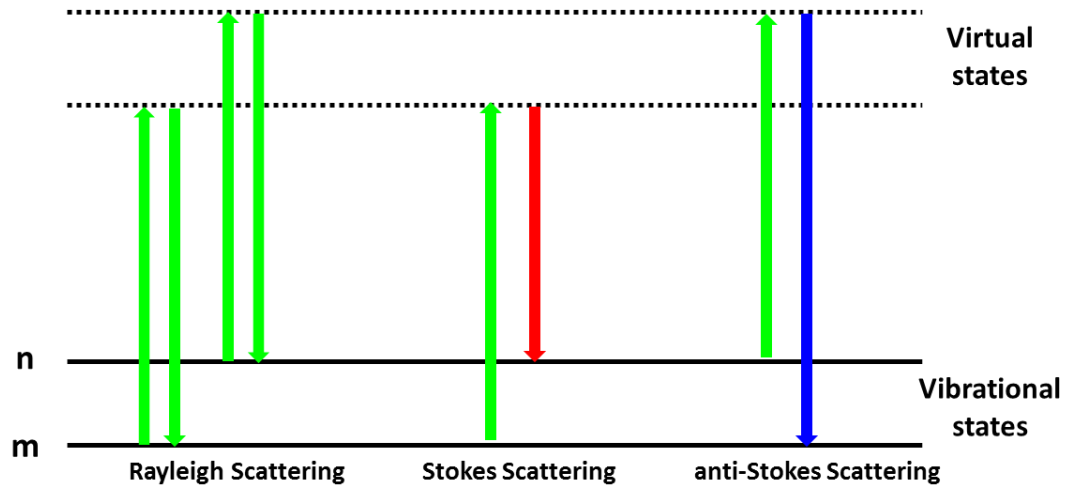

Figure 3.9: Schematic diagram of energy transition involved in (a) Rayleigh scattering and b-c) Raman scattering where interaction of photon with molecular vibrational mode either results in Stokes scattering (energy lose red shifted) or anti-Stokes (energy gained blue shifted).

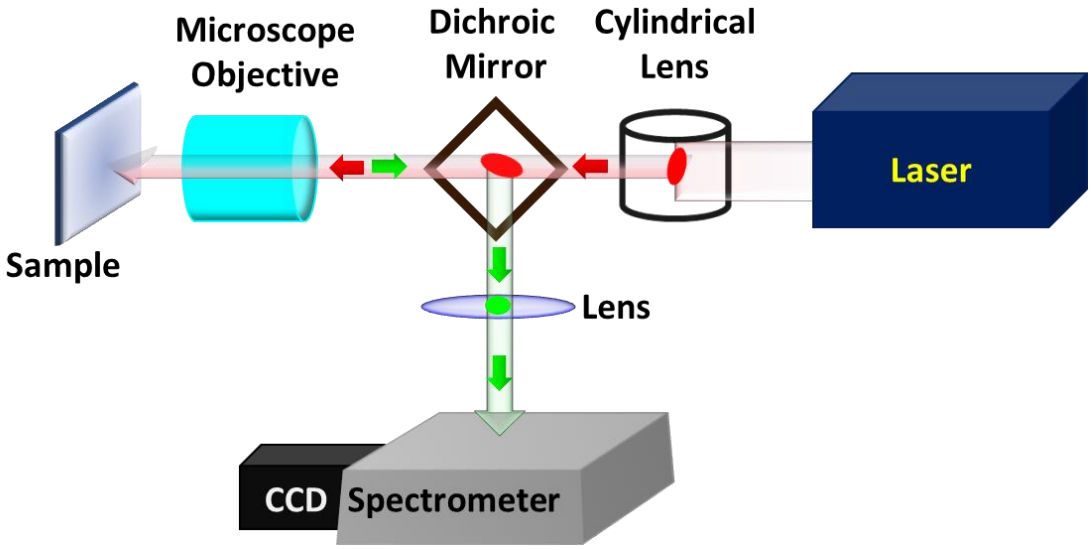

Figure 3.10: Schematic representation of Raman spectrometer.

Figure 3.10 shows the components of a Raman spectrometer, where a laser (coloured red) is generated and passed through lenses to focus on sample. A scattered and Raman-shifted light (coloured green) is filtered out from the laser light by a dichroic mirror and detected in the detector.

3.2.5 Fourier transform Infrared spectroscopy (FTIR)

Fourier transform infrared spectroscopy (FTIR) relies on the detection of vibrational frequencies. Here, a beam of light containing a range of mid-infrared frequencies (400-4000 cm^{-1}) is used to determine the chemical composition of the sample material. In this context, the unit in wavenumbers ($\bar{\nu}$) is used instead of wavelengths (λ). The wavenumber is the reciprocal of the wavelength.

When a beam of light passes through the sample, sample molecules absorb specific frequencies that are characteristic of the material structure. Unlike Raman spectroscopy, here absorbed frequency needs to be exactly like the vibrational frequency of the molecules.

A molecule has many vibrational modes depending on the number of atoms and the structure of the molecule. Structural arrangement of molecules, whether it is linear or non-linear, describes the degree of vibrational freedom. If a molecule is linear, the

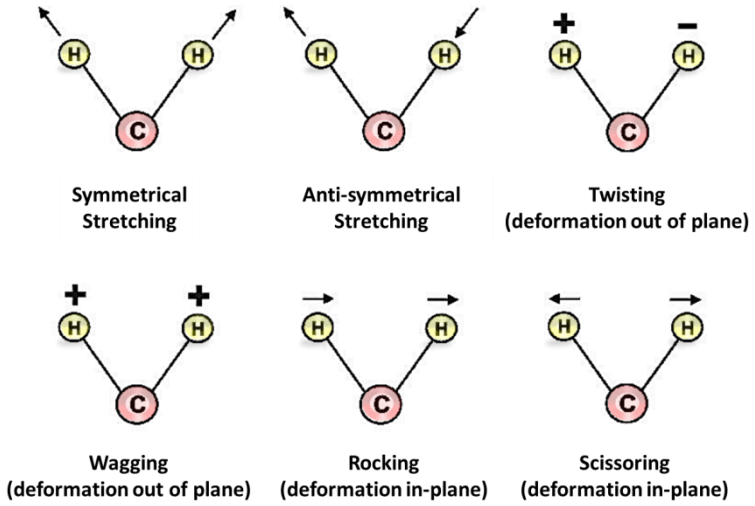

Figure 3.11: Shows possible vibrations in a molecule where symmetrical stretching vibrations can't be detected by FTIR.

vibrational freedom will be $3N$-5, where N is the number of atoms in the molecule. A vibrational mode can only be detected if there is a change in the dipole that describes the charge difference in the atoms of that molecule. For example, symmetric molecules like O_2 cannot be observed in FTIR measurements. There can be many types of vibrations in a molecule as shown in figure 3.11. These vibration frequencies are characteristic of vibration in a molecule and will be absorbed by the molecule. The absence of a given frequency in the recorded spectra indicates its absorption and

therefore is indicative of a particular molecular vibration being active in the sample, which can be related to the chemical composition.

3.2.6 Photoluminescence spectroscopy (PL)

In semiconductors, photoluminescence (PL) is the emission of light when a material is excited with the energy greater than the bandgap; upon excitation, electrons are raised from the valence band to excited states. This excess energy can be dissipated by the emission of the light and is called as photoluminescence.

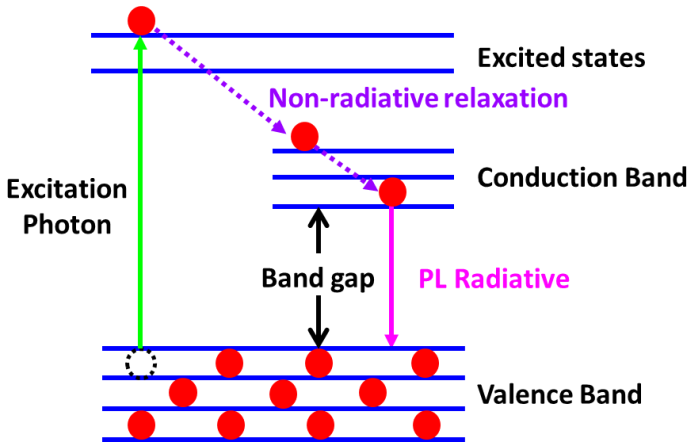

Figure 3.12: Illustrate the radiative and non-radiative emission after excitation, also depicting the emission band gap.

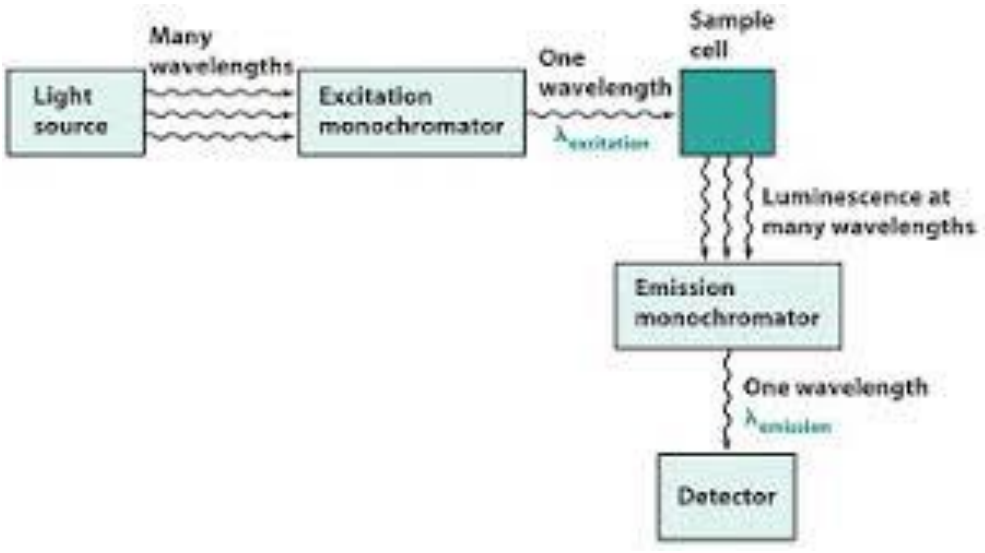

figure 3. 13 Schematic of basic working principle of a photoluminescence spectroscopy.[2]

Three major phenomena can give rise to photoluminescence. First is resonant radiation, where an equivalent energy photon is emitted of the absorbed photon. The life span between absorbed and emitted photon is 10 nanoseconds. Second

phenomenon is fluorescence where the excess energy of the excited electron is lost through non-radiative relaxation (e.g. vibrational relaxation, internal conversion etc.) before electrons reach the lower energy states in the conduction band as shown in figure 3.12. Therefore, emitted photon has energy lower than absorbed photon. This transition happens within short lifetime of 10^{-8} – 10^{-4} second. Third is phosphorescence, which is radiational transition and absorbed photon undergoes intersystem crossing into a state with a different spin multiplicity. Lifespan of phosphorescence is usually from 10^{-4} – 10^{-2} second.

The PL spectrum can provide information about the bandgap, band structure of the material, impurity levels and recombination mechanisms. However, at nanoscale level, the surface characteristic of the material can largely influence the PL emission and the assumption of a band to band transition is not valid anymore. PL measurements can be carried out from either solid or liquid samples.

Figure 3.13 shows basic working principle of a photoluminescence spectroscopy. A light source emits different wavelength photons which passes through excitation monochromator to select a desired excitation wavelength. This selected wavelength photon passes through the sample cell and emits luminescence at different wavelengths. Emission monochromator selects the desired wavelength and passes to the detector, from where it can be recorded.

3.2.7 Ultraviolet-visible absorption spectroscopy (UV-Vis) and bandgap measurement

Ultraviolet-visible spectroscopy (UV-Vis) accessorised with suitable components allows measuring the absorption, transmission and scattering of light when interacting with a sample in the ultraviolet and visible range. In standard transmission mode, a spectrometer records the degree of light that has been transmitted at each particular wavelength. This spectrum is often represented as absorbance (A) versus wavelength (λ).

Basic UV-Vis spectrometer optical arrangement is presented in the figure 3.14. It consists of deuterium (UV light source), a tungsten lamp (visible light source), (Deuterium + Tungsten lamp) emits continuous radiation and component wavelength of this light is separated by a diffraction grating. A slit is placed next to the grating

sends a narrow monochromatic light into a rotating disc. This disc directs the light monochromator, detector, filter, beam splitter and sample holder. A light source towards the sample cell and the reference cell. The sample cell contains the solution

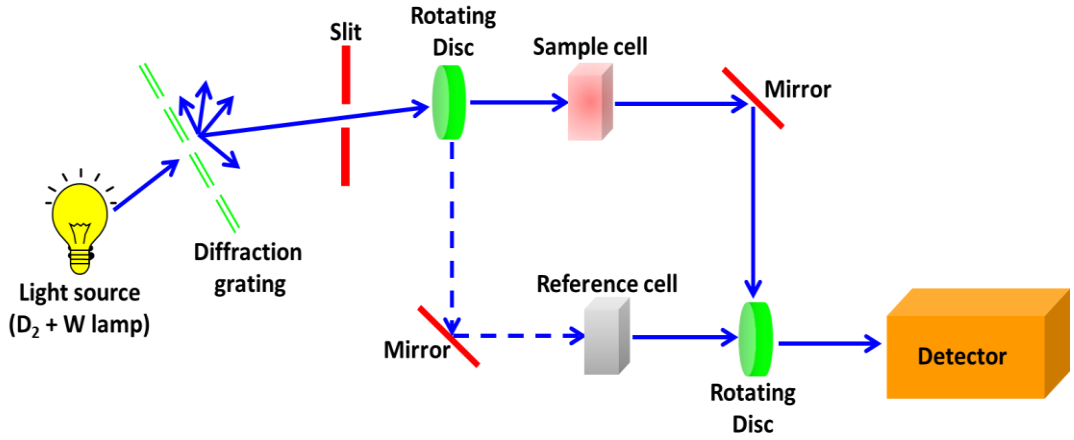

Figure 3.14: Schematic of ultraviolet-visible (UV-Vis) spectroscopy.

with the sample particle and reference cell contains pure solvent. After passing through cells, another rotating disc transmits these light intensities to the detector. These intensities are converted into current signal by the detector and read by computer. Computer compares these transmitted intensities and the transmittance is calculated by using equation 3:[3]

$$T = \frac{I(l)}{I_o} \tag{3}$$

where *I(l)* intensity of the transmitted light, I_o incident light intensity and T is the transmittance.

With this basic transmission mode, integrating sphere is also used. Integrating spheres, in combination with UV/Vis and UV/Vis/NIR spectrophotometer, is an extremely useful accessory for high precision reflectance and scattered transmittance measurements on any solid or liquid sample. Liquid samples were placed inside the integrating sphere and solid samples were placed on the backside of integrating sphere covered with spectralon plate as shown in figure 3.15. Total transmission, reflectance and scattering (T+R+S) were measured using integrating sphere. These measurements were used to calculate absorption coefficient (α).

Absorption coefficient calculation for solid sample:

The light going through a sample can be expressed as follows:

$$I(x) - I(x + dx) = -I(x)(\mu_a + \mu_s)dx \quad (4)$$

which describes the difference in light before and after going through the *dx* of the sample and extinction coefficient (μ) is the sum of absorption coefficient and scattering coefficient.

$$\mu = \mu_a + \mu_s \quad (5)$$

Change in the light intensity through the sample thickness x can be analysed by arranging equation (4) & (5) and integrating it over the travelled distance:

$$\int_{I(0)}^{I(x)} \frac{dI(x')}{I(x')} = \int_0^x -\mu dx'$$

$$\ln I(x) - \ln I(0) = -\mu x$$

$$\ln \frac{I(x)}{I(0)} = -\mu x$$

$$\frac{I(x)}{I(0)} = e^{-\mu x}$$

$$I(x) = I(0)e^{-\mu x}$$

The relation between initial light intensity (I_o) to the light intensity after crossing t thick *I (t)* is given by:

$$I(t) = I(0)e^{-\mu t}$$

$$I(t) = I_0(1 - R)e^{-\mu t} \quad (6)$$

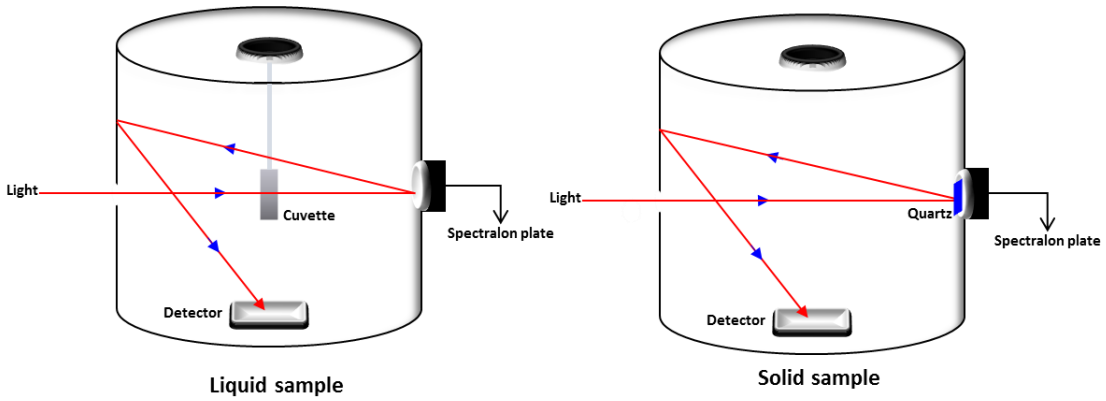

Figure 3.15: Showing integrating sphere with liquid (quartz cuvette) and solid (quartz substrate) sample position.

Where, R is the reflectance and μ is the attenuation coefficient. According to equation (3) and (5), T is:

$$T = \frac{I(t)}{I_0} = (1-R)e^{-\mu t}$$

$$\frac{T}{(1-R)} = e^{-\mu t}$$

$$\ln\frac{T}{(1-R)} = -\mu t$$

$$\mu = -\frac{1}{t}\ln\frac{T}{(1-R)} \quad (7)$$

When light travel from 0 to t distance within the sample, absorbed light intensity $I_a(t)$ can be written as:

$$I_a(t) = \int_0^t I(x)\mu_a dx$$

$$= \int_0^t I(0)e^{-\mu x}\mu_a dx$$

$$= \mu_a(I_0 - RI_0)\int_0^t e^{-\mu x}dx$$

$$= \mu_a I_0(1-R)\frac{(1-e^{-\mu t})}{\mu} \quad (8)$$

According to energy conversion low, absorption (*Abs*) is:

$$1 = T+R+S+Abs$$

$$Abs = 1-(T+R+S) \quad (9)$$

$$Abs = 1-(T+R+S) = \frac{I_a(t)}{I_0} = \mu_a(1-R)\frac{(1-e^{-\mu t})}{\mu}$$

$$\mu_a = \frac{\mu}{(1-R)(1-e^{-\mu t})}[1-(T+R+S)]$$

$$\mu_a = \frac{-\frac{1}{t}\ln\frac{T}{(1-R)}}{(1-R)-(1-R)e^{-\mu t}}[1-(T+R+S)]$$

$$= \frac{-\frac{1}{t}\ln\frac{T}{(1-R)}}{(1-R)-T}[1-(T+R+S)]$$

$$\mu_a = -\frac{1}{t}\left\{\frac{\ln\frac{T}{(1-R)}}{1-R-T}[1-(T+R+S)]\right\} \quad (10)$$

Where, μ_a is the absorption coefficient. In all the measurements, it is assumed that scattering is negligible ($S << R + T$) then R can be written as

$$I_a = \int_0^L I(x)\,\mu_a dx$$

$$(T+R+S)-T = (T+R+0)-T = R$$

$$R = (T+R+S)-T \tag{11}$$

By putting value from equation (11) to equation (10):

$$\mu_a = -\frac{1}{t}\left\{\frac{\ln\frac{T}{\left(1-\left((T+R+S)-T\right)\right)}}{1-\left((T+R+S)-T\right)-T}[1-(T+R+S)]\right\}$$

$$= -\frac{1}{t}\left\{\frac{\ln\frac{T}{(1-(T+R+S)+T)}}{1-(T+R+S)}[1-(T+R+S)]\right\}$$

$$\mu_a = -\frac{1}{t}\left\{\ln\frac{T}{(1-(T+R+S)+T)}\right\}$$

Here, *t* is not used in calculation and a value proportional to absorption coefficient is calculated.

Absorption coefficient calculation for liquid sample:

In liquid sample, reflectance is considered to be zero. From equation (7), $I_a(l)$ will be:

$$I_a(l) = \frac{\mu_a}{\mu}\, I_o(1-e^{-\mu l}) \tag{12}$$

$$Abs = \frac{I_a(L)}{I_o} = \frac{\mu_a}{\mu}\,(1-e^{-\mu l}) \tag{13}$$

Where, μ_α is the absorption coefficient and *l* is the path length.

Similarly, equation (6) can be written as:

$$\mu = -\frac{1}{l}\ln T \tag{14}$$

According to energy conservation low absorption (Abs) can be written as:

$$Abs = 1-(T+R+S)$$

Where T is the transmittance, R is the reflectance and S is the scattered light. It is assumed that reflectance is negligible for all the measurement so *A* can be written as:

$$Abs = 1-(T+S) \tag{15}$$

According to equation (13) and (15):

$$1 - (T + S) = \frac{\mu_a}{\mu}(1 - e^{-\mu l})$$

$$\mu_a = \frac{(1-(T+S))\mu}{(1-e^{-\mu l})} \quad (16)$$

According to equation (14) and (16), absorption coefficient can be written as:

$$\mu_a = \frac{(1-(T+S))(-lnT)}{l(1-T)} \quad (17)$$

After calculating absorption coefficient for liquid or solid sample, the bandgap of sample can be estimated using Tauc relation equation (18)[4]

$$(\mu_a h\nu)^{1/n} = \beta(h\nu - E_g) \quad (18)$$

where β is a material dependent constant, h Planck's constant, E_g is the bandgap energy of the material and n is an index, which can have different values (2, 3, 1/2 and 1/3) corresponding to indirect allowed, indirect forbidden, direct allowed and direct forbidden transitions. The bandgap of material is estimated by plotting $(\mu_a h\nu)^{1/n}$ vs. $h\nu$. By extrapolating the linear region near the absorption edge on the energy scale, the material bandgap energy can be estimated.

3.2.8 Kelvin probe measurement (KP)

Techniques based on a Kelvin probe produce non-contact and non-destructive surface sensitive measurements which are used to determine the work function (ϕ) of a material by measuring the contact potential difference (CPD) between sample surfaces and vibrating gold (Au) tip. In this measurement, we assume that ϕ of the Au electrode (-5.1 eV) does not change during the measurement. Therefore, all changes in CPD are attributed to surface change of the sample. Contact potential of a material depends on the work function of the material where the work function is the minimum amount of energy required to release electrons from the materials surface.

Energy level of two conducting samples with different ϕ can be seen in figure 3.16a. When two materials are bought into contact (figure 3.16b), electrons in the material with the lower work function flow to the one with the higher work function. If these materials are placed into a parallel plate capacitor, equal and opposite surface charge forms on the plates. Because of this charge over the capacitor, a voltage is developed called contact potential. This potential can be measured by applying an external

backing potential to the capacitor until this surface charge disappears. This value of backing potential will be equal to the contact potential as shown in figure 3.16c.

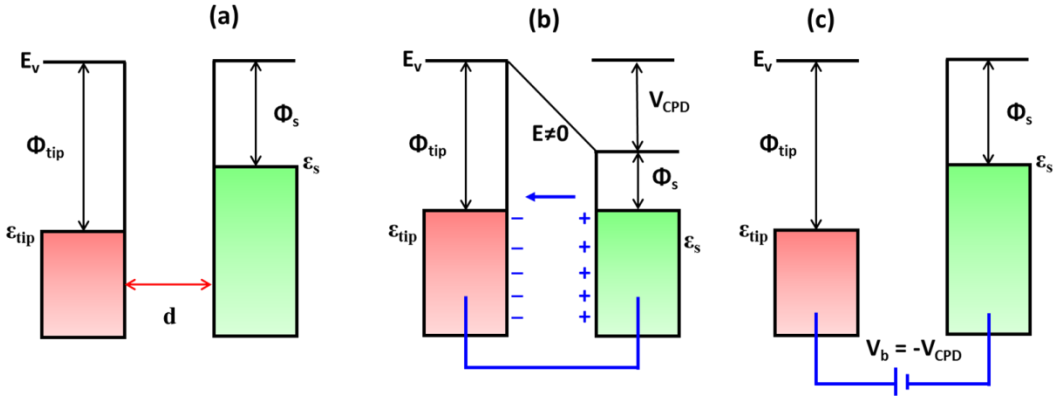

Figure 3.16: a) Energy level diagram for two conducting material, where ϕ is the work functions of the materials; (b) Two surfaces are equally and oppositely charged when external electrical contact is made and (c) A variable "backing potential" V_b applied until electric field between plates vanishes.

This measurement can only be used once because of charged surface. Before starting another measurement, charge must be dissipated. Therefore, a sinusoidal voltage $V_{ac}\sin(\omega t)$ is applied to the Au tip of the probe that results in an electrostatic force between the sample and the tip. A constant bias V_{off} is applied from the feedback loop that nullifies the CPD between the tip and the sample. When the surface of the tip is close to the sample surface, an electrostatic force $F(\omega)$ is given by:

$$F(\omega) = -\frac{dc}{dz}\left(V_{off} - V_s\right)V_{ac}\sin(\omega t) \qquad (19)$$

where d*c*/dz is the capacitance gradient between the tip and the sample, V_s is the surface potential (difference in ϕ of tip and sample), ω is the equal to 76 Hz. The tip vibrates, and V_s is counterbalanced by V_{off} through the feedback loop and $F(\omega)$ is compensated between the tip and sample. To obtain the absolute ϕ of the sample, CPD of the tip is measured using standard Au reference (CPD_{Au}) and ϕ is calculated using the following formula:

$$\Phi = 5100 - CPD_{Au} + CPD_{sample} \qquad (20)$$

Where 5100 is the ϕ of the Au in meV, CPD_{sample} is the CPD between the tip and the sample surface. All the kelvin prob measurements were performed by my lab mates Dr. Conor Rocks and Dr. Tamilselvan Velusamy.

3.2.9 Thermogravimetric Analysis (TGA)

Thermogravimetric analysis is based on the measurement of weight change as a function of temperature (constant or variable) in the presence of a gas. This weight change can be the result of many thermal reactions for e.g., evaporation, decomposition, gas absorption and dehydration.

Figure 3.17 shows a typical setup of a TGA system which consists of a sample pan with precision balance within a furnace. This sample pan is connected to the sensor assembly, which is connected to the data collection assembly. Gas inlet and outlet are used to maintain a controlled gas environment when the experiment is running. According to the results requirement, this gas can be an inert or a reactive gas that flows over the sample and exists through the gas outlet.

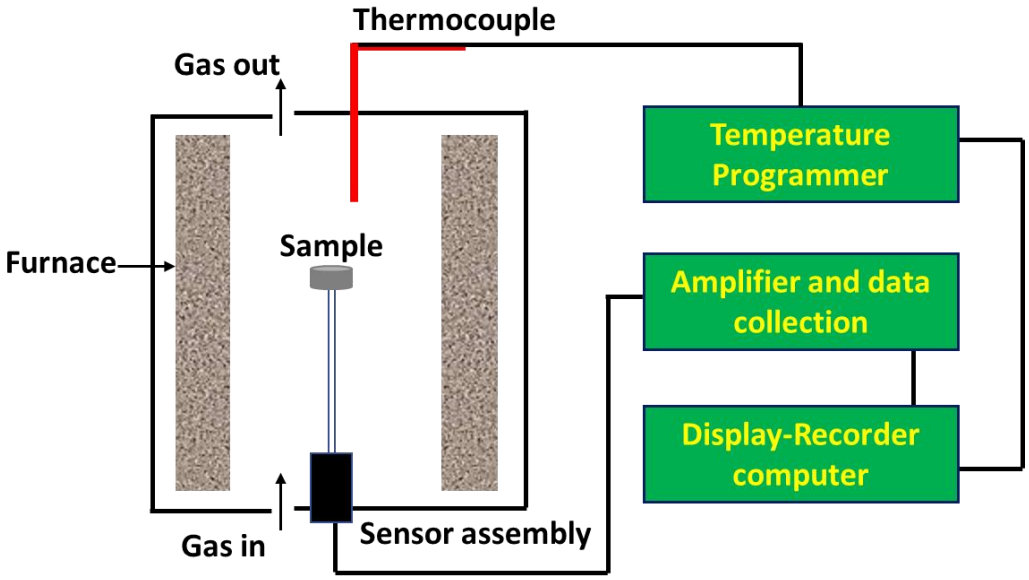

Figure 3.17: Schematic diagram of TGA apparatus.

The sample is heated by increasing the furnace temperature. Furnace temperature can go as high as 1600 ^{o}C. Heating changes the sample weight and the weight change affects the equilibrium of the microbalance. This imbalance is backed by the force coil by generating electromagnetic force and these forces are proportional to the weight change of the sample. That's how the weight change is monitored and recorded throughout the experiment.

3.2.10 Cyclic voltammetry (CV) measurement

Cyclic voltammetry (CV) is the one of the most important technique to understand the electrochemical properties of a material. CV can also be useful to understand thermodynamics and kinetics of heterogeneous electron transfer reactions providing information of electron transfer process at an electrode.

A linear potential sweep (a potential that increases or decreases linearly with time) is applied on a working electrode. When the potential passes the formal potential E^o of an analyte, current flows through the electrode either because of the oxidation or the reduction of the analyte. The current is proportional to the concentration of the analyte in solution. The resulting plot between current vs. potential is known as cyclic voltammogram.

A basic schematic of a CV measurement cell is shown in figure 3.18a. It consists of three electrodes (working, reference and auxiliary) immersed into the test solution (0.5 M H_2SO_4 aqueous solution is used for the results reported throughout this thesis). A potential is applied and maintained between the working and reference electrode by a potentiostat and the current is measured at the working electrode. Charge flows between the working electrode and the counter electrode.

Figure 3.18b shows a typical voltammogram where only redox electrochemical reactions are taking place. This is the result of oxidation and reduction of the analyte by applying a sweep potential. Figure 3.18c shows another voltammogram where a rectangular graph is generated, which is generally observed when no electrochemical reactions are taking place, and this results essentially in a behaviour that resembles the one of a capacitor. The latter is often referred to as electrical double layer capacitance (EDLC). The corresponding capacitance can be calculated by the following equation:[5]

$$\text{Specific capacitance } (C_s) = \frac{\int \text{Idv}}{ms\Delta V} \quad (21)$$

$$\text{Areal capacitance } (C_a) = \frac{\int \text{Idv}}{As\Delta V} \quad (22)$$

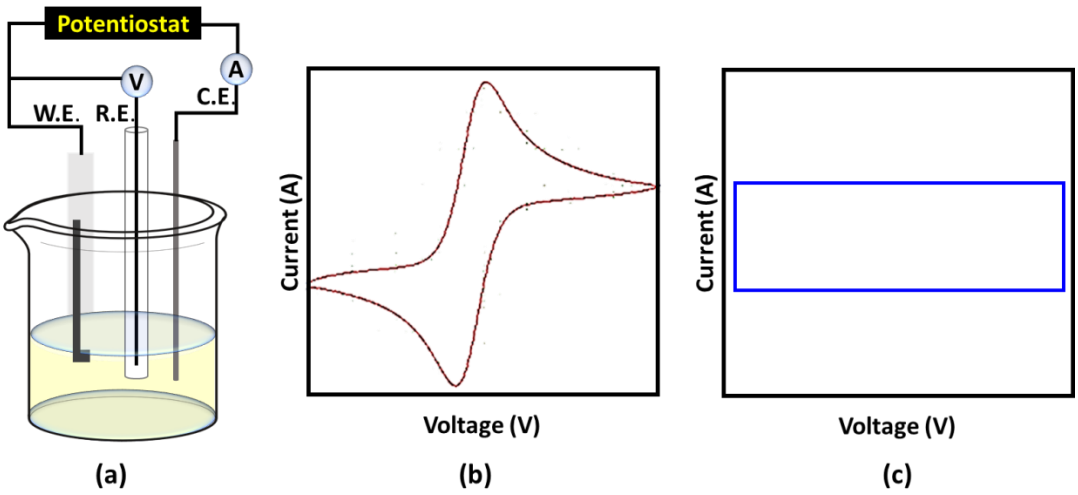

Figure 3.18: (a) Basic reactor for CV measurement; W.E. (working Electrode) R.E. (Reference Electrode) and C.E. (Counter Electrode), (b) Voltammogram because of redox reaction and (c) Voltammogram because of electrostatic reaction.

where, $\int Idv$ is the area under the voltammogram, m is the mass of active material, s is the scan rate, ΔV is the potential window and A is the area of the electrode containing the active material. The specific capacitance is the measurement of the charge storage per gram of active material. Areal capacitance is the measurement of charge storage per centimetre square area.

3.2.11 Solar cells current-voltage characteristics

Figure 3.19 shows the setup used for Current-voltage (IV) measurements. IV measurement were recorded using Keithley 2400 sourcemeter under AM 1.5

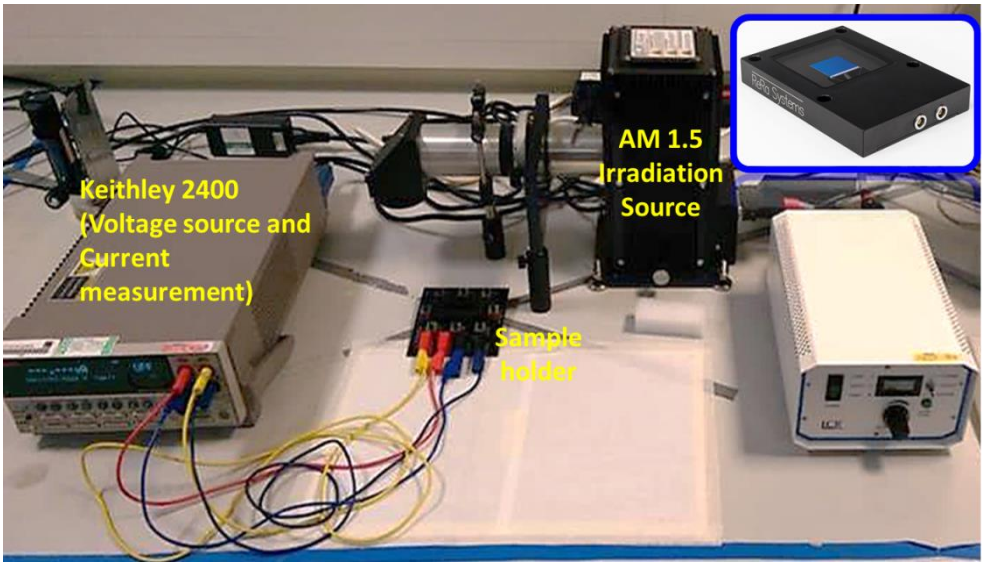

Figure 3.19: Current-Voltage measurement system where Inset shows crystalline silicon reference solar cell.

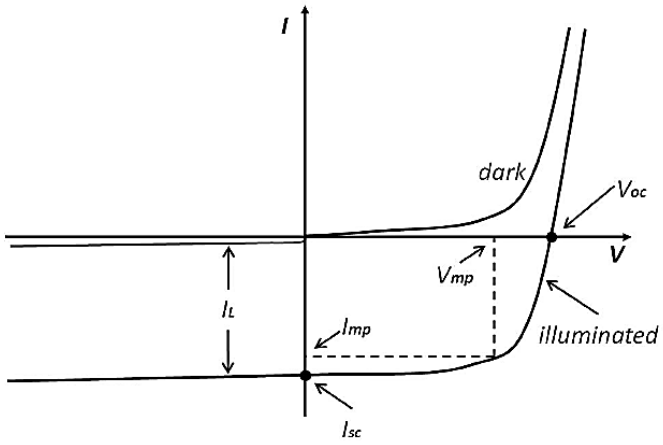

Figure 3.20: Characteristics of an ideal solar cell in dark and after illumination.[6]

irradiation in ambient conditions. Before measuring the current-voltage characteristics (I-V) of a sample solar cell, the system is calibrated with standard crystalline silicon solar cell shown in the inset of figure 3.19. IV characteristics of a typical solar cell are presented in figure 3.20. under dark and illuminated conditions. Several parameters can be analysed from IV curve including short circuit current (I_{sc}), open circuit voltage (V_{oc}) and maximum power point (P_{mp}) = $V_{mp}\, I_{mp}$ as shown in figure 3.20.

The short circuit current (I_{sc}) found at voltage equal to zero, corresponds to the photogenerated current under illumination and when the device is connected in a short circuit.

The open circuit voltage (V_{oc}) found at current equal to zero and it is the maximum voltage available from the solar cell.

The maximum power point (P_{mp}) This is the one of main parameter in determining the solar cell efficiency. This is the multiplication of I_{mp} and $V_{mp,}$ which is a maximum square formed inside I-V curve as shown in figure 3.20.

The Fill Factor (FF) is used to quantify the quality of the device and represents the ratio of actual power achievable from the device (P_{mp}) and the product of its I_{sc} and V_{oc}.

$$FF = \frac{P_{mp}}{V_{oc}I_{sc}} = \frac{V_{mp}I_{mp}}{V_{oc}I_{sc}} \qquad (23)$$

The conversion efficiency (η) is the main parameter used to evaluate solar cell performance and is defined by the ration of maximum output power and the input power (P_{in}).

$$\eta = \frac{P_{mp}}{P_{in}} = \frac{V_{oc} I_{sc} FF}{P_{in}} \tag{24}$$

3.3 Reference:

1. Cao, G. *Synthesis, Properties and Applications*. (2004). doi:10.1142/9789814340571

2. Barron, A. R. Photoluminescence Spectroscopy and its Applications. 1–11 (2011).

3. Techniques, C. Chapter – 2 characterization techniques 2.1. 35–49

4. Hassanien, A. S. & Akl, A. A. Effect of Se addition on optical and electrical properties of chalcogenide CdSSe thin films. *Superlattices and Microstructures* **89,** 153–169 (2016).

5. Zhang, L. & Gong, H. Improvement in flexibility and volumetric performance for supercapacitor application and the effect of Ni–Fe ratio on electrode behaviour. *J. Mater. Chem. A* **3,** 7607–7615 (2015).

6. Sidi, P., Sukoco, D., Purnomo, W., Sudibyo, H. & Hartanto, D. Electric Energy Management and Engineering in Solar Cell System. *Solar Cells - Research and Application Perspectives* (2013). doi:10.5772/52572

Chapter 4: Synthesis of ZnO based Nanomaterials by Hybrid Plasma-Liquid Electrochemical Etching Method

4.1 Introduction

This chapter describes the synthesis of zinc-based semiconductors by plasma liquid system. The synthesis of zinc peroxide (ZnO_2), ZnO and N-doped ZnO (N-ZnO) nanoparticles with solutions made from ethanol, water and ethylenediamine (EDA) will be presented. Nanoparticles are produced for all three materials without any surfactant or reducing agents.

Section 4.2 will describe the experimental setup used throughout this work. In section 4.3, impact of synthesis current on ZnO_2 properties will be analysed by using different characterization technique. Also, a proposed synthesis mechanism for ZnO_2 will be discussed. At the end, synthesis of N-doped ZnO will be presented. A detailed characterization study revealed the interesting properties about doped ZnO, for e.g., effect of doping on absorption edge, on emission properties etc. Also, an analogy will be presented to identify the dopant position in the ZnO lattice. Electrochemical studies will be demonstrated to study the changes in storage capacity by changing the doping concentration.

4.2 Experimental Setup

Figure 4.1 shows the schematic diagram of hybrid plasma-liquid reactor. This reactor is consisting of Zinc foil (Goodfellow, ZN000270/3 and 0.125 mm) and nickle capillary (Goodfellow, 0.8 mm internal diameter, 1 mm outer diameter) connected to the power supply and a liquid solution as shown in figure 4.1a. Zinc foil, nickel capillary and liquid solution act as an anode, cathode and electrolyte, respectively. He gas was used as a carrier gas in this system to generate plasma. The flow of He was kept constant at 50 standard cubic centimetres per minute (sccm). Zinc foil was immersed into the electrolyte while nickel capillary was adjusted at ~1mm distance from liquid surface. High voltage (HV) was applied through a 100 kΩ ballast resistor to the zinc foil and the Ni tube (figure 4.1a). The microplasma was generated between nickel capillary and liquid surface as shown in figure 4.1b. The synthesis time was 30

minutes for all experiments. Synthesis started as soon as the microplasma is generated and the presence of nanoparticles (NPs) can be inferred by naked eye depending on the optical nature of synthesized material. Here, the current and electrolyte will be changed to synthesis different materials (section 4.3 & 4.4).

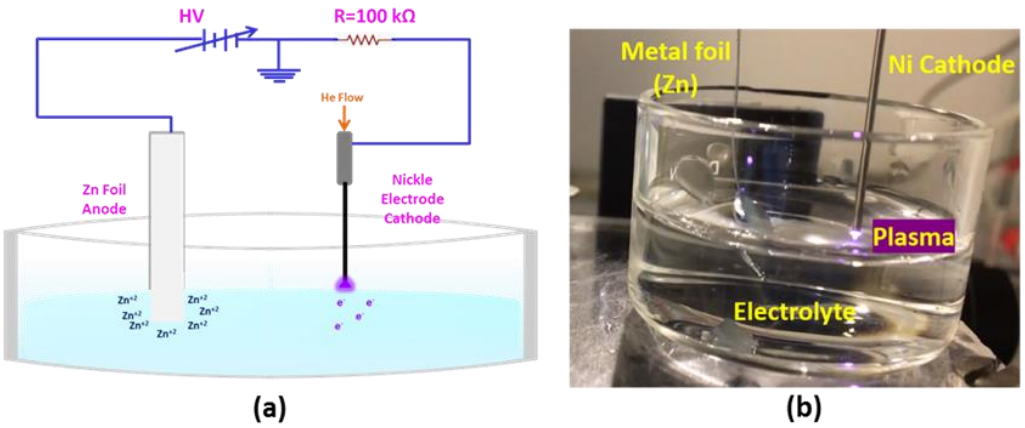

Figure 4.18: (a) Schematic diagram of the hybrid plasma liquid system showing Zn anode and nickle cathode connected to high voltage (HV); (b) shows the real-time microplasma.

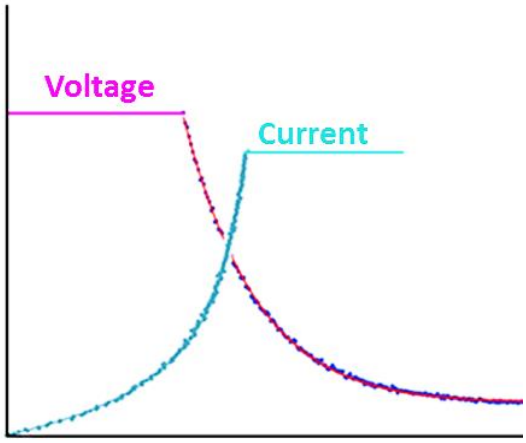

Figure 4.1: Typical behaviour of the voltage and current in a hybrid-plasma liquid reactor where voltage starts to decrease as soon as current reaches to the set value.

Voltage and current behaviour in the system can be seen in figure 4.2 where normally, at initial, voltage remains constant until the current reaches to the set value. According to electrolyte conductivity, process can take time to achieve the desired value of current. The current value is maintained constant throughout the whole process. However, as the liquid evaporates in the process, the distance between liquid and Ni capillary increases and can change current value. Therefore, in every 10 min, the process was stopped to adjust the volume by adding 1 mL of electrolyte to compensate

the evaporated liquid loss so that the distance between the Ni capillary and the electrolyte surface can be kept constant appreciably over the 30 min process. Meanwhile, this addition of electrolyte helps in dissipating the heat by stirring the solution.

4.3 Synthesis of ZnO_2 nanoparticles in ethanol

4.3.1 Experimental parameters

Here, 10 mL of ethanol is used as an electrolyte for plasma processing. In order to understand the effect of current on the synthesis process and material properties, three different process current 0.5 mA, 1.0 mA and 2.0 mA were used. Particles were produced at all currents. Synthesis current, corresponding phase and produced particle size are given in the table 1.

Table 4: Experimental details and summary of the results.

Current	Phase	Particle size
0.5 mA	$Zn(OH)_2$ & ZnO_2	< 40 nm
1 mA	ZnO_2	< 8 nm
2 mA	ZnO_2	~ 2-5 nm

4.3.2 Material Characterization

TEM analysis was performed to understand crystal structure, morphology and crystallinity. Liquid samples were drop casted on carbon coated copper grid. TEM images can be seen in figure 4.3 where nanoparticle (NP) morphology resulted for all samples. Figure 4.3a-f is from the sample produced at 0.5 mA, which show particles with various sizes from less than 10 nm up to 40 nm. Measurements of inter-planer (d-spacing) distance of the atomic arrangements by HRTEM has shown that smaller particles are generally ZnO_2 (4.3c) while bigger particles correspond to $Zn(OH)_2$ (4.3f). Figure 4.3c and 4.3f are representative HRTEM images corresponding to figures 4.3a-b and 4.3d-e, respectively. In the first case (figure 4.3c) the inter-planer spacing is 0.279 nm, which is very well correlated to the ZnO_2 plane (111) with d-spacing of 0.280 nm (JCPDS: 01-077-2414).[9] In the second case (figure 4.3f), the inter-planer spacing for bigger particles is 0.339 nm which matches well with the orthorhombic $Zn(OH)_2$ plane (240) with d-spacing of 0.327 nm (JCPDS: 00-020-1437) ; there is no ZnO_2 plane near this d-spacing value, which therefore confirm the assignment. This

analysis of the sample produced at 0.5 mA therefore concludes that mix ZnO_2 and $Zn(OH)_2$ phase is produced at these synthesis conditions. Figure 4.3g-i is images from the sample produced at 1 mA where all the particles exhibit sizes below ~8 nm. The

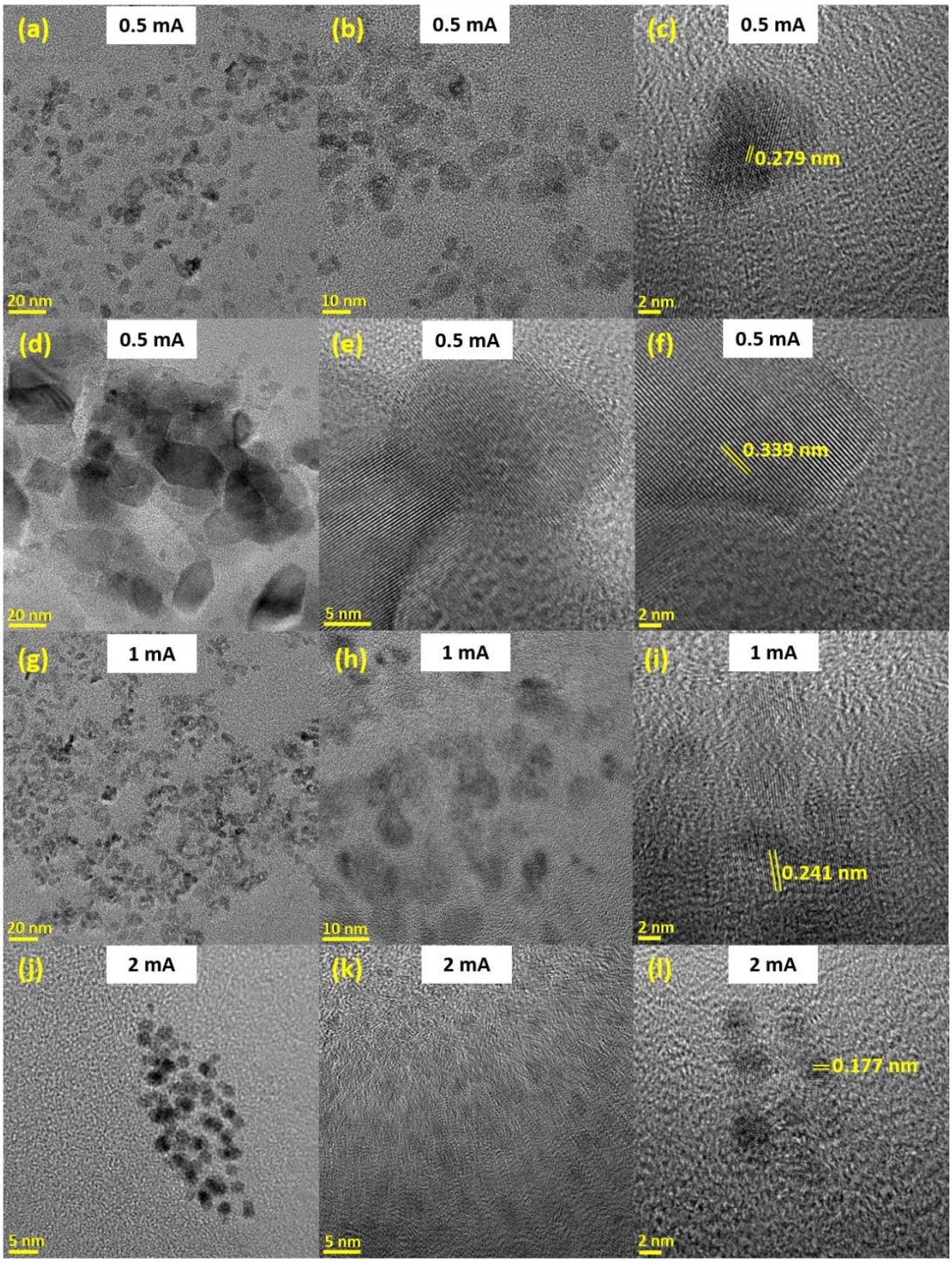

Figure 4.2: High resolution transmission electron microscopy (HRTEM) images of the ZnO_2 sample synthesised at 0.5 mA (a-f), 1 mA (g-i) and 2 mA (j-l). Calculated lattice spacing is also presented in the

d-spacing value is 0.241 nm as shown in image 4.3i and corresponds to that of the (200) plane of ZnO_2 which is 0.243 nm. Figure 4.3j-l are from the sample produced at

2 mA. The particle size is in this case ~2-5 nm and the d-spacing is 0.177 nm as shown in figure 4.3l, which corresponds very well to the (220) plane of ZnO_2 (0.172 nm).

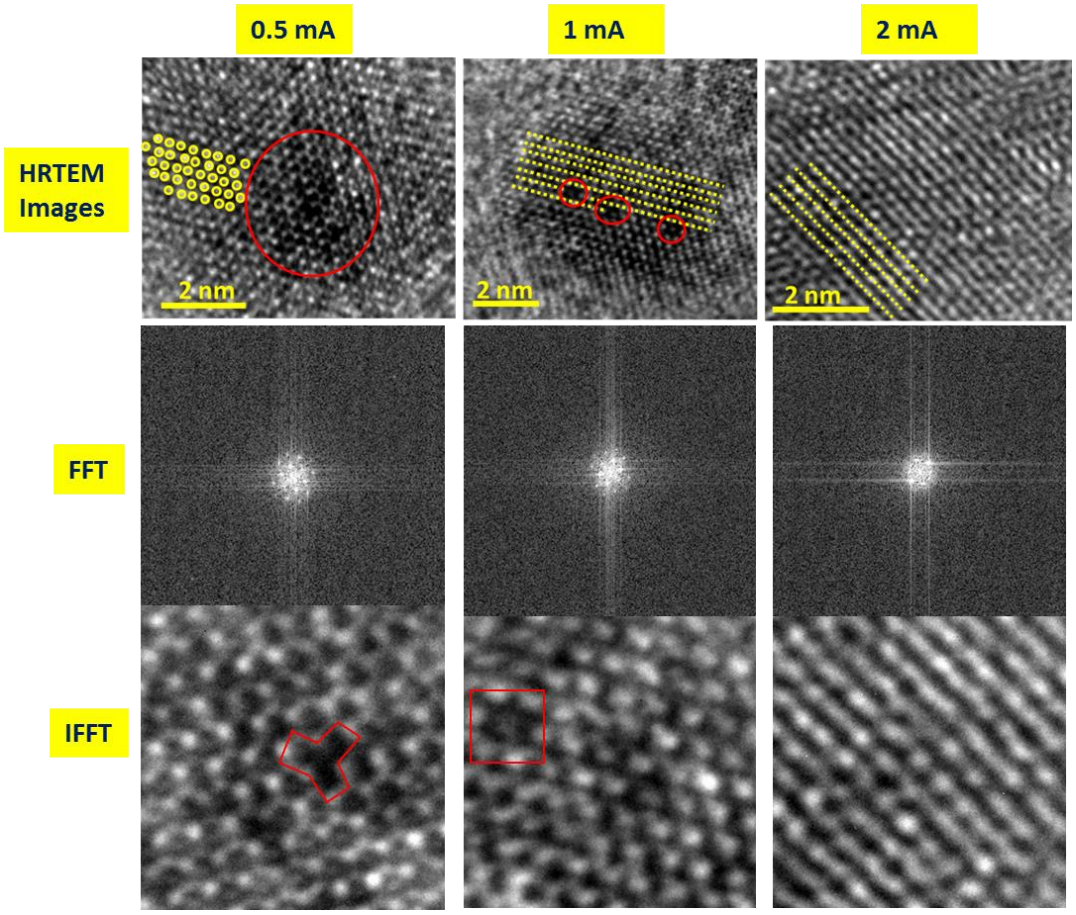

Figure 4.3: Defect observation by HRTEM in sample 0.5 mA,1 mA and 2 mA. HRTEM images shows perfectly arranged atom (yellow color) and defects (red). FFT of corresponding HRTEM images shows sharper spot and defined pattern for 2 mA sample. Inverse FFT (IFFT) clearly shows atomic misarrangement and vacancy in 0.5 mA particles (red polygon), less effective or little mismatch can be seen for sample 1 mA (red square), while atomic arrangement is perfectly arranged in sample 2 mA.

We have carried out further HRTEM analysis to provide insights into possible defects in figure 4.4. In HRTEM images, Yellow dots and lines present perfectly arranged atoms in the plane. Red circles in sample 0.5 mA and 1 mA shows vacancies in the atomic arrangement. Sample 2 mA shows perfectly arranged atomic planes without any defects. FFT was generated for all three samples. FFT of 2 mA shows brighter and defined pattern while other two samples show random orientation of spots. This is the result of not having perfect atomic alignment and defects. IFFT images were created for all samples. The IFFT shows clear vacancy in sample 0.5 mA, represented by red polygon in figure 4.4. Sample 1 mA also shows missing atom while 2 mA IFFT showed perfectly oriented atomic arrangement. This analysis shows that nanoparticles

synthesised with 0.5 mA current has vacancy defects and broken bonds, 1 mA sample shows little speculation about broken bonds and missing atom while 2 mA sample shows perfectly aligned atomic arrangement.

XRD is recorded for all samples as shown in figure 4.5a. XRD was recorded by drop-casting synthesised sample on to the silicon wafer, dried and then powder was collected to record the spectrum. XRD patterns in figure 4.5a for the samples produced at 1 mA and 2 mA show peaks corresponding to the (111), (200) and (220) lattice planes of ZnO_2 at 31.88°, 36.83° and 53.24° (2θ) respectively, which are in very good agreement with the JCPDS card 01-077-2414 that the sample produced at 0.5 mA, however, has also two extra peaks at 27.31° and 43.26° which corresponds to $Zn(OH)_2$ (JCPDS: 00-020-1437).

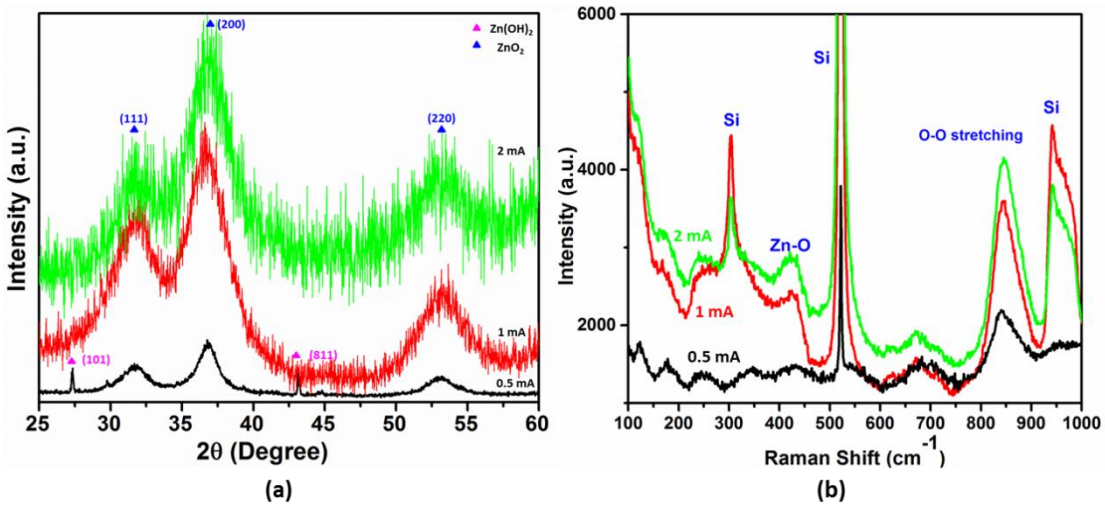

Figure 4.4: (a) X-ray diffraction spectra and (b) Raman spectroscopy of sample 0.5 mA, 1 mA, 2 mA; XRD clearly shows $Zn(OH)_2$ peak in sample 0.5 mA and Raman shows more intense characteristic peak of ZnO_2 in sample 1 mA and 2 mA than 0.5 mA.

Figure 4.5b shows the Raman spectra for all samples. For Raman spectrum, samples were also drop-casted on silicon wafer and dried. The peak at 435 cm^{-1} corresponds to the stretching mode of the Zn^{+2}-O^{-2} bond in ZnO[15], which results shifted to 425 cm^{-1} due to the different vibrational modes in ZnO_2 compared to ZnO. Another peak was observed at 843 cm^{-1} which correlates to the O-O bond of the peroxo ion (O_2^{-2}). This value is very much in agreement with previously reported value of O-O bond in ZnO_2.[13,15]All other peaks are from the silicon substrate. In the sample produced with the lowest current (0.5 mA), the 425 cm^{-1} peak is not intense, which could be simply due to a lower number of Zn-O and the presence of $Zn(OH)_2$.

The XPS spectrum of the NPs is presented in figure 4.6. Thick layer of sample was deposited on silicon wafer by drop cast. The survey spectrum shows only peaks related to Zn, C and O as shown in figure 4.6a. High resolution XPS spectra were used to analyse the materials properties. The Zn 2p doublet core level spectrum is shown in figure 4.6b. Binding energy at ~1021.3 eV and ~1044.5 correspond to Zn $2p_{3/2}$ and Zn $2p_{1/2}$, respectively. However, deconvolution revealed that the sample produced at 0.5 mA exhibited a shift of the peaks corresponding to Zn $2p_{3/2}$ (1022.1 eV) and Zn $2p_{1/2}$ (1044.2 eV) to lower energies; furthermore additional low-intensity peaks were also de-convoluted and positioned at 1022.64 eV and 1046.21 eV, which can be ascribed to the presence of $Zn(OH)_2$.[16]

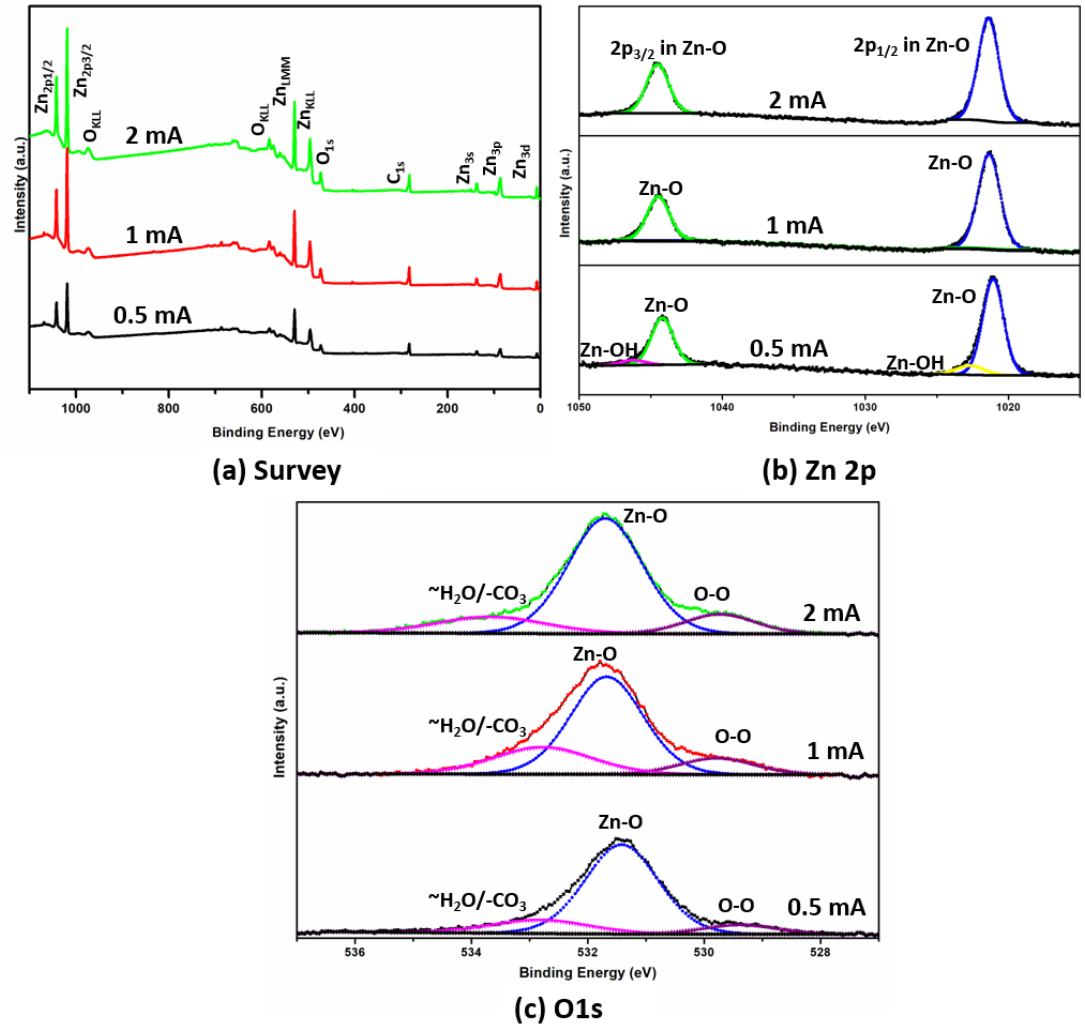

Figure 4.5: X-ray photoelectron spectra of sample 0.5 mA, 1 mA and 2 mA (a) Survey, (b) Zn 2p and (c) O 1s.

Figure 4.6c shows O 1s high resolution peak. After deconvolution, three peaks are observed for all samples. One small peak at ~529.4-529.7 eV corresponds to O-O covalent bond originating from ZnO_2. Second peak with highest intensity is observed

at ~531.4-531.7 eV, belongs to O-Zn in ZnO_2.[8] In ZnO_2, each oxygen is bonded to both zinc and oxygen. Because O-O bond is a covalent bond and Zn-O bond, which has both ionic and covalent characteristics,[17,18] binding energy should be higher for Zn-O bond than O-O bond in ZnO_2. The de-convoluted oxygen peak at higher energies (>532 eV) relates to adsorbed H_2O or CO_3.[19] Overall, XPS provides chemical evidence of Zn and O elements where oxygen peak is noticeably differ from commonly observed oxygen peak in ZnO, both in the shape as well as in the position of the peak.

According to observed results from TEM, HRTEM, XRD, Raman and XPS, it can be concluded that synthesised samples were ZnO_2 in all three conditions. However, 0.5 mA has both ZnO_2 and $Zn(OH)_2$ crystals as confirmed with TEM (figure 4.3), XRD (figure 4.4a) and XPS (figure 4.6b). HRTEM revealed that dominant vacancy defects and broken bonds were present in the sample 0.5 mA (figure 4.4). According to HRTEM and Raman results, it can be concluded that by increasing synthesis current, crystallinity and purity of ZnO_2 was improved.

4.3.3 Optical properties

Figure 4.7a shows the UV-Vis spectrum of the synthesised samples recorded in liquid sample, with the measurements taken on the same day of the synthesis. While a weak trend can be observed (i.e. a lower bandgap for samples produced at higher current) all samples essentially exhibit very similar bandgap values (figure 4.7c and table 2, as-synthesized). Transmittance measurements after three days (figure 4.7b) show some minor changes in the bandgap for the samples synthesized at 0.5 mA and 1 mA (figure 4.7d, and table 2 "after 3 days"), which may be due post-synthesis relaxation of defects and vacancies. However, the sample produced at higher current (2 mA) exhibit dramatic changes in the optical properties with a much higher bandgap, 4.2 eV; this could be due to agglomeration and sedimentation, which would leave smaller nanoparticles float with a higher bandgap as previously reported.[9] A range of bandgap for ZnO_2 has been theoretically calculated and experimentally measured. ZnO_2 is an indirect bandgap material with cubic crystal structure. According to theoretical calculations, ZnO_2 bandgap value can vary from 1.7-3.2 eV[20,21] while experimental values are very different than theoretical values, that is, 3.7-4.5 eV.[9,22] In our experiment, we have observed band gap value from 3.4-4.2 eV according to current and time.

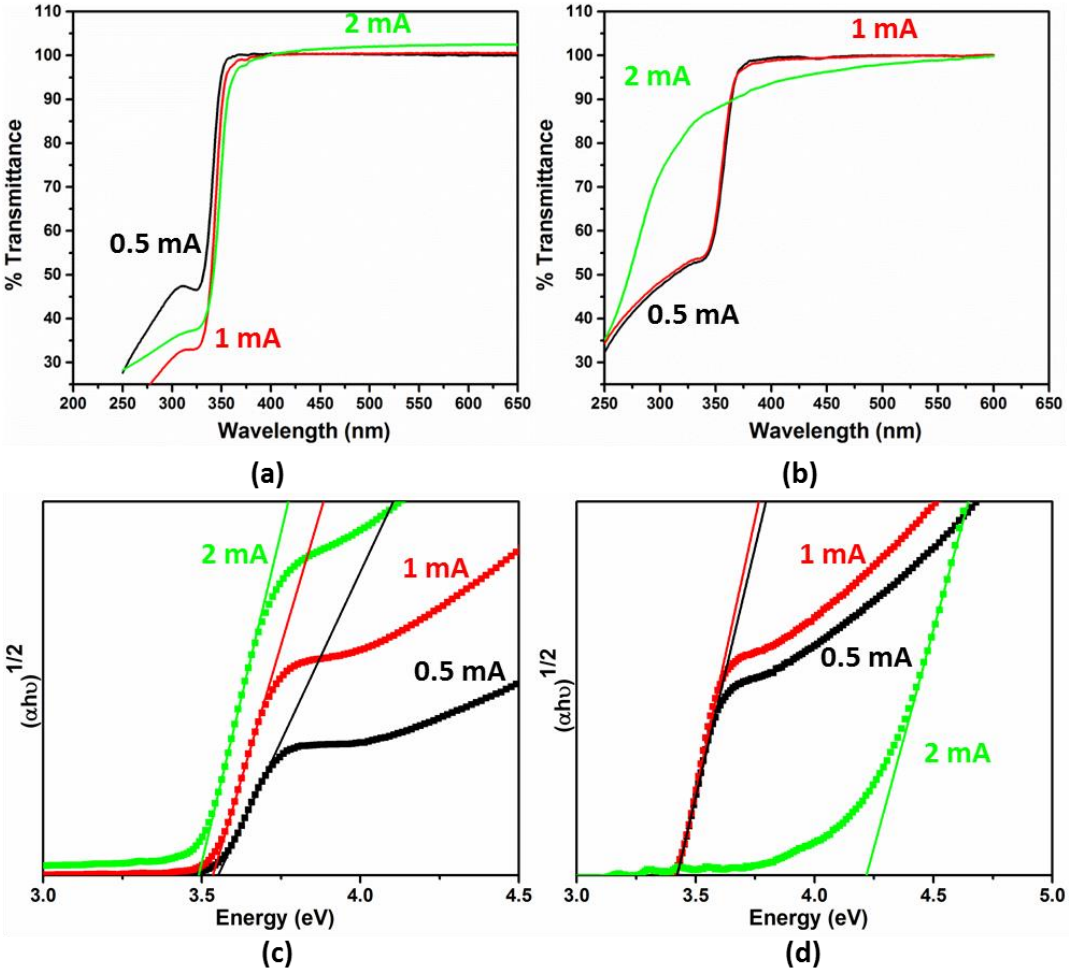

Figure 4.6: UV-Vis spectrum of sample 0.5 mA (Black), 1 mA (Red) and 2 mA (Green) on the (a) sample day of synthesis and (b) after three days. Inset shows the calculated band-gap of all three samples.

Table 5: Summary of bandgap values from transmittance measurements taken on the same day and after three days.

Sample	**Bandgap (eV)**	
	As-synthesized	After 3 days
0.5 mA	3.55 eV	3.4 eV
1 mA	3.53 eV	3.4 eV
2 mA	3.49 eV	4.2 eV

Photoluminescence emission at various excitation wavelengths corresponding to the three synthesis conditions is shown in figure 4.8; measurements were taken shortly after synthesis. Non-negligible emission is only observed for samples produced at 0.5 mA and 1 mA.

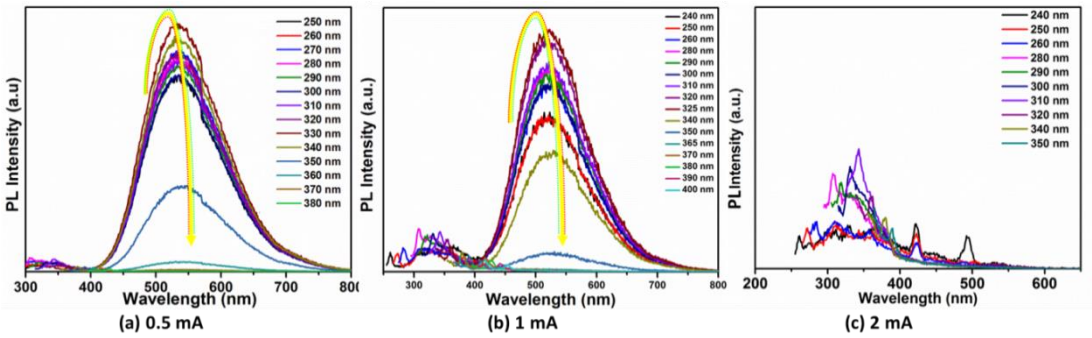

Figure 4.7: Photoluminescence spectra of (a) 0.5 mA, (b) 1 mA and (c)2 mA at different excitation wavelengths.

The peak is observed at ~ 540 nm at excitation ranging from ~ 240 nm to ~400 nm for both samples. The highest intensity of emission is recorded with the excitation wavelength ~330 nm. PL was only stable for sample 0.5 mA for longer period. Emission from 1 mA disappeared after one day.

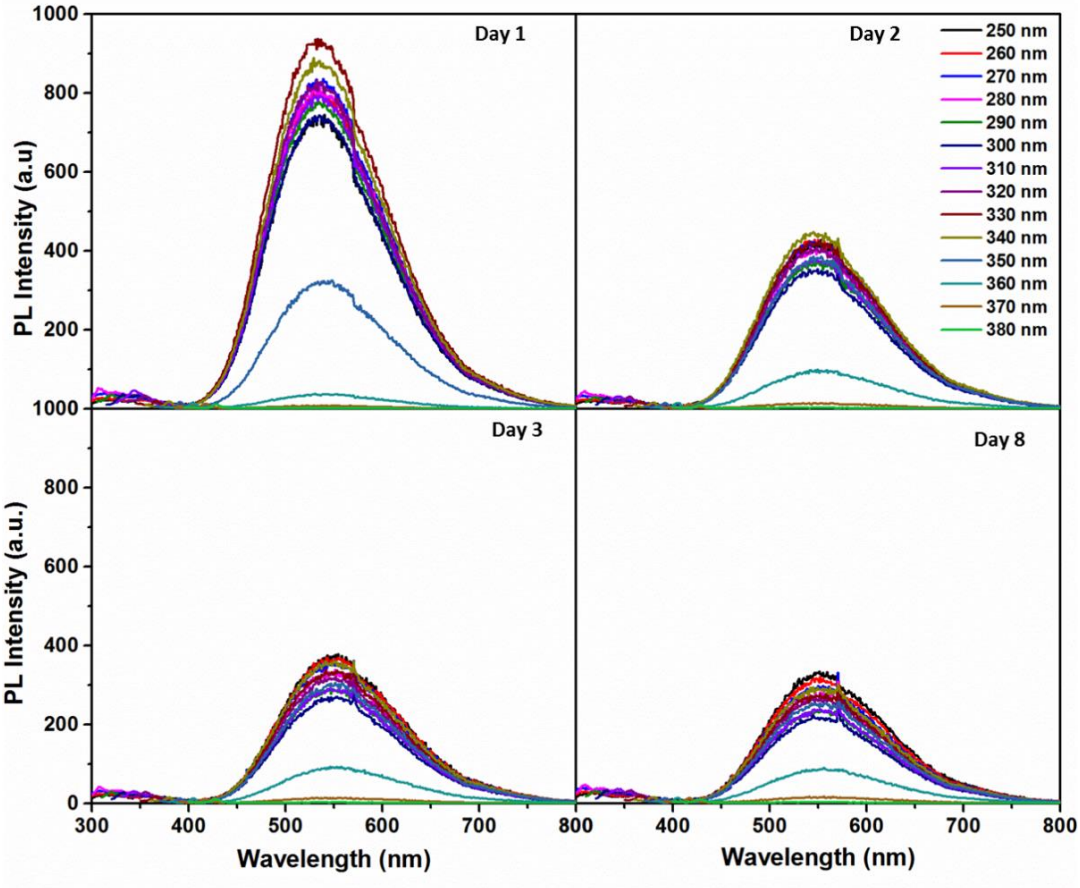

Figure 4.8: PL emission spectra for sample synthesised at 0.5 mA over 8days and after 8 days it was stable.

Previously, ZnO_2 emission in the yellow-green region has been observed and ascribed to surface dangling bonds, defects and oxygen vacancies.[10,23] According to observed trend in these samples, it can be stated that a stronger and stable emission occurs for

sample synthesized at lower current (0.5 mA & 1 mA) and we also interpret that, in terms of an increased defect density as previously demonstrated by TEM analysis (figure 4.4). Although, nanoparticles synthesised at 1 mA also showed defects according to HRTEM results (figure 4.4) but PL was suppressed after one day of synthesis due to relaxation of some defects. For the sample produced at 0.5 mA, the PL intensity also decreased during the first few days after synthesis, however it eventually stabilized within eight days after synthesis (figure 4.8).

This behaviour of PL spectra suggests that with time some defects are supressed, possibly associated with surface defects that become passivated by further oxidation due to water vapour and deeper defects were stable, responsible for the stable PL in sample 0.5 mA. Again, as the current increases defect related emission decreases because of improvement in overall crystallinity of the material.

4.3.4 Synthesis mechanism for ZnO_2 nanoparticle formation

In this work plasma was generated with helium gas in open air.[24,25] Plasma liquid system in open air is a complex system to understand because of many neutral and charged species contribution and parallel pathways. To understand the possible synthesis mechanism, few contributions from radicals can be neglected.[26–28] Here, we consider contribution from environmental oxygen and plasma gas. Plasma is consist of electrons, neutral species like O, O_2, O_3, charged species like O^+, O_2^+, O_3^+,O^-, O_2^- and O_3^- and other excited plasma gas species.[24,25] Various studies reporting on the basic mechanisms at the plasma-ethanol interface have confirmed H_2O_2 formation due to radical reactions.[29–32] A qualitative analysis of possible reactions[26,33] leads to the primary chemical pathways for H_2O_2 production:

$$e_{gas} + H_2O_{(g)} \rightarrow OH^{\bullet}_{(g)} + H^-_{(g)} \quad (1)$$

$$2\ OH^{\bullet}_{(g)} \rightarrow H_2O_{2(g)} \quad (2)$$

$$H_2O_{2(g)} \rightarrow H_2O_{2(l)} \quad (3)$$

$$2\ OH^{\bullet}_{(g)} \rightarrow OH^{\bullet}_{(l)}$$

$$2\ OH^{\bullet}_{(l)} \rightarrow H_2O_{2(l)} \quad (4)$$

The formation of ZnO_2 NPs can be discussed according to the two pathways. First, where hydrogen peroxide plays an important role in the formation of ZnO_2 by following reaction:

$$4\ H_2O_{(l)} \rightarrow 4\ H^+_{(l)} + 4\ OH^-_{(l)} \quad (5)$$

$$2\ Zn_{(s)} \rightarrow 2\ Zn^{+2}_{(l)} + 4\ e^-_{(l)} \quad (6)$$

$$2\ Zn^{+2}_{(l)} + 4\ OH^-_{(l)} \rightarrow 2\ Zn(OH)_{2(s)} \quad (7)$$

$$2\ Zn(OH)_{2(s)} + 2\ H_2O_{2(l)} \rightarrow 2\ ZnO_{2(s)} + 4\ H_2O_{(l)} \quad (8)$$

In second path, where oxygen plasma species play an important part in the formation of ZnO_2 by reaction with $Zn(OH)_2$ and produces H_2O_2 by following reaction:

$$Zn(OH)_{2(s)} + O_{2(l)}\ (\text{Reactive species}) \rightarrow ZnO_{2(s)} + H_2O_{2(l)} \quad (9)$$

Reaction (6) is to represent anodic dissolution[33] at the zinc electrode. Zinc and hydroxide ions react and form zinc hydroxide $Zn(OH)_2$ as shown in reaction (7). In the first pathway where $Zn(OH)_2$ then reacts with H_2O_2 to produce ZnO_2 and water molecule. The reaction of $Zn(OH)_2$ with H_2O_2 has been reported previously in chemical synthesis to produce ZnO_2.[11] In this reaction, water molecules are produced that can again contribute in H_2O_2 and $Zn(OH)_2$ formation. In second pathway, $Zn(OH)_2$ reacts with generated oxygen species in the plasma. In this reaction H_2O_2 is formed as a by-product. Previously, similar report was presented where $Zn(OH)_2$ was converted into ZnO_2 by constant bombardment of the neutral and charged oxygen species present in the DC glow discharge.[25]

As it can be seen, in first pathway, H_2O_2 is consumed and in the second pathway H_2O_2 is produced. To find out the pathway, we have measured the H_2O_2 concentration. Reference solution was produced by replacing Zn foil with carbon rod to know the H_2O_2 concentration without zinc.

The production of H_2O_2 was measured by adding an H_2O_2 scavenger. Here, titanium (IV) oxysulfate in sulfuric acid solution (Ti-S) is used as H_2O_2 scavenger. A calibration curve is produced with known concentration of H_2O_2 in water as shown in figure 4.11a. In this process, hydrogen peroxide (H_2O_2) reacts with Ti^{+4} ions yield a yellow-coloured

solution of perititanic acid (H_2TiO_4 or $TiO_2.H_2O_2$).[34,35] UV-Vis measurements of this solution can be used to detect the perititanic compound at 407 nm.

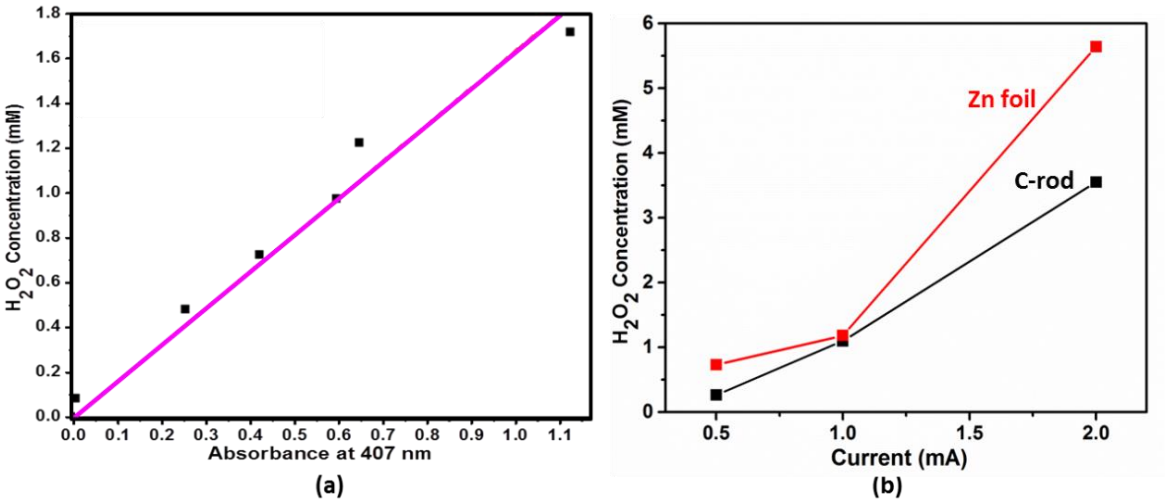

Figure 4.9: (a) Calibration curve for the assessment of H_2O_2 concentration by the absorbance intensity at 407 nm. The curve was made by adding titanium oxysulfate to solutions of known concentration and assessing the optical absorbance and (b) assessment of H_2O_2 concentration in plasma treated ethanol and synthesized ZnO_2 solution by measuring optical absorbance and using equation 8.

$$Ti^{+4} + H_2O_2 + 2H_2O \rightarrow H_2TiO_4 + 4H^+ \quad (10)$$

Ti-S was therefore mixed with samples after synthesis in a 1:2 ratio, respectively and the absorbance spectrum was taken. Absorbance spectra showed broad peaks at 407 nm as expected. The absorbance at 407 nm was plotted on the x-axis and the H_2O_2 concentration on the y-axis as shown in figure 4.10a. The results were fitted linearly to produce the calibration curve, which has allowed for the quantification of H_2O_2 concentration in the plasma-treated samples (figure 4.10b). The linear fit was the following:

$$H_2O_2(mM) = 1.63007 * A \quad (11)$$

where *A* is the absorbance of the solution after adding Ti-S. The concentration of H_2O_2 in the plasma treated samples at the different conditions is presented in figure 4.10b. Interestingly, H_2O_2 concentration is higher in Zn foil containing solution than C-rod. According to H_2O_2 concentration measurement, it can be concluded that second pathway (reaction 9) seems to be more favourable in production of ZnO_2 because of higher concentration of H_2O_2 at these synthesis conditions. Further, it can be supported with the TEM and XRD where at lower current (0.5 mA), $Zn(OH)_2$ was still present

in the solution. It can be suggest that oxygen species concentration was not enough at lower current to reduce all $Zn(OH)_2$. As the current increases, $Zn(OH)_2$ completely reduced to ZnO_2.

4.4 Synthesis of ZnO and doped ZnO in aqueous solution

4.4.1 Experimental Parameter

Here, 10 mL of deionized water is used as an electrolyte to synthesize ZnO. Ethylenediamine (EDA) is used as precursor for doped ZnO synthesis. Different EDA concentration is used to change the doping level in the material, keeping total volume constant to 10 mL as shown in table 3. Each sample is assigned a name according to EDA concentration and will be used throughout the chapter. Synthesis current was kept constant at 6 mA in all process.

3 kV of high voltage is used in the process. In the synthesis of EDA00 voltage is reduced to 1.1 kV after 10 min processing time because of generated ions in the process to achieve the desired current. While in all EDA containing process, the current reaches to the 6 mA as soon

Table 6: Summary of sample name and EDA concetration.

Sample Name	EDA Volume (mL)	Water (mL)
EDA00	0.0 mL	10 mL
EDA0.25	0.25 mL	9.75 mL
EDA1.0	1.0 mL	9.0 mL
EDA1.5	1.5 mL	8.5 mL
EDA3.0	3.0 mL	7.0 mL

as process starts because of the higher conductivity of the solution. After the synthesis process, all samples are drop-casted on silicon wafer to evaporate any remaining solution. Further, sample was heated at 90 ^oC for 2 h and at 400 ^oC for 1.5 h to produce N doped ZnO (N:ZnO).

In chemical synthesis, EDA has been used as a passivation agent to produce ZnO but no doping was observed.[36] Flake like ZnO structure were produced in controlled size because of EDA passivation in reaction. However, here because of the plasma processing and chelating nature of EDA, it forms an organometallic complex with Zn

ions in such a way that bounds nitrogen to zinc. Suggested synthesis mechanism will be presented in section 4.4.5.

4.4.2 Material Characterization

TEM, HRTEM micrograph and selective area electron diffraction (SAED) pattern of all colloidal samples are shown in the figure 4.11, where column represents TEM images, HRTEM, and SAED pattern of the samples and each raw represents the sample.

TEM images show particle morphology for all the samples. It can be seen from the figure 4.11a, b that as EDA concentration increases, particle size has been reduced and led to agglomeration of particles. The lattice images and crystalline nature of particles are clearly observed in HRTEM images (figure 4.11b&d). The SAED pattern consists of series of dotted rings which confirmed the wurtzite structure of ZnO nanoparticles (figure 4.11c). SAED pattern of sample EDA00 showed (100), (002), (101), (102), (210) and higher planes of wurtzite ZnO. At lowest EDA concentration (EDA0.25), all the planes of ZnO were present as EDA00 but the brightness was less. Further increase in EDA concentration, reduced the plane intensity and wasn't visible in SAED pattern. For EDA1.0, only three planes were clearly visible that are (100), (102) and (210) planes of ZnO. By further increase in EDA concentration, another ZnO (102) plane disappeared in SAED pattern (EDA1.5 & EDA3.0).

Lattice spacing is calculated for (100) plane for all samples. Because of the agglomeration and different plane visibility in HRTEM images for each sample, lattice spacing is calculated by SAED patterns that shows a steady slight increase from 0.285 nm to 0.306 nm (EDA00 to EDA3.0). This lattice expansion is a first result which may be evidence of the incorporation of dopant in the nanoparticles, which will be discussed in more detail later. Further from HRTEM images (figure 4.11d), distortion in atomic arrangement is clearly visible for higher EDA concentration samples (EDA1.5 & EDA 3.0). This is also can be related to incorporation of dopant, that created distortion in the atomic arrangement and stress or strain were created in the lattice structure.

Because of the agglomeration, it was hard to analyse size distribution. Manually, particle size was analysed for 20 particles for every sample. A box charge is created to analyse the size distribution as shown in figure 4.12. Box represents 75 % of the

particle fell in this size range. Centre line divides the box in 25 % and 75 % of particle size. Whisker represents the 10 % to 90 % particles range. Square symbol within the box represents average particle size. Solid pentagon and star represent maximum and minimum size for every sample. Average particle size for corresponding EDA volume

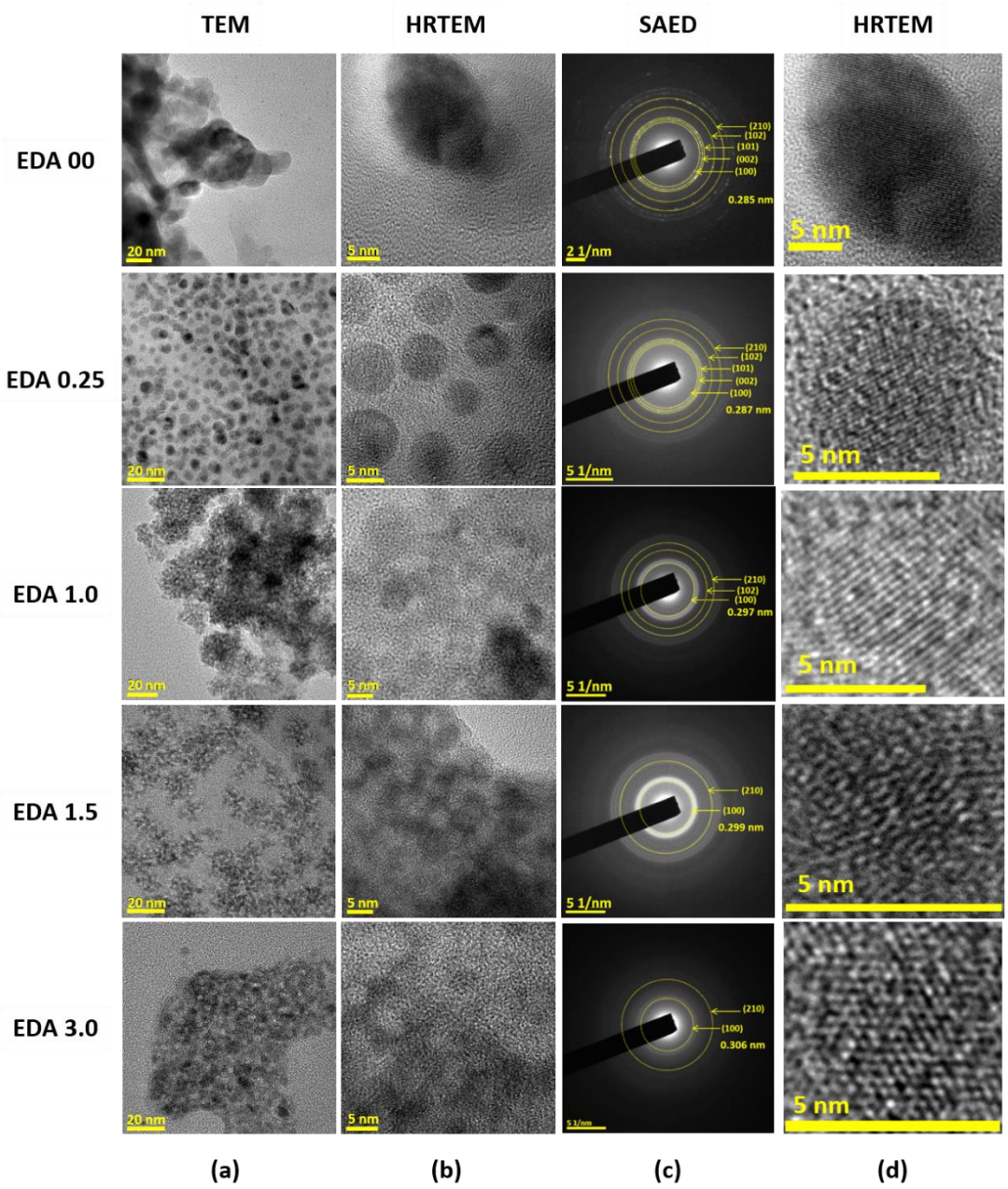

Figure 4.10: Transmission electron microscope analysis can be seen where column represents TEM images (a-b), selective-area electron diffraction (SAED) (c) and high-resolution TEM images (d) of nanoparticles of EDA00, EDA0.25, EDA1.0, EDA1.5 and EDA3.0.

can be seen in figure 4.12b where average particle size decreases from 15 nm to 2.6 nm as EDA volume increases in solution from EDA00 to EDA1.5. Further increase in EDA (EDA3.0), increased the particle size to 3.4 nm.

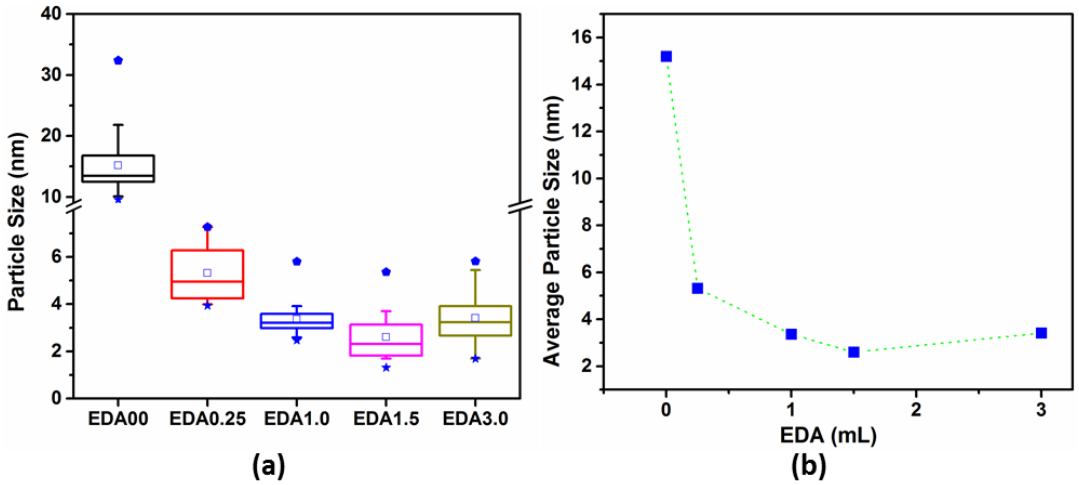

Figure 4.11: (a) shows box chart of particle size for all samples, where line with in the box divide the25-75 percentage of particle size, square symbol represents mean particle size, solid pentagon represents maximum size and solid star represents minimum size for that particular sample, (b) shows average particle size corresponding to EDA volume.

The crystalline nature of material and purity was further verified by XRD analysis of the powder sample, as shown in figure 4.13a. All five samples have shown characteristic ZnO wurtzite (100), (002), (101), (102), (110) and (103) plane peaks.[37] At higher EDA concentration, some peaks starts to disappear[38], such as (102) and (103), because of the distortion of the corresponding plane and other planes such as (002) and (101) starts to overlap because of the broadening effect.

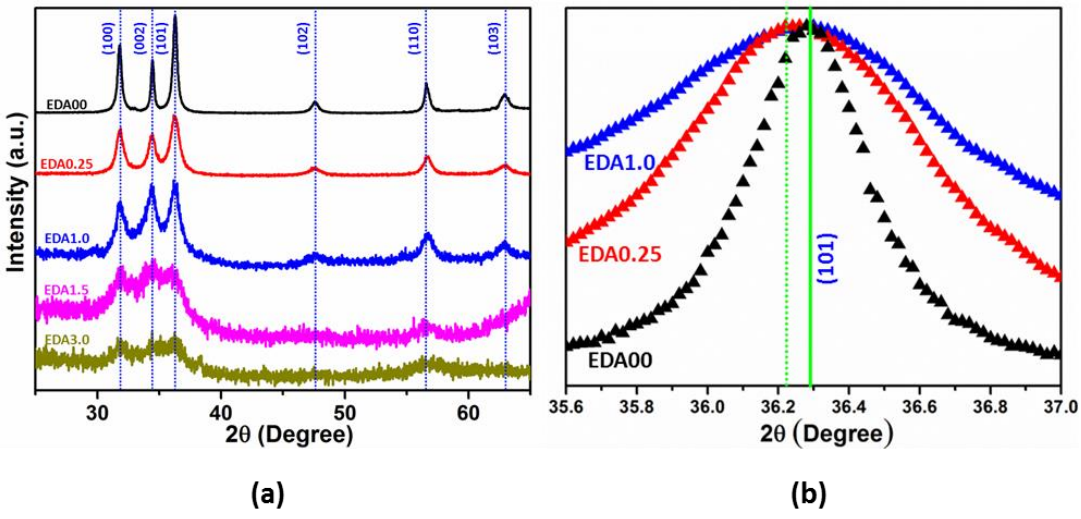

Figure 4.12: (a) X- ray diffraction pattern of the powders samples EDA00, EDA0.25, EDA1.0, EDA1.5 and EDA3.0, (b) Observed peak shift in (101) peak of EDA00 (Black), EDA0.25 (Red) and EDA1.0 (Blue) as well as a broader FWHM of N:ZnO with normalized peak position.

This is in part due to the reduction of nanoparticles size, however, consistent with TEM analysis, doping may also play a role here.[39] Additional evidence of doping can be

inferred by the peak positions. Peak position shift as well as peak broadening can be seen in figure 4.13b that can result from increased doping concentration.

High resolution XPS was performed to analyse chemical composition, oxidation states and chemical states. XPS high resolution peak of Zn 2p, O 1s, N 1s and C 1s is shown in figure 4.14a-d.

For the samples produced with no EDA, the binding energy at 1021.7 eV and 1044.84 eV are attributed to $Zn_{2p3/2}$ and $Zn_{2p1/2}$ electrons (figure 4.14a black line).[19] The BE difference between these two peaks is 23.14 eV which suggest that Zn is in Zn^{+2} states, confirming the chemical composition of ZnO. This splitting is also influence by electronic environment of lattice. With doping, electronic environment changes in the lattice. The Zn 2p splitting difference can be seen in table 4 for all samples. There is a clear shift in the Zn 2p doublet for the sample produced with 3 mL EDA (figure 4.14a green line), however the splitting is still close to 23 eV. The sample produced with 0.25 mL EDA also presents some peculiar differences, in particular the doublet peaks are broadened, and the peak related to $Zn_{2p3/2}$ is shifted to higher energy (figure 4.14a red line). The resulting splitting is considerably lower than expected (<23 eV), although this may be also the result of difficulties in identifying the peak position due to the broadening. Electronic environment changes should affect the Zn 2p doublet position, however no large changes in Zn 2p position was reported in this experiment. Therefore, chemical changes will be described later in this chapter with the help of Auger kinetic energy and modified Auger parameter.

In the XPS spectra, the asymmetric O 1s peaks were observed with a shoulder at higher binding energy (figure 4.14b). O 1s spectra were fitted into two peaks centred at 530.0-530.6 eV and 531.3-531.2 eV as shown in figure 4.14b. The first peak at ~530 eV corresponds to O^{-2} in Zn-O binding.[19,40,41] The second peak at ~531.5 eV correlates to the oxygen-deficient region in the ZnO matrix,[42] however when at higher energies (>532 eV, sample without EDA), it can be attributed to adsorbed oxygen such as $–H_2O$ or $–CO_3$ species. Peak at higher energy >532 eV was only observed in the sample EDA00 and oxygen-deficient region (~531.5) was not present in sample EDA00 or combination of both oxygen-deficient region and adsorbed O species. The samples produced with EDA resulted in O-deficient peaks (~531 eV), which can be justified due to the replacement of O with N atoms where two N atoms will balance the charge

neutrality of three O, leaving behind an O vacancy.

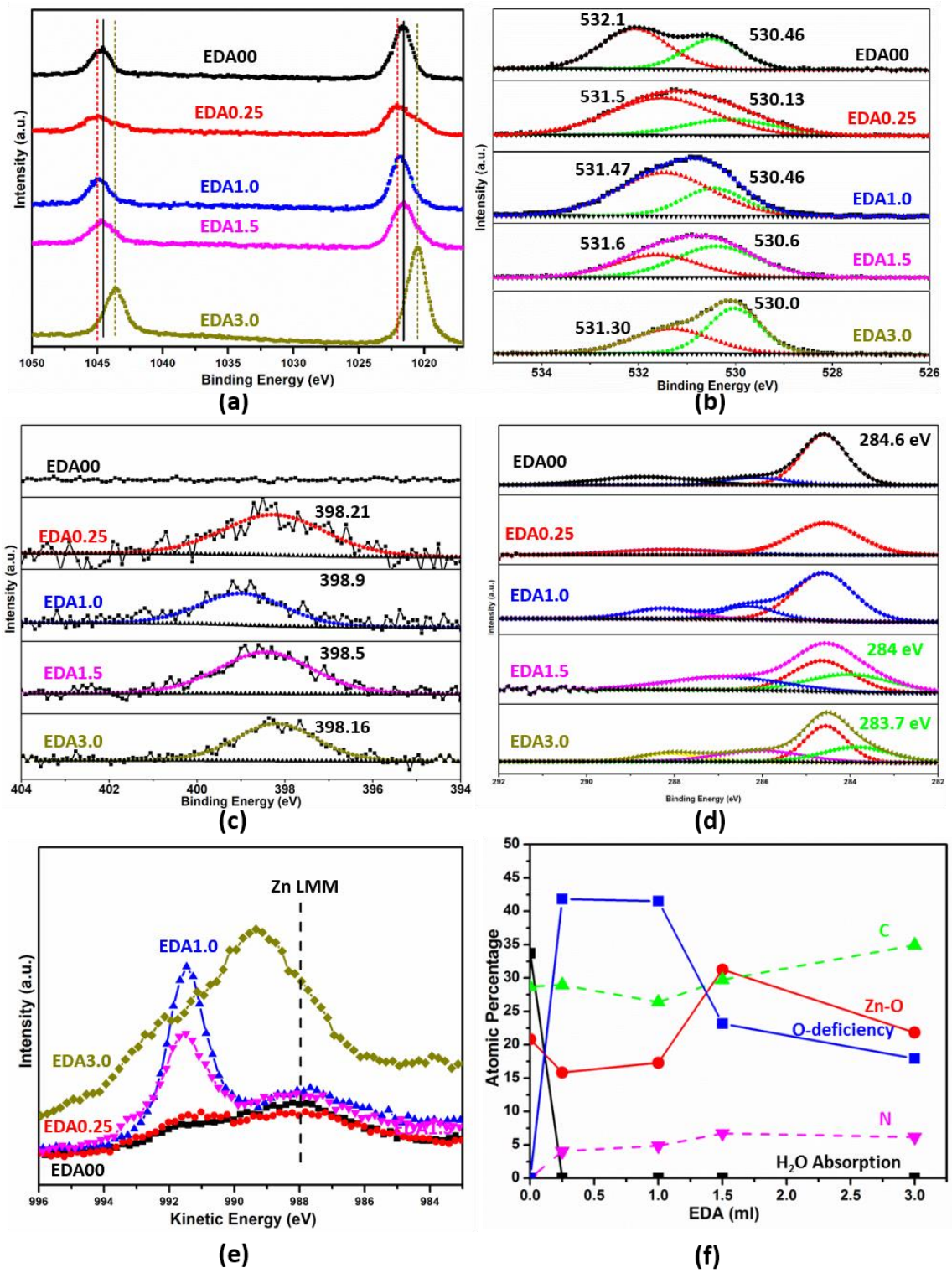

Figure 4.13: X-ray photoelectron spectrum (XPS) of (a) Zn 2p doublet; (b) O 1s; (c) N 1s; (d) C 1s; (e) Auger Kinetic Energy; and (f) Atomic percentage of H_2O absorption, nitrogen 'N', O-deficiency in lattice, oxygen percentage involved in Zn-O bonding and carbon 'C' in different EDA quantity samples.

The core level spectrum of the N 1s region is shown in figure 4.14c, centred at 398.16-398.90 eV for the different samples with a full-width-half maximum of 2.0-2.6 eV, which suggests that only one chemical state of N is present.[43] The peak of 398.16-398.90 eV lies in between the typical binding energy found for zinc nitride (~396-397 eV) and NO type species (above 400 eV), and can be attributed to the N 1s of oxynitride (O-Zn-N).[43–45] Nitrogen peak was absent in EDA00, suggesting no contribution of environmental nitrogen. Our results suggest that the chemical state of N_2 does not exist in these samples because the binding energy for N_2 is at 404 eV.[43,44] Similarly, the absence of a peak at 399.6 eV implies no amine left from the precursor which would exhibit N-H bonding.[44] Therefore, observed peak only present the N bonded to Zn in ZnO.

Table 7: Zn 2p doublet splitting energy difference for all sample.

Sample	Zn $2p_{3/2}$	Zn $2p_{1/2}$	Zn $2p_{1/2}$- Zn $2p_{3/2}$ splitting
EDA00	1021.7	1044.84	23.14
EDA0.25	1022.1	1044.89	22.79
EDA1.0	1021.8	1044.94	23.14
EDA1.5	1021.6	1044.67	23.07
EDA3.0	1020.6	1043.57	22.97

Figure 4.14d shows C 1s peak for all samples. In all samples, calibration peak (284.6 eV) and peak at higher energy > 286 eV is present in all samples. Peak at higher energy attribute to the C bonded to oxygen (C-O & C=O) from environment. Sample EDA1.5 & EDA3.0 have one more peak at lower energy at 284 eV and 283.7 eV, respectively. Peak at 284 eV in EDA 1.5 represents graphitic carbon left on the sample surface during the synthesis process. While peak in EDA3.0 at 283.7 eV represents Zn-C bond.[46]

It is difficult to observe larger shift and changes in Zn 2p peak of Zn related compounds as chemical state changes. Therefore, we examined the chemical bonding state of the nanoparticles by considering the Auger Zn LMM peaks as they are related to deeper electron transitions and are also unaffected by the source energy (figure 4.14e).

A peak at 988.7 eV is observed for sample EDA00 (Figure 4.14e black line). As the EDA concentration starts to increase, another peak at 991.7 eV starts to appear until EDA1.5 as shows in figure 4.14e. Sample EDA3.0 shows a combined peak centred at

989.7 eV where nitrogen and carbon both act as a dopant. In literature, ZnO LMM auger peak has observed at ~ 988.3 eV[47] which is near to the observed auger energy peak (988.7 eV). Another observed peak at 991.7 eV can be proof of electronic environment change due to doping and can be related to oxynitride bond. Similarly, to the photoelectron peaks, the chemical shift in Auger peaks are related to changes in valence electron density. An increase in valence electron density causes the increase in Auger electron kinetic energy.[48] Therefore, the chemical shifts for the Auger peaks indicate that Zn–N bonds have less iconicity than Zn–O bonds. However, Auger electron kinetic energy decreases for samples with 3 mL EDA; this anomalous behaviour could be attributed to three binding atoms, i.e. O, C and N, and their respective doping sites. In figure 4.14f, it is shown that drastic increase in carbon percentage while reduction in o deficient region, Zn-O bond and a slight decrease in nitrogen percentage at 3 mL of EDA. It should also be noted that O^- defects are higher at lower doping concentration. With this, percentage of incorporated nitrogen is also saturate after a certain amount of nitrogen incorporation.

Atomic percentage of nitrogen and carbon doping is calculated by XPS results (figure 4.14f). In EDA0.25, 3 % of nitrogen doping was observed. As the EDA concentration increases, nitrogen doping concentration also increases till EDA1.5. Sample EDA1.0 and EDA1.5 showed 4.83 % and 6.72 % of nitrogen doping. In sample EDA3.0, nitrogen concentration decreased slightly to the 6.15 % and 8 % of carbon doping was observed. However, figure 4.14f shows total concentration (including environmental carbon) of carbon in all samples. Doped carbon concentration was calculated separately for sample EDA3.0. Although, this analysis of doping is quantitative, but it gives fair amount of idea about the doping trend.

It can be confirmed by TEM, XRD and XPS analysis that sample synthesised without EDA (EDA00) corresponds to chemical nature of ZnO. As the EDA concentration increases (sample EDA0.25 to EDA3.0), nitrogen doping concentration also increases in ZnO crystal. EDA3,0 shows both carbon and nitrogen doping.

FTIR measurements were limited at 520 cm^{-1}; unfortunately a typical metal oxide bonding response is in the 430-450 cm^{-1} range and therefore the actual ZnO bond vibration could not be measured. However other fingerprint of interest were present

above 520 cm^{-1} and are reported in figure 4.15a. In particular the prominent peak at 900 cm^{-1} relates to Zn-OH bonding.[38]

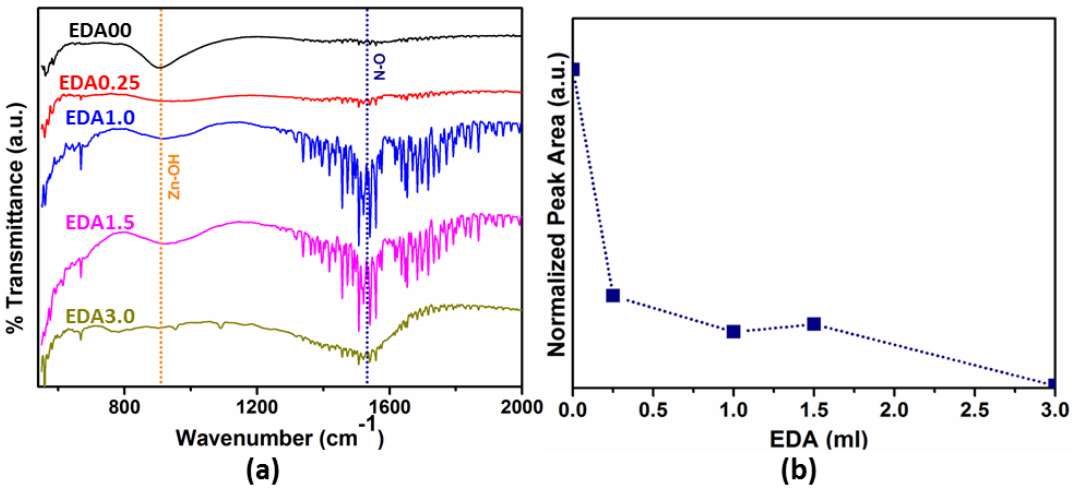

Figure 4.14: (a) Fourier Transform Infrared Spectroscopy of EDA00, EDA0.25, EDA1.0, EDA1.5 and EDA3.0, (b) normalized peak area of Zn-OH peak at different EDA.

The normalized area of the Zn-OH peak in all samples is plotted in figure 4.15b, which shows that as doping increases in the ZnO lattice, the surface -OH adsorption decreases that can be further supported with XPS (figure 4.14f). Doping with N and C atoms is expected to decrease the hydrophilic nature of ZnO. Further, the peak at 1528 cm^{-1} corresponds to N-O stretching vibrations and the intensity increases as doping increases.

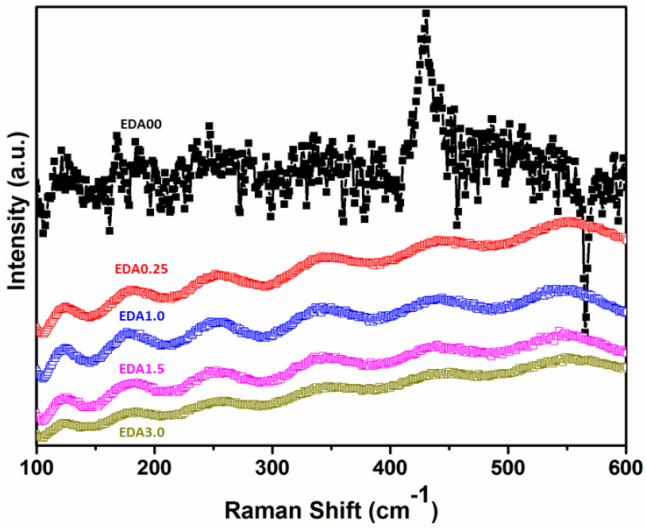

Figure 4.15: Raman spectra of EDA00, EDA0.25, EDA1.0, EDA1.5 and EDA3.0.

Raman spectum was recorded for all the samples as shown in figure 4.16. One peak observed in pure ZnO spectra at 430 cm^{-1} correlates to the E2 vibration of wurtzite ZnO. The other samples did not produce reliable measurements due to very strong fluoroscence.

4.4.3 Optical properties and energy band diagram (EBD)

Optical properties are measured by ultraviolet-visible diffuse reflectance spectrum for all samples. Figure 4.17a shows clearly the impact of doping on the reflectance, which decreases drastically from ~ 60% to ~ 13% at 380 nm corresponding to an inter-band transition at 3.2 eV for increasing doing concentration in ZnO. Thus, pure ZnO (EDA00) showed strong absorption in the UV region while doped samples clearly shows absorption tail in visible region remarkably spanning half the visible region. Figure 4.17b shows the sharp cut-off starting at 365 nm, is assigned to the absorbance of pure phase of ZnO (EDA00). Doping in the ZnO lattice should increase defects by introducing interband N 2p states in the band structure, that will widen the absorption window and red-shift the absorption edge of ZnO, as can be seen in figure 4.17b (spectra with various amount of EDA).[37,49] Figure 4.18 shows the corresponding bandgap for all samples determined from Tauc plot using reflectance measurement. For that, absorption coefficient is calculated according to assumptions made in section 3.2.7. The bandgap for pure ZnO nanoparticles is 3.23 eV (without EDA) and for the samples with various concentrations of EDA, expected to be N-doped ZnO nanoparticles, the bandgap varies between 3.12 eV and 3.21 eV, i.e. lower than the un-doped samples as expected. At the highest amount of EDA (3 mL) where we expect C and N co-doping the bandgap is the lowest recorded for these samples, i.e. 2.98 eV.

To address the accuracy of bandgap, measurements are also performed in liquid medium. An average of three measurements showed slight variation of bandgap from solid measurements. The bandgap for pure ZnO (EDA00) is 3.3 eV and for doped samples EDA0.25, EDA1.0, EDA1.5 and EDA3.0 are 3.08 eV, 3.12eV, 3.21 eV and 2.98 eV, respectively. According to solid and liquid measurements, it can be concluded that bandgap value is very consistent with number of measurements in liquid and solid with average bandgap of 3.3.26 eV, 3.1 eV, 3.12 eV, 3.12 eV and 2.98 eV for sample EDA00, EDA0.25, EDA1.0, EDA1.5 and EDA3.0, respectively.

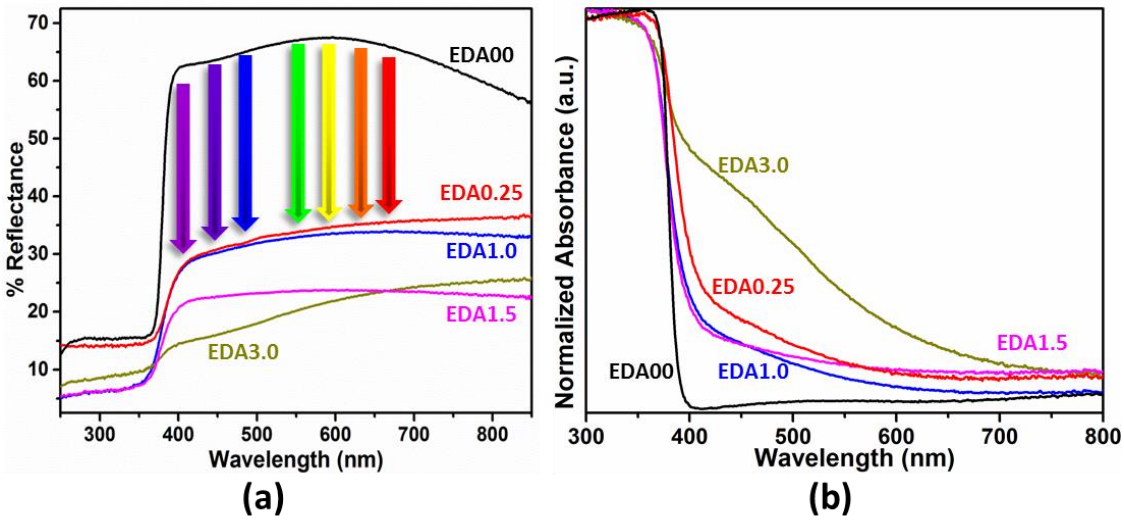

Figure 4.16: (A) Reflactance spectra and (B)Normalized absorbance spectra of pure ZnO and doped ZnO with various EDA concentration.

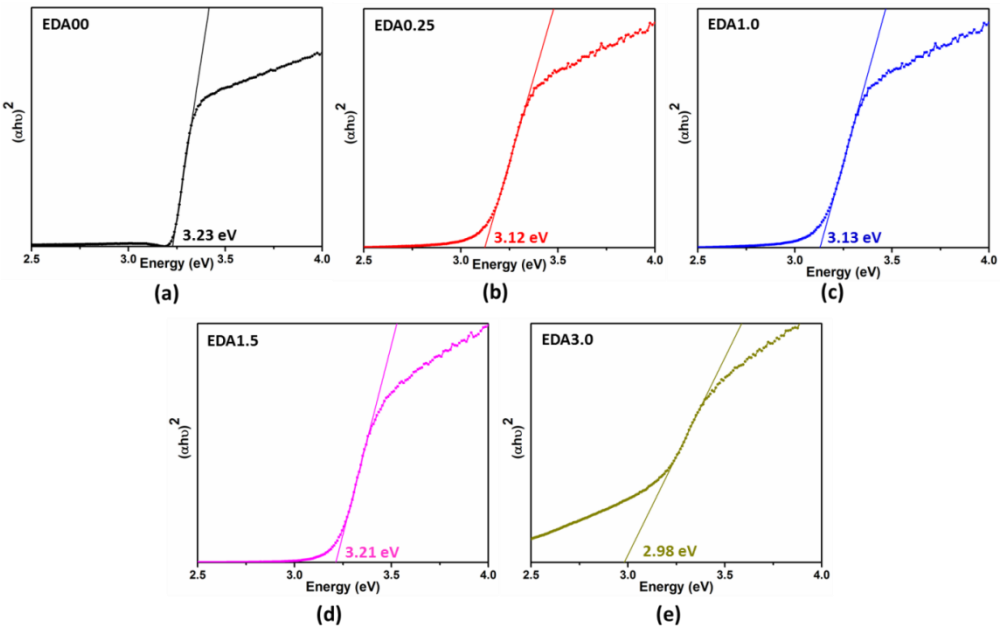

Figure 4.17: Shows the calculated bandgap by UV-Vis diffuse reflectance spectra for (a) EDA00, (b) EDA0.25, (c) EDA1.0, (d) EDA1.5 and (e) EDA3.0 by Tauc plot.

Valence band maxima (VBM) edges and Fermi level are determined by XPS (figure 4.19a) and by Kelvin probe (figure 4.19b) measurements, respectively. The difference between Fermi level energy (E_f) and valence band maximum energy (E_{VBM}) was evaluated by extrapolating the leading edge of the XPS spectra to the baseline as shown in the Figure 4.19a for all samples. Fermi levels for the different samples did not change appreciably, all remaining within a small range from -5.06 eV to -5.14 eV (figure 4.19b). As it can be seen in figure 4.19a, the difference between E_f and E_{VBM} is

lower for EDA0.25 compared to the undoped sample (EDA00) and for all other samples, it is higher than EDA00. The difference between E_f and E_{VMB} varies from 2.11 eV to 2.62 eV.

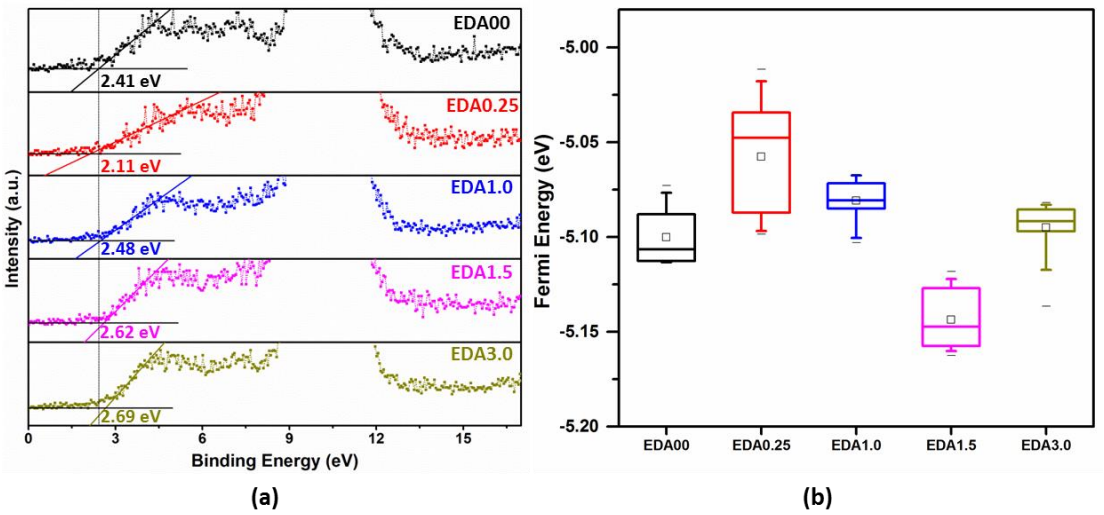

Figure 4.18: (a) XPS valence band spectra measurement and (b) Fermi level measurement by kelvin probe of EDA00, EDA0.25, EDA1.0, EDA1.5 and EDA3.0.

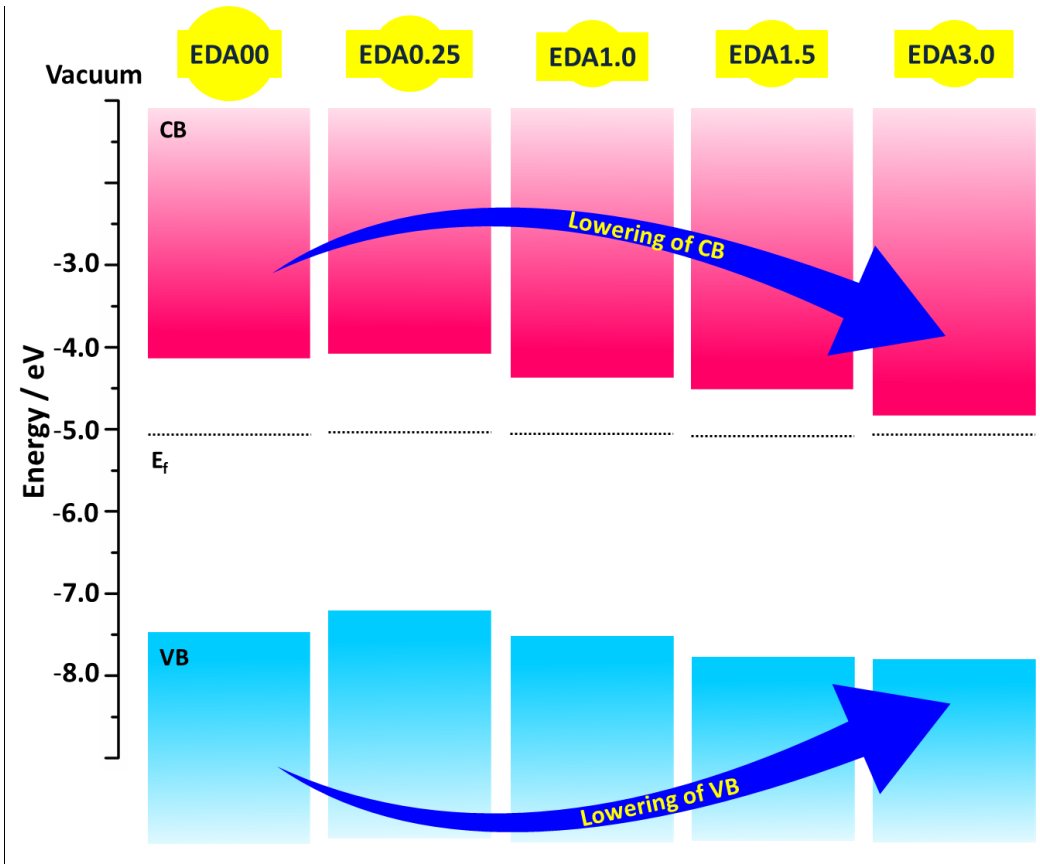

Figure 4.19: Energy band diagram of EDA00, EDA0.25, EDA1.0, EDA1.5 and EDA3.0 where VB and CB stand for valence band and conduction band.

The complete band structure of all samples is shown in Figure 4.20. The position of the valence band edges was calculated from the XPS results ($E_f - E_{VBM}$) and using the Fermi level (E_f) value from Kelvin probe measurements. The corresponding conduction band edges were found adding the value of the measured bandgap to the valence band edge.

Overall, the initial incorporation of N atoms in the ZnO nanoparticles (EDA0.25) seems to provide upward shift of the valence band edge decreases the energy gap with the Fermi level and at the same time increase that between the conduction band minimum and Ferm level. However, as N-doping further increases, the valance band maximum is lowered and departs further from the Fermi level and extended the conduction band edge.

4.4.4 Doping, Defects and its effect on photoluminescence

According to TEM analysis, where distortion in crystal structure was seen, can be described by the difference in ionic radii of N^{3-} (132 pm)[37] and C^{4-} (260 pm)[50] which is higher than O^{-2} (126 pm)[37]. This difference in radius of C, N and O created stress and strain in the lattice and disturbed the crystal structure and orientation of atoms. This is observed in HRTEM images of high concentration EDA sample (EDA1.5 & EDA3.0) where atom alignment has been distorted can be seen in figure 4.11d. Some planes are not visible in SAED pattern (figure 4.11c) as doping increases, same behaviour is observed in XRD (figure 4.13). That again justifies the fact that, grain growth hampered in certain plans because of the doping and that reduces the size.

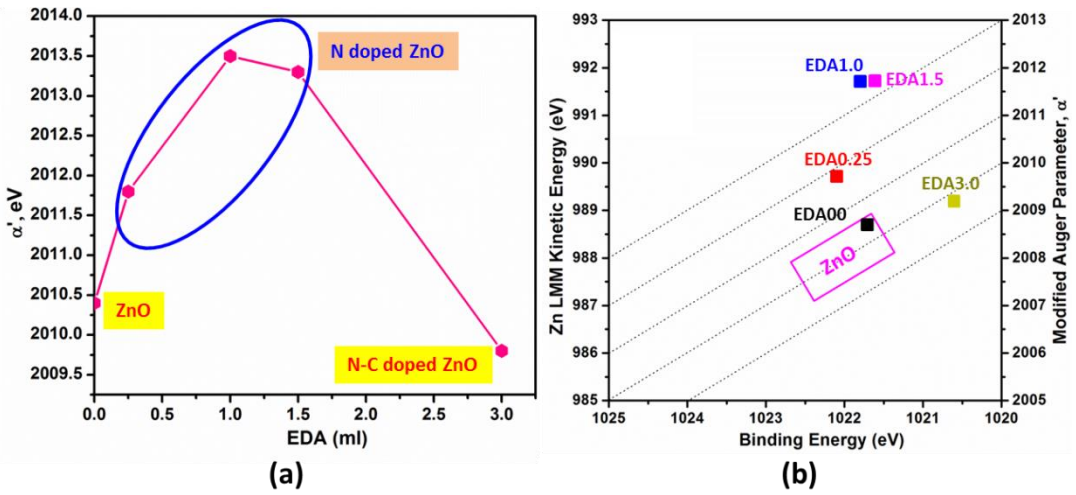

Figure 4.20: (a) Modified auger parameter with respect to the EDA conc. (b) Wagner plot for all the five samples, indicating standard ZnO position by pink square.

Peak broadening in XRD can be described due to reduction in particle size as well as decreased crystallinity as nitrogen incorporation increases in ZnO lattice. This kind of behaviour has been previously observed in N doped ZnO.[37,50,51] Figure 4.13b is the expanded view in small angle range for highest intensity peak (101). This shift in XRD peak towards lower 2θ value suggests that the lattice size is expanding after the doping. This is due to obvious reason of the higher ionic radii of $N3^-$ compared to O^{2-}, leading to expansion of the lattices upon doping. This reaffirms our claim of nitrogen doping in the ZnO lattice.

Further, changes in chemical environment because of doping in ZnO lattice were analysed by Auger parameter. While the Auger energy can describe changes in the chemical state, interference from static charges may still affect the actual interpretation. To eleminate this effect, the Auger parameter (α) can be used. Since the chemical shifts of photoelectrons and Auger electrons are different, the differences between their kinetic energies constitute the Auger parameter. Auger parameter still depends upon the photon energy used and to make this parameter independent of all conditions, a modified auger parameter (α') can be considered:[48]

$$\alpha' = \text{Kinetic Energy}_{\text{Auger}} + \text{Binding Energy}_{\text{photoelectron}} \quad (9)$$

The α' parameter is plotted in figure 4.21a with respect to EDA concentration used and this can be clearly correlated to the incorporation of dopant in the lattice. At lower EDA concentration, α' increases until the incorporation of carbon starts; at 1.5 mL and 3 mL EDA, the modified Auger paramter decreases.. Higher value of α' is due to conduction electrons and associated screening energy. Shift in the α' corresponds to the polarizability of oxygen or nitrogen ions. This shift is the measurement of polarizibility of the environment of the affected atom (Zn). Nitrogen shows more polarizibility than oxygen.[52] Therefore, N doped ZnO shows more α' than undoped sample as shown in figure 4.21a. At 3 mL of EDA (EDA3.0), carbon also play part as dopant with nitrogen and that decreases the α' lower than undoped ZnO. An interesting visualization of ZnO chemical state can be produced with a Wagner plot as shown in figure 4.21b.[53,54] This is a plot with the photoelectron binding energy on the x-axis and on the y-axis the Auger energy and the modified Auger parameter. Every chemical state then occupies a unique position on the two dimentional grid. The position for standard stochiometric ZnO has been identified within a squared region, which

contains also our samples produced with no EDA (EDA00). It is very clear from the wagner plot that pure ZnO lies in the standard unique assigned position of ZnO and all other samples have very different chemical environment than ZnO. Because of the dopant, electron cloud is changed in the lattice and that lead to different position of doped ZnO.

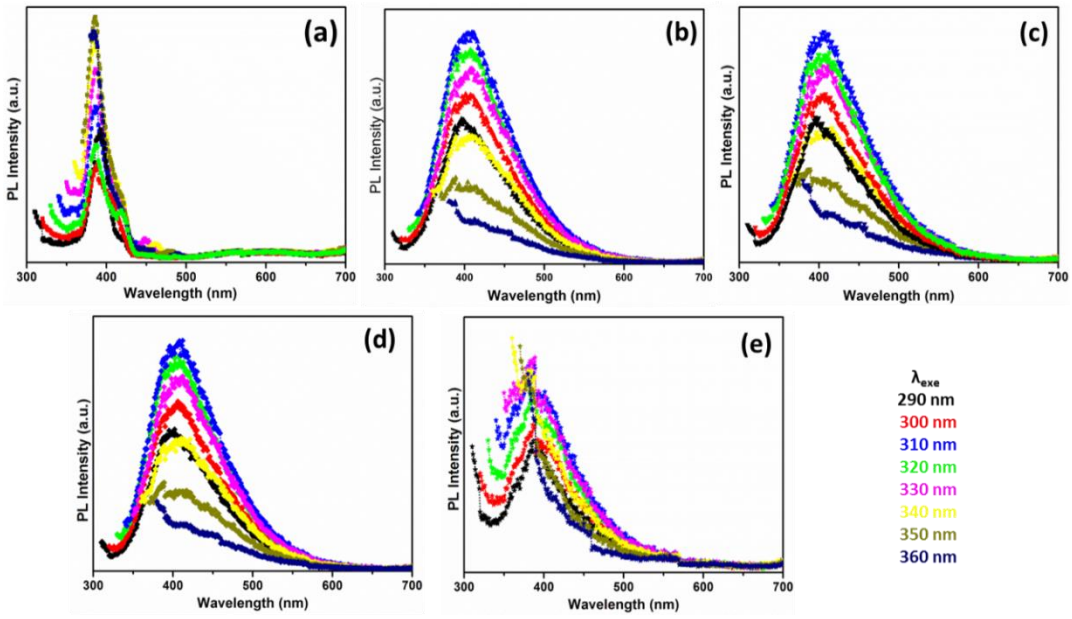

Figure 4.21: Photoluminescence spectrum of (a) EDA00, (b) EDA0.25, (c) EDA1.0, (d) EDA1.5, and (e) EDA3.0.

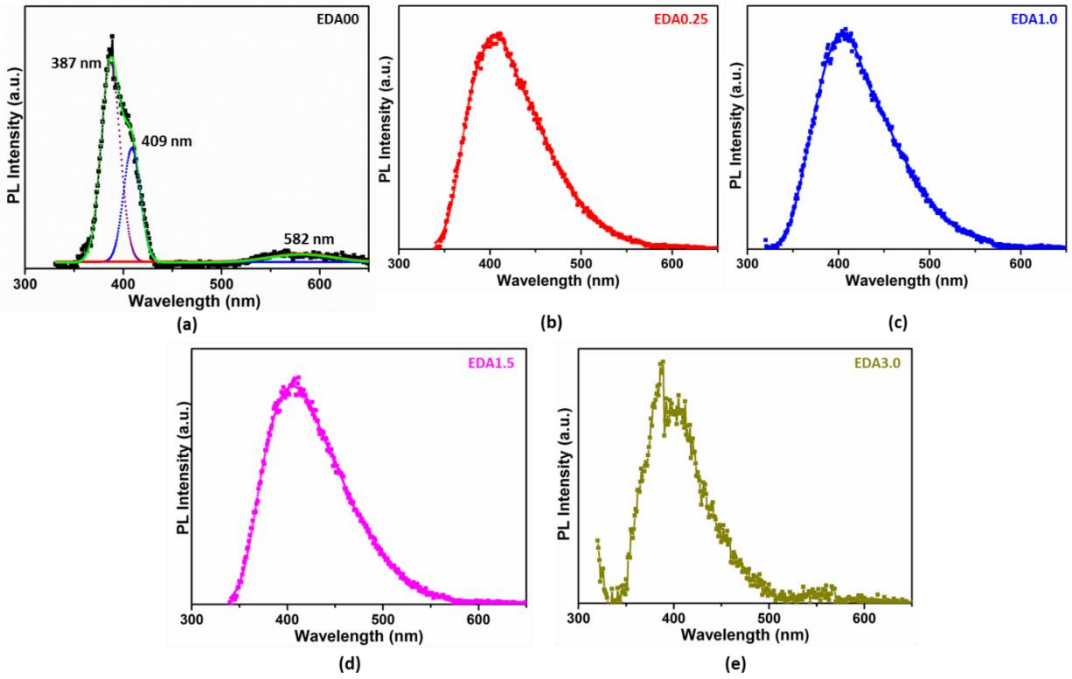

Figure 4.22: Highest intensity PL spectra of (a) EDA00 at λ_{exc} 350 nm and de-convoluted spectrum showed three peaks, 387 nm, 409 nm and 582 nm, (b)EDA0.25, (c) EDA1.0, (d) EDA1.5 at at λ_{exc} 310 nm and (e)EDA3.0 at at λ_{exc} 330 nm.

Effect of doping was further confirmed with photoluminescence measurements as shown in figure 4.22. Photoluminescence of all samples was measured with excitation from 290 nm to 360.

Photoluminescence of ZnO can be divided into two regions: (1) emission in the ultraviolet region due to excitonic emission or near band-edge emission and (2) emission in the visible region due to defects. The emission intensity is highest at 350 nm excitation wavelength which is in good agreement with highest absorbance wavelength at 365 nm (figure 4.17b) for ZnO. For N-doped ZnO, the highest emission intensity is observed with λ_{exc} 310 nm. For C-N doped ZnO, highest emission intensity was observed with λ_{exc} 330 nm.

In order to better understand PL emission, we have de-convoluted the PL spectra (figure 4.23a) for un-doped ZnO nanoparticles, de-convolution showed three peaks. Peak at 387 nm corresponds to excitonic near band egde emission, another emission at 409 nm is observed and originate from Zn vacancies in the ZnO lattice (V_{Zn}) as shown in figure 4.24a.[38] Low emission at 582 nm is associated with interstitial oxygen (figure 4.24a, O_i). For the doped samples, the emission is centred just above 400 nm, however the peak has broadened covering the visible region up to ~600 nm as can be seen in figure 4.23b-d. The incorporation of defects and dopant states in the bandgap are responsible for the emission in the visible in N doped ZnO (N:ZnO) by introducing energy levels in the band arrangement as it is shown in figure 4.24b.

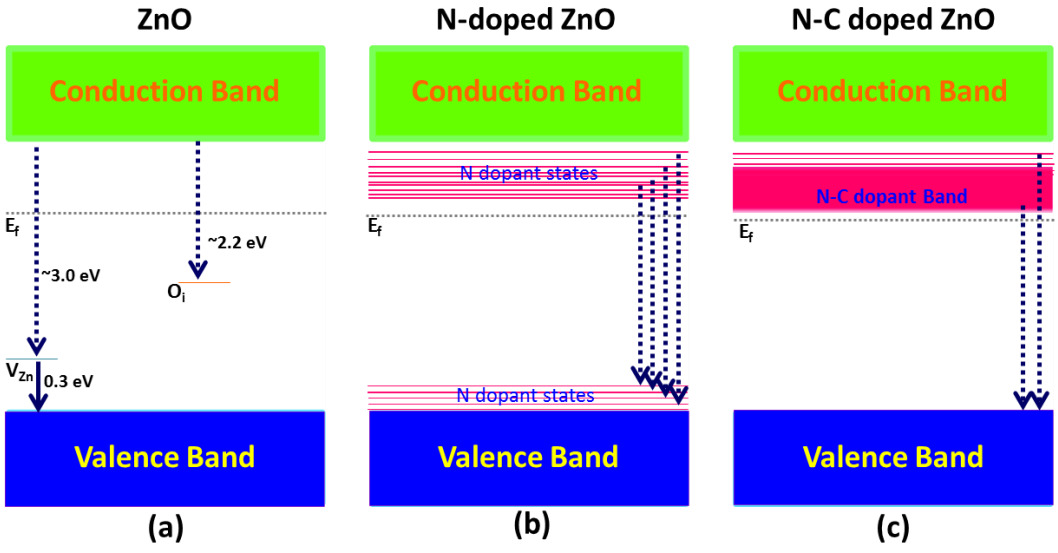

Figure 4.23: The different defect level in (a) ZnO (EDA00), (b) N doped ZnO (DEA0.25, EDA1.0 and EDA1.5) and (c) N-C doped ZnO (EDA3.0).

Further, as the dopant concentration keeps increasing, dopant atoms interact and form a band that reduces the emission wavelength range and intensity of visible emission in N-C doped ZnO as shown in figure 4.24c. N-C doped ZnO (N-C:ZnO) only shows UV and blue-visible emission (figure 4.23e).

4.4.5 Synthesis mechanism

In EDA containing water solution, ammonium and hydroxide ions are created in the solution as per equation (11):

$$2\ H_2NCH_2CH_2NH_2 + 4\ H_2O \rightarrow 2\ {}^{+}H_3NCH_2CH_2NH_3^{+} + 4\ OH^{-} \qquad (11)$$

The synthesis is initiated as soon as the microplasma is generated and the presence of NPs is clearly visible by naked eye after a few minutes.

With EDA, metal ions form metallic complexes as shown in figure 4.25. Similar kind of compound formation has been reported in literature with different solvents and EDA.[56] As the synthesis process proceeds, possible compound formation can be seen in figure 4.26. EDA and water generate ammonium ions and hydroxide ions as suggested in equation 11 and figure 4.26. After plasma processing, transparent solution contains ionic form of organomatellic complexes. After drop casting on silicon, it evaporates excess water from the solution. Later heating at 90 ^{o}C, excess water or moisture is removed, and corresponding possible compound can be seen in figure 4.26. Further heating at 400 ^{o}C, broke the EDA-Zn complexes molecule and formed doped zinc oxide. Further confirmation of the process is done with TGA as shown in figure 4.27.

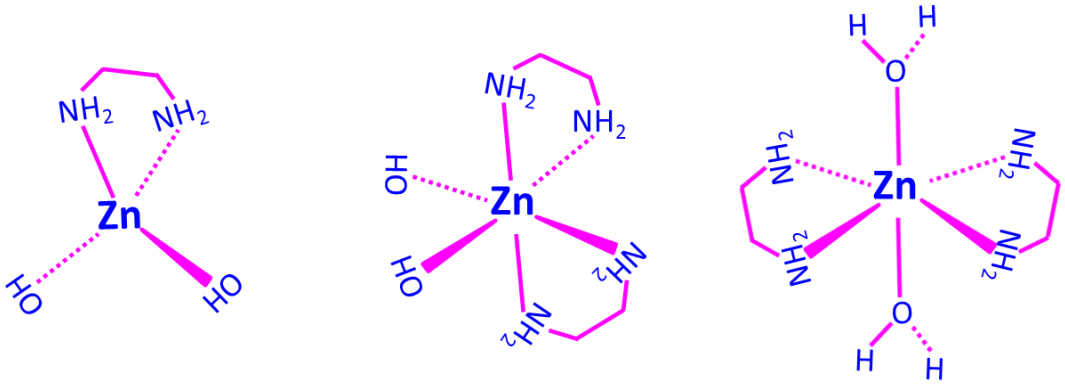

Figure 4.24: Few of the possible structural combinations of zinc metal organic complexes (a) MonoethylenediamineZinchydroxide (b) Di-ethylenediamineZinchydroxide and (c) Di-ethylenediamineZincdihydroxide.

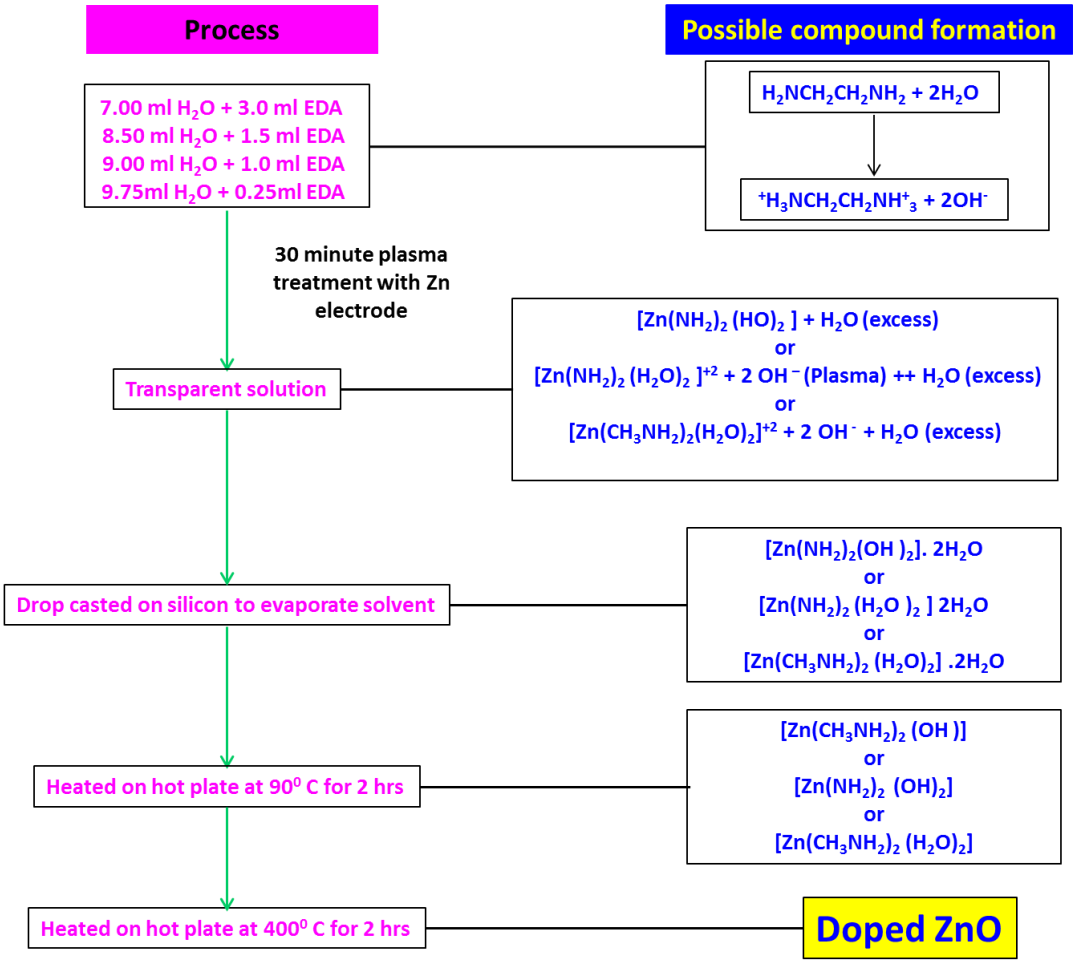

Figure 4.25: Shows possible compound formation according to process of synthesizing doped ZnO.

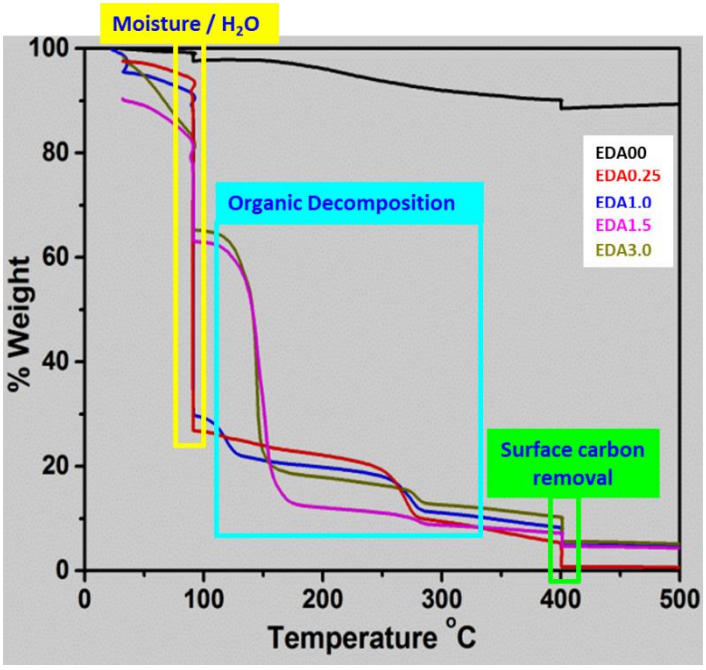

Figure 4.26: Thermogravimetric analysis of samples to produce EDA00, EDA0.25, EDA1.0, EDA1.5 and EDA3.0.

4.4.6 Discussion on dopant site in the ZnO lattice

A dopant can generally occupy two different sites in a lattice, i.e. either substituting a native atom or by occupying an interstitial site in the crystal structure lattice. The incorporation of dopants in the lattice depends on the synthesis process[60,61] and the type/location of the dopants can be inferred from material characterization results.

According to the absorbance measurement (figure 4.17b), a rough idea about dopant sites can be assumed. An extended absorption tail and bandgap reduction is generally related to substitutional dopant (S_d) rather than interstitial dopant (I_d).[38] EDA0.25 showed an extended absorption tail in the visible region (figure 4.17b, EDA0.25) and a lower bandgap (figure 4.18b) compared to pure ZnO. On this basis, it could be speculated that EDA0.25 exhibits either substitutional dopants only or a combination of S_d and I_d with a higher contribution of S_d. For sample EDA1.0, the bandgap is about the same as for EDA0.25 and lower than un-doped ZnO but the absorption tail is reduced compared to EDA0.25 (figure 4.17b, EDA1.0), suggesting a major contribution of substitutional doping with an increasing contribution of interstitial dopants. Further increase in dopant concentration (EDA1.5), induced a larger bandgap (figure 4.18d) without changing much the absorption tail compared to EDA1.0, confirming more I_d than S_d. For sample EDA3.0, there is a significant change in the bandgap as well as an extended visible absorption tail suggesting more S_d. This UV-Vis analysis is supported by XRD, XPS and EBD results.

According to our XRD (figure 4.13), in sample EDA0.25, a shift in the XRD peak of the (101) plane exist from 36.28^o to 36.25^o. This shift suggests an expansion of the lattice. According to Vegard's law, [63,64] doping of nitrogen will only expand the lattice if it substitutes O atoms due to the size difference between N and O atoms. To understand the expansion of the crystal, lattice parameters "*a*" and "*c*" are calculated for EDA00, EDA0.25 and EDA1.0 (figure 4.28).[63,64] Sample EDA00 produced values of *a* (3.25 Å) and *c* (5.20 Å) that are very well in agreement with the values found in the literature for un-doped ZnO (a = 3.25 Å and c = 5.20 Å).[65] At small dopant concentration, sample EDA0.25, the lattice parameters are only slightly changed along the anisotropic c-axis (a = 3.25 Å and c = 5.21 Å), confirming substitution dopants. At higher dopant concentration, EDA1.0, the lattice parameter *a* is unchanged (3.25 Å) while *c* is decreased (4.94 Å). This suggests a compression along the *c*-axis, corresponding to an increasing contribution of interstitial doping. At higher

concentrations of doping (EDA1.5 and EDA3.0), it is hard to observe peak shifts in the XRD spectra because of the broadening and distortion of the peaks. As the dopant concentration increases, amorphisation (disorder) of the crystal structure is seen (figure 4.13).[64] Therefore, the dopant site estimation in EDA1.5 and EDA3.0 could not be satisfactorily carried out on the basis of XRD measurements.

These results can be further corroborated with N 1s XPS spectra (figure 4.14c) where a shift in N 1s peak to higher energy is related to interstitial nitrogen in the lattice.[66,67] The nitrogen peaks for EDA1.0 and EDA1.5 are shifted to higher energy than EDA0.25, which confirm the increasing contribution of interstitial doping as EDA concentration was increased. However, for the sample EDA3.0, the N 1s XPS peak goes back to an energy value close to that for the EDA0.25 sample, which supports substitutional doping for nitrogen.

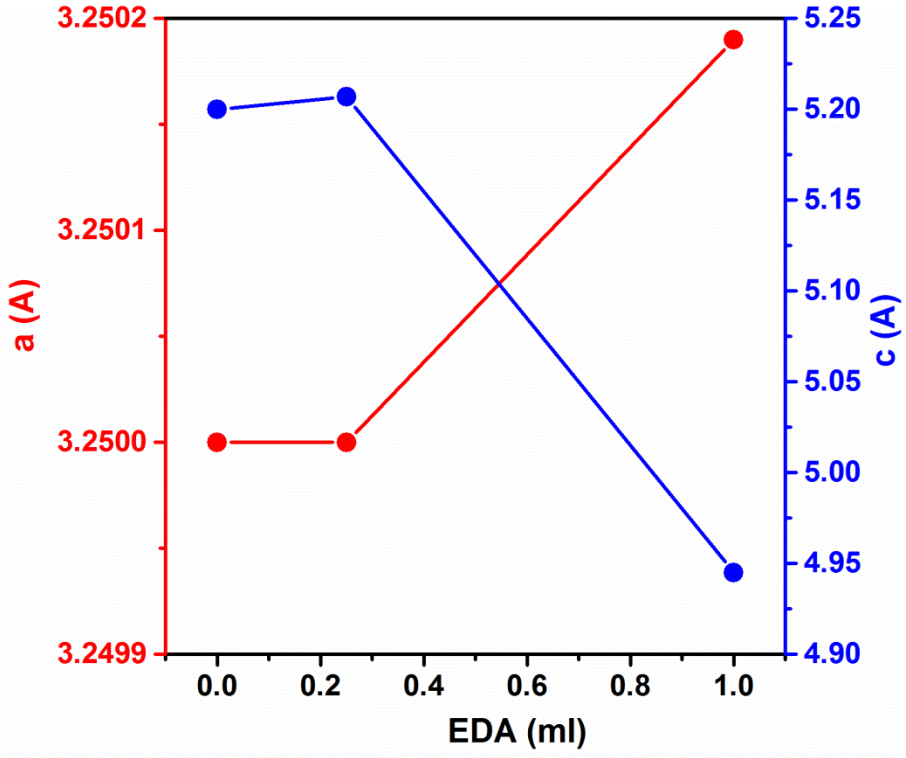

Figure 4.27: Measured lattice parameter a and c for ZnO (0.0 mL of EDA) and N doped ZnO (0.25 mL and 1.0 mL of EDA).

In summary, EDA0.25 exhibits only substitutional nitrogen doping possibly due to the low doping concentration. Increasing the N doping concentration contribute to increase interstitial doping, as observed for samples EDA1.0 and EDA1.5. When nitrogen and carbon co-doping is observed, sample EDA3.0, substitutional doping appears to be dominant again. Reduction of bandgap in EDA0.25 and EDA3.0 can be mainly the outcome of hybridization of 2p (from C or N) and O 2p states.[62]

4.4.7 Cyclic voltammetry measurement and energy storage application

To understand storage performance of ZnO and doped ZnO, electrochemical measurements were carried out in a three-electrode cell with a 0.5 M H_2SO_4 aqueous electrolyte. Figure 4.29 presents the capacitance-voltage (CV) curves of the ZnO and doped ZnO nanoparticles deposited on electrodes and measured at the scan rate from 5 mV s^{-1} to 100 mV s^{-1} in the potential range of -1.0 V to 0.8 V. All samples display a redox peak pair around -0.49 V and -0.38 V (E vs Ag/AgCl), showing a typical pseudo-capacitive behaviour of transition metal oxide. These redox peaks are more prominent at higher scan rate than lower scan rate. Another peak is also observed at 0.44 V which is irreversible; however, this peak is lower for samples produced with a higher EDA concentration.

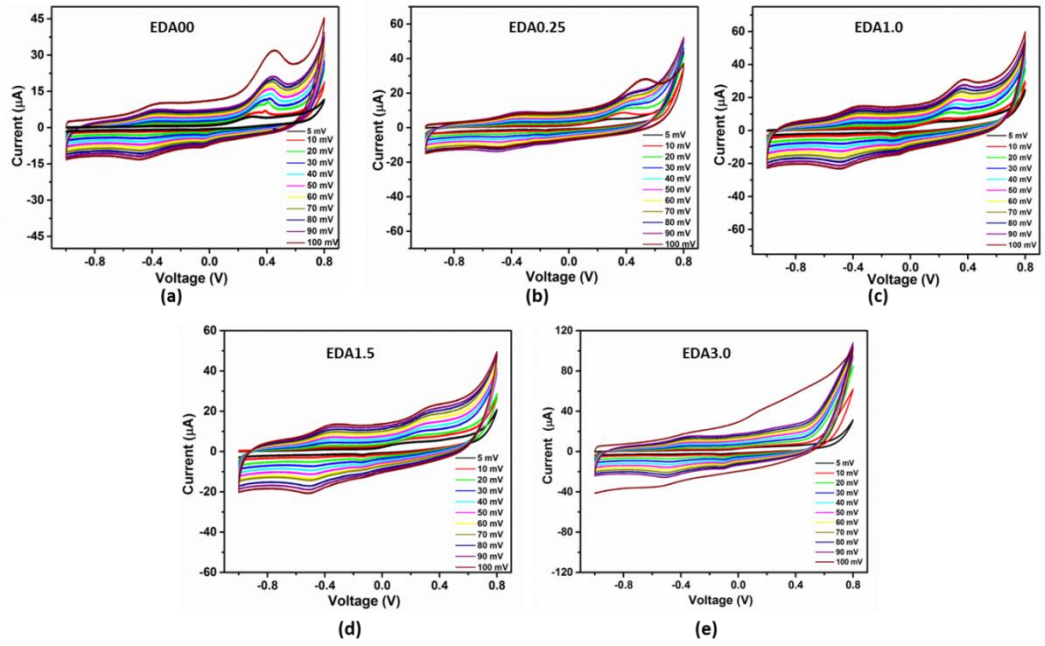

Figure 4.28: CV curve of (a) ZnO (EDA00), (b-d) N doped ZnO (EDA0.25, EDA1.0 & EDA1.5) and (e) N-C doped ZnO at scan rate from 5 mV/cm^{-1} to 100 mV/cm^{-1}.

The area under the CV curves can be used to calculate the areal capacitance. The calculated areal capacitance for the different samples is plotted in figure 4.30a vs. scan rate. As the scan rate increases C_a changes drastically for all samples.

Figure 4.30b shows the observed trend of areal capacitance at 5 mV s^{-1} scan rate vs. EDA amounts. The areal capacitance is generally higher for doped-ZnO nanoparticles; however, it decreases as N-doping increases. The highest value of areal capacitance is measured for the N/C co-doping. One of the factors that can affect the overall reaction

and storage performance is the particles size. As the particles size decreases, the surface area increases, and it provides more sites for electrochemical reactions. This would generally justify a higher areal capacitance for N-doped samples compared to un-doped ZnO nanoparticles. However other factors are in play and influence the measurements of doped nanoparticles. Hydrophilicity is another factor that can enhance interfacial properties. However, here we have already seen in figure 4.14a and 4.15f that doped nanoparticles exhibited a lower hydrophilicity. These observations suggest that increase in areal capacitance is the result of doping than any other factor.

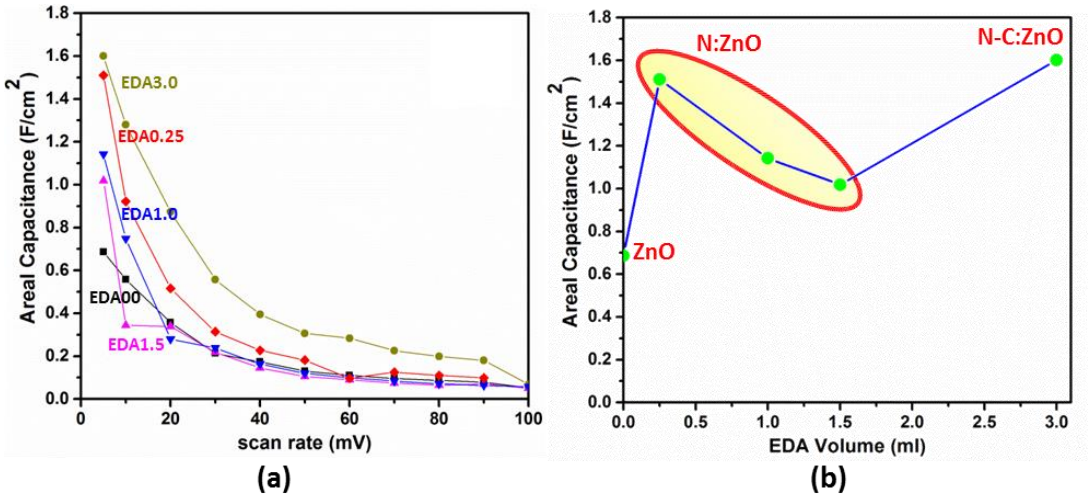

Figure 4.29: (a) Areal capacitance vs scan rate plot for EDA00, EDA0.25, EDA1.0, EDA1.5, EDA3.0 and (b) represents change in areal capacitance at 5 mV/sec with varying EDA volume.

It is confirmed with the CV results that substitutional doped sample (EDA0.25 and EDA3.0) showed more capacitance. A moderate substitutional N-doping level (EDA0.25) is demonstrated to be favourable for better electrochemical performance that can be due to a preserved crystallinity and low electrical resistance.[68] Moreover, a greater degree of substitutional doping, sample EDA3.0, shows the best supercapacitance performance which can be ascribed to an expanded lattice spacing and high electron density.

4.5 Conclusion

Hybrid plasma- liquid microplasma has shown the potential of synthesising different Zn based semiconductors with different electrolyte.

Detail characterization has proved ZnO_2 synthesis with ethanol electrolyte and defect relation with synthesis current. At lower synthesis current, $Zn(OH)_2$ impurity and crystal defects were observed. Defect density decreased as the synthesis current increases to 2 mA. Hydrogen peroxide measurement and $Zn(OH)_2$ impurity at lower current suggested that oxygen species played active role in the production of ZnO_2 from $Zn(OH)_2$.

Dopant ZnO was also synthesised with DI water-EDA electrolyte. Doping in ZnO shifted the adsorption edge in the visible region. Detail characterization analysis helped in understanding whether synthesised doped ZnO is substitutional or interstitial dopant dominant. Substitutional dopant affected ZnO properties more significantly than interstitial dominant ZnO. Moreover, substitutional dopant dominant samples (EDA0.25 and EDA3.0) showed higher absorption in the visible region and high charge storage capacity in initial electrochemical tests.

4.6 References

1. Ibarra, L., Marcos-Fernández, A. & Alzorriz, M. Mechanistic approach to the curing of carboxylated nitrile rubber (XNBR) by zinc peroxide/zinc oxide. *Polymer (Guildf).* **43,** 1649–1655 (2002).

2. Ibarra, L. & Alzorriz, M. Ionic elastomers based on carboxylated nitrile rubber (XNBR) and zinc peroxide: Influence of carboxylic group content on properties. *J. Appl. Polym. Sci.* **84,** 605–615 (2002).

3. Hsu, C. C. & Wu, N. L. Synthesis and photocatalytic activity of ZnO/ZnO2 composite. *J. Photochem. Photobiol. A Chem.* **172,** 269–274 (2005).

4. Gondal, M. A., Drmosh, Q. A., Yamani, Z. H. & Saleh, T. A. Synthesis of ZnO2 nanoparticles by laser ablation in liquid and their annealing transformation into ZnO nanoparticles. *Appl. Surf. Sci.* **256,** 298–304 (2009).

5. Wolanov, Y., Prikhodchenko, P. V, Medvedev, A. G., Pedahzur, R. & Lev, O. Moderate pH. (2013).

6. Palma-Palma, H. E., Camacho-López, M., Camacho-López, M. A. & Vilchis-Néstor, A. R. Preparation of zinc peroxide nanoparticles by laser ablation of solid in liquids. *Superf. y Vacio* **28,** 74–77 (2015).

7. Sun, M., Hao, W., Wang, C. & Wang, T. A simple and green approach for preparation of ZnO2and ZnO under sunlight irradiation. *Chem. Phys. Lett.* **443,** 342–346 (2007).

8. Kim, K. A., Cha, J. R., Gong, M. S. & Kim, J. G. Preparation of zno2 nanoparticles using organometallic zinc(ii) isobutylcarbamate in organic solvent. *Bull. Korean Chem. Soc.* **35,** 431–435 (2014).

9. Chen, W. *et al.* Synthesis, Thermal Stability and Properties of ZnO_2 Nanoparticles. *J. Phys. Chem. C* **113,** 1320–1324 (2009).

10. Bai, H. & Liu, X. Green hydrothermal synthesis and photoluminescence property of ZnO2nanoparticles. *Mater. Lett.* **64,** 341–343 (2010).

11. Escobedo-Morales, A. *et al.* Structural and vibrational properties of

hydrothermally grown ZnO2nanoparticles. *J. Cryst. Growth* **316,** 37–41 (2011).

12. Drmosh, Q. A., Gondal, M. A., Yamani, Z. H. & Saleh, T. A. Spectroscopic characterization approach to study surfactants effect on ZnO2 nanoparticles synthesis by laser ablation process. *Appl. Surf. Sci.* **256,** 4661–4666 (2010).

13. Wolanov, Y., Prikhodchenko, P. V, Medvedev, A. G., Pedahzur, R. & Lev, O. Moderate pH. *Environ. Sci. Technol.* **47,** 8769−8774 (2013).

14. Verma, S. & Jain, S. L. Nanosized zinc peroxide (ZnO_2): a novel inorganic oxidant for the oxidation of aromatic alcohols to carbonyl compounds. *Inorg. Chem. Front.* **1,** 534 (2014).

15. Uekawa, N. *et al.* Nonstoichiometric properties of zinc oxide nanoparticles prepared by decomposition of zinc peroxide. *Phys. Chem. Chem. Phys.* **5,** 929–934 (2003).

16. Dake, L. S., Baer, D. R. & Zachara, J. M. Auger parameter measurements of zinc compounds relevant to zinc transport in the environment. *Surf. Interface Anal.* **14,** 71–75 (1989).

17. Morkoc, H. & Ozgur, U. *General Properties of ZnO*. *Zinc Oxide: Fundamentals, Materials and Device Technology* (2009). doi:10.1002/9783527623945.ch1

18. Boussard, P., Siegbahn, P. E. M. & Wahlgren, U. Cluster Models of Zinc Oxide Including Ionic and Covalent Effects. *Surf. Sci.* **33,** 192–193 (1993).

19. Jain, G., Macias-Montero, M., Velusamy, T., Maguire, P. & Mariotti, D. Porous zinc oxide nanocrystalline film deposition by atmospheric pressure plasma: Fabrication and energy band estimation. *Plasma Process. Polym. Jain, G., Macias-Montero, M., Velusamy, T., Maguire, P. Mariotti, D. Porous zinc oxide nanocrystalline Film Depos. by Atmos. Press. plasma Fabr. energy band Estim. Plasma Process. Polym. 14, 1–8* **14,** 1–8 (2017).

20. Bouibes, A., Zaoui, A., Luo, W. & Ahuja, R. Promising optical characteristics of zinc peroxide from first-principles investigation. *Solid State Commun.* **263,** 6–9 (2017).

21. Thapa, R., Ghosh, S., Sinthika, S., Mathan Kumar, E. & Park, N. Magnetic, elastic and optical properties of zinc peroxide (ZnO2): First principles study. *J. Alloys Compd.* **620,** 156–163 (2015).

22. L. Companion, A. Spectra Peroxide of Zinc. *J. Phys. Chem. Solids* **23,** 1685–1688 (1962).

23. Feng, G., Yang, L., Wang, T., Zhang, J. & Lou, T. Hydrothermal preparation of nanocrystalline ZnO2. *Particuology* **10,** 388–391 (2012).

24. Sze S. M. *Semiconductor Sensors*. (Wiley, New york, 1994).

25. Ghosh, S., Bhattacharyya, R., Saha, H., Chaudhuri, C. R. & Mukherjee, N. Functionalized ZnO/ZnO $_2$ n–N straddling heterostructure achieved by oxygen plasma bombardment for highly selective methane sensing. *Phys. Chem. Chem. Phys.* **17,** 27777–27788 (2015).

26. Mariotti, D., Patel, J., Švrček, V. & Maguire, P. Plasma-liquid interactions at atmospheric pressure for nanomaterials synthesis and surface engineering. *Plasma Process. Polym.* **9,** 1074–1085 (2012).

27. Švrček, V., Mariotti, D. & Kondo, M. Microplasma-induced surface engineering of silicon nanocrystals in colloidal dispersion. *Appl. Phys. Lett.* **97,** 3–6 (2010).

28. Lee, S. W., Liang, D., Gao, X. P. A. & Sankaran, R. M. Direct Writing of Metal Nanoparticles by Localized Plasma Electrochemical Reduction of Metal Cations in Polymer Films. *Adv. Funct. Mater.* **21,** 2155–2161 (2011).

29. Patel, J., Němcová, L., Maguire, P., Graham, W. G. & Mariotti, D. Synthesis of surfactant-free electrostatically stabilized gold nanoparticles by plasma-induced liquid chemistry. *Nanotechnology* **24,** (2013).

30. Mariotti, D., Švrček, V., Hamilton, J. W. J., Schmidt, M. & Kondo, M. Silicon nanocrystals in liquid media: Optical properties and surface stabilization by microplasma-induced non-equilibrium liquid chemistry. *Adv. Funct. Mater.* **22,** 954–964 (2012).

31. Velusamy, T. *et al.* Ultra-small CuO nanoparticles with tailored energy-band

diagram synthesized by a hybrid plasma-liquid process. *Plasma Process. Polym.* **14,** 1–8 (2017).

32. Mitra, S. *et al.* Microplasma-induce liquid chemistry for stabilizing of silicon nanocrystals optical properties in water. *Plasma Process. Polym.* **24,** 158–163 (2014).

33. Locke, B. R. & Shih, K. Y. Review of the methods to form hydrogen peroxide in electrical discharge plasma with liquid water. *Plasma Sources Sci. Technol.* **20,** (2011).

34. Eisenberg, G. Colorimetric Determination of Hydrogen Peroxide. *Ind. Eng. Chem. Anal. Ed.* **15,** 327–328 (1943).

35. Lukeš, P. *Watertreatment by Pulsed Streamer Corona Discharge*. (2001).

36. Harish, S. *et al.* Controlled synthesis of organic ligand passivated ZnO nanostructures and their photocatalytic activity under visible light irradiation. *Dalt. Trans.* **44,** 10490–10498 (2015).

37. Game, O. *et al.* Concurrent synthetic control of dopant (nitrogen) and defect complexes to realize broadband (UV–650 nm) absorption in ZnO nanorods for superior photo-electrochemical performance. *J. Mater. Chem.* **22,** 17302 (2012).

38. Lynch, J. *et al.* Substitutional or interstitial site selective nitrogen doping in TiO2nanostructures. *J. Phys. Chem. C* **119,** 7443–7452 (2015).

39. Karmakar, R., Neogi, S. K., Banerjee, A. & Bandyopadhyay, S. Structural; morphological; optical and magnetic properties of Mn doped ferromagnetic ZnO thin film. *Appl. Surf. Sci.* **263,** 671–677 (2012).

40. Hsieh, P. T., Chen, Y. C., Kao, K. S. & Wang, C. M. Luminescence mechanism of ZnO thin film investigated by XPS measurement. *Appl. Phys. A Mater. Sci. Process.* **90,** 317–321 (2008).

41. Bai, S. *et al.* Quantum-sized ZnO nanoparticles: Synthesis, characterization and sensing properties for NO2. *J. Mater. Chem.* **21,** 12288 (2011).

42. Dillip, G. R. *et al.* Oxygen Vacancy-Induced Structural, Optical, and Enhanced Supercapacitive Performance of Zinc Oxide Anchored Graphitic Carbon Nanofiber Hybrid Electrodes. *ACS Appl. Mater. Interfaces* **8,** 5025–5039 (2016).

43. Yang, X. *et al.* Nitrogen-Doped ZnO Nanowire Arrays for Photoelectrochemical Water Splitting 2009. *Nano Lett.* 2–7 (2009). doi:10.1021/nl900772q

44. Wang, M. *et al.* N Doping to ZnO Nanorods for Photoelectrochemical Water Splitting under Visible Light: Engineered Impurity Distribution and Terraced Band Structure. *Sci. Rep.* **5,** (2015).

45. Zno, N., Qin, H., Li, W., Xia, Y. & He, T. Photocatalytic Activity of Heterostructures Based on ZnO and. *Appl. Mater. Interfaces* 3152–3156 (2011). doi:dx.doi.org/10.1021/am200655h

46. Liang, P. *et al.* Photocatalysis of C, N-doped ZnO derived from ZIF-8 for dye degradation and water oxidation. *RSC Adv.* **6,** 95903–95909 (2016).

47. Bera, S., Dhara, S., Velmurugan, S. & Tyagi, A. K. Analysis on Binding Energy and Auger Parameter for Estimating Size and Stoichiometry of ZnO Nanorods. *Int. J. Spectrosc.* **2012,** 1–4 (2012).

48. Futsuhara, M., Yoshioka, K. & Takai, O. Structural, electrical and optical properties of zinc nitride thin films prepared by reactive rf magnetron sputtering. *Thin Solid Films* **322,** 274–281 (1998).

49. Achouri, F. *et al.* Porous Mn-doped ZnO nanoparticles for enhanced solar and visible light photocatalysis. *Mater. Des.* **101,** 309–316 (2016).

50. Cho, S., Jang, J.-W., Lee, J. S. & Lee, K.-H. Carbon-doped ZnO nanostructures synthesized using vitamin C for visible light photocatalysis. *CrystEngComm* **12,** 3929 (2010).

51. Jindal, K., Tomar, M. & Gupta, V. Nitrogen-doped zinc oxide thin films biosensor for determination of uric acid. *Analyst* **138,** 4353 (2013).

52. Schwerdtfeger, P. Table of experimental and calculated static dipole

polarizabilities for the electronic ground states of the neutral elements (in atomic units). *Seattlecentral.Edu. http://seattlecentral.edu/faculty/dwick/polarizability2.pdf.* 1–23 (2013).

53. Wagner, C. D. THE AUGER PARAMETER , ITS UTILITY AND ADVANTAGES : measurements of photoelectron energies , and to an increasing extent , from lines are usually larger than those of the photoelectron lines . with a final core level vacancy The concept of the Auger parame. **47,** 283–313 (1988).

54. Wagner, C. D., Gale, L. H. & Raymond, R. H. Two-Dimensional Chemical State Plots: a Standardized Data Set for Use in Identifying Chemical States By X-Ray Photoelectron Spectroscopy. *Anal Chem* **51,** 466–482 (1979).

55. Eßmann, R. Influence of coordination on N-H...X− hydrogen bonds. Part 1. [Zn(NH3)4]Br2 and [Zn(NH3)4]I2. *J. Mol. Struct.* **356,** 201–206 (1995).

56. John M Haschke and Wesley W. Wendlandt. The thermal decomposition of metal oxalate complexes. *Anal. Chim. Acta* **32,** 386–393 (1965).

57. El Naggar, A. M. A., Nassar, I. M. & Gobara, H. M. Enhanced hydrogen production from water via a photo-catalyzed reaction using chalcogenide d-element nanoparticles induced by UV light. *Nanoscale* **5,** 9994 (2013).

58. Musat, V., Tabacaru, A., Vasile, B. S. & Surdu, V.-A. Size-dependent photoluminescence of zinc oxide quantum dots through organosilane functionalization. *Rsc Adv.* **4,** 63128–63136 (2014).

59. Kiefer, W., Mazzolini, A. P. & Stoddart, P. R. Recent Advances in linear and nonlinear Raman spectroscopy I. *J. Raman Spectrosc.* **38,** 1538–1553 (2007).

60. Yan, Y., Zhang, S. B. & Pantelides, S. T. Control of doping by impurity chemical potentials: Predictions for p-type Zno. *Phys. Rev. Lett.* **86,** 5723–5726 (2001).

61. Perkins, C. L., Lee, S. H., Li, X., Asher, S. E. & Coutts, T. J. Identification of nitrogen chemical states in N-doped ZnO via x-ray photoelectron spectroscopy. *J. Appl. Phys.* **97,** (2005).

62. Pan, J., Wang, S., Chen, Q., Hu, J. & Wang, J. Band-structure engineering of ZnO by anion-cation co-doping for enhanced photo-electrochemical activity. *ChemPhysChem* **15,** 1611–1618 (2014).

63. Pearson, G. L. & Bardeen, J. Electrical properties of pure silicon and silicon alloys containing boron and phosphorus. *Phys. Rev.* **75,** 865–883 (1949).

64. Nakrela A., Benramdanea N., Bouzidi A., Kebbaba Z., Medles M., M. C. Site location of Al-dopant in ZnO lattice by exploiting the structural and optical characterisation of ZnO:Al thin film. *Results Phys.* **18,** 2211–3797 (2016).

65. Dulub, O., Batzill, M. & Diebold, U. Growth of copper on single crystalline ZnO: surface study of a model catalyst. *Top. Catal.* **36,** 65–76 (2005).

66. Breeson, A. C., Sankar, G., Goh, G. K. L. & Palgrave, R. G. Rutile to anatase phase transition induced by N doping in highly oriented TiO 2 films. *Phys. Chem. Chem. Phys.* **18,** 24722–24728 (2016).

67. Yu, Z. *et al.* Crystallinity-dependent substitutional nitrogen doping in ZnO and its improved visible light photocatalytic activity. *J. Colloid Interface Sci.* **400,** 18–23 (2013).

68. Hu, Y., Liu, H., Ke, Q. & Wang, J. Effects of nitrogen doping on supercapacitor performance of a mesoporous carbon electrode produced by a hydrothermal soft-templating process. *J. Mater. Chem. A* **2,** 11753 (2014).

Chapter 5: Synthesis of Porous ZnO and Hydroxyl Passivated ZnO Quantum Dots by Gas- Phase Plasma

5.1 Introduction

This chapter describes the synthesis of different ZnO nanostructures, specifically porous film and quantum dots, by gas phase plasma system. Synthesis is performed with solid zinc precursor (Zinc wire) and environmental oxygen.

Firstly, section 5.2 will describe the experimental setup used throughout this work. In section 5.3, synthesis and characterization of porous ZnO will be discussed. Later in this section, porous ZnO will be used as electron transport layer with active materials like methylammonium lead iodide ($MAPbI_3$) perovskite and N doped carbon quantum dots. A detailed study will be presented on compatibility of porous ZnO with these active materials, as an electron transport layer. Section 5.4 will lead to the synthesis of ZnO quantum dots where smaller size of quantum dots will show interesting property of surface defect passivation. A details characterization will be presented to claim the hydroxyl passivation of quantum dot surface and observed changes in materials property.

5.2 Experimental setup

In this section, the reactor used in this chapter will be described. The plasma system consisted of a stainless-steel tube with quartz capillary (1 mm outer diameter and 0.7 mm internal diameter) containing a 99.99% pure zinc wire (Purchased from Alfa Aesar, Heysham, UK) of 0.25 mm diameter and a copper power electrode as shown in the figure 5.1a. Quartz tube is mounted inside larger metal tubing with diameter 1/8 of an inch using glue (Araldie Precision adhesive). The zinc wire acted as a ground electrode and radio frequency (RF) power (MKS Elite 300, 13.56 MHz) at 40 W is applied to the copper electrode via a matching unit; 150 standard cubic centimetre per minute (sccm) helium gas flow rate was used. The matching unit was between the electrode and the power supply, to reduce reflected power loss and to ensure plasma stability. The plasma was generated between the powered electrode and the zinc wire as shown in the figure 5.1b. The distance between the capillary and the substrate was ~1.5 cm. Atmospheric oxygen was consumed to oxide the material.

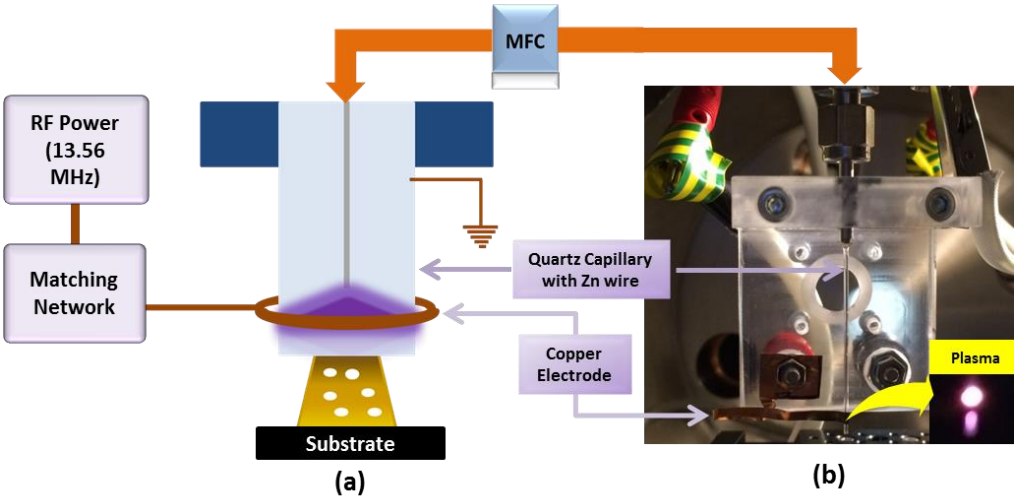

Figure 5.1: (a) Schematic of RF microplasma reactor and (b) corresponding photograph of plasma reactor with plasma.

5.3 Synthesis of porous ZnO nanocrystalline film

In this section, results obtained during the attempt of synthesizing porous ZnO nanocrystalline film will be discussed. Majority of results in this section are already published.[1]

5.3.1 Experimental parameters

In this experiment, He gas was used as a carrier gas to ignite the plasma. The wire tip is aligned at the same height of the powered electrode. The wire position is a very

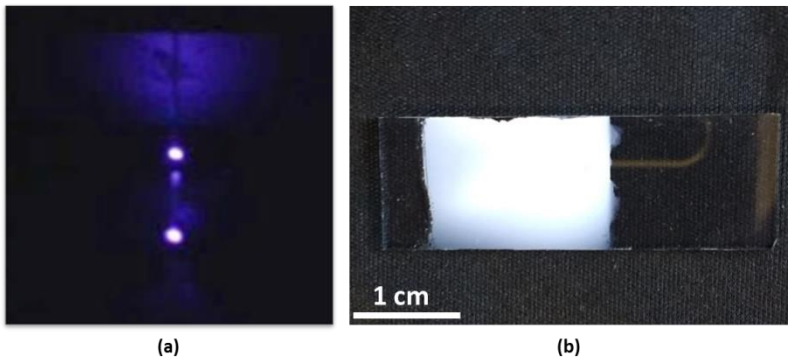

Figure 5.2: (a) Photo of the plasma in operation and (b) Deposited ZnO film (white region) on indium-tin oxide-coated glass substrate.

important parameter to produce this ZnO nanocrystalline porous film. The wire consumption was quick, about ~1 cm in 10-20 s. This system allows the deposition of the film on various substrates, including temperature-sensitive ones. Furthermore,

because the operating conditions are at atmospheric pressure, we were able to collect nanocrystallites (NCs) in colloids by replacing the substrate with a vial containing ethanol. This, in particular, confirmed that nanocrystallites were produced prior to deposition and that film formation was not due to radicals or ions depositing on the substrate but rather due to the aggregation of various nanoscale crystals. Figure 5.2a and 5.2b display the photo of the plasma in operation and the film deposited on an indium-doped tin oxide (ITO) coated glass substrate.

5.3.2 Material Characterization

HRTEM micrograph and selective area electron diffraction (SAED) pattern are shown in figure 5.3a, 5.3b and 5.3c. HRTEM was performed by collecting the sample in ethanol and drop-casting on carbon coated gold grids. Figure 5.3a shows larger particles as well as small crystallites. The lattice fringes of the particles were clearly observed in HRTEM as shown in figure 5.3b. The interplanar spacing was calculated and found to be 0.24 nm and 0.26 nm which correspond to (101) and (002) planes of wurtzite ZnO, respectively. ZnO planes can be also observed in the SAED pattern in figure 5.3c.

Table 8: Calculated d-spacing with SAED pattern and its comparison with standard ZnO d-spacing.

Calculated d-spacing with SAED pattern	Expected value for ZnO planes	Corresponding planes
0.290 nm	0.281 nm	(100)
0.277 nm	0.260 nm	(002)
0.252 nm	0.247 nm	(101)
0.203 nm	0.191 nm	(102)
0.174 nm	0.162 nm	(210)
0.157 nm	0.147 nm	(103)
1.45 Å	1.40 Å	(200)

The SAED pattern consists of series of dotted rings which confirmed the polycrystalline nature and wurtzite structure of synthesised ZnO nanoparticles. Lattice spacing calculations are performed with SAED pattern as shown in table 1. Calculated d-spacing is very well match with corresponding to standard value of ZnO planes (JCPDS 00-036-1451).

The nature of material and purity and crystallinity was further verified by XRD analysis of the ZnO film on a glass substrate, as shown in figure 5.3d. The peaks at 31.7°, 34.4°, 36.2°, 47.5°, 56.6° and 62.8° correspond to the (100), (002), (101), (102), (110) and (103) planes of wurtzite zinc oxide, respectively.[2] XRD measurements also show the orientation of the planes, i.e. a strong orientation along [101] direction as well as [100]. The average grain size was calculated using Williamson-Hall method (W-H).

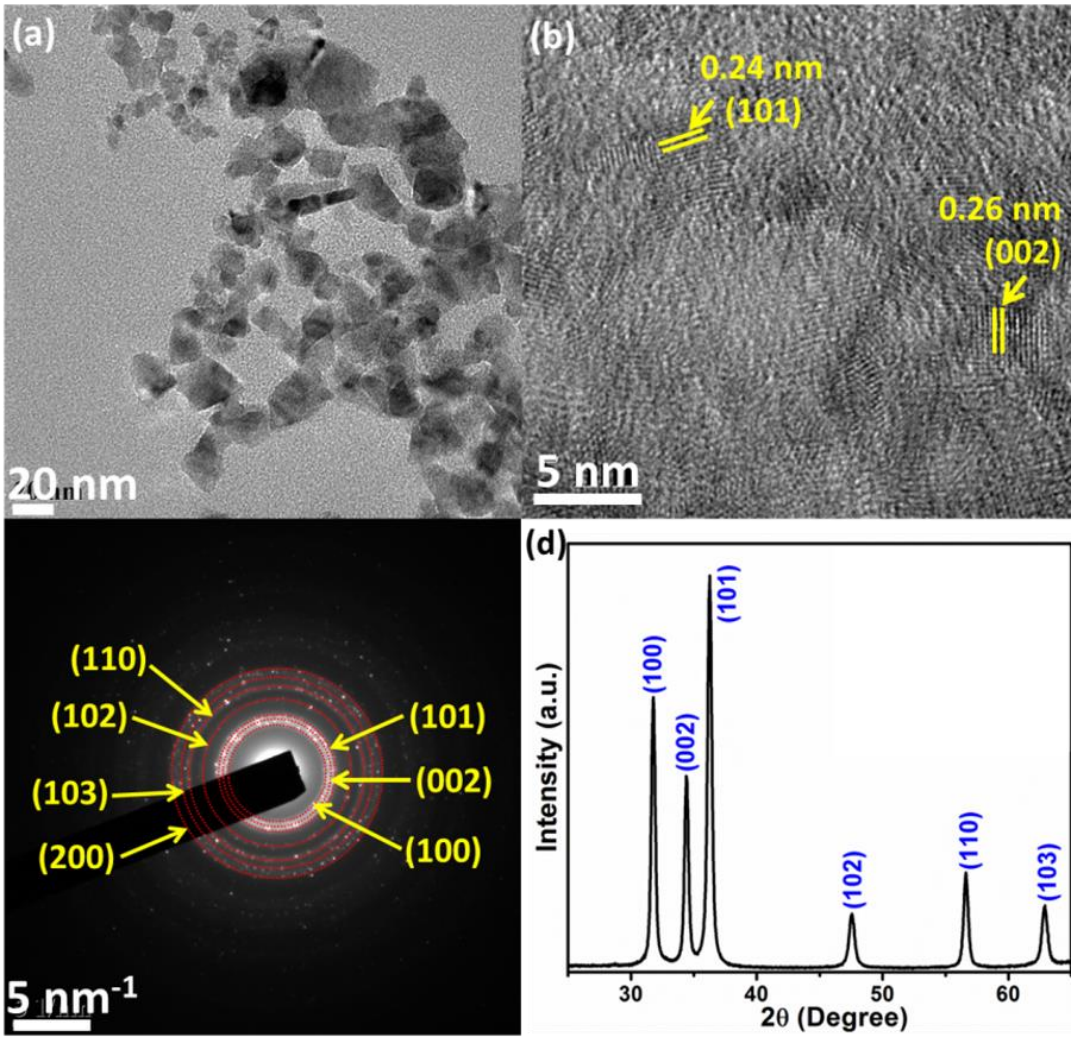

Figure 5.3: (a) Transmission electron microscope (TEM) image and (b) high-resolution TEM image of ZnO nanocrystallites. (c) Selective-area electron diffraction of the ZnO samples. (d) X-ray diffraction pattern of ZnO film and inset Scherrer particle size calculation.

Average particle size can be calculated by Scherrer equation as shown below:

$$D = K\lambda/\beta_D \cos\theta \quad (1)$$

where D is the grain size, K is the shape factor, λ is the X-ray wavelength (0.154 nm for Cu K_α), β_D is the instrumental broadening and θ is the Bragg angle. The instrument-corrected broadening β_D can be calculated by:

$$\beta_D^2 = [\beta_{measures}^2 - \beta_{instrumental}^2] \quad (2)$$

With the instrumental broadening, there is strain-induced broadening also arises because of crystal imperfections and distortions that is $\varepsilon \approx \beta_s/\tan\theta$. This strain induced broadening is a function of tanθ and not 1/cosθ as in Scherrer equation. This fundamental difference allows for a separation of reflection broadening when small crystalline size and microstains are present together in the material. Size and strain broadening are considered as an additive compound of total integral breadth of a Bragg peak. The distinct θ dependency of both effect separated the size and strain broadening in the analysis of Williamson and Hall.[3] Therefore,

$$\beta_{hkl} = \beta_s + \beta_D \quad (3)$$

$$\beta_{hkl} = (K\lambda/D\cos\theta) + (4\varepsilon\tan\theta) \quad (4)$$

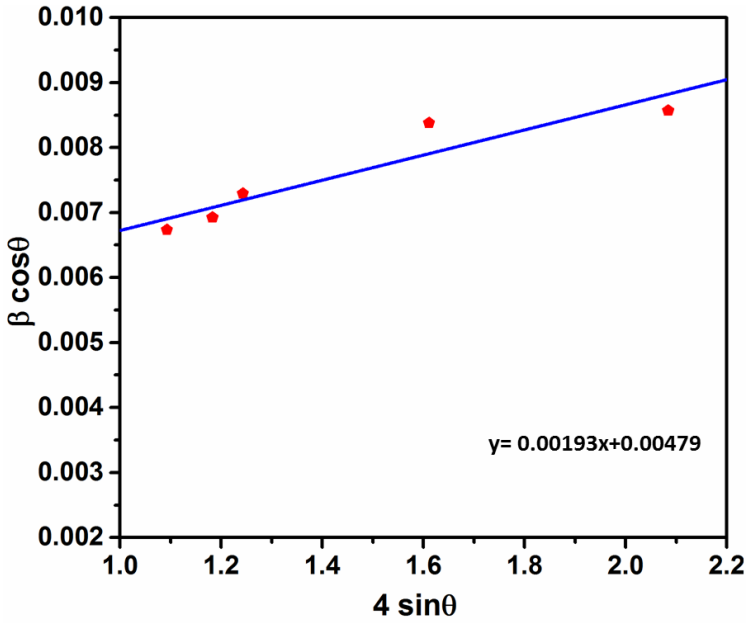

Figure 5.4: The W-H analysis of ZnO nanoparticles. Fit to the data, the size and strain are extracted from the y-intercept and slope of the fit, respectively.

By rearranging equation 4:

$$\beta_{hkl}\cos\theta = (K\lambda/D) + (4\varepsilon\sin\theta) \quad (5)$$

The term (βcosθ) was plotted with (4sinθ) for all peaks as shown in figure 5.4. The intercept on y-axis gives the value of particle size which is 32.15 nm.

The surface morphology of the film deposited on a silicon substrate was then analysed by SEM as shown in figure 5.5a. The porous nature of the film can be seen in the SEM image, which shows a high degree of uniformity. High porosity can also be observed in the cross-section SEM image, shown in figure 5.5b. This can be very useful in dye sensitised solar cell, in gas

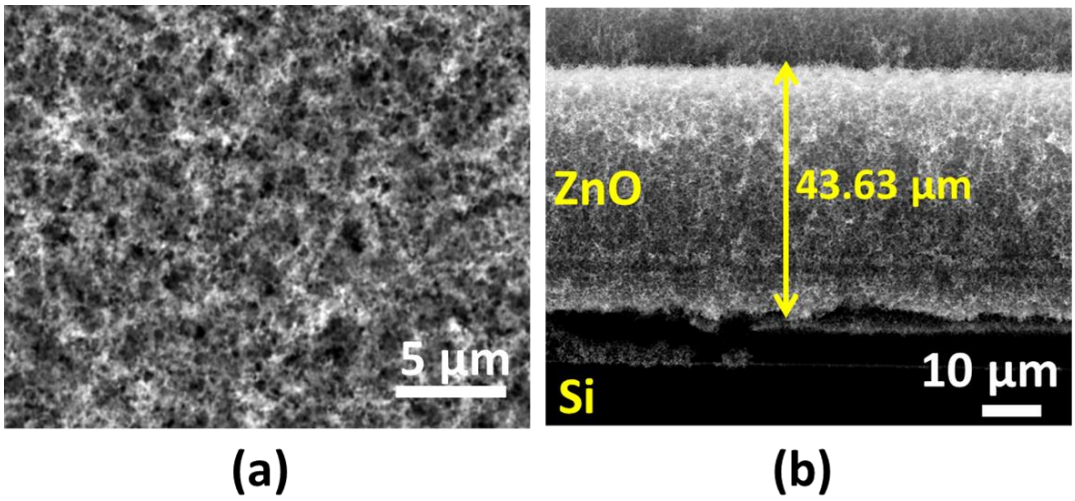

Figure 5.5: Scanning electron microscope image (a) Porous zinc oxide film grown on Si substrate (b) Cross section of the deposited film.

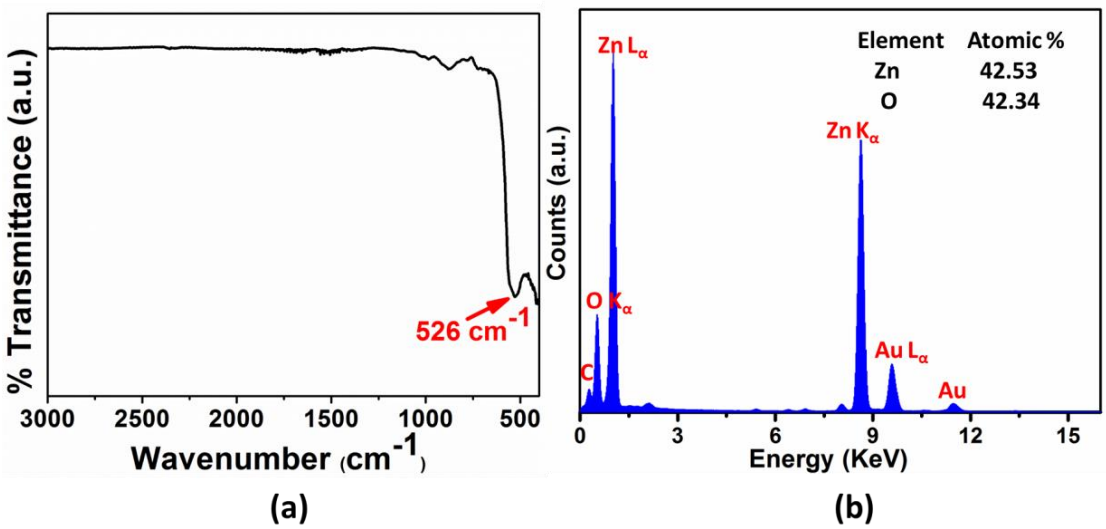

Figure 5.6: (a) Fourier transform infrared spectrum of prepared ZnO film, (b) Energy-dispersive X-ray analysis of ZnO.

sensing application and in many other applications also.[4–6] The measured thickness of the film is 43.63 µm which was deposited under static conditions covering an area of 2.125 cm^2 in 10 s. Because of the high deposition rate of 4.363 µm/s, this technique can be very useful for bulk deposition of ZnO porous film in a single step.

The chemical composition of the film was analysed by FTIR, TEM-EDX and XPS. The ZnO film was deposited on a silicon substrate to identify the nature of the chemical bonds by Fourier transform infrared spectroscopy. The FTIR of ZnO shows stretching vibrations at 436-529 cm^{-1}.[7–10] In particular, a peak at 526 cm^{-1} can be observed in figure 5.6a, which correspond to ZnO. No other peak could be observed in the FTIR spectrum. TEM-EDX performed on the colloidal samples (as in figure 5.3a-b) also confirms ZnO composition. The presence of Zn and O and the atomic percentage of the individual element can be seen in figure 5.6b. The peaks of gold and carbon are originating from the TEM grid.

Raman spectroscopy was carried out to study the vibrational properties of porous ZnO. Raman spectroscopy was performed by depositing the film on a molybdenum foil to exclude any interference from the background. Spectrum was recorded at room temperature in the range of 250–650 cm^{-1} as shown in figure 5.7.

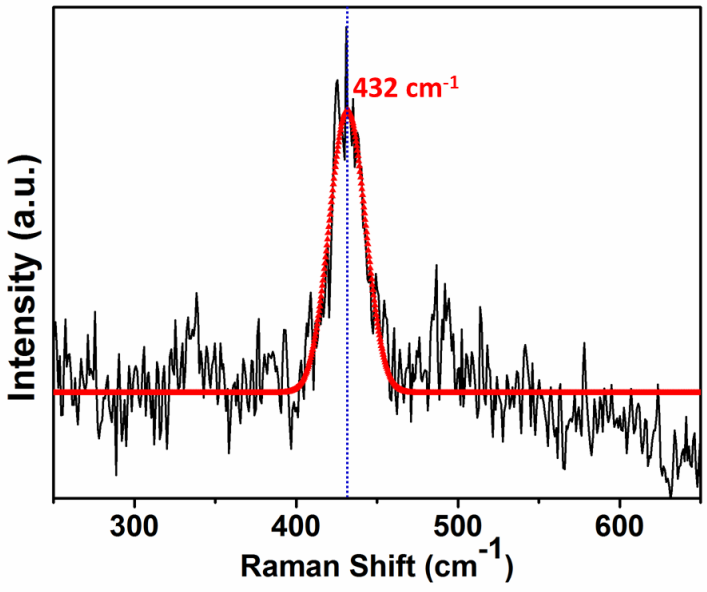

Figure 5.7: A typical Raman spectrum at room temperature of porous ZnO film.

Only one vibrational peak was observed at 432 cm^{-1} which can be assigned to a fundamental optical E2 (high) mode.[11,12] This Raman peak of a ZnO crystal is the band

characteristics of hexagonal wurtzite phase. Other phonon or multiple scattering peaks were absent in our measurement. A peak that is usually reported at 580 cm^{-1} related to intrinsic defects, such as an oxygen vacancy and interstitial zinc also did not appear suggesting stoichiometric ZnO as previously confirmed by EDX (see composition in figure 5.6b).[11]

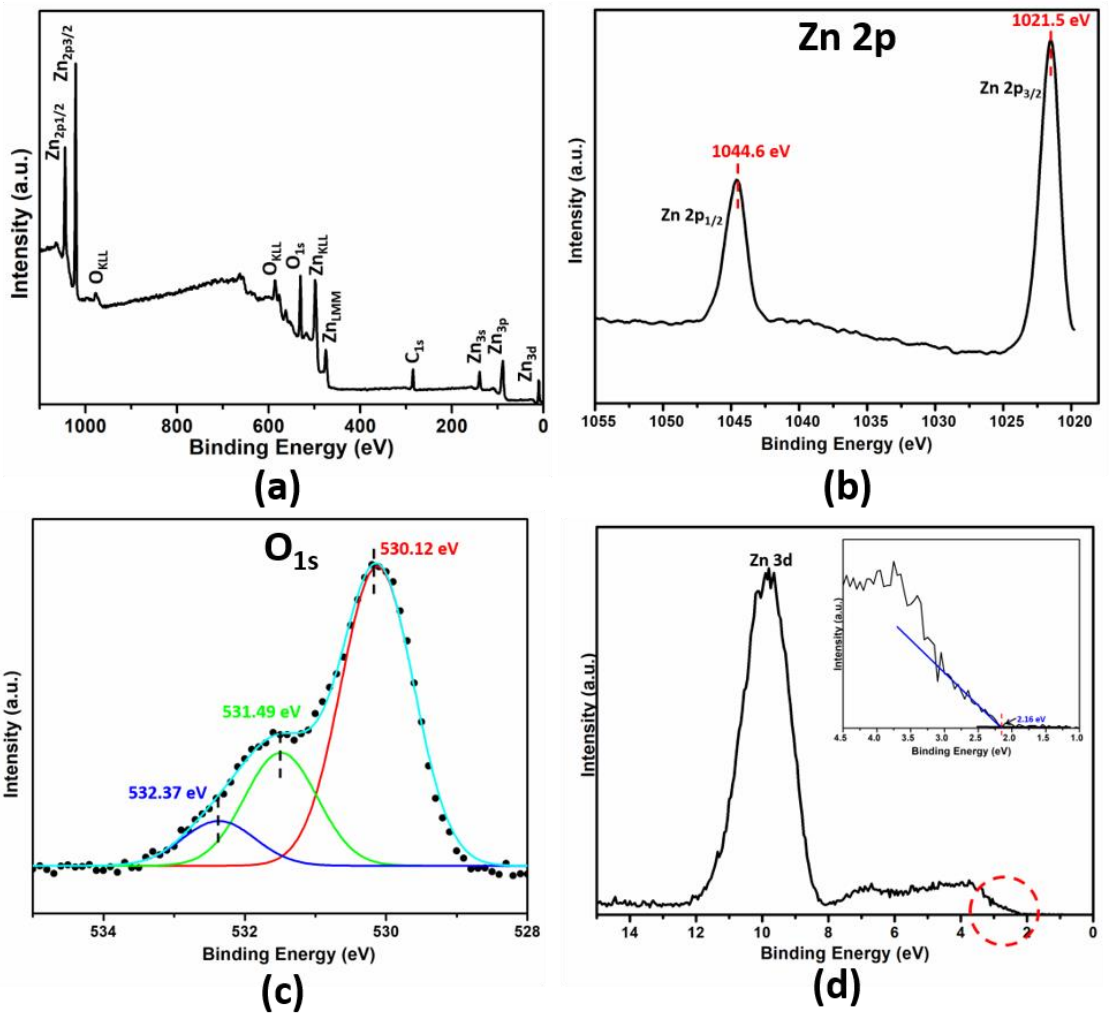

Figure 5.8: (a) X-ray photoelectron spectrum (XPS) survey scan of ZnO; (b) Zn 2p; (c) O 1s; (d) onset of the XPS spectra of ZnO and inset shows Ef –EVBM.

XPS was performed to analyse further the chemical composition and oxidation states. Sample was prepared by direct deposition of ZnO film on silicon substrate. XPS survey shows Zn and O peaks as shown in figure 5.8a and confirms ZnO formation. Binding energy at 1021.5 eV and 1044.6 eV are attributed to the binding energy of $Zn_{2p3/2}$ and $Zn_{2p1/2}$ electrons as shown in figure 5.8b. The BE difference between these two peaks is 23.1 eV which suggest that Zn is in Zn^{+2} state, confirming ZnO formation.[13–15]

In the XPS spectra, the asymmetric O 1s peak was observed with a shoulder at higher binding energy. O 1s spectrum was fitted into three peaks centred at 530.12 eV, 531.49 eV and 532.37 eV, figure 5.8c. The first peak at 530.12 eV corresponds to O^{-2} in Zn-O binding. The peak at 531.49 eV correlates to the oxygen-deficient region in ZnO matrix or OH group adsorbed on ZnO surface. Higher energy peak at 532.37 eV can be attributed to chemisorbed oxygen such as H_2O or -CO_3 species.[16,17]

According to obtained characterization results, it can be confirmed with TEM and XRD that crystalline wurtzite ZnO has produced in this process with range of size. SEM results confirmed the porous nature of the deposited ZnO film. Further, FTIR, EDXand XPS confirmed the chemical composition of the ZnO and purity. Raman spectroscopy confirmed further purity and chemical confirmation.

5.3.3 Optical properties and energy band diagram (EBD)

To characterise the bandgap of the ZnO film, we have carried out UV-Vis absorption spectroscopy. UV-Vis was performed by collecting ZnO directly in ethanol and calculated the corresponding bandgap by Tauc plot. The result of this technique shows a strong excitonic absorption peak at 362 nm (figure 5.9a), which is close to the excitonic peak observed for bulk ZnO.[2,18]

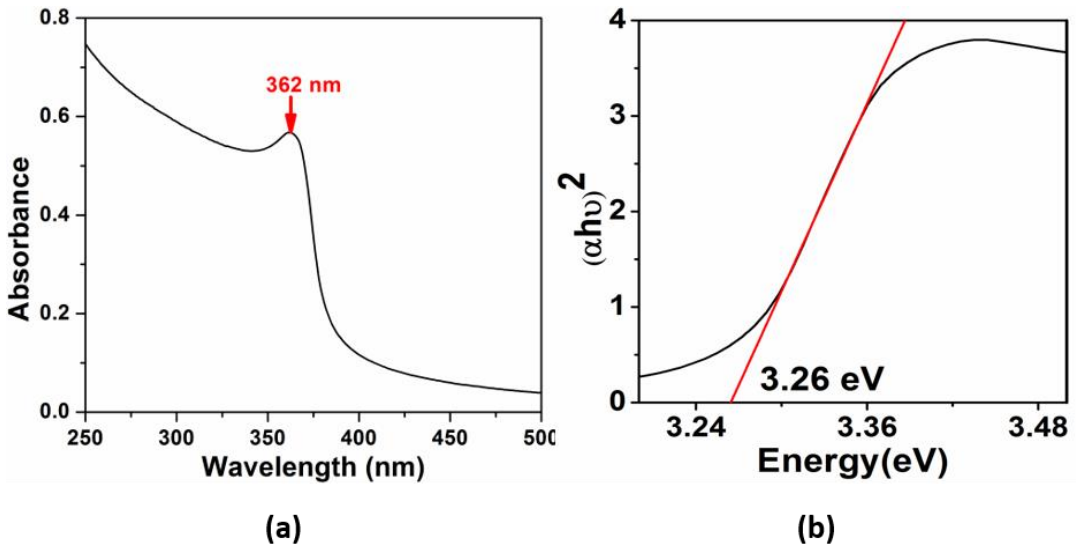

Figure 5.9: (a) Ultra-violet/visible absorbance spectrum of ZnO and (b) corresponding Tauc plot showing bandgap of 3.26 eV.

ZnO is expected to have a direct bandgap, we can use absorbance to determine the bandgap value through a Tauc plot (figure 5.9b). This is done by plotting $(Ahv)^2$ vs. hv

where *A* is the absorbance and *hv* is the photon energy. The Tauc plot is shown in the figure 5.9b. The direct bandgap is confirmed by the linear region of the plot and the intercept produces a bandgap of 3.26 eV.

ZnO generally shows photoluminescence in the UV and Visible region. UV emission corresponds to the bandgap excitonic emission and the visible emission is due to defects. In particular, visible emission could be due to recombination of the conduction band electrons with deep-trap holes or recombination of electron present in near conduction band traps with holes in the valence band.[19]

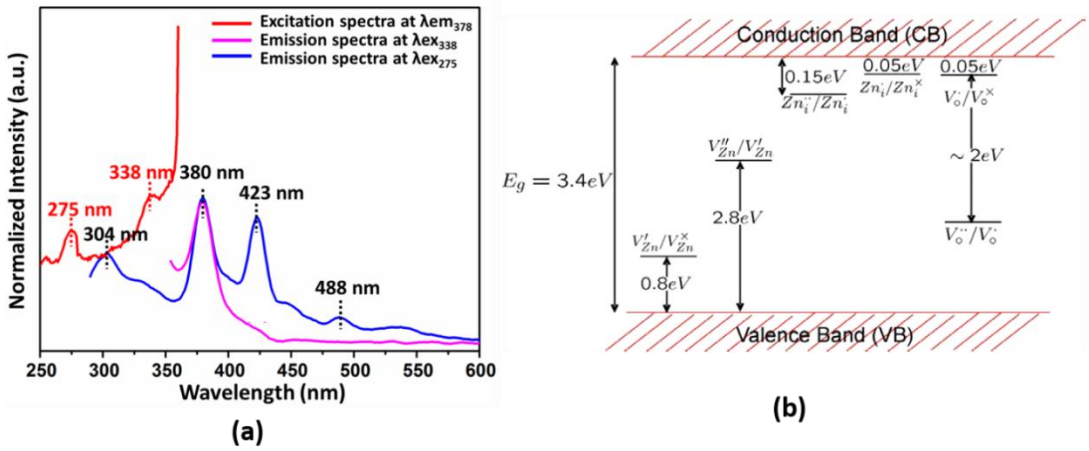

Figure 5.10: Photoluminescence spectra of ZnO shows a) Excitation spectra at λem378 b) high-intensity excitonic peak at λex338 and c) violet-blue emission as well with the excitonic peak at lower wavelength (λex275).

We have recorded excitation and emission spectra of ZnO. ZnO colloidal solution in ethanol was used to measure the photoluminescence (PL). Excitation spectra at emission wavelength 378 nm shows peaks at two excitation wavelengths, 275 nm and 338 nm (figure 5.10a red). We have then measured PL emission with excitation at these two these wavelengths (338 nm and 275 nm). Emission spectra are shown in figure 5.10a pink (λex_{338}) and 5.10a blue (λex_{275}) where both emissions in the UV as well as in the visible region are observed. At λex_{338} only excitonic emission is observed at 380 nm. At $\lambda ex_{275,}$ there are four peaks in the emission spectrum at 304 nm, 380 nm, 423 nm and 488 nm. In both cases, the peak at 380 nm is originated from excitonic recombination and consistent with the bandgap measurement of ZnO as shown in figure 5.9. Other than the excitonic peak, all other peaks in the visible region are considered to be from defects in literature.[19,20]

In our measurements, we do not expect emission to originate from interstitial vacancies or deep traps in the material, because the material characterization has shown very limited defects being present (e.g. see Raman spectrum in figure 5.7, XPS analysis in figure 5.8b and EDX in figure 5.6b). However, there is visible emission at 423 nm and 488 nm at λex_{275} which shows some defects in the material.

In ZnO, there are number of different intrinsic defects with different ionization energies have been reported. The donor defects are: $Zn_i^{\bullet\bullet}$, $Zn_i^{\bullet}$, Zn_i^{x}, $V_o^{\bullet\bullet}$, $V_o^{\bullet\bullet}$, V_o and the acceptor defects are V_{Zn}'', V_{Zn}' where a dot indicates positive charge, a prime indicates negative charge, a cross indicates zero charge and i, Zn, O and V denote interstitial site, zinc, oxygen and vacancy, respectively. [20,21] The energies of these defects vary from ~ 0.05-2.8 eV[22] as shown in figure 5.10b. Defects having high energy are deep defects and others considered as shallow defects. Mostly, Zn interstitials and oxygen vacancies are most predominant ionic defects. However, defect domination in undoped ZnO is still not clear.

In observed results, emissions in the violet, blue region are considered to be from structural defects mainly zinc interstitials related defects according to energy profile (figure 5.10b).[23] Another peak at 304 nm in UV region is also related to emission from zinc interstitials (Zn_i) to valence band transition as the position of Zn_i level is 0.15 eV -0.22 eV below conduction band.[24] There is no emission related to defect states at near the band gap excitation wavelength. Overall, there was only Zn_i emissions was observed only at λex_{275} excitation wavelength.

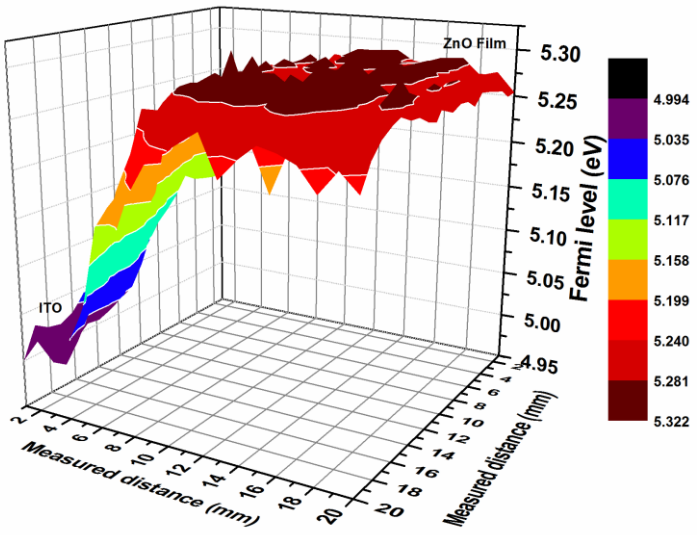

Figure 5.11: Fermi level measurement of ZnO film by scanning Kelvin probe on ITO substrate.

The sample was deposited on ITO-conducting surface to carry out Kelvin probe measurements, to find out Fermi level of the film. The Fermi level was obtained by measuring the contact potential difference (CPD) between the ZnO sample and a reference electrode with the Kelvin probe. In our case, the Fermi level of ZnO is -5.27 eV as can be seen in figure 5.11. This value matches well with reported value of ZnO Fermi level (-5.2 eV).[25,26]

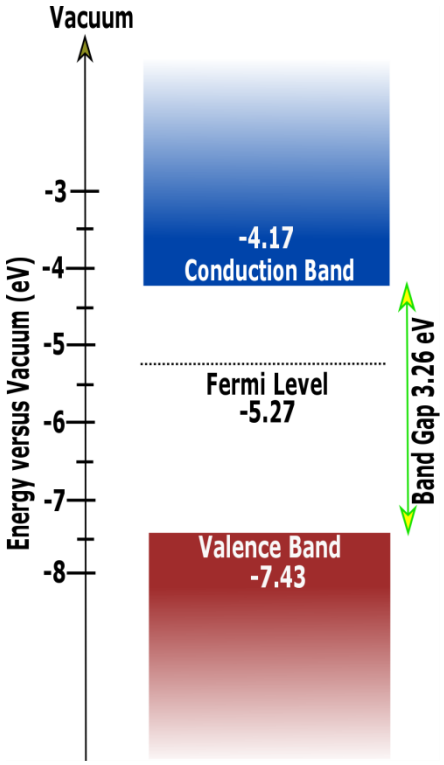

Figure 5.12: Corresponding energy band diagram of ZnO Estimatedwith XPS, kelvin prob and bandgap measurements.

The difference between Fermi level energy (E_f) and valence band maximum (E_{VBM}) was evaluated also from the XPS spectra as shown in figure 5.8d by extrapolating the leading edge of the XPS spectra to the baseline as shown in the inset of figure 5.8d. This produced a value of (E_f - E_{VBM}) = 2.16 eV.

The complete band diagram of ZnO has been determined and shown in figure 5.12. The position of the valence band edge was calculated from the XPS results (E_f - E_{VBM} = 2.16 eV) and using the Fermi level value from Kelvin probe measurements, i.e. E_{VBM} = E_f - 2.16 eV = -5.27 eV - 2.16 eV = -7.43 eV. The corresponding conduction band edge was also found adding the value of the measured bandgap energy to the valence band edge, yielding a value of -4.17 eV. The overall band diagram is in good agreement with

reported literature values.[26–28]

5.3.4 Introduction to photovoltaic devices with the ZnO porous films

The ZnO films produced as described above will be used and tested here as an electron transport layer (ETL) in solar cells. ETL is a key component in solar cells for the extraction and transport of photogenerated electrons. Titanium oxide (TiO_2) has been used most frequently in solid state solar cells as an ETL.[29–32] Electron injection rate are very high for TiO_2 when used in combination with organo-halide perovskite absorbers; however because of the low electron mobility in TiO_2, electron recombination rate can be also high.[33,34] In addition to that, TiO_2 ETL layers require high-temperature processing which represents a limitation for application on various flexible substrates.[35,36] For this reasons, there is interest in finding alternative and complementary materials to be used as ETL.

ZnO films produced by the method described above can be a potential alternative for ETL because of ZnO wide-bandgap, good transparency, high electron mobility (200-300 $cm^2\ V^{-1}\ s^{-1}$), room-temperature processing and n-type conductivity.[37,38] In addition, ZnO energy levels are very similar as TiO_2 and therefore can produce suitable alignment with a range of absorbers/contacts.[37,39,40]

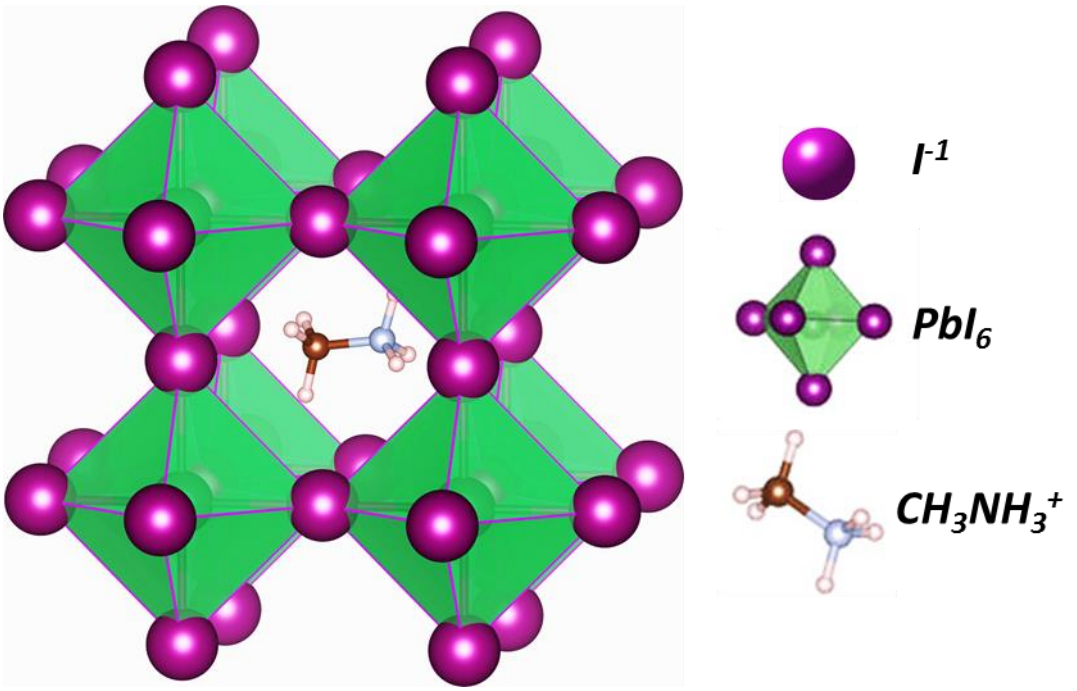

Figure 5.13: Perovskite structure of $CH_3NH_3PbI_3$ where PbI_6 octahedra consist of 3D framework where $CH_3NH_3^+$ fits into the framework.[41]

To exemplify the applicability of the ZnO films and demonstrate the possibility of using our plasma process for solar cell fabrication, perovskite solar cells (PSC) are considered here, where organo-halide perovskites have been used as absorber.

Perovskite is a word that can be used for any material having structure like $CaTiO_3$ with general formula ABX_3, where A, B, X are monovalent cation, bivalent cation and X is monovalent anion, respectively. A and B are coordinated to 12 X and 6 X anions, respectively. Here, we have used methyl ammonium lead iodide ($CH_3NH_3PbI_3$; $MAPbI_3$) as the active material in solar cell where B is the lead (Pb) atom and X is iodine (I). The basic $MAPbI_3$ unit cell is represented in figure 5.13 where PbI_6 octahedra consist of three-dimensional (3D) framework where $CH_3NH_3^+$ fits into the framework.

There have been many reports where ZnO is used as ETL in $MAPbI_3$ perovskite cell, e.g. as a compact ZnO layer or as ZnO nanorods.[42] Different ZnO nanostructures like nanowires, nanorods, nanoshells etc. have been used in perovskite solar cells (PSCs).[43–46] Here, we have explored the possibility of using porous ZnO in PSC. The structure of the device includes ITO/porous ZnO/$MAPbI_3$/Spiro OMeTDA/Au. Band alignment of the device is presented in figure 5.14a.

Device Preparation

- **Deposition of porous ZnO:**

A very thick layer (95 μm) of porous ZnO was deposited directly on ITO-coated glass substrates directly from system as shown in figure 5.14b (before). Different annealing temperatures were used to improve the ZnO film interface with the adjacent layers.

- **$CH_3NH_3PbI_3$ thin film fabrication:**

Methylammonium lead iodide ($CH_3NH_3PbI_3$) perovskite powder (0.23 gm) is mixed in 2.5 mL of dimethyl-formamide (DMF) at 60 ^oC. This solution is deposited onto porous ZnO using both spin and spray coating deposition. For spin coating, 400 μL of solution is deposited at 2000 rpm for 30 s. For spray coating, the solution is sprayed in air on to porous ZnO layer and annealed for 2 min at 100 ^oC. We have observed that the ZnO layer is affected by DMF and reduces ZnO layer thickness leaving behind only a ~1 μm thickness as shown in figure 5.14b (after).

- **Deposition of hole transport layer:**

The hole transport layer was prepared by dissolving 0.063 g 2,2′,7,7′-tetrakis[N,N-di(4-methoxyphenyl)amino]-9,9′-spirobi-fluorene (Spiro MeOTAD) in 1 mL chlorobenzene and 20 µL of butylpyridine and deposited by spin-coating (1500 rpm for 20 s).

- **Deposition of metal contacts:**

Finally, gold (Au) or palladium (Pd) contacts were deposited using a Moorfield minilab DC/RF magnetron box sputter system using argon plasma at constant current of 0.15 A for 50 min at a working pressure of 1.5 x 10^{-2} mbar. Energy band diagrams show that the ZnO film acts as an electron transport/hole blocking material with the Au contact creating a Schottky barrier at the back electrode.

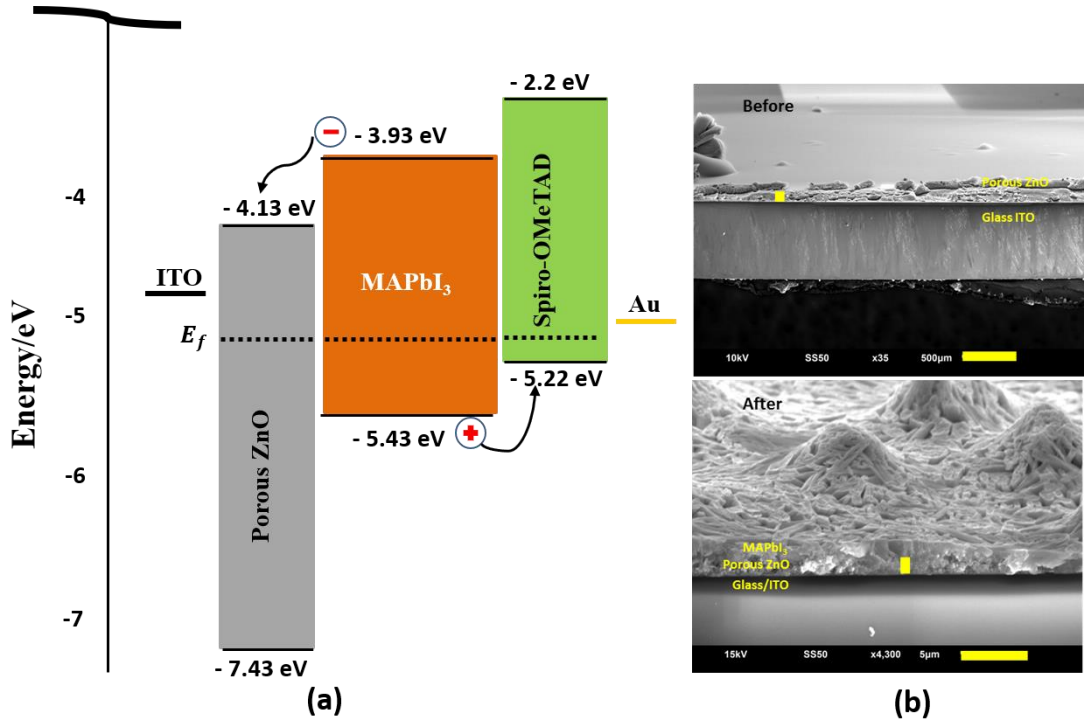

Figure 5.14: (a) Non-equilibrated band diagram for cell and (b) SEM images of ITO/Porous ZnO before and after perovskite deposition.

Firstly, devices prepared by spin coating of perovskite will be discussed. The porous ZnO film was directly deposited on ITO substrates. The perovskite and spiro layers were then spin coated on top of the ZnO layer. Current-voltage (I-V) characteristics were measured as shown in figure 5.15a. It can be seen from the graph that this device architecture does not show any rectification and were shunting. As it can be seen in

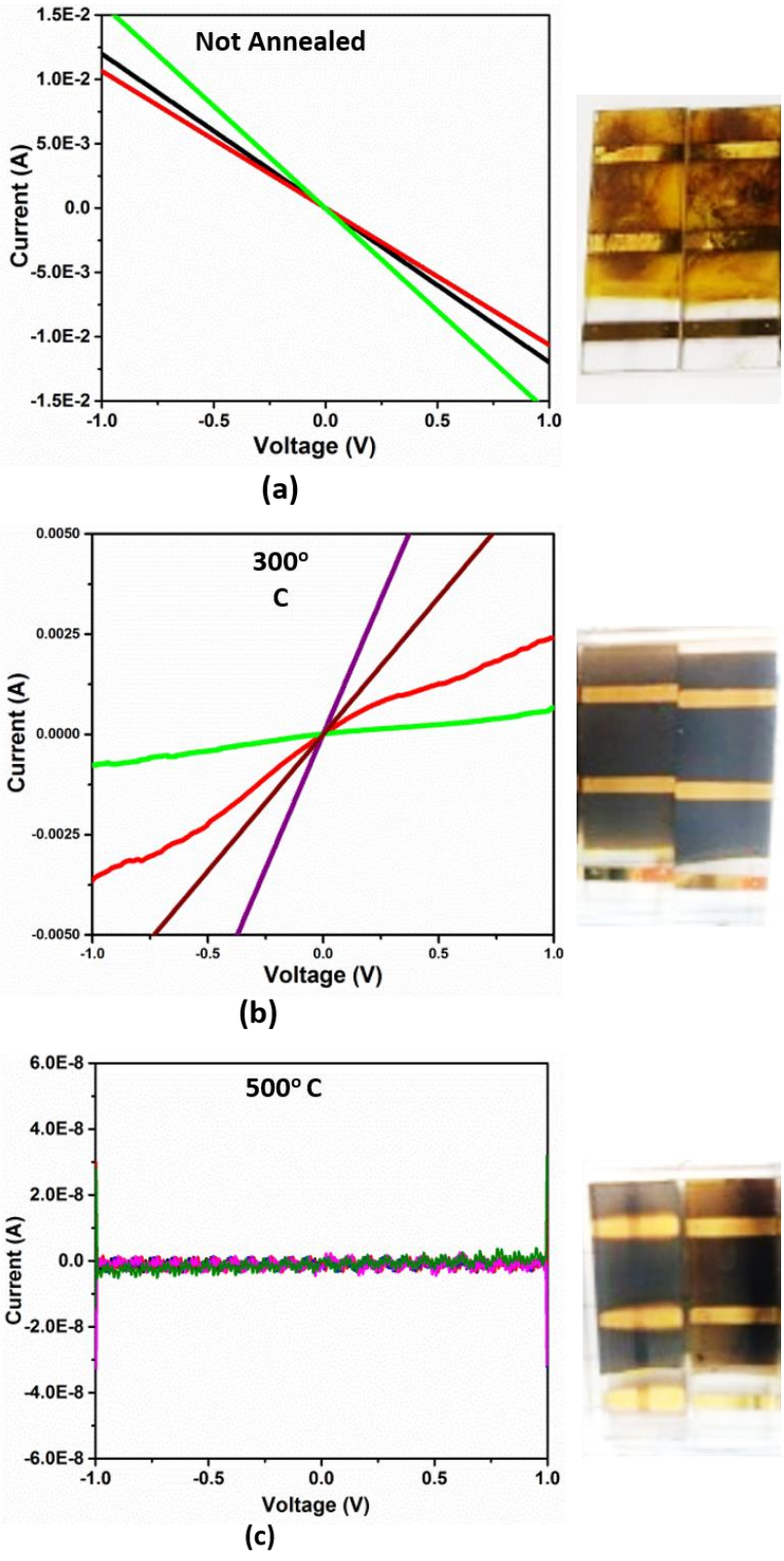

Figure 5.15: I-V characteristic of cell where perovskite is deposited by spin coating and Porous ZnO was deposited directly from our plasma system where ZnO layer was (a) not annealed (b) annealed at 300 ^{O}C and (c) annealed at 500 ^{O}C and corresponding device photographs where degradation of perovskite is clearly visible for not annealed.

corresponding device photograph of figure 5.15a, the perovskite layer was not stable on top of the porous ZnO and started to degrade into yellow PbI_2 precursor of perovskite.[47,48] In order to solve this issue, we tried annealing the ETL and remove any surface hydroxyl group as these can be the reason for perovskite degradation.[49] Deposited porous ZnO were annealed at 300 ^oC and 500 ^oC after deposition. At 500 ^oC annealing condition, instead of ITO, FTO substrate is used as ITO is sensitive at this temperature. As it can be seen in figure 5.15b-c, at 300 ^oC only short circuit current was observed and we did not observe any rectification behaviour. At 500 ^oC (figure 5.15c), we observed no current possibly due to the adverse effect of heat onto the FTO substrate which has deformed the substrate (observed by naked eye). That might have increased the resistance for current flow.

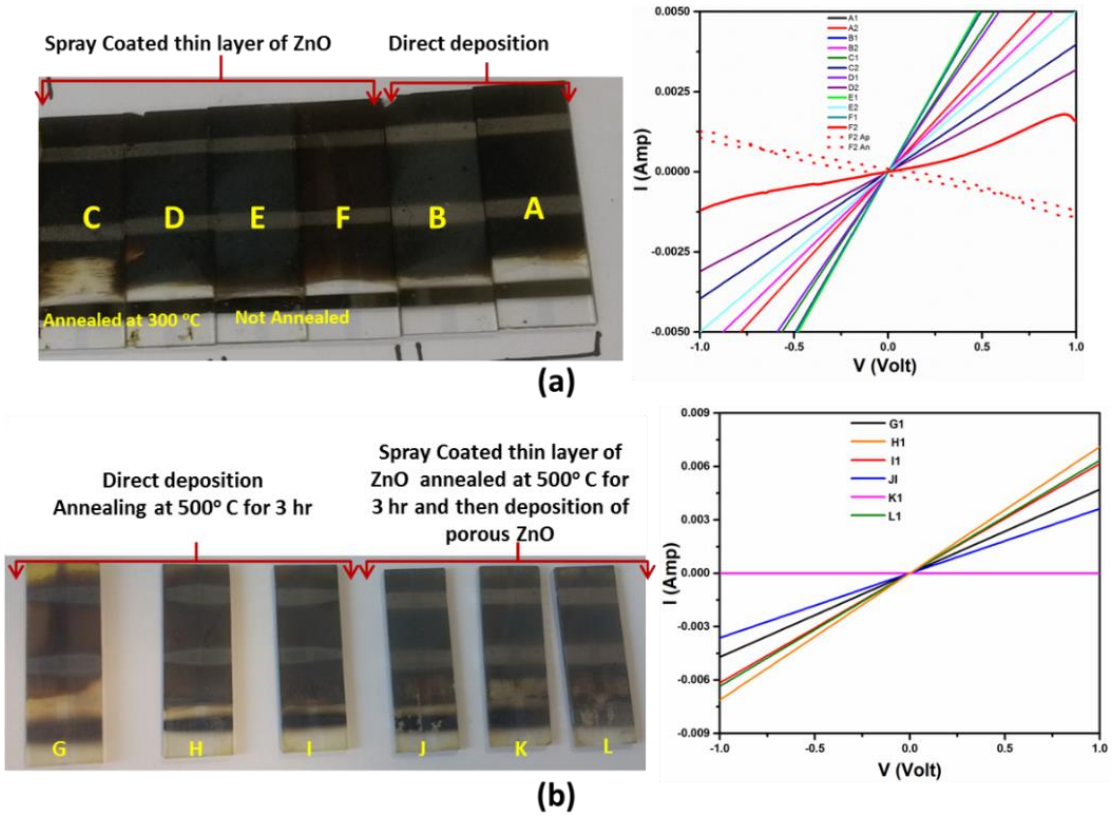

Figure 5.16: (a) and (b) Spray coated perovskite solar cell with different deposition conditions from porous ZnO as stated in the images and their corresponding I-V characteristics. In figure (a) cell A-B where porous ZnO was deposited onto the ITO substrate and used without annealing, cell C-F where a thin layer of ZnO (collected from the system into ethanol) was spray coated on ITO, this spray coated thin film was annealed at 300 ^oC (C-D) and not annealed (E-F) before depositing porous ZnO film. Dotted line in (a) shows illuminated curve for device F. In figure (b) cell G-I where porous film was deposited onto FTO and annealed at 500 ^oC and cell J-L where a spray coated thin film of ZnO (like cell C-F) deposited and annealed at 500 ^oC before porous ZnO deposition.

One of the main issues observed during the fabrication of these devices was the poor adhesion of the ZnO layer onto the ITO surface. This eventually contributed to disrupt the layer uniformity while $MAPbI_3$ spin coating. To address this issue, spray coating of $MAPbI_3$ was also tested.

Here, ETL was deposited by two process: first, ZnO film was directly deposited onto ITO (figure 5.16a A-B) and second, a thin layer of ZnO NPs were spray coated on ITO, which were collected from the system directly into ethanol, before porous ZnO deposition (cell C-F and J-L) to promote better compact layer. This spray coated ZnO layer was annealed at 300 ^{o}C (figure 5.16a C,D) and 500 ^{o}C (figure 5.16b J,K,L) before porous ZnO deposition to improve the adhesion and compactness of the layer. This time palladium (Pd) was used as metal contact. However, no change was observed in the I-V characteristics than spin coated devices. These devices were also prone to shunting as can be seen in figure 5.16a,b.

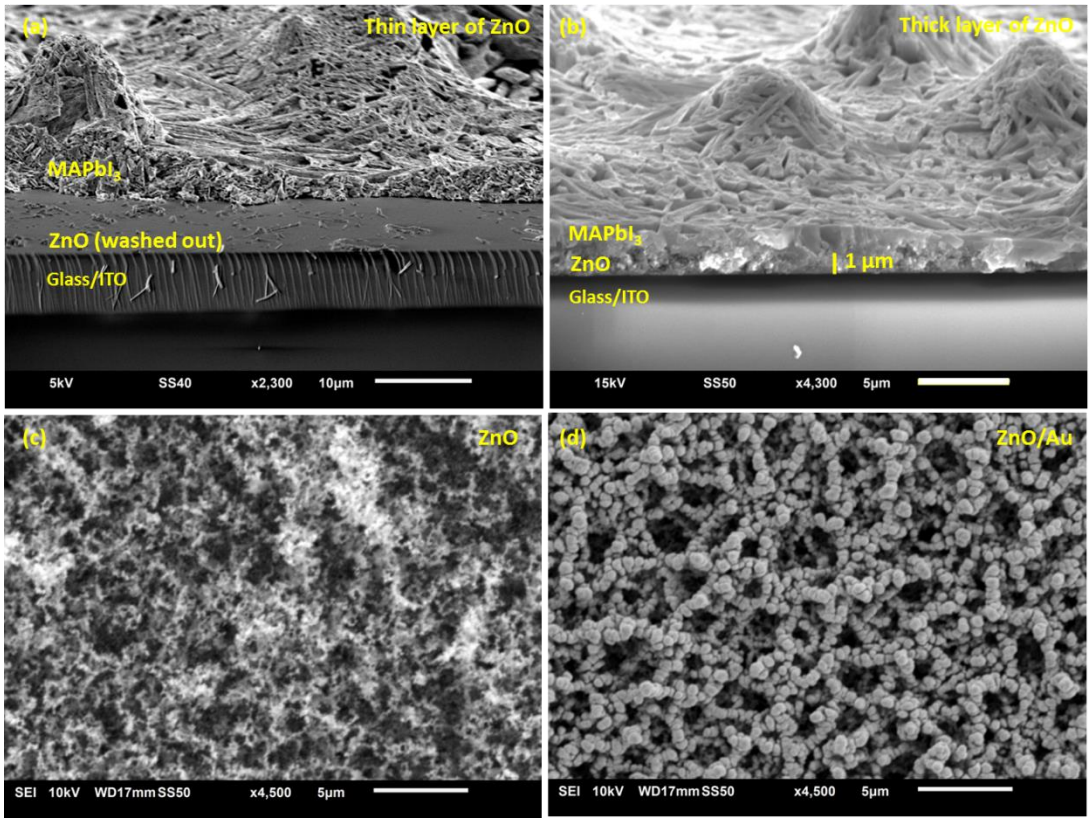

Figure 5.17: (a) SEM image of Glass/ITO/thin ZnO (washed out in process)/ MAPbI3 (b) Glass/ITO/ thick ZnO layer / MAPbI3 (c) Porous ZnO and (d) Au/ZnO.

These attempts of device fabrication identified several issues with the device fabrication and resulting performance. However, several options are possible to

improve the fabrication process. As a first attempt to device fabrication using atmospheric pressure plasma deposition, this was indeed encouraging. To understand better how and what to improve, we have carried out additional analyses of the ZnO/$MAPbI_3$ film.

The effect of the ZnO film thickness is studied by recording SEM before and after $MAPbI_3$ deposition. XRD of $MAPbI_3$ and ZnO/ $MAPbI_3$ is also measured to see the effect of ZnO layer on the crystallization of $MAPbI_3$. It can be seen in figure 5.17a that when ZnO thickness is in the order of 10-15 μm, after $MAPbI_3$ deposition, it wasn't seen onto the substrate which suggest that attempt of perovskite deposition affected the ZnO porous film intactness onto the substrate. We therefore increased the thickness of the porous ZnO film to ~82 μm (figure 5.14b), which it was reduced to ~1μm (figure 5.17b) after depositing the $MAPbI_3$ layer. These SEM images conclude that the perovskite deposition step reduces the ZnO layer significantly, which also complicate the control of the ETL thickness.

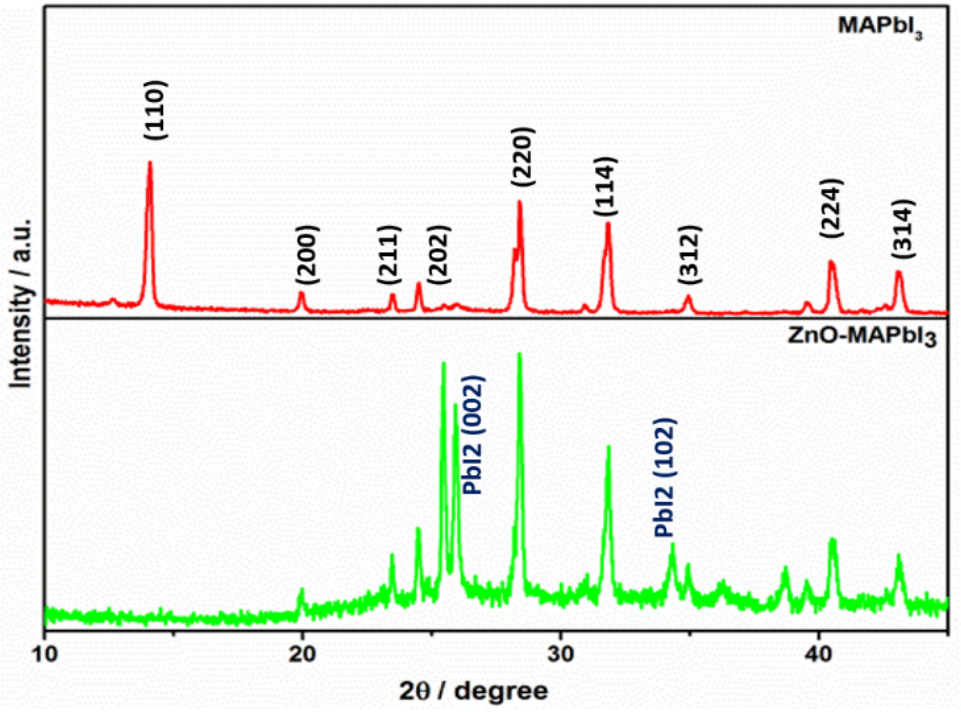

Figure 5.18: XRD of $MAPbI_3$ and ZnO deposited $MAPbI_3$ films where ZnO-$MAPbI_3$ clearly shows PbI_2 (002) and (102) plane peak and $MAPbI_3$ most intense plane (110) peak also disappeared.

Another important feature is represented by the surface topography in part determined by the porosity of this ZnO layer (figure 5.17c). The surface topography can be made

clearer by sputtering gold onto the ZnO layer as shown in figure 5.17d. After gold deposition, large pores can be seen clearly in the film. This surface might have contributed to the formation of pillar-like structures and may be responsible for the degradation or improper crystallization of the perovskite. Poor crystallization was confirmed by XRD of $MAPbI_3$ and ZnO/$MAPbI_3$ as shown in figure 5.18. It can be see clearly that the most prominent peaks of $MAPbI_3$ are missing and PbI_2 peaks are instead observed in the ZnO- $MAPbI_3$ spectrum. Previously, the origin of the thermal instability observed in perovskite solar cells fabricated using ZnO electron-transport layers. The basic nature of the ZnO surface leads to deprotonation of the methylammonium cation, leading to loss of methylamine and the formation of PbI_2.[49]

This suggests that overall different aspects need to be addressed before this ZnO film deposition method can be used for perovskite devices. In our observations, we can make a note that this type of porous ZnO is not a good transport layer for these types of perovskite devices even after annealing because of the high porosity.

In another attempt, porous ZnO layer was used as a transport layer for a quantum dot (QD) solar cell, specifically nitrogen-doped carbon dots (NC-QDs) were used as absorber. ITO and Al are used as electrodes and the band alignment of the materials can be seen in figure 5.19.

NC-QDs were synthesised according to a procedure previously published in the Darragh *et al.* paper.[50] The ETL was deposited directly onto ITO-coated glass substrates and the NC-QDs were subsequently deposited by spray coating using an atomizer (Sonozap Ultra Sonic Atomizer) operating at a power of 5 W. 5 mL of NC-QD solution was loaded into a syringe which is connected to a pump. The flow rate of 0.15 mL/min was used through the atomizer. The distance between the atomizer tip and substrate was 10 cm. The substrate was on a hotplate at 170 °C throughout deposition and left for 10 minutes after deposition.

Aluminium contacts were deposited using a plasma-assisted magnetron sputtering. The plasma was produced at 317 V and 0.15 A. Deposition was carried out for 50 minutes. The illuminated I-V characterization has shown 0.00114% device efficiency with 0.88 V open circuit voltage and 12% fill factor. However, also in this case, while this first attempt demonstrates fabrication capability, substantial more work is required to understand the device issues and understand the optimum parameters such as film thickness, temperature etc.

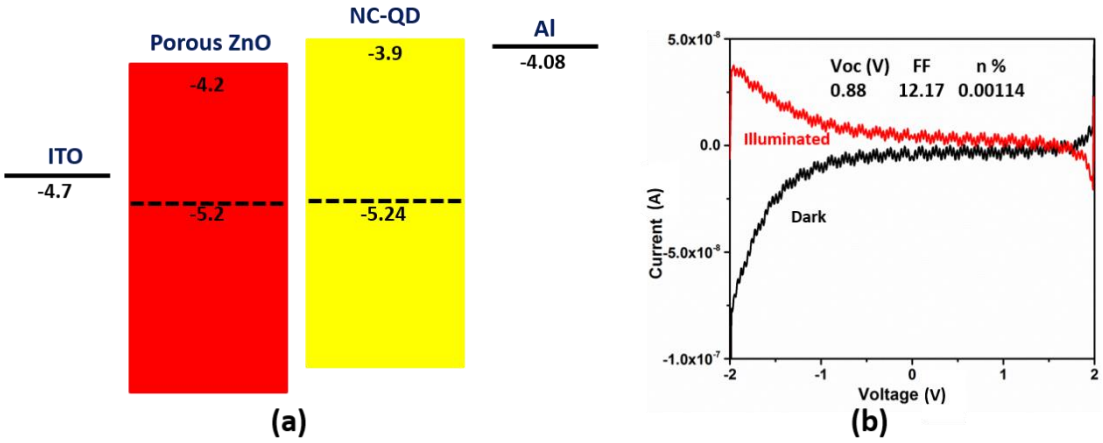

Figure 5.19: a) non-equilibrated band diagram of ITO/Porous ZnO/ NC-QD/Al device architecture and (b) I-V measurement in dark and illumination, showing V_{oc}, Fill factor (FF) and efficiency (n%).

5.4 Synthesis of hydroxyl passivated ZnO quantum dots

5.4.1 Experimental parameters

The same system is used (figure 5.1 where wire tip position was aligned 2 mm below the powered electrode. The plasma was first ignited with He gas and subsequently Ar gas was used for synthesis. The effect of different values of gas flow and applied power has been studied (table 2). Synthesis time was kept constant to two minutes for all synthesis conditions.

Table 9: Experimental parameters tested to understand synthesized structure to produce quantum dots.

Gas Flow	100 sccm	150 sccm	200 sccm
Power (W)	20	20	20
	30	30	30
	40	40	40
	50	50	50

A survey SEM analysis was carried out for all the samples to identify the favourable deposition condition for quantum dots and can be seen in figure 5.20. At 20 W power, bigger size particles ~ 5 µm size were produced. Similar trend was observed for 30 W power at 100 sccm (5.20 d) and 200 sccm (5.20 f) and 40 W at 100 sccm (5.20 g). At 50 W, porous complex structures were produced for all flow rates (5.20 j-l). Figure 5.20h-i were found to produce a more uniform, repeatable and reliable deposition.

Specifically, synthesis at 40 W and 150 sccm gas flow rate produced QDs as will be shown here to follow.

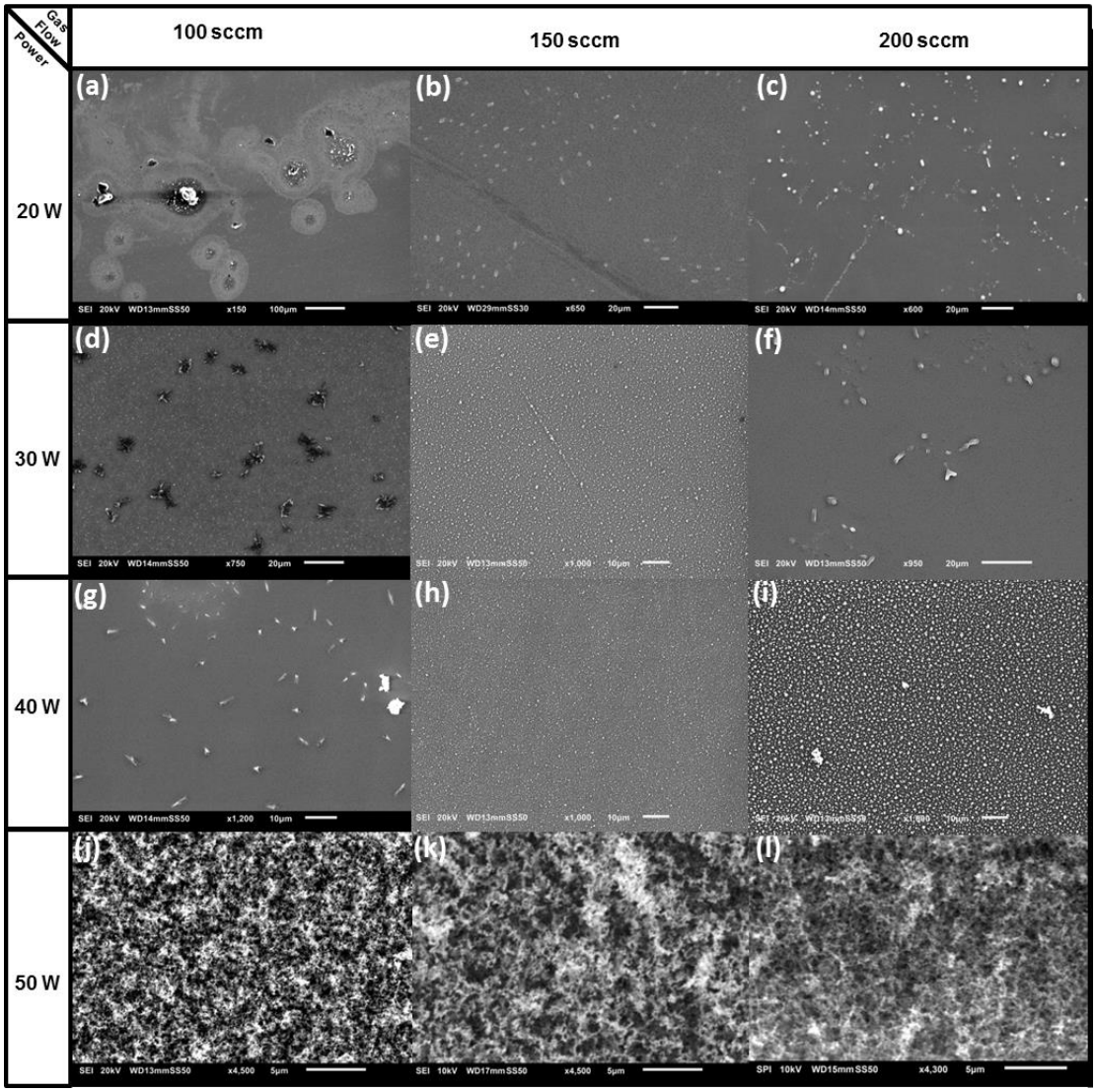

Figure 5.20: SEM images of ZnO synthesis on different gas flow (100-200 sccm) and power (20-50 W).

5.4.2 Material Characterization

A typical SEM image of the ZnO QDs deposited on a silicon substrate is shown in figure 5.21, which shows relatively good uniformity of the film over a micrometer range. Of course, the resolution of the SEM is not enough to identify the QDs and the morphology observed in figure 5.21 is due to agglomerated ZnO QDs when deposited directly on a substrate.

TEM and HRTEM were performed by collecting the sample in ethanol and drop-casting on carbon-coated gold grids. TEM images have revealed the crystalline nature of the sample as shown in figure 5.22. The inter-planar spacing was calculated and

found to be 0.247 nm and 0.193 nm which is a good match with (101) and (102) planes of wurtzite ZnO (figure 5.22b), respectively. ZnO planes (100), (102) and (110) can also be observed in the SAED pattern in figure 5.22c. The histogram in figure 5.22d shows the size distribution of the QDs with mean diameter of 1.9 nm.

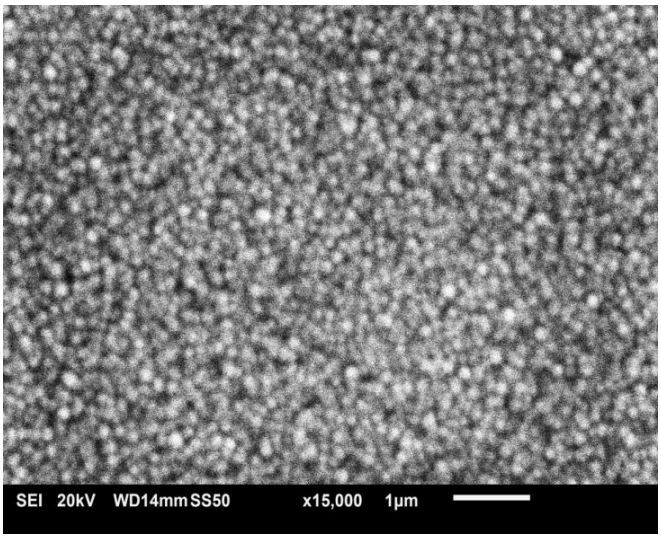

Figure 5.21: Scanning electron microscope image of particle deposition at 40 W with 150 sccm of Ar flow.

The ZnO QDs were deposited on a silicon substrate to form a film and to identify the crystallinity by XRD. XRD analysis is shown in figure 5.23a. The diffraction peak at scattering angle (2θ) 31.77°, 34.4°, 36.27°, 47.49° and 56.25° corresponds to (100), (002), (101), 102) and (110) crystalline planes of ZnO, respectively. These values match with the wurtzite ZnO structure (JCPDS: 08-0075).

Sample was prepared by depositing ZnO QD on silicon substrate. FTIR measurements are performed in nitrogen environment and can be seen in figure 5.23b. Four peaks are observed at 925 cm^{-1}, 1410 cm^{-1}, 1640 cm^{-1} and 3480 cm^{-1} in this graph. The broad band in the range of 3200-3700 cm^{-1} is assigned to stretching vibration of OH.[66–68] Non-bonding OH stretching appears at higher frequency near 3600 cm^{-1} while inter-molecular hydrogen bonding shifts the peak to lower frequency near 3550-3200 cm^{-1}.[68] Bending vibration of OH can be seen at 1395-1440 cm^{-1} and 910-950 cm^{-1}.[68,69] Peaks at 925 cm^{-1}, 1410 cm^{-1} and 3480 cm^{-1} correspond to OH bending and stretching vibration. The inter-molecular hydrogen bonding between OH molecules suggests that OH is abundant.[68] The small peak at 1640 cm^{-1} corresponds to OH vibration in H_2O.[68,70] Specific ZnO-related peaks (~436-529 cm^{-1}) can be only observed in part as these were just outside the available range. We should note that the OH-related peaks

at 925 cm^{-1} and 1410 cm^{-1} are not generally observed for adsorbed water[71] and therefore suggest the presence of OH-terminations at the ZnO QD surfaces (see further below for more evidence).

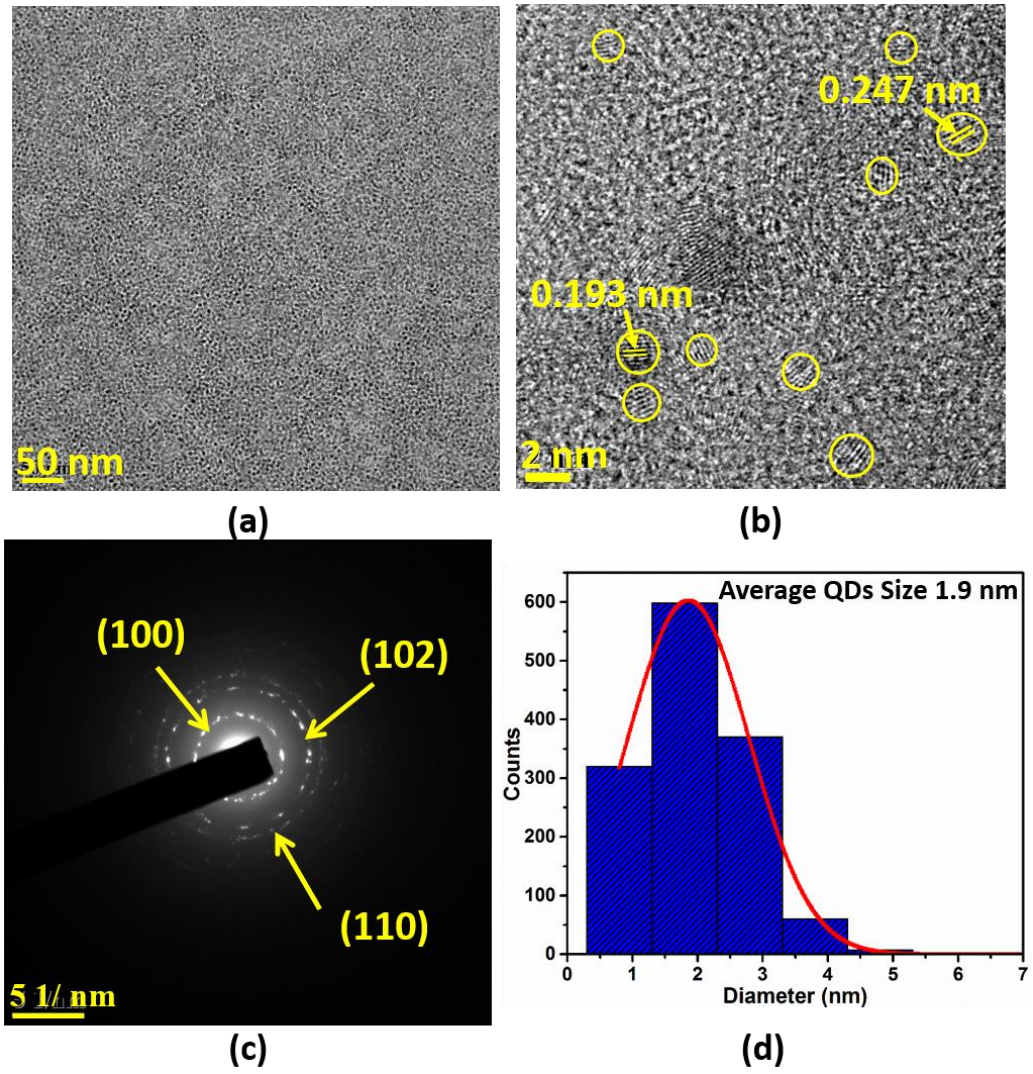

Figure 5.22: (a) and (b) Transmission electron microscope images of ZnO QD, (c) SAED pattern and (d) Particle size analysis.

XPS was performed to analyse further the chemical composition and oxidation state of ZnO. ZnO film was deposited onto silicon to perform XPS. XPS survey shows Zn and O peaks as shown in figure 5.24a and confirms ZnO formation. Binding energy at 1021.94 eV and 1045.14 eV are attributed to binding energy of $Zn_{2p3/2}$ and $Zn_{2p1/2}$ electrons as shown in figure 5.24b. The BE difference between these two peaks is 23.2 eV, which is close to that reported in the literature (23.1 eV) and confirms that Zn is in the Zn^{+2} state as expected for ZnO.[13–15]

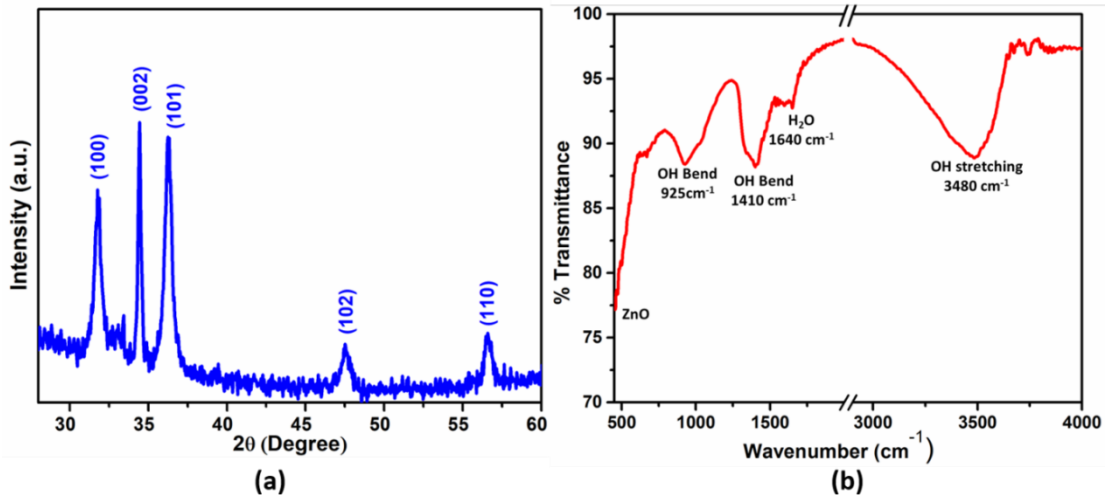

figure 5.23: (a) X-ray diffraction and (b) FTIR spectrum of ZnO quantum dots where XRD confirms wurtzite crystalline nature of ZnO and FTIR shows -OH prone ZnO QDs.

In the XPS spectra, the asymmetric O 1s peak was observed with a shoulder at higher binding energy. O 1s spectrum was fitted by two peaks centred at 531.74 eV and 532.88 eV (Figure 5.24c). The peak in the range of 529-530.5 eV corresponds to O^{-2} in Zn-O binding. However, in our sample we do not observe any peak in this range. The first peak at 531.74 eV can be ascribed to O-H groups, which is consistent with a strong presence of hydroxyl groups detected by FTIR measurements. The higher energy peak at 532.88 eV can be attributed to adsorbed oxygen in H_2O or $-CO_3$ species.[16,17] While the $Zn_{2p3/2}$ and $Zn_{2p1/2}$ peaks clearly demonstrate the chemical composition of ZnO, we do not observe a clear contribution from Zn-O bonds in the O 1s. However, it is possible that the peak measured at 531.74 is in fact a combination of OH as well as Zn-O, with the latter that may appear shifted due to the small size of the QDs or much lower in intensity due to the volume-to-surface ratio.

To confirm further the chemical state of the ZnO QDs, zinc LMM Auger spectrum is also recorded as shown in figure 5.24d. Auger peaks of metallic zinc, zinc hydroxide and zinc oxide appear at 992 eV, 986.5 eV and 988.6 eV respectively. Our recorded value at 988.9 eV is in very good agreement with the literature value for ZnO at 988.6 eV.[72] This supports the formation of ZnO and where the Auger signal can be considered more reliable than XPS due to the interrogation of deeper electronic states.

Overall the combined material characterization of the ZnO QDs confirms the crystal structure (HRTEM, SAED, XRD) and chemical composition (FTIR, XPS). Moreover, XPS and FTIR analysis indicate the strong presence of bonded OH groups which are

not to be assigned to adsorbed moisture and therefore strongly support the formation of OH-terminations. This will be further supported by PL measurements.

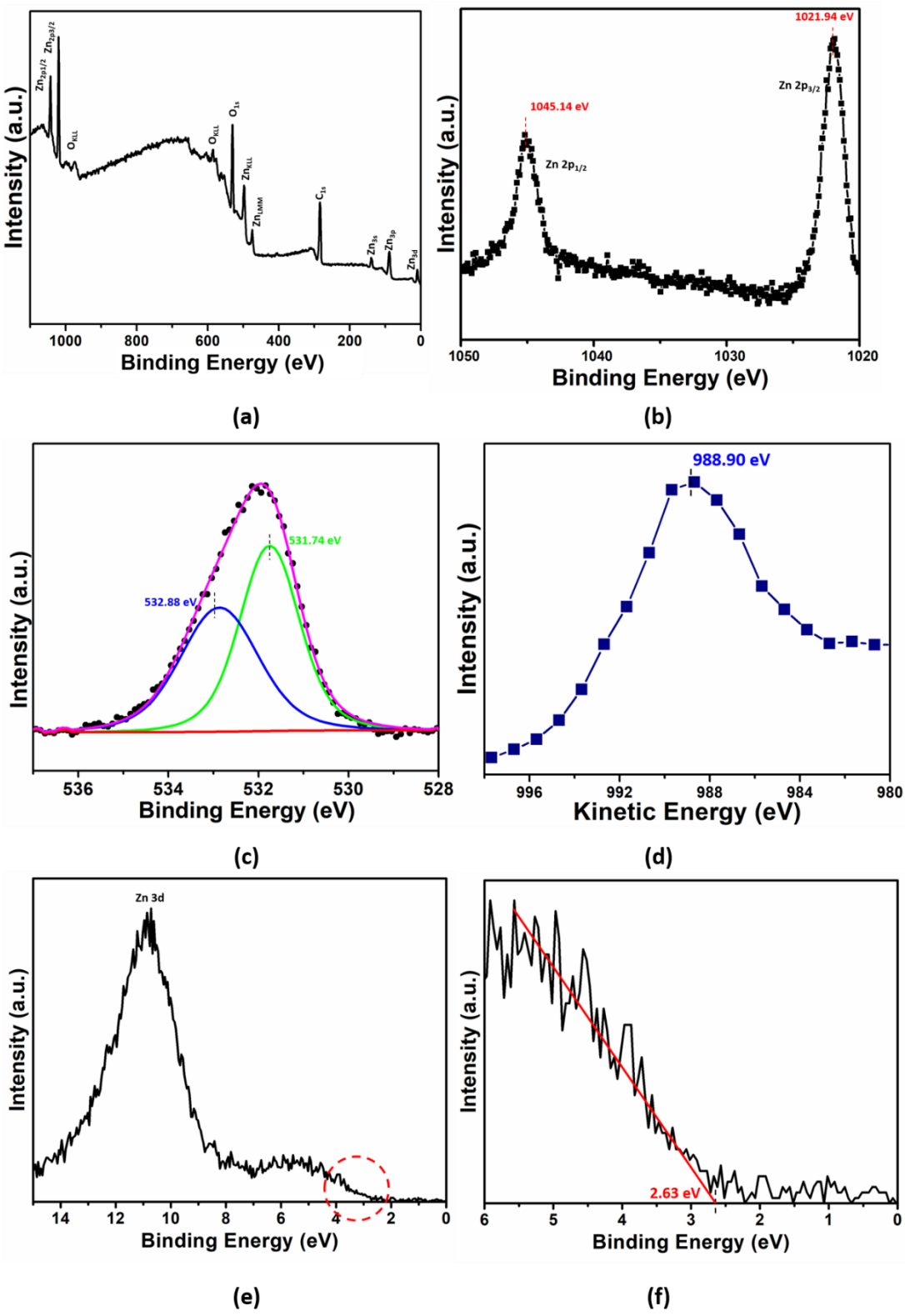

Figure 5.24: (a) X-ray photoelectron spectrum (XPS) survey scan of ZnO; (b) Zn 2p; (c) O 1s; (d) shows Zn LMM Auger Electron Spectra; (e) onset of the XPS spectra of ZnO and (f) shows Ef –EVBM.

5.4.3 Optical properties and energy band diagram:

The UV-Vis transmission spectrum is recorded from ZnO QDs in ethanol colloids as shown in figure 5.25a. The absorption features of the direct bandgap semiconductors (such as ZnO) can be described from the following relation[18]:

$$(\alpha h\nu)^2 \propto (h\nu - E_g) \tag{6}$$

where α is the absorption coefficient, $h\nu$ is the photon energy and E_g is the bandgap.

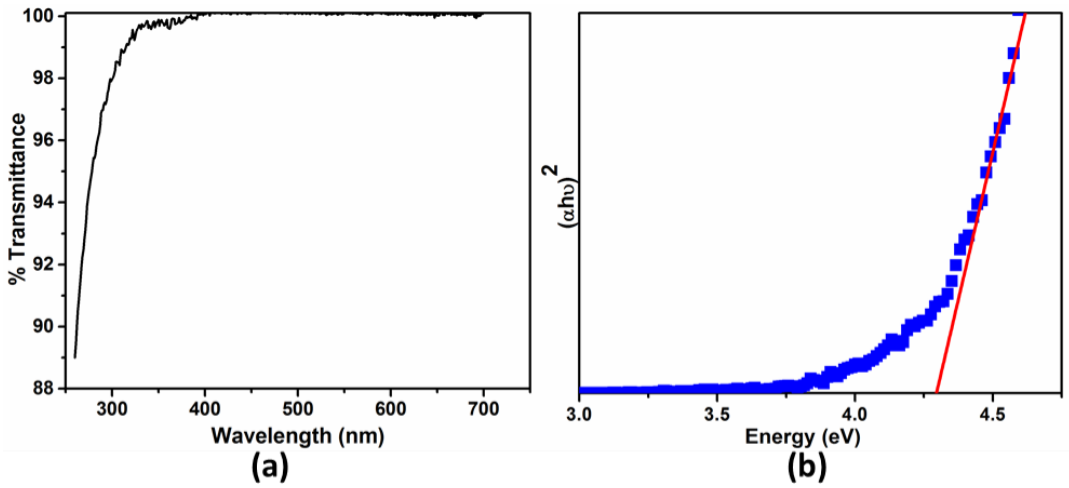

Figure 5.25: Transmittance spectrum of ZnO QDs and in inset shows Tauc plot and band gap of ZnO QDs.

Figure 5.25b reports the Tauc plot according to equation (6). The linear region of the plot supports the direct nature of the bandgap and the intercept gives a bandgap of 4.27 eV. The relationship between the bandgap and particle size can be estimated according to various theoretical models.[73–75] Changes in the bandgap follows an exponential trend and can be seen for QDs with diameters below 4 nm.[75] Our ZnO QDs are therefore expected to be in the confinement regime and having a large bandgap.

Here, we have used the effective mass model for spherical particles with coulombic interaction.[76,77] The theoretical value of the bandgap was calculated using the mean diameter (1.9 nm) that we previously measured and used in the following equation:

$$E^* = E_g^{Bulk} + \frac{\hbar^2\pi^2}{2er^2}\left(\frac{1}{m_e m_o} + \frac{1}{m_h m_o}\right) - \frac{1.8e}{4\pi\varepsilon\varepsilon_0 r}$$

(7) where $\hbar$ represents Plank's constant divided by 2π, r is the particle radius, m_o is the mass of free electron, m_e and m_h is the effective mass of electrons and holes (for ZnO, m_e = 0.29 and m_h = 1.21),[78] ε is the relative permittivity of ZnO (5.7), ε_o is permittivity of free space. The theoretical calculated bandgap is 4.6 eV. The difference

between theoretical and experimental values can be due to a range of factors where theoretical calculations generally assume chemically unaltered surfaces with respect to the QD core.[75] However, experimentally, surface terminations are unavoidable (such as -OH) and are known to drastically affect the properties of quantum confined systems.[79]

The difference between the Fermi level (E_f) and valance band maximum (E_{VBM}) was evaluated from the XPS spectra shown in figure 5.24e, f. This was done by extrapolating the leading edge of the XPS spectra to the baseline as shown in the figure 5.24f. This produced a value of 2.63 eV (E_f - E_{VBM}).

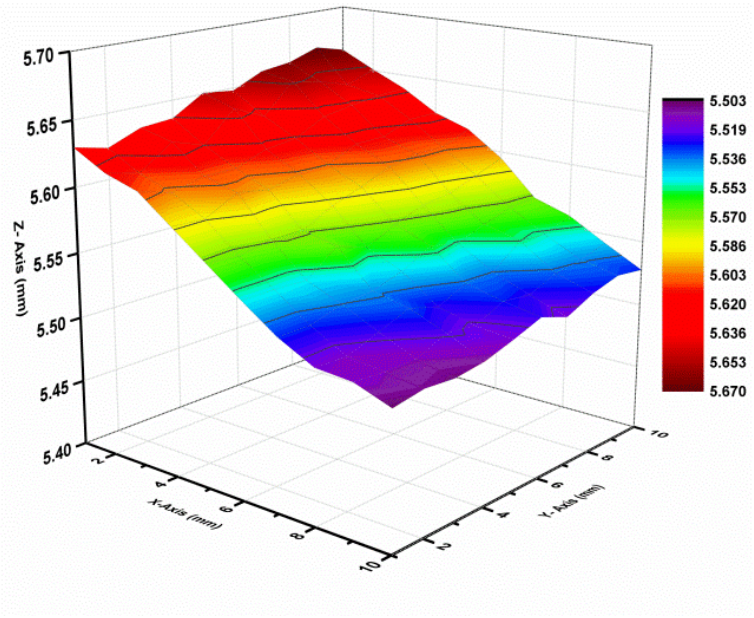

Figure 5.26: Fermi level measurement of ZnO QDs by scanning Kelvin probe on ITO substrate.

The samples were deposited on glass substrates coated with indium-doped tin-oxide to carry out Kelvin probe measurements, to find out Fermi level of the films. The Fermi level was then obtained by measuring the contact potential difference (CPD) between the ZnO sample and a reference electrode. The calibration of the system was carried out by measuring the work function (Φ) of a known gold reference (5.1 eV). On this basis, the Fermi level of our ZnO QDs was measured to be -5.57 eV as shown in figure 5.26, which is more negative than the Fermi level of bulk ZnO (-5.2 eV).[25] This difference is the result of changes in charge distribution and electric environment in quantum confined systems.[80,81]

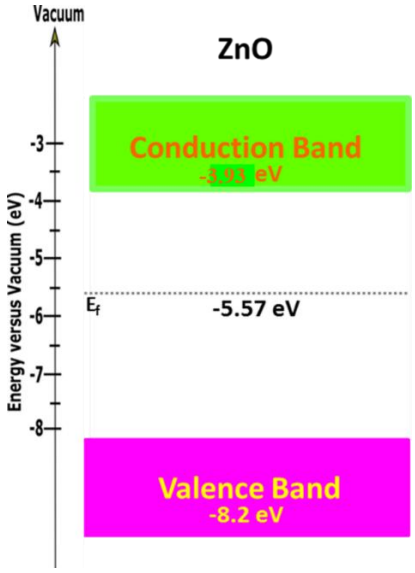

Figure 5.27: Estimated energy band diagram of ZnO by XPS, Kelvin prob and bandgap measurements.

The complete band structure of ZnO is depicted in figure 5.27. The position of the valence band edge was calculated from the XPS results (E_f - E_{VBM} = 2.63 eV) and using the Fermi level value from Kelvin probe measurements, i.e. $E_{VBM} = E_f$ – 2.63 eV = -5.57 eV – 2.63 eV = -8.2eV. The corresponding conduction band edge was also found adding the value of the measured bandgap energy to the valence band edge, yielding a value of -3.93 eV.

5.4.4 Impact of hydroxyl passivation on photoluminescence property of ZnO

ZnO QDs were collected in ethanol to perform photoluminescence. We have recorded emission spectra of ZnO QDs at UV excitation wavelength 230 nm as shown in figure 5.28a, which exhibits emission only in the UV. ZnO generally shows PL in the UV and visible region. Figure 5.28b is a schematic diagram depicting the emission behaviour in three systems, bulk ZnO, ZnO QDs and hydroxyl passivated ZnO. Blue and green arrows show the origin of UV and visible emissions, respectively. Particularly, in ZnO, visible emission generally originate from different zinc and oxygen defects.[82–84] Visible emission is described in terms of recombination of conduction band electron with deep-trap holes or recombination of electron present in near-conduction band traps with holes in the valance band.[19] Emission behaviour in QDs largely depends on the size of the QDs and quantum confinement regime. As the particle size reduces, the intensity of the UV emission generally increases without affecting the visible emission as shown in figure 5.28b, ZnO QDs.[85] Our PL spectrum

shows only UV emission without any peak in the visible range (figure 5.28a-b, OH-ZnO QDs) that again corroborates defect-free ZnO QDs.

The main PL emission peak close to 334 nm and the corresponding Stokes' shift (i.e. the difference between the onset of the absorption and the maximum of the PL emission spectra) is > 200 meV. Experimentally, there have been many reports on significant Stokes' shifts in many quantum dots e.g. CdSe,[86] PbS[87] etc. Stokes' shift varying from 60 meV to 180 meV has been observed in ZnO nanodots for diameters decreasing from 14.5 nm to 6.5 nm, so that the shift observed in our measurements is consistent with our mean diameter of 1.9 nm. The reason for a higher Stokes shift is related to enhancement of exciton localization in smaller particles.[88]

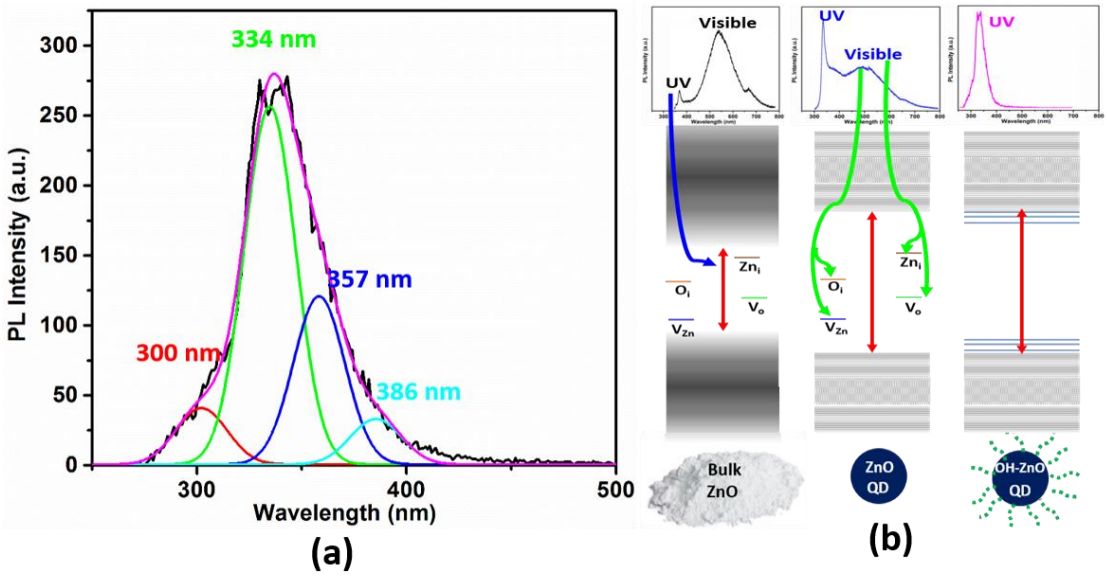

Figure 5.28: Photoluminescence spectra of ZnO QD shows a) emission at 230 nm excitation wavelength and b) A comparative representation of band structure in bulk ZnO, ZnO QD and hydroxide passivated ZnO QD.

However, deconvolution of the PL emission spectrum shows different wavelength emission at 300 nm, 334 nm, 357 nm and 386 nm. A small peak at 300 nm (4.13 eV) is related to excitonic emission. A prominent peak is observed at 334 nm (3.71 eV) with two other peaks at 357 nm (3.47 eV) and 386 nm (3.21 eV) which are red-shifted with respect to the excitonic emission.

The origin of the peak at 334 nm can be the outcome of ionized acceptor-exciton complex.[62] Theoretically, Fonoberov *et al.* have shown that when an ionized acceptor-exciton complex is present in the system, the position of the UV peak is hundreds of

meV lower in energy than that for the confined exciton.[62] Another possibility is that the emission originate from exciton localization.[88]

The emission at 357 nm (3.47 eV) and 386 nm (3.21 eV) on the other hand could be due to the strong molecular interaction of OH with Zn surface defects which introduce extra bands close to the conduction/valence band edges as represented in figure 8b (OH-ZnO QDs). Furthermore, the strong interaction between empty Zn 3d, 4s and 4p molecular orbital and O lone-pair orbital of OH was observed in other reports where UV photoelectron spectroscopy results showed an increase of the emission in the area between the Zn 4s/O 2p and the Zn 3d band and a redistribution of the emission in the O 2p band was observed.[89,90]

Overall the PL analysis supports our material characterization where typical emission due to defects is not observed and where emission at 334 nm can be ascribed to OH-terminations, also consistent with our chemical analysis. This confirms the formation of defect-free OH-passivated ZnO QDs.

In some cases, reported in the literature,[56] OH was observed on the surface of ZnO QDs; however this was clearly due to adsorbed water as they could not confirm Zn-OH bonding. Furthermore, visible emission was still observed indicating that OH did not contribute to passivate surface defects. Because of the strong confinement and very small size of QDs, the surface is highly reactive because of many surface O- and Zn-based defects, which can also contribute to surface degradation and changes in the opto-electronic properties. Many different approaches have been used to passivate these surface defects to reduce the visible emission contribution.[54,55] However, these were generally post-synthesis methods. In our process, OH terminations are formed during synthesis which allows for the formation Zn-OH bonds within the plasma environment. The absence of any visible emission suggests the stabilization of surface defects, which is not the result of post-synthesis passivation.

5.4 Conclusion

Porous nanocrystalline ZnO films were synthesised and deposited by RF atmospheric pressure plasma in ambient conditions. Structural, chemical and optical properties confirm that the ZnO films to be stoichiometric with very low defect density. We have also carried out a complete experimental determination of the band energy diagram

which confirms the film to preserve the required and desired energetics expected from ZnO films.

The process and porous ZnO films were then used as transport layers in solar cells with $MAPbI_3$ and NC-QD active materials. Detailed SEM and XRD analysis show that the surface topography could represent a challenge in the application of the porous ZnO film $MAPbI_3$ while preliminary results show a more positive indication towards its use for QD-based devices. However, in general both the process and the material has shown positive aspects that suggest the potential future avenues for atmospheric pressure plasma to be integrated in solar cell fabrication. The control of the thickness/porosity, scalability and grain size are all aspects that would need to be investigated in detail with respect to the specific application in photovoltaics.

Later, a simplest method to synthesize hydroxyl-passivated ZnO QDs by non-thermal atmospheric pressure plasma was demonstrated which is unique and very simple in terms of managing precursors and its operation. Further, we investigated size and crystal structure by TEM and XRD to confirm wurtzite ZnO crystal structure. This is the smallest ZnO QDs produced so far with average diameter of 1.9 nm. Because of the sufficiently small size, a strong confinement effect is observed on the bandgap. The PL study reveals interesting aspects of these defect-free QDs where the emission spectra is limited to the UV region; this is the result of the introduction of energy states near to conduction and valence edge, which removes O- and Zn-based defects that would normally lead to deeper trap states. This observation is further supported with the FTIR and XPS analysis where the strong OH bonding on the surface is confirmed with intact ZnO core. This OH terminated ZnO QDs are stable in air over the period of more than 18 months. This again supports our claim of OH termination, because of the OH-bonding on the surface of the QDs do not migrate into the lattice structure and preserve their emission properties for very long time. This unique property can be promising for many emission related applications.

5.5 References

1. Jain, G., Macias-Montero, M., Velusamy, T., Maguire, P. & Mariotti, D. Porous zinc oxide nanocrystalline film deposition by atmospheric pressure plasma: Fabrication and energy band estimation. *Plasma Process. Polym.* **14,** 1–8 (2017).

2. Apurba Sinhamahapatra, Arnab Kanti Giri, Provas Pal, Sandip Kumar Pahari, H. C. B. and A. B. P. A rapid and green synthetic approach for hierarchically assembled porous ZnO nanoflakes with enhanced catalytic activity. *J.Mater.Chem.* **22,** 17227–17235 (2012).

3. Khorsand Zak, A., Abd. Majid, W. H., Abrishami, M. E. & Yousefi, R. X-ray analysis of ZnO nanoparticles by Williamson-Hall and size-strain plot methods. *Solid State Sci.* **13,** 251–256 (2011).

4. Wang, L., Zhang, X. & Chen, K. Nano-scaled hierarchical porous ZnO nanostructures : fabrication and application in dye-sensitized solar cells 3. 4860–4864 (2013). doi:10.1039/c3ce40134k

5. Wang, H.-J. *et al.* Porous zinc oxide films: Controlled synthesis, cytotoxicity and photocatalytic activity. *Chem. Eng. J.* **178,** 8–14 (2011).

6. Zhang, J. *et al.* Hierarchically Porous ZnO Architectures for Gas Sensor Application & DESIGN 2009. 5–10 (2009).

7. Becheri, A., Dürr, M., Lo Nostro, P. & Baglioni, P. Synthesis and characterization of zinc oxide nanoparticles: Application to textiles as UV-absorbers. *J. Nanoparticle Res.* **10,** 679–689 (2008).

8. Habibi, M. H. & Rahmati, M. H. Fabrication and characterization of ZnO@CdS core-shell nanostructure using acetate precursors: XRD, FESEM, DRS, FTIR studies and effects of cadmium ion concentration on band gap. *Spectrochim. Acta - Part A Mol. Biomol. Spectrosc.* **133,** 13–18 (2014).

9. Singh, J. *et al.* Synthesis, band-gap tuning, structural and optical investigations of Mg doped ZnO nanowires. *CrystEngComm* **14,** 5898 (2012).

10. Šarić, A., Musić, S. & Ivanda, M. Varying the microstructural properties of ZnO

particles using different synthesis routes. *J. Mol. Struct.* **993,** 219–224 (2011).

11. Shi, L., Bao, K., Cao, J. & Qian, Y. Sunlight-assisted fabrication of a hierarchical ZnO nanorod array structure. *CrystEngComm* **11,** 2009 (2009).

12. Lo, S. S. & Huang, D. Morphological variation and Raman spectroscopy of Zno hollow microspheres prepared by a chemical colloidal process. *Langmuir* **26,** 6762–6766 (2010).

13. Ramgir, N. S. *et al.* ZnO multipods, submicron wires, and spherical structures and their unique field emission behavior. *J. Phys. Chem. B* **110,** 18236–18242 (2006).

14. Wang, M. *et al.* N Doping to ZnO Nanorods for Photoelectrochemical Water Splitting under Visible Light: Engineered Impurity Distribution and Terraced Band Structure. *Sci. Rep.* **5,** 12925 (2015).

15. Alshammari, A. S. *et al.* Visible-light photocatalysis on C-doped ZnO derived from polymer-assisted pyrolysis. *RSC Adv.* **5,** 27690–27698 (2015).

16. Wang, H., Baek, S., Song, J., Lee, J. & Lim, S. Microstructural and optical characteristics of solution-grown Ga-doped ZnO nanorod arrays. *Nanotechnology* **19,** 075607 (2008).

17. Singh, V. P. & Rath, C. Passivation of native defects of ZnO by doping Mg detected through various spectroscopic techniques. *RSC Adv.* **5,** 44390–44397 (2015).

18. Pesika, N. S., Stebe, K. J. & Searson, P. C. Determination of the particle size distribution of quantum nanocrystals from absorbance spectra. *Adv. Mater.* **15,** 1289–1291 (2003).

19. Xiong, H.-M. Photoluminescent ZnO nanoparticles modified by polymers. *J. Mater. Chem.* **20,** 4251 (2010).

20. Das, D. & Mondal, P. Photoluminescence phenomena prevailing in c-axis oriented intrinsic ZnO thin films prepared by RF magnetron sputtering. *RSC Adv.* **4,** 35735 (2014).

21. Schmidt-Mende, L. & MacManus-Driscoll, J. L. ZnO - nanostructures, defects, and devices. *Mater. Today* **10,** 40–48 (2007).

22. Han, J., Mantas, P. Q. & Senos, A. M. R. Defect chemistry and electrical characteristics of undoped and Mn-doped ZnO. *J. Eur. Ceram. Soc.* **22,** 49–59 (2002).

23. Kumari, C., Pandey, A. & Dixit, A. Zn interstitial defects and their contribution as efficient light blue emitters in Zn rich ZnO thin films. *J. Alloys Compd.* **735,** 2318–2323 (2018).

24. Kumar, V. *et al.* Origin of the red emission in zinc oxide nanophosphors. *Mater. Lett.* **101,** 57–60 (2013).

25. Ghosh, S. *et al.* ZnO/Ag nanohybrid: synthesis, characterization, synergistic antibacterial activity and its mechanism. *RSC Adv.* **2,** 930 (2012).

26. Kyaw, a K. K. *et al.* Top-illuminated dye-sensitized solar cells with a room-temperature-processed ZnO photoanode on metal substrates and a Pt-coated Ga-doped ZnO counter electrode. *J. Phys. D. Appl. Phys.* **44,** 045102 (2011).

27. Wang, X., Summers, C. J. & Wang, Z. L. Self-attraction among aligned Au/ZnO nanorods under electron beam. *Appl. Phys. Lett.* **86,** 2004–2006 (2005).

28. Bai, X., Wang, E. G., Gao, P. & Wang, Z. L. Measuring the work function at a nanobelt tip and at a nanoparticle surface. *Nano Lett.* **3,** 1147–1150 (2003).

29. Luther, J. M. *et al.* Stability assessment on a 3% bilayer PbS/ZnO quantum dot heterojunction solar cell. *Adv. Mater.* **22,** 3704–3707 (2010).

30. Chang, L. Y., Lunt, R. R., Brown, P. R., Bulovi??, V. & Bawendi, M. G. Low-temperature solution-processed solar cells based on PbS colloidal quantum dot/CdS heterojunctions. *Nano Lett.* **13,** 994–999 (2013).

31. O'Regan, B. C. *et al.* Optoelectronic studies of methylammonium lead iodide perovskite solar cells with mesoporous TiO<inf>2</inf>: Separation of electronic and chemical charge storage, understanding two recombination lifetimes, and the evolution of band offsets during J - V hy. *J. Am. Chem. Soc.* **137,** 5087–5099 (2015).

32. Barkhouse, D. A. R. *et al.* Depleted bulk heterojunction colloidal quantum dot photovoltaics. *Adv. Mater.* **23,** 3134–3138 (2011).

33. Gubbala, S., Chakrapani, V., Kumar, V. & Sunkara, M. K. Band-edge engineered hybrid structures for dye-sensitized solar cells based on SnO2 nanowires. *Adv. Funct. Mater.* **18,** 2411–2418 (2008).

34. Hendry, E., Koeberg, M., O'Regan, B. & Bonn, M. Local field effects on electron transport in nanostructured TiO2revealed by terahertz spectroscopy. *Nano Lett.* **6,** 755–759 (2006).

35. Roldán-Carmona, C. *et al.* Flexible high efficiency perovskite solar cells. *Energy Environ. Sci.* **7,** 994 (2014).

36. Beiley, Z. M. M. & McGehee, M. D. D. Modeling low cost hybrid tandem photovoltaics with the potential for efficiencies exceeding 20%. *Energy Environ. Sci.* **5,** 9173 (2012).

37. Özgür, Ü. *et al.* A comprehensive review of ZnO materials and devices. *J. Appl. Phys.* **98,** 1–103 (2005).

38. Chen, L.-C. & Tseng, Z.-L. ZnO-Based Electron Transporting Layer for Perovskite Solar Cells. *Nanostructured Sol. Cells* (2017). doi:10.5772/65056

39. Bae, H. S., Yoon, M. H., Kim, J. H. & Im, S. Photodetecting properties of ZnO-based thin-film transistors. *Appl. Phys. Lett.* **83,** 5313–5315 (2003).

40. Tang, H., Prasad, K., Sanjinès, R., Schmid, P. E. & Lévy, F. Electrical and optical properties of TiO $_2$ anatase thin films. *J. Appl. Phys.* **75,** 2042–2047 (1994).

41. Eames, C. *et al.* Ionic transport in hybrid lead iodide perovskite solar cells. *Nat. Commun.* **6,** 2–9 (2015).

42. Kumar, M. H. *et al.* Flexible, low-temperature, solution processed ZnO-based perovskite solid state solar cells. *Chem. Commun.* **49,** 11089 (2013).

43. Zhang, J., Barboux, P. & Pauporté, T. Electrochemical design of nanostructured ZnO charge carrier layers for efficient solid-state perovskite-sensitized solar

cells. *Adv. Energy Mater.* **4,** 1–8 (2014).

44. Son, D.-Y., Im, J.-H., Kim, H.-S. & Park, N.-G. 11% Efficient Perovskite Solar Cell Based on ZnO Nanorods: An Effective Charge Collection System. *J. Phys. Chem. C* **118,** 16567–16573 (2014).

45. Chandiran, A. K. *et al.* Quantum-confined ZnO nanoshell photoanodes for mesoscopic solar cells. *Nano Lett.* **14,** 1190–1195 (2014).

46. Mahmood, K., Swain, B. S. & Amassian, A. 16.1% Efficient Hysteresis-Free Mesostructured Perovskite Solar Cells Based on Synergistically Improved ZnO Nanorod Arrays. *Adv. Energy Mater.* **5,** 1–11 (2015).

47. Rocks, C., Svrcek, V., Maguire, P. & Mariotti, D. Understanding surface chemistry during $MAPbI_3$ spray deposition and its effect on photovoltaic performance. *J. Mater. Chem. C* **5,** 902–916 (2017).

48. Li, G., Zhang, T. & Zhao, Y. Hydrochloric acid accelerated formation of planar $CH_3NH_3PbI_3$ perovskite with high humidity tolerance. *J. Mater. Chem. A* **3,** 19674–19678 (2015).

49. Yang, J., Siempelkamp, B. D., Mosconi, E., De Angelis, F. & Kelly, T. L. Origin of the Thermal Instability in $CH_3NH_3PbI_3$ Thin Films Deposited on ZnO. *Chem. Mater.* **27,** 4229–4236 (2015).

50. Carolan, D. *et al.* Environmentally friendly nitrogen-doped carbon quantum dots for next generation solar cells. *Sustain. Energy Fuels* **00,** 1–9 (2017).

51. Patra, M. K. *et al.* Synthesis of stable dispersion of ZnO quantum dots in aqueous medium showing visible emission from bluish green to yellow. *J. Lumin.* **129,** 320–324 (2009).

52. Johnston, K. *et al.* Identification of donor-related impurities in ZnO using photoluminescence and radiotracer techniques. *Phys. Rev. B - Condens. Matter Mater. Phys.* **73,** 1–7 (2006).

53. Fonoberov, V. A., Alim, K. A., Balandin, A. A., Xiu, F. & Liu, J. Photoluminescence investigation of the carrier recombination processes in ZnO quantum dots and nanocrystals. *Phys. Rev. B - Condens. Matter Mater. Phys.*

73, 1–9 (2006).

54. Guo, L. *et al.* Highly monodisperse polymer-capped ZnO nanoparticles: Preparation and optical properties. *Appl. Phys. Lett.* **76,** 2901 (2000).

55. Choy, W. C. H. *et al.* Photoluminescence and Electron Paramagnetic Resonance of ZnO Tetrapod Structures **. *Adv. Funct. Mater.* 856–864 (2004). doi:10.1002/adfm.200305082

56. Felbier, P. *et al.* Highly luminescent ZnO quantum dots made in a nonthermal plasma. *Adv. Funct. Mater.* **24,** 1988–1993 (2014).

57. Brookes, I. M., Muryn, C. A. & Thornton, G. Imaging water dissociation on TiO2(110). *Phys. Rev. Lett.* **87,** 266103–1–266103–4 (2001).

58. Schaub, R. *et al.* Oxygen vacancies as active sites for water dissociation on rutile TiO2(110). *Phys. Rev. Lett.* **87,** 266104–1–266104–4 (2001).

59. Kunat, M., Girol, S. G., Burghaus, U. & Wo, C. The Interaction of Water with the Oxygen-Terminated , Polar Surface of ZnO. 14350–14356 (2003). doi:10.1021/jp030675z

60. Fonoberov, V. A. & Balandin, A. A. Radiative lifetime of excitons in ZnO nanocrystals: The dead-layer effect. *Phys. Rev. B - Condens. Matter Mater. Phys.* **70,** 1–5 (2004).

61. Shu-Lin Zhang. *Raman Spectroscopy and its Application in Nanostructures*. (John wiley & sons, 2012). doi:10.1002/9781119961659

62. Fonoberov, V. A. & Balandin, A. A. Origin of ultraviolet photoluminescence in ZnO quantum dots: Confined excitons versus surface-bound impurity exciton complexes. *Appl. Phys. Lett.* **85,** 5971–5973 (2004).

63. Fonoberov, V. A. & Balandin, A. A. ZnO Quantum Dots: Physical Properties and Optoelectronic Applications. *J. Nanoelectron. Optoelectron.* **1,** 19–38 (2006).

64. Wang, N., Yang, Y. & Yang, G. Great blue-shift of luminescence of ZnO nanoparticle array constructed from ZnO quantum dots. *Nanoscale Res. Lett.* **6,**

338 (2011).

65. Gu, Y., Kuskovsky, I. L., Yin, M., O'Brien, S. & Neumark, G. F. Quantum confinement in ZnO nanorods. *Appl. Phys. Lett.* **85,** 3833–3835 (2004).

66. Thi, V. H. & Lee, B. Effective photocatalytic degradation of paracetamol using La-doped ZnO photocatalyst under visible light irradiation. *Mater. Res. Bull.* **96,** 171–182 (2017).

67. Pang, B. *et al.* Preparation and characterization of antibacterial paper coated with sodium lignosulfonate stabilized. *RSC Adv.* **6,** 9753–9759 (2016).

68. Mohan, J. *Organic Spectroscopy: Principles and Applications*. (Narosa Publishing House Pvt, 2004).

69. Williams, D. H. & Flemming, I. *Spectroscopy Methods In Organic Chemistry*. (McGraw-Hill Higher Education, 2008).

70. Nichols, A. Accounting for the species-dependence of the 3500 cm-1 H2Ot infrared molar absorptivity coefficient : Implications for hydrate .... (2017). doi:10.2138/am-2017-5952CCBY

71. Jain, G., Macias-Montero, M., Velusamy, T., Maguire, P. & Mariotti, D. Porous zinc oxide nanocrystalline film deposition by atmospheric pressure plasma: Fabrication and energy band estimation. *Plasma Process. Polym.* **14,** (2017).

72. Strohmeier, B. R. & Hercules, D. M. Characterization of the Interaction Zinc Ions and y-Alumina. *J. Catal.* **86,** 266–279 (1984).

73. Hybertsen, M. S. Absorption and emission of light in nanoscale silicon structures. *Phys. Rev. Lett.* **72,** 1514–1517 (1994).

74. Efros, A. L. & Rosen, M. The Electronic Structure of Semiconductor Nanocrystals. *Annu. Rev. Mater. Sci.* **30,** 475–521 (2000).

75. Jacobsson, T. J. & Edvinsson, T. Absorption and fluorescence spectroscopy of growing ZnO quantum dots: Size and band gap correlation and evidence of mobile trap states. *Inorg. Chem.* **50,** 9578–9586 (2011).

76. Brus, L. Electronic wave functions in semiconductor clusters: Experiment and

theory. *J. Phys. Chem.* **90,** 2555–2560 (1986).

77. Brus, L. E. Electron-electron and electron-hole interactions in small semiconductor crystallites: The size dependence of the lowest excited electronic state. *J. Chem. Phys.* **80,** 4403–4409 (1984).

78. Gupta, A. *et al.* Hydrogen sensing based on nanoporous silica-embedded ultra dense ZnO nanobundles. *RSC Adv.* **4,** 7476–7482 (2014).

79. Bürkle, M. *et al.* Bandgap Engineering in OH-Functionalized Silicon Nanocrystals: Interplay between Surface Functionalization and Quantum Confinement. *Adv. Funct. Mater.* **27,** 1–7 (2017).

80. Scanlon, M. D., Peljo, P., Méndez, M. A., Smirnov, E. & Girault, H. H. Charging and discharging at the nanoscale: Fermi level equilibration of metallic nanoparticles. *Chem. Sci.* **6,** 2705–2720 (2015).

81. Jakob, M., Levanon, H. & Kamat, P. V. Charge distribution between UV-irradiated TiO2 and gold nanoparticles: Determination of shift in the Fermi level. *Nano Lett.* **3,** 353–358 (2003).

82. Schejn, A. *et al.* Size-controlled synthesis of ZnO quantum dots in microreactors. *Nanotechnology* **25,** 145606 (2014).

83. Guo, L. *et al.* Highly monodisperse polymer-capped ZnO nanoparticles: Preparation and optical properties. *Appl. Phys. Lett.* **76,** 2901–2903 (2000).

84. Zhang, L., Yin, L., Wang, C., Qi, Y. & Xiang, D. Origin of Visible Photoluminescence of ZnO Quantum Dots : Defect-Dependent and Size-Dependent. 9651–9658 (2010).

85. Fonoberov, V. A., Alim, K. A. & Balandin, A. A. Photoluminescence investigation of the carrier recombination processes in ZnO quantum dots and nanocrystals. 1–9 (2006). doi:10.1103/PhysRevB.73.165317

86. Chen, Z., Hellstr, S., Ning, Z., Yu, Z. & Fu, Y. Exciton Polariton Contribution to the Stokes Shift in Colloidal Quantum Dots †. 5286–5293 (2011). doi:10.1021/jp109608t

87. Cloutier, S. G. Impact of Different Surface Ligands on the Optical Properties of PbS Quantum Dot Solids. 1858–1870 (2015). doi:10.3390/ma8041858

88. Lu, J. G. *et al.* Self-assembled ZnO quantum dots with tunable optical properties. *Appl. Phys. Lett.* **89,** 4–6 (2006).

89. Zwicker C and Jacobi K. Site-specific interaction of H2O with ZnO single-crystal surfaces studied by thermal desorption and UV Photoelectron Spectroscopy. *Surf. Sci.* **131,** 179–194 (1983).

90. Cox PA, H. V. *The Surface Science of Metal Oxides. New*. (York: Cambridge University Press; 1994., 1994).

Chapter 6: Synthesis of Zinc Nitride Nanocrystals by Gas-Phase Plasma

6.1 Introduction

The main motivation of the work is to produce an alternative material, zinc nitride (Zn_3N_2), for energy applications as stated in section 2.4.5. This chapter describes production of zinc nitride (Zn_3N_2) nanocrystals (NCs) by radio-frequency (RF) atmospheric pressure plasmas (APPs) using easy-to-use precursors and avoiding highly reactive chemicals.

Specifically, we will demonstrate the possibility of Zn_3N_2 synthesis using a high purity metallic zinc wire and nitrogen-containing gas, i.e. N_2 first and then NH_3, as zinc and nitrogen precursors, respectively. Detail characterization will be presented to understand the produced material chemical nature.

6.2 Experimental Setup

This system was designed and developed from scracth as part of this project. Figure 6.1a shows the in-house built system for the synthesis of zinc nitride. The microplasma reactor (figure 6.1b) is housed in a stainless-steel chamber connected to gas feedthrough and a RF power source. The chamber is connected to a rotary vacuum pump to ensure operation in a controlled environment, i.e. in nitrogen. The chamber is evacuated to a base pressure of less than 2.0 Torr. An x-y stage is placed under the reactor so to be able to move the deposition substrate.

The plasma reactor consists of a stainless-steel tube with a quartz capillary (1 mm outer diameter and 0.7 mm internal diameter) containing a 99.99% pure zinc wire (0.25 mm diameter; Purchased from Alfa Aesar, Heysham, UK) and two copper electrodes; RF electrode (powered) and ground electrode, as shown in the figure 6.1b-c. The quartz tube is mounted and glued (Araldie Precision adhesive) inside larger metal tubing with the diameter of 1/8 of an inch. A small hole is drilled in middle of the copper electrodes to insert the quartz capillary. The zinc wire and one of the copper electrodes acted as a ground electrode, while RF power was applied to the other copper electrode via a matching unit. Plasma was generated between the RF electrode and grounded zinc wire. The distance between the capillary end and the collector (i.e. a solid substrate or ethanol surface in a vial) was between 2 mm and 5 mm. The gases supplied to the

reactor were mixed before entering the chamber into a single gas line. The gas flows were controlled by separate mass flow controllers (MFCs). The background gases for sustaining the plasma were Ar or He. Pure N_2 (oxygen free, 99.99 %, BOC: 300-00-0023) gas or 10% ammonia pre-mixed with argon were used as nitrogen precursors. The gas lines in which the Ar-NH_3 mixture flows are purged with Ar after every experiment. The regulator that is used on the ammonia bottle is a BOC model HP1500.

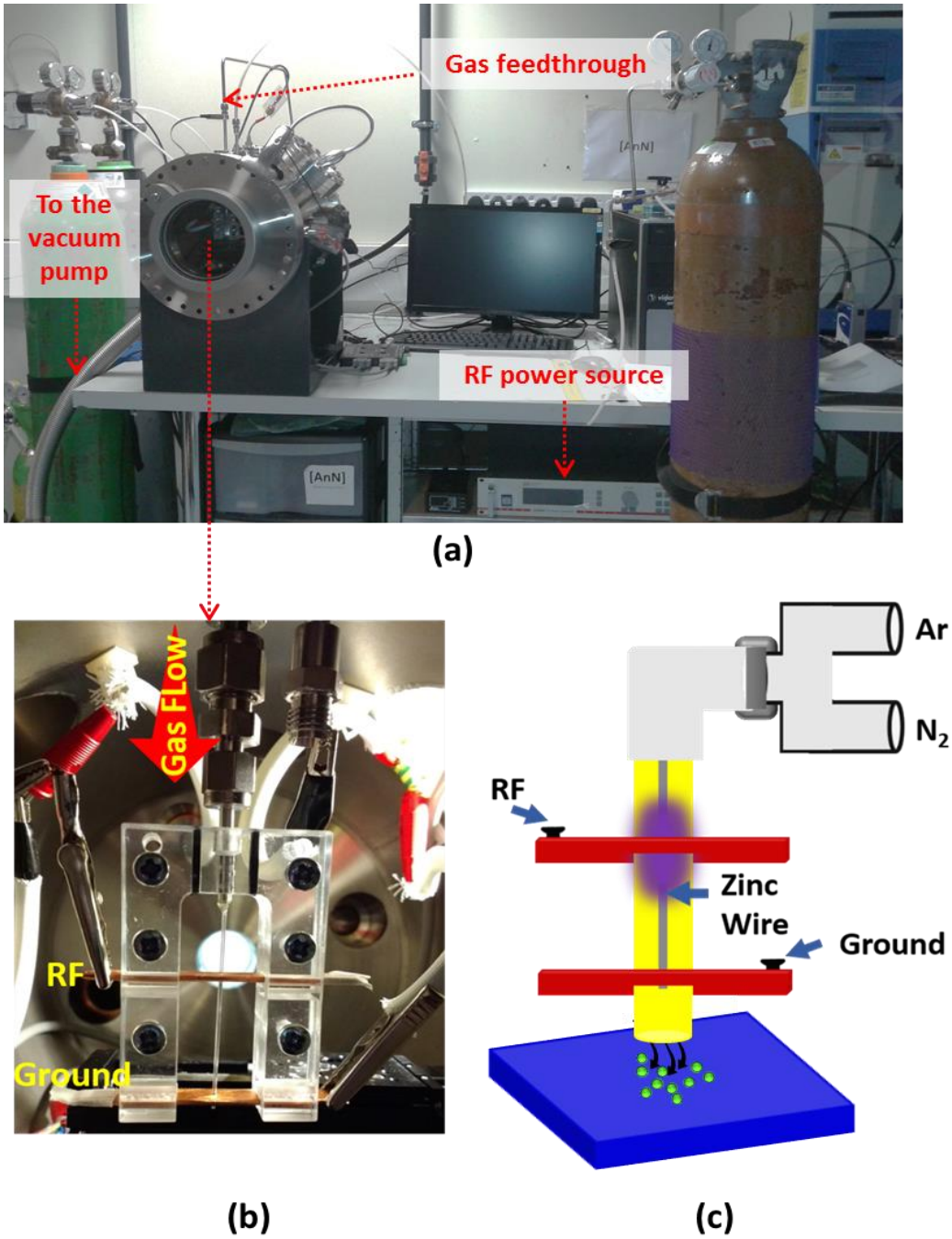

Figure 6.1: (a) stainless steel chamber connected to the gas feedthrough, vacuum pump and RF power supply (b) showing the real-time plasma reactor showing RF powered electrode and ground electrode with gas flow direction (c) Schematic diagram for the atmospheric pressure plasma.

The RF power source operate at a frequency of 13.56 MHz (MKS Elite 300, 13.56 MHz) that is connected to a manual tunable matching network (MFJ-989D); the matching network is needed for tuning the impedance in the circuit. The matching unit is placed between the reactor and the power source, to reduce the reflected power and to ensure plasma stability. The matching box basically consists of a 500 pF wide-spread air-variable capacitor and a rotary inductor for continuous coverage of the high frequency spectrum. The reflected power to the power supply was < 2 W for all the different plasma conditions investigated. The suppression of the reflected power ensures that the system can operate for a long period of time without heating or damaging the circuit components of the power supply.

6.3 Synthesis of Zn_3N_2 using molecular nitrogen gas

6.3.1 Experimental parameters

Table 1 shows the flow rates for Ar and N_2. The power applied in this set of experiment was 80 W.

Table 10: Experimental details of atmospheric-pressure plasma method used to synthesize Zn_3N_2 quantum dot by using nitrogen gas.

Sample	Ar	N_2
0.0% N_2	200 sccm	0
12.5% N_2	175 sccm	25 sccm
25.0% N_2	150 sccm	50 sccm
37.5% N_2	125 sccm	75 sccm
50.0% N_2	100 sccm	100 sccm

6.3.2 Material Characterization

For transmission electron microscopy (TEM), samples were collected in ethanol and then drop-casted on carbon-coated copper grid and dried. Figure 6.2 show the high resolution TEM (HRTEM) images of the resulting nanocrystals (NCs) produced at different nitrogen concentration 0.0% (6.2a-b), 12.5% (6.2c-d), 25.0% (6.2e-f), 37.5% (6.2g-h) and 50.0% (6.2i-j). HRTEM images were used to determine the lattice spacing for different NCs. Table 2 summarizes the values of lattice spacing that were encountered for each synthesis conditions; separate columns in table 2 are then used to report the expected lattice spacing for Zn_2N_3, metallic zinc and zinc oxide so that corresponding NCs phases could be identified.

The sample synthesised at 0.0% N_2 (figure 6.2a-b) shows particles with diameters < 10 nm. Figure 6.2b shows a measured d-spacing of 2.05 Å which resembles the (101) plane of metallic zinc (0.209 nm). Other values measured from HRTEM analysis (i.e. 0.205 nm, 0.206 nm, 0.235 nm) were also identified with the (101) and (100) planes of metallic zinc with lattice spacing of 0.209 nm and 0.231 nm, respectively (table 2). This supports that Zn NCs were produced at 0% N_2.

Figure 6.2c-d shows micrograph corresponding to the 12.5% N_2 sample where two ranges of particles were observed; relatively large particles ~10 nm and other smaller particles < 5 nm. The measured lattice spacing for the bigger particles and smaller particles are 0.235 nm and 0.277, respectively. The first value can be assigned to the Zn_2N_3 (411) plane (0.23 nm) or to the metallic zinc (100) plane (0.231 nm), see also table 2. Another values of 0.277 nm can be assigned to the Zn_2N_3 (222) plane (0.282 nm) or ZnO (100) plane (0.281 nm). Other values (table 2) also appeared and correspond to a range of different planes of metallic zinc, ZnO or Zn_2N_3, which suggest that at this synthesis conditions a mix of different phases were produced.

A similar result is obtained for the sample synthesized with 25.0% N_2, with values of lattice spacing corresponding to mix phases (table 2). In this case interconnected crystal structure (figure 6.2e, yellow contour) and particles with diameters smaller than < 5 nm (figure 6.2f) were observed. The larger structures in figure 6.2e exhibit d-spacing of 0.234 nm and 0.231 nm, which can relate to Zn_2N_3 (411) plane (0.23 nm) and metallic Zn (100) plane (0.231 nm). In figure 6.2f, the lattice spacing for smaller particles is 0.268 nm, 0.269 nm and 0.271 nm and can be assigned to Zn_2N_3 (321) or (222) planes with d-spacing of 0.261 nm or 0.282 nm, respectively. However, these values are very close to ZnO (100) and (002) planes with d-spacing of 0.281 nm and 0.260 nm, respectively. Other values (table 2) also appeared and correspond to a range of different planes of metallic zinc, ZnO or Zn_2N_3.

Figure 6.2g-h shows micrograph corresponding to 37.5% N_2 sample only with particles with diameters less than < 5 nm. The lattice spacing observed at these conditions and shown in figure 6.2g-h resulted in values of 0.225 nm and 0.226 nm which again could correspond to various phases where the closest assignment is for Zn_2N_3 (411) plane (0.23 nm) and Zn (100) plane (0.231 nm). Table 2. shows other values observed at these synthesis conditions confirming the presence of various phases including metallic zinc, ZnO and Zn_2N_3.

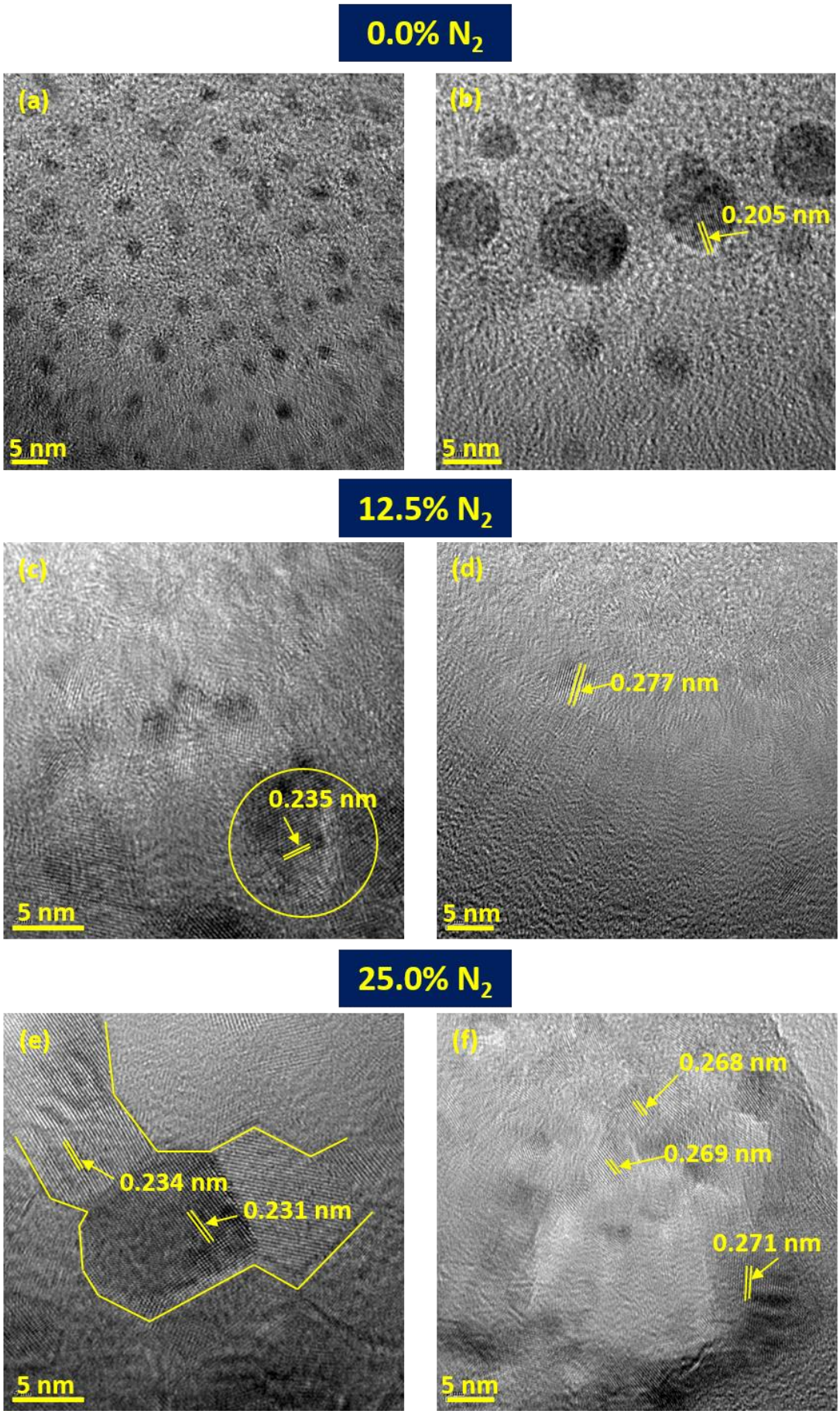
0.0% N2
(a)
5 nm
(b)
0.205 nm
5 nm
12.5% N2
(c)
0.235 nm
5 nm
(d)
0.277 nm
5 nm
25.0% N2
(e)
0.234 nm
0.231 nm
5 nm
(f)
0.268 nm
0.269 nm
0.271 nm
5 nm

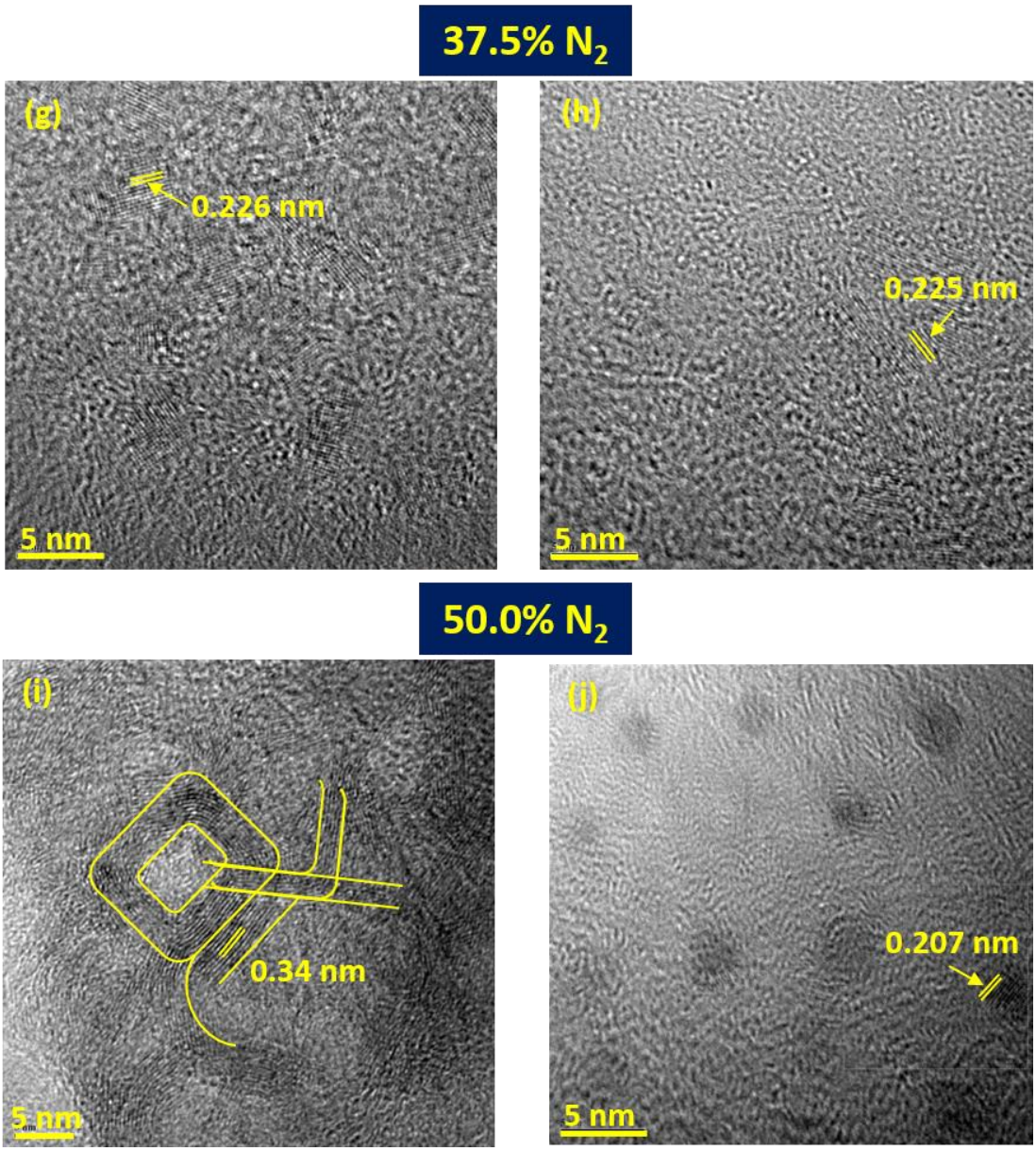

Figure 6.2: HRTEM images of synthesised material at different gas flow combination (a-b) 0.0% N_2, (c-d) 12.5% N_2, (e-f) 25.0% N_2, (g-h) 37.5% N_2 and (i-j) 50.0% N_2. These images show some other morphology especially in sample 12.5% N_2, 25.0% N_2 and 50.0% N_2.

Finally, at 50.0% N_2, similar conclusions can be drawn where mix phases (table 2) and a variety of morphologies were observed. Specifically, for the images of figure 6.2i-j, interconnected crystal structure (6.2i, yellow contour) and particles with diameters smaller than < 5 nm (6.2f) were observed. The lattice spacing reported in figure 6.2i is 0.34 nm, which can only relate to Zn_2N_3 (220) plane (0.345 nm). In figure 6.2j, the value measured is 0.207 nm which could be ascribed to Zn_2N_3 (332) plane (0.208 nm) or Zn (101) plane (0.209 nm) and, respectively. Table 2 shows other values corresponding to different planes of metallic zinc, ZnO and Zn_2N_3. According to these

measurements, the majority of the nanoparticles are nearly spherical with a diameter below 10 nm and are well separated from each other (figure 6.2 a,b,d,f,g,h,j). However, at the various synthesis conditions larger particles as well as non-spherical structures can be found (figure 6.2 c,e,i).

Table 11: Measured lattice spacing by HRTEM for sample 0.0% N_2, 12.5% N_2, 25.0% N_2, 37.5 % N_2 and 50.0% N_2 and compared with Zn_2N_3 (JCPDS: 00-03500762), ZnO (JCPDS: 00-36-1451) and Zn (JCPDS: 03-065-3358).

Sample	**Measured Lattice spacing**	**Zn_2N_3**	**Zn**	**ZnO**
0.0% N_2	0.205 nm	-	0.209 nm (101)	-
	0.206 nm	-	0.209 nm (101)	-
	0.235 nm	-	0.231 nm (100)	-
12.5% N_2	0.236 nm	0.23 nm (411)	0.231 nm (100)	-
	0.273 nm	0.282 nm (222)	-	0.281 nm (100)
	0.270 nm	0.261 nm (321)		0.26 nm (002)
	0.315 nm	0.282 nm (222) or 0.345 nm (220)		0.281 nm (100)
25.0% N_2	0.235 nm	0.230 nm (411)	0.231 nm (100)	-
	0.237 nm	0.244 nm (400)	0.247 nm (002)	0.247 nm (101)
	0.271 nm	0.261 nm (321)	-	0.26 nm (002)
	0.274 nm	0.282 nm (222)	-	0.281 nm (100)
37.5% N_2	0.227 nm	0.23 nm (411)	0.231 nm (100)	-
	0.226 nm	0.23 nm (411)	0.231 nm (100)	-
	0.230 nm	0.23 nm (411)	0.231 nm (100)	-
	0.243 nm	0.244 nm (400)	0.247 nm (002)	0.247 nm (101)
50.0% N_2	0.172 nm	0.172 nm (400)	0.168 nm (102)	0.162 nm (102)
	0.211 nm	0.218 nm (420)	0.209 nm (101)	0.191 nm (102)
	0.231 nm	0.230 nm (411)	0.231 nm (100)	0.247 nm (101)

Similarly, the interpretation of the lattice spacing is not straightforward due to the presence of a range of nanoparticles and other structure, which confirm the presence of mixed phases. Based on TEM and HRTEM analysis, the only reliable set of results therefore appears to be the one at 0.0% N_2 where metallic zinc nanoparticles have been produced. For these reasons not all the conditions above have been characterized fully. High resolution XPS spectra of 12.5% N_2, 37.5% N_2 and 50.0% N_2 samples are shown in figure 6.3. Samples were directly deposited onto silicon substrate to perform XPS.

The Zn 2p doublet core level spectrum clearly shows the presence of Zn in the samples as shown in figure 6.3a-c. Binding energy at ~1022.1-1022.6 eV and ~1045.1-1045.7 eV corresponds to Zn $2p_{3/2}$ and Zn $2p_{1/2}$, respectively. The FWHM of the Zn 2p doublet in Zn^0 is generally found to be ~0.82 eV and 1.00 eV for Zn $2p_{3/2}$ and Zn $2p_{1/2}$,

respectively. Table 3 shows the FWHM of Zn 2p doublet which confirms that Zn is present in Zn^{+2} state.

Table 12: Measured FWHM of Zn 2p doublet to understand the ionic state to Zn.

Sample Name	FWHM of Zn $2p_{3/2}$	FWHM of Zn $2p_{1/2}$
12.5% N_2	1.65 eV	1.71 eV
37.5% N_2	1.90 eV	2.10 eV
50.0% N_2	1.71 eV	1.79 eV

Figure 6.3d-f shows N 1s spectrum of all three samples. Nitrogen bonding with metal in metal nitrides generally exhibit a peak at ~396-397 eV,[1–4] which is not observed in any of the samples. All samples show a peak at 400.6 eV, which is generally assigned to chemisorbed N_2^+.[5] However, nitrogen in ZnO has been reported to produce a peak at 399.8 eV, which could be the source of the 400.6 eV in this case.[6] The peaks at ~ 402.6 eV (figure 6.3d,f) and 406.5 eV (figure 6.3d) corresponds to nitrogen bonds with oxygen, the first relating to oxidised nitrogen[7] and the second to N_2O bonding.[8] This observation shows only oxygen bonded nitrogen species onto the synthesised material.

O 1s peak corresponding to these samples is shown in figure 6.3g-i. O 1s peak deconvolution shows two peaks at 530.7 eV and 532.3-532.7 eV.[9] Generally, the peak at lower energy corresponds to zinc oxide and the higher energy peak relates to adsorbed oxygen species. The peak corresponding to ZnO, at 530.7 eV, is very small and only present in the sample produced with 12.5% N_2 (figure 6.3g); however, the O 1s is very intense and therefore could have overshadowed peaks coming from ZnO.

According to material characterization TEM and XPS, samples synthesised at different nitrogen concentration 12.5% N_2, 37.5% N_2 and 50.0% N_2, appear to contain a range of bonding arrangements including Zn bonded to N and O species. The analysis of the FWHM of the XPS Zn 2p doublet peak supports the Zn^{+2} state of Zn; however, while N 1s and O 1s do not provide strong evidence for the same, Zn^{+2} cannot be excluded completely.

6.3.3 Optical measurement

Samples were collected directly in ethanol to measure the optical properties by UV-Vis spectroscopy. UV-Vis optical transmission is reported in figure 6.4a. As the concentration of nitrogen increases in the gas mixture, the absorption increases till the

nitrogen concentration reaches 37.5 %. The sample synthesized at 37.5% N_2 shows two absorbance peaks at 314 nm and 354 nm while absorbance decreases significantly for 50.0% N_2. Zn_2N_3 shows both direct and indirect bandgap according to previous values in literature.[10–13] Therefore, direct and indirect bandgap are determined by Tauc plot (figure 6.4b-e and figure 6.5a-c), however also in this case the interpretation might be affected by the various products, variety of structure, size, phases and should be taken with care.

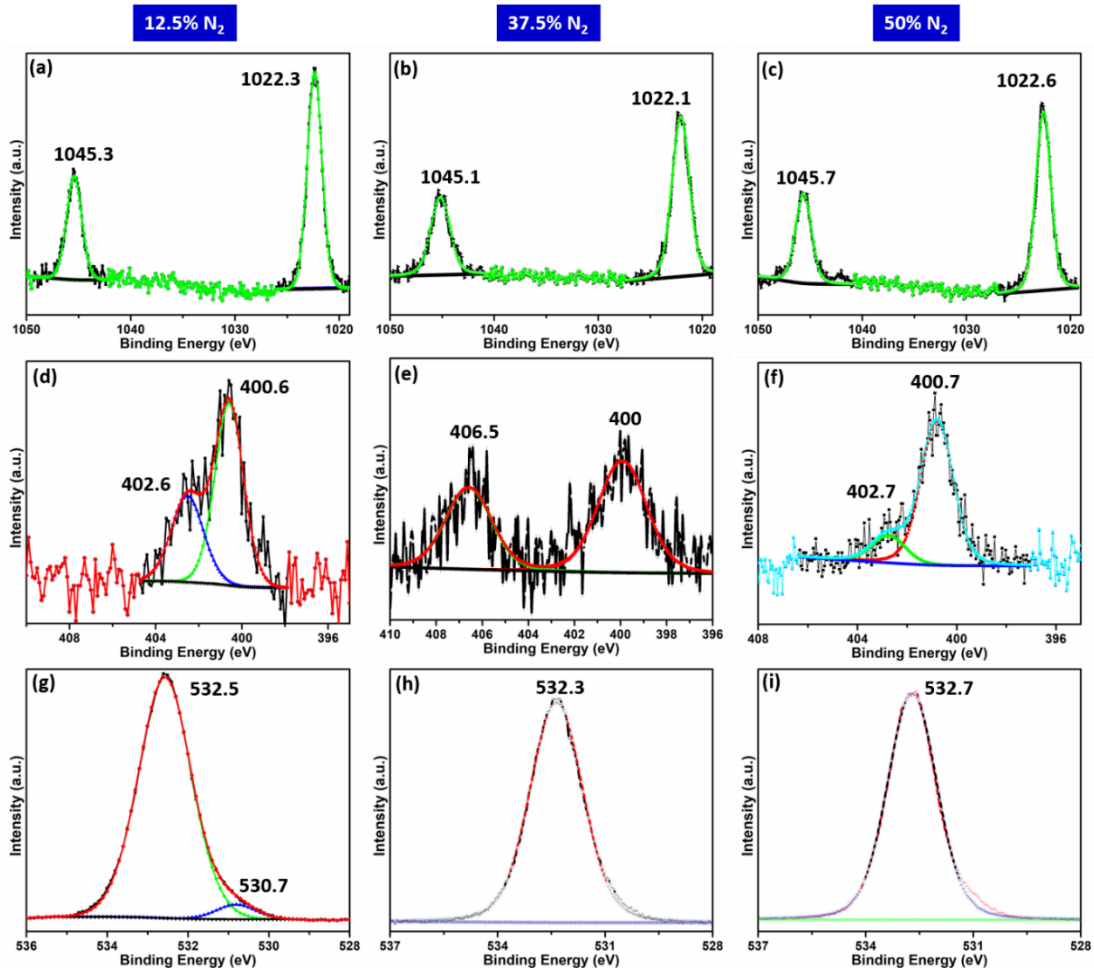

Figure 6.3: High resolution XPS spectra of (a-c) Zn 2p, (d-f) N 1s and (g-i) O 1s for sample 12.5% N_2, 37.5% N_2 and 50.0% N_2.

Figure 6.4 shows Tauc plot for direct bandgap transition of all samples. The sample synthesised at 0.0% N_2 does not show any bandgap in the range measured. This could be due to both the metallic nature and low concentration of the NPs or to widening of the bandgap because of quantum confinement. The bandgap values could be extracted adequately from the Tauc plots (figure 6.4b and 6.4e) of all samples except for the sample produced with 37.5% N_2, which did not present clear trends for

linear fitting (figure 6.4d). The bandgap values are 3.9 eV and 3.58 eV for samples produced with 12.5%and 50.0% N_2 concentrations, respectively. The sample in figure 6.4d (37.5% N_2) could relate to a bandgap of 3.25 eV or 3.72 eV.

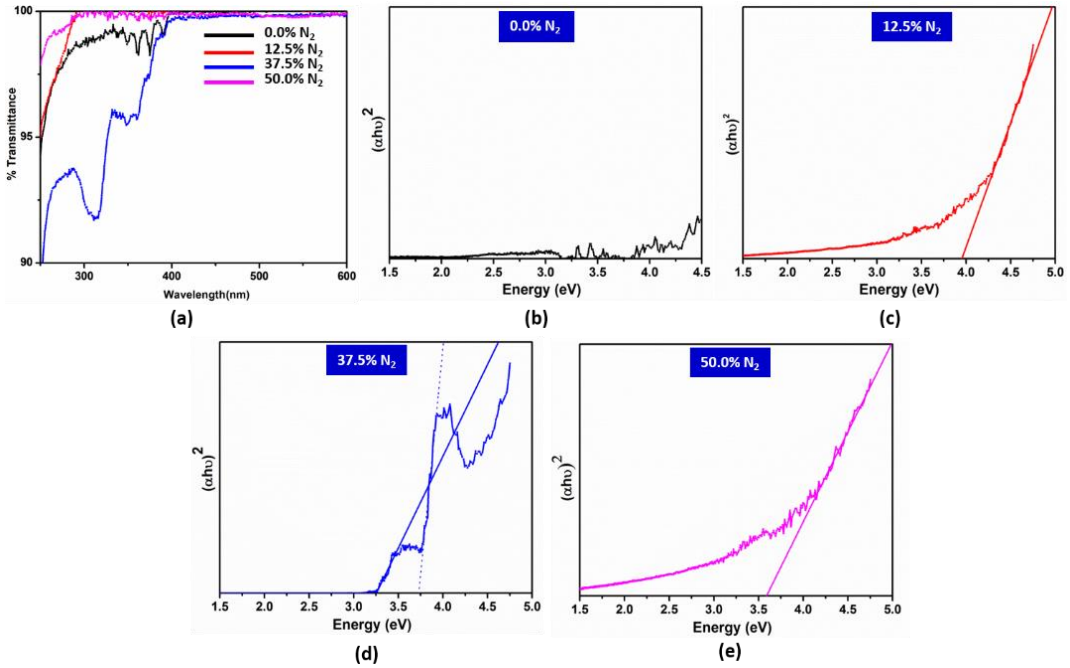

Figure 6.4: (a) shows transmittance of all samples recorded by UV-Vis spectroscopy in ethanol and (b-f) represents the measured direct bandgap of all samples (b) 0.0% N_2, (c) 12.5% N_2, (d) 25.0% N_2, (e) 37.5% N_2 and (f) 50.0% N2 by Tauc plot.

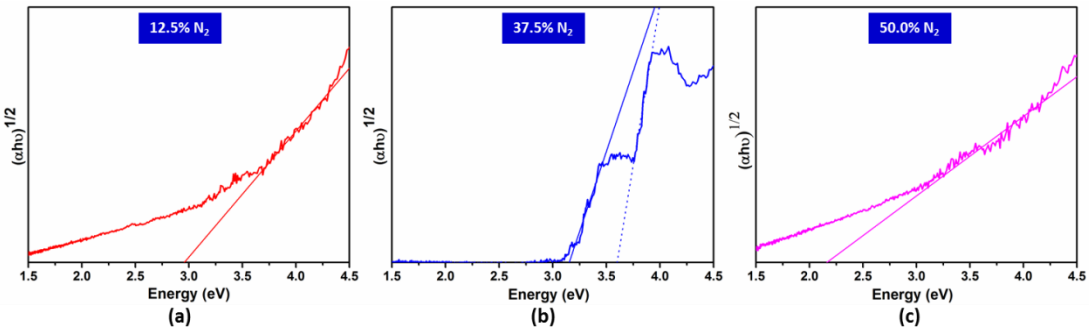

Figure 6.5: Measured indirect bandgap of all samples (a) 12.5% N_2, (b) 37.5% N_2 and (c) 50.0% N_2 by Tauc plot.

Figure 6.5 shows measured indirect bandgap for sample 12.5% N_2, 37.5% N_2 and 50.0% N_2. Similar to direct bandgap measurement, the indirect bandgap values could be extracted adequately from the Tauc plots (figure 6.5a and 6.5c) of all samples except for the sample produced with 37.5% N_2 (figure 6.4d). The indirect bandgap values are 2.95 eV and 2.16 eV for samples produced with 12.5% and 50.0% N_2 concentrations, respectively. The sample in figure 6.5b (37.5% N_2) could relate to a bandgap of 3.15 eV or 3.60 eV.

In the literature, Zn_2N_3 bandgap is reported to be in the range 1.2-3.3 eV[14–18] with the direct and indirect bandgap measurement. However, with quantum confinement, this value is expected to increase.

6.3.4 Discussion

Synthesis with 12.5% N_2, 37.5% N_2 and 50.0% N_2 confirmed particle formation; however, the assignment of crystal structures was difficult with TEM results. From XPS (figure 6.3) results, it can be confirming the formation of zinc bounded to different nitrogen and oxygen species. XPS also confirms different oxygen, nitrogen and zinc species. A point that may be worth making is that the NCs produced have either no absorption in the visible range or the concentration is relatively low.

Overall the materials characterization has proven difficult, likely due to the presence of mixed morphology and phases. It is however clear that metallic zinc and zinc nitrides have been synthesized where oxidation may have occurred post-synthesis when the samples have been exposed to air. It is also reasonable to assume that oxidation has taken place on the Zn-nitride phase; this is supported by various experimental evidence of Zn-O-N bonding as well as by the Zn NPs produced a 0.0% N_2, which do not appear to have undergone extensive oxidation.

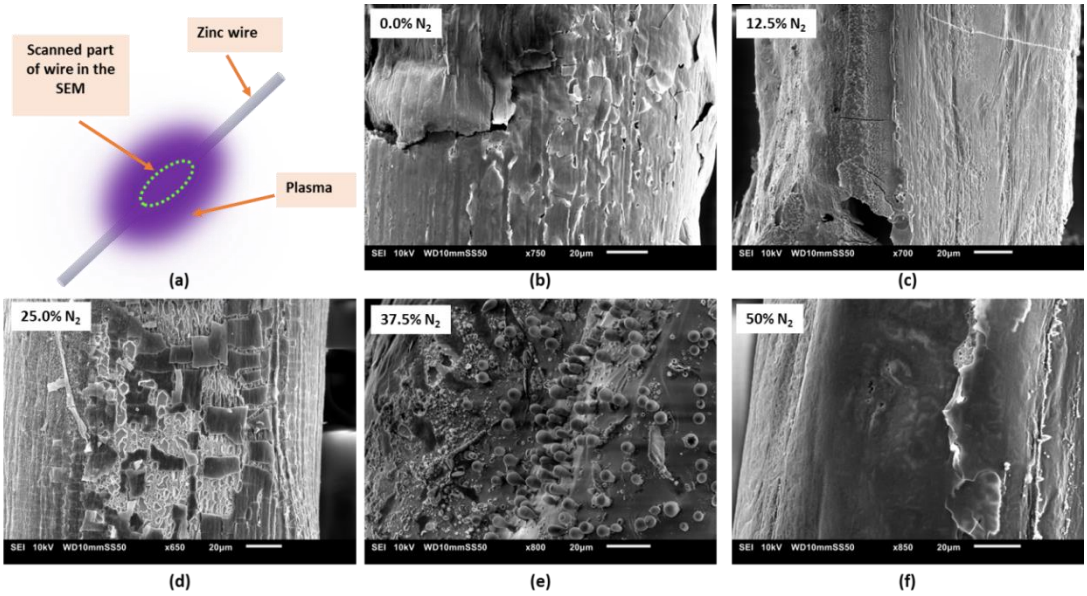

Figure 6.6: SEM images of zinc wire after the plasma treatment.

According to these results, the process is not yet reliable at this stage and improvements are needed. Energy kinetics of this plasma does not lead to the production of pure zinc nitride. This could be due to either the low density of reactive atomic nitrogen species in this type of plasma or due to high gas temperature that could decompose any synthesised zinc nitride; the decomposition temperature of zinc nitride is ~700 ^{o}C.[19]

In order to provide some more information on the synthesis process, we have analysed the zinc wire by SEM after being used for synthesis (figure 6.6). As the nitrogen concentration increases, plasma temperature increases and at 37.5% N_2, evidence of melting could be observed on the wire.

On this basis and with the current experimental set-up, the use of a different nitrogen precursor might provide better opportunities to improve the process and achieve the synthesis conditions required for zinc nitride NCs. For instance, ammonia could represent a more suitable nitrogen precursor to generate active nitrogen species in this case.

6.4 Synthesis of Zn_3N_2 by using ammonia gas with lower He flow

6.4.1 Experimental parameters

The same setup is used in this process as described in section 6.2 except that the grounded and RF copper electrode position was exchanged with each other. In this set of experiments, a mixture of He, Ar and NH_3 was used. Ammonia was supplied by a pre-mixed NH_3-Ar bottle at 10% ammonia. Different combinations of He and NH_3-Ar mixtures were used as reported in table 4. The applied power was kept constant to 70 W in all experiments. Deposition time (2 min) was kept constant for all experiments.

Table 13: The experimental details of atmospheric-pressure plasma method used to synthesize Zn_3N_2 quantum dot by using ammonia

Sample	He	10% NH_3-Ar
0.0% NH_3	300 sccm	0
0.7% NH_3	280 sccm	20 sccm
1.0% NH_3	270 sccm	30 sccm

6.4.2 Material characterization

Samples were collected in ethanol, drop-casted onto carbon coated copper grid to perform HRTEM. HRTEM images show particle morphology for 0.0% NH_3, 0.7% NH_3 and 1.0% NH_3 in figure 6.7a-c. Lattice spacing of the particles are clearly

observed. The measured inter-planer spacing is 0.257 nm for sample 0.0% NH_3 and this value can be correlated with the Zn (002)

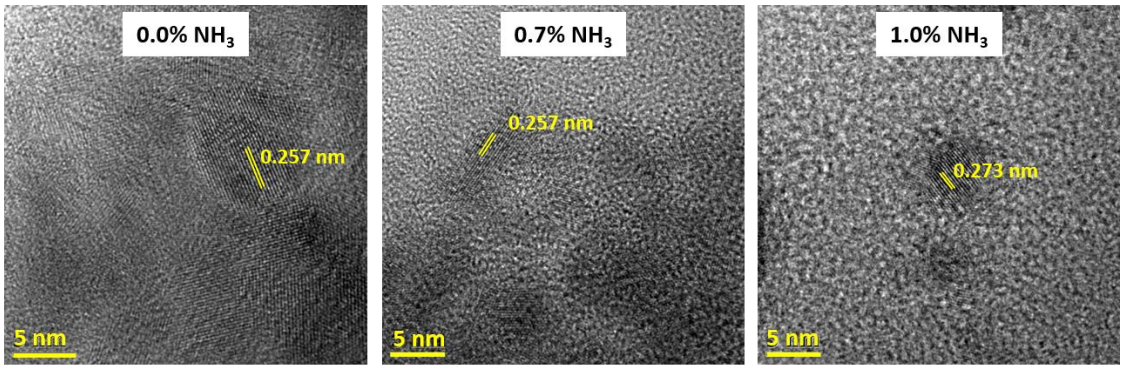

Figure 6.7: HRTEM images of synthesized sample (a) 0.0% NH_3, (b) 0.7% NH_3 and (c) 1.0% NH_3 and calculated spacing between atomic arrangements.

plane with a d-spacing of 0.247 nm (JCPDS: 03-065-3358). Inter-planer spacing for 0.7% NH_3 is 0.257 nm which can be matched to the Zn_2N_3 (321) plane with d-spacing of 0.26 nm (JCPDS: 04-012-6365); however, the latter can also correspond to the Zn (002) plane with lattice spacing of 0.247 nm. The calculated d-spacing value is 0.273 nm for 1.0% NH_3. This could indicate both the d-spacing of a (222) plane in Zn_2N_3 (0.28 nm) or could be attributed to a ZnO (100) plane with d-spacing of 0.281 nm. It seems very clear that from HRTEM observations many Zn_2N_3 planes overlap with pure zinc or zinc oxide, which complicates the analysis and conclusions.

Samples were directly deposited onto silicon substrate to perform XPS. XPS results from samples synthesized at 0.0% NH_3, 0.7% NH_3 and 1.0% NH_3 are shown in figure 6.8. Zn 2p peak confirms the Presence of zinc as shown in figure 6.8a.

Nitrogen 1s peak is not observed in the sample with 0.0% NH_3 (figure 6.8b) as expected. The nitrogen peak was detected in samples 0.7% NH_3 and 1.0% NH_3. As nitrogen bonding with a metal is expected in the range ~396-397 eV, we can associate the peaks at 397.7 eV and 397.8 eV (figure 6.8b) to Zn-N bonds, possibly with a degree of oxidation.[20] The peaks at 399.6 eV and 400 eV can be ascribed to N-H[21]. These results seem to suggest that nitrogen is bonded with Zn where a degree of oxidation has taken place.

O 1s peak deconvolution shows two peaks at ~529.9-530.1 eV and ~531.4-531.5 eV (figure 6.8c). The peaks at lower energy correspond to zinc oxide and higher energy peak relates to adsorbed oxygen species. The peak corresponding to ZnO is present in

all the samples. This may suggest that oxidation takes place as soon as samples are exposed to open air.

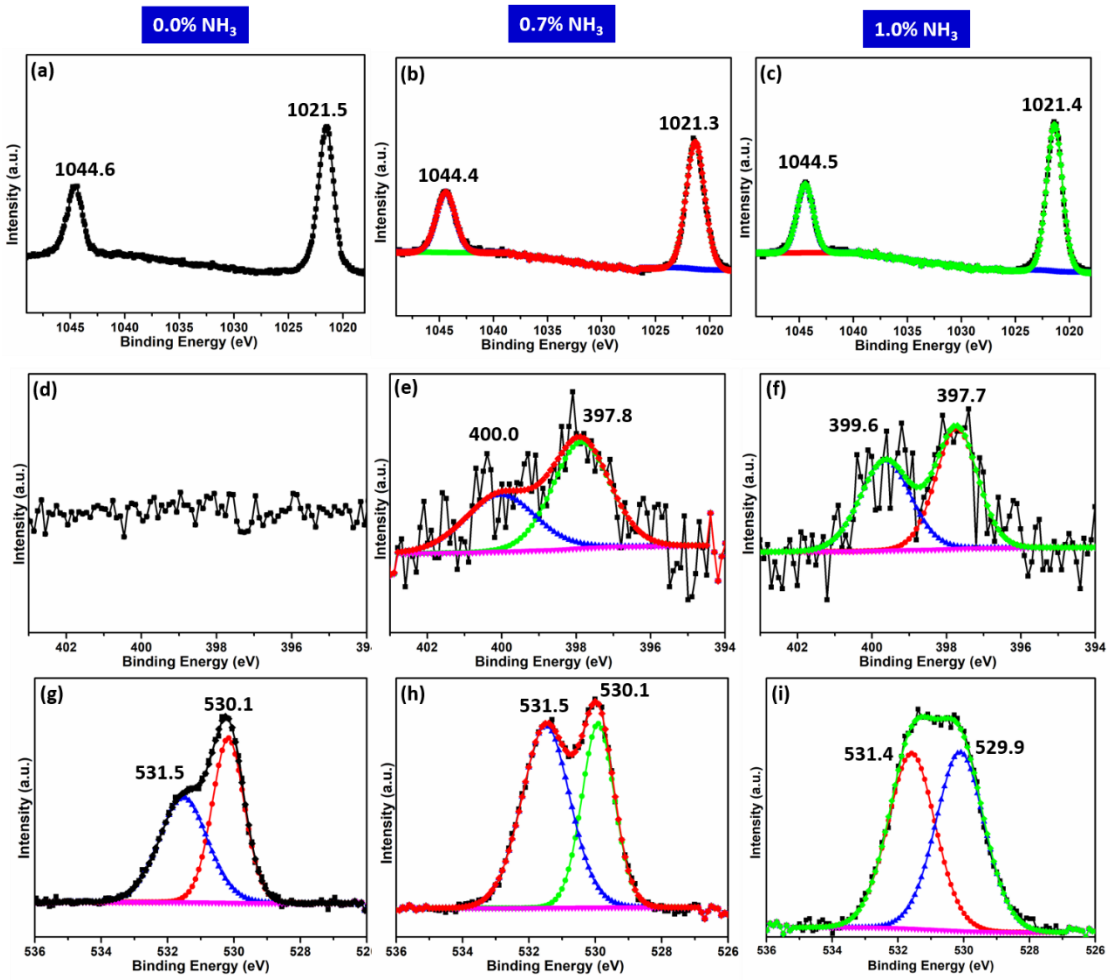

Figure 6.8: High resolution XPS spectra of (a-c) Zn 2p, (d-f) N 1s and (g-i) O 1s for sample 0.0% N_2, 0.7% N_2 and 1.0% N_2.

6.4.3 Optical measurement

All the samples were deposited on quartz substrates to measure transmittance, presented in figure 6.9. As the ammonia mixture concentration increases from 0.0% to 1.0% NH_3, the transmittance decreases (i.e. absorption increases) in the region 300-400 nm.

As previously stated, zinc nitride can exhibit both direct and indirect bandgap transitions; corresponding Tauc plots are in figure 6.10. Figure 6.10a shows that the direct bandgap for 0.7% NH_3 and 1.0% NH_3 samples is 3.6 eV and 3.54 eV, respectively. The indirect bandgap (figure 6.10b) for both samples is ~0.2 eV lower than the direct bandgap, i.e. 3.4 eV and 3.38 eV for 0.7% NH_3 and 1.0% NH_3

respectively. The bandgap did not change significantly by increasing NH_3 concentration for direct and indirect bandgap measurements.

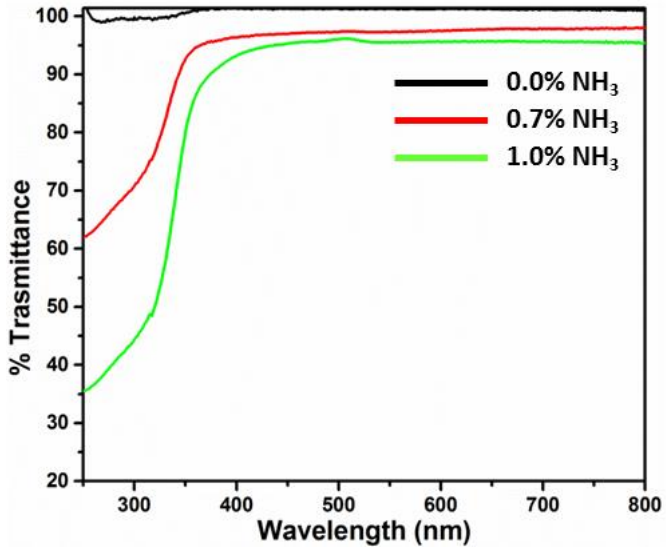

Figure 6.9: Transmission spectra of the deposited material on quartz substrate at various NH_3 concentrations.

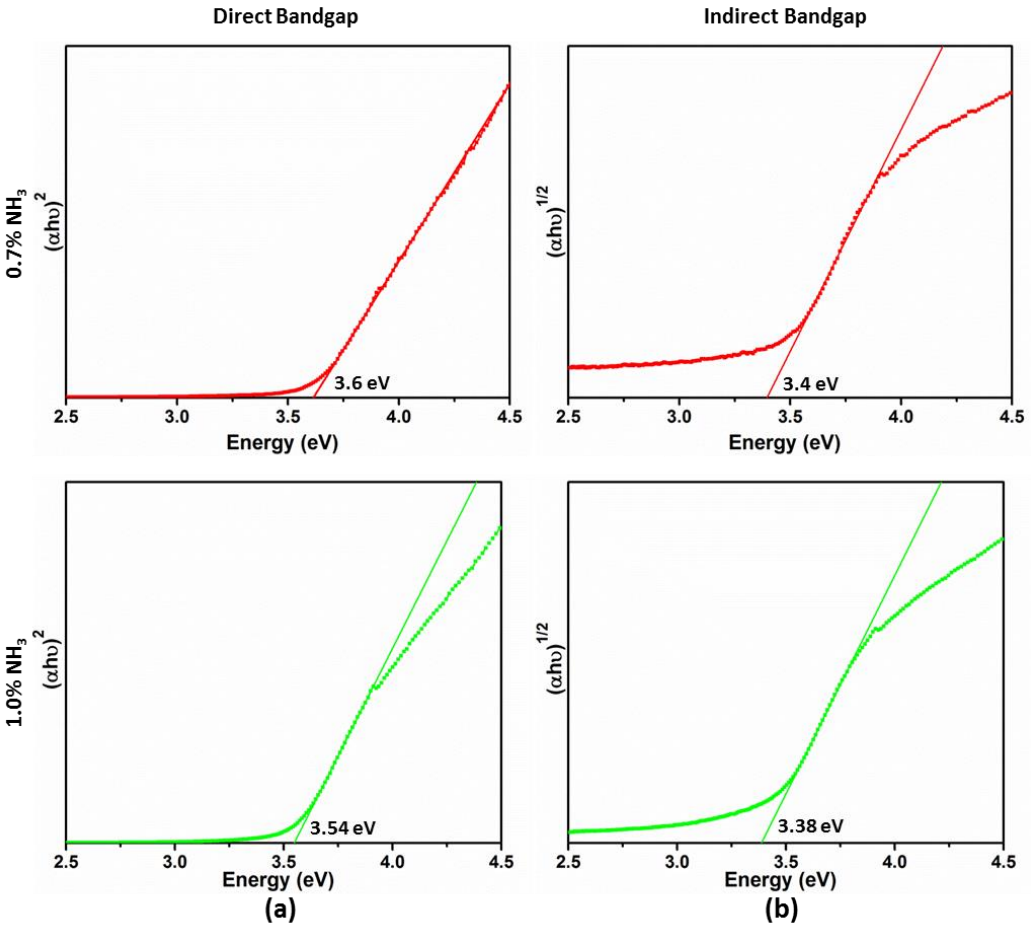

Figure 6.10: Measured direct and indirect bandgap for sample synthesised at 0.7% NH_3 and 1.0% NH_3 by Tauc plot.

6.4.4 Discussion

According to TEM, XPS and UV-Vis measurements, these initial experiments produced zinc nitride NCs; however, we should note that the plasma process did present repeatability issues visually determined from plasma instability. To improve the stability and repeatability of the process, background He gas flow was increased, which was successful in ensuring a stable glow at various conditions.

6.5 Synthesis of Zn_2N_3 using ammonia with high He flow

6.5.1 Experimental parameters

The new synthesis conditions are reported in table 5. The applied power was kept constant to 70 W in all experiments. Deposition time (2 min) was kept constant for all experiments. Preliminary optical and Raman measurement suggested that only 0.5% NH_3 sample shows the possibility of Zn_2N_3 formation. Therefore, only 0.5% NH_3 sample will be characterized further.

Table 14: Experimental parameter after increasing He gas flow.

Sample	He	10% NH_3-Ar
0.0% NH_3	400 sccm	0
0.5% NH_3	400 sccm	20 sccm
1.1% NH_3	400 sccm	50 sccm

6.5.2 Material characterization

For TEM analysis, 0.5% NH_3 sample was collected in toluene and then drop-casted on carbon-coated copper grid and dried. TEM and SAED pattern can be seen in figure 6.11. Figure 6.11a-c shows that particles are agglomerated. The values of the lattice spacing determined from HRTEM images of the particles (figure 6.11c) were 0.344 nm, 0.343 nm, 0.333 nm and 0.345 nm which correspond to zinc nitride (220) plane with a d-spacing of 0.345 nm.

The SAED patterns (figure 6.11d) shows the polycrystalline nature of the NCs agglomerates; the rings correspond to the (220), (321), (400), (422), (620), (640), (840) and (931) planes of zinc nitride. Table 6 presents the d-spacing measured by SAED and corresponding planes of zinc nitride, zinc oxide and zinc for comparison. Two planes, (220) and (620), observed in the measurements do not belong to any of the planes of zinc oxide and metallic zinc, supporting the formation of zinc nitride.

XPS is recorded to analyse further the chemical composition and oxidation states of the sample synthesized at 0.5% NH_3. The sample was directly deposited on a silicon substrate to record XPS. Figure 6.12a shows survey spectra with clear peaks from zinc, oxygen and nitrogen. Binding energy at 1021.2 eV and 1044.4 eV are attributed to the binding energy of $Zn2p_{3/2}$ and $Zn2p_{1/2}$ electrons as shown in the figure 6.12b.

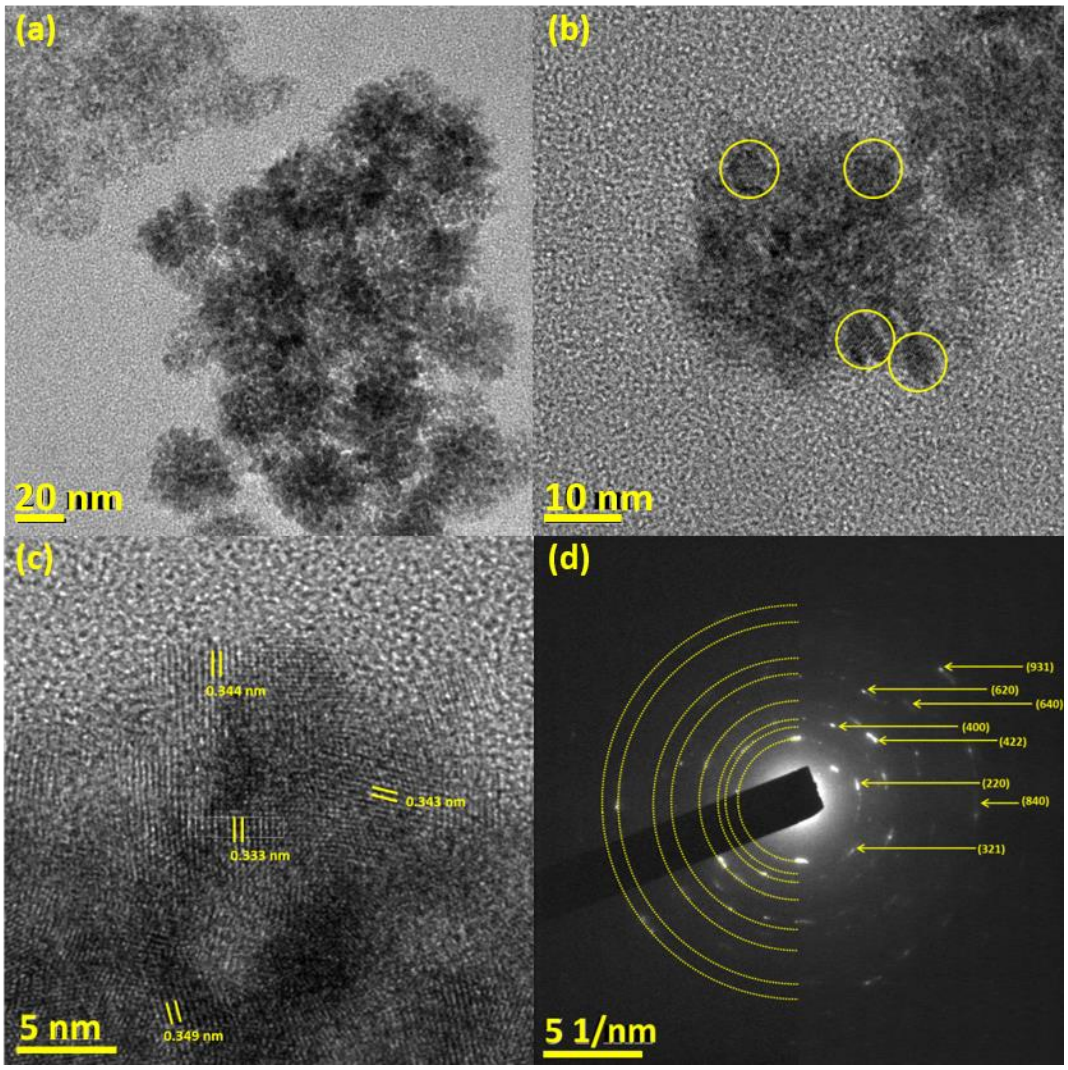

Figure 6.11: shows the results obtained from TEM analysis (a) TEM micrograph, (b-c) HRTEM micrographs and (d) SAED pattern for sample 0.5% NH_3.

Figure 6.12c shows N 1s peak, de-convoluted in two peaks at ~ 397.7 eV, corresponding to N-Zn /N-Zn-O bonds[20] and ~ 399.5 eV corresponding to N-H.[21] In the XPS high resolution spectra, the asymmetric O 1s peak was observed with a shoulder at higher binding energy. O 1s spectrum is fitted into two peaks centred at 529.8 eV and 531.4 eV, Figure 6.12d. The first peak at 529.8 eV corresponds to O^{-2} in Zn-O binding.[27] The peak at 531.4 eV correlates to the O-H group adsorbed on the surface.

Table 15: Calculated d-spacing from SAED pattern and their comparison with the lattice spacing of zinc nitride, zinc oxide and metallic zinc to confirm the material crystallinity.

Measured d-spacing from SAED patterns	**Zinc nitride**	**Zinc Oxide**	**Metallic Zinc**
0.327 nm (220)	0.345 nm	-	-
0.269 nm (321)	0.261 nm	0.260 nm	-
0.243 nm (400)	0.244 nm	0.247 nm	0.243 nm
0.199 nm (422)	0.199 nm	0.191 nm	0.209 nm
0.135 nm (640)	0.135 nm	0.135 nm	0.134 nm
0.155 nm (620)	0.154 nm	-	-
0.109 nm (840)	0.109 nm	0.109 nm	0.109 nm
0.100 nm (931)	0.100 nm	0.104 nm	0.101 nm

To carry out Raman analysis, samples were deposited directly on molybdenum foil. A peak at ~270 cm^{-1} is generally is considered to originate from Zn-N vibrations.[22–24]Local nitrogen vibration has been observed close to 570 cm^{-1}, according to previous reports.[24,25] ZnO generally presents an intense E_2 vibration mode at 437 cm^{-1}, A_1 longitudinal vibration at 574 cm^{-1} and a multi-phonon process peak at ~560 cm^{-1}.[23,26] The Raman spectra for the 0.0% NH_3 sample (figure 6.13) do not show any peak, probably as expected for metallic zinc. A prominent feature at 271 cm^{-1} was observed in the sample with 0.5% NH_3 suggesting the presence of Zn- N bonds. However, the same peak was not observed for the sample synthesized at 1.1% NH_3, although this could be due to the much weaker Raman signal for this sample. Peak ~ 440 cm^{-1} could be attributed to ZnO, while the peak at 553 cm^{-1} and 569 cm^{-1} could be assigned to either local nitrogen vibration as well as ZnO.

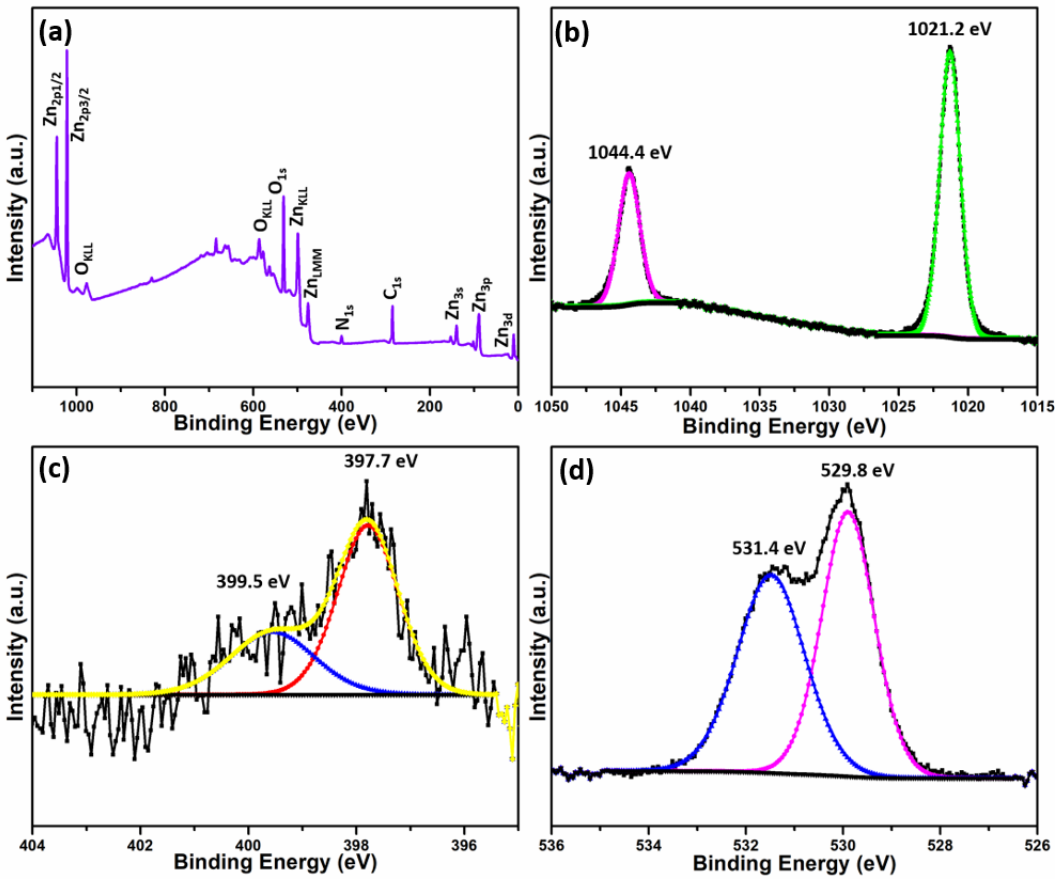

Figure 6.12: Show XPS spectra of sample 0.47% NH_3 (a) survey spectrum, (b) Zn2p doublet, (c) N 1s and (d) O 1s.

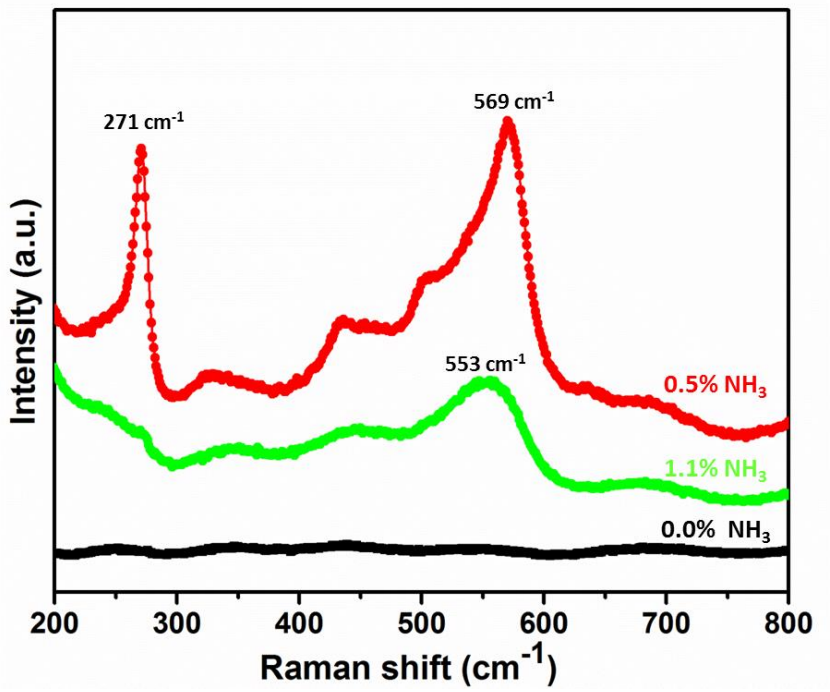

Figure 6.13: Raman spectra recorded for all three samples (0.0% - 1.1% NH_3).

6.5.3 Optical measurement

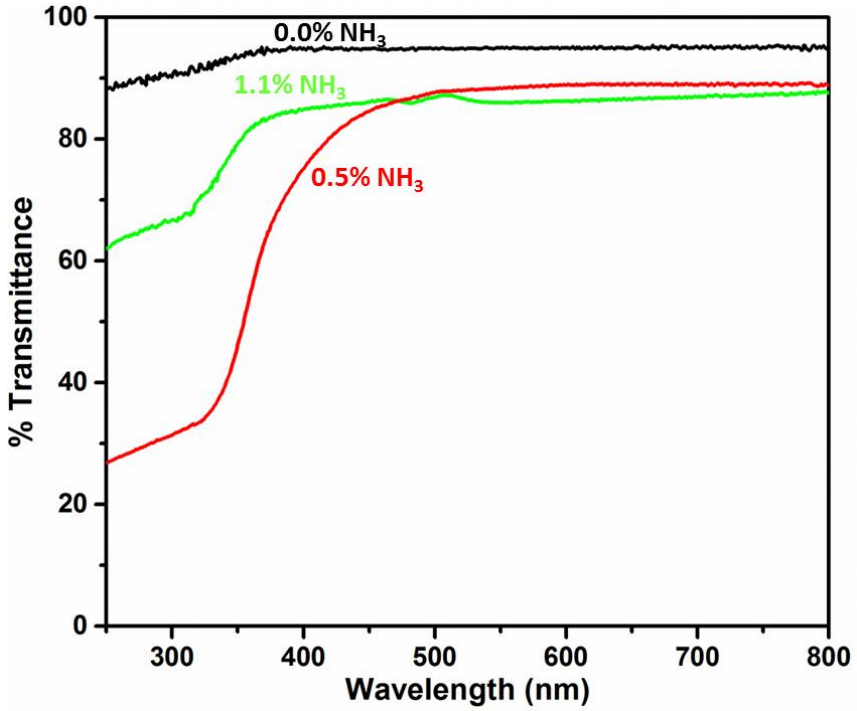

Figure 6.15: Transmittance measurements recorded by UV-Vis spectroscopy for sample synthesised at 0.0% NH_3, 0.5% NH_3 and 1.0% NH_3.

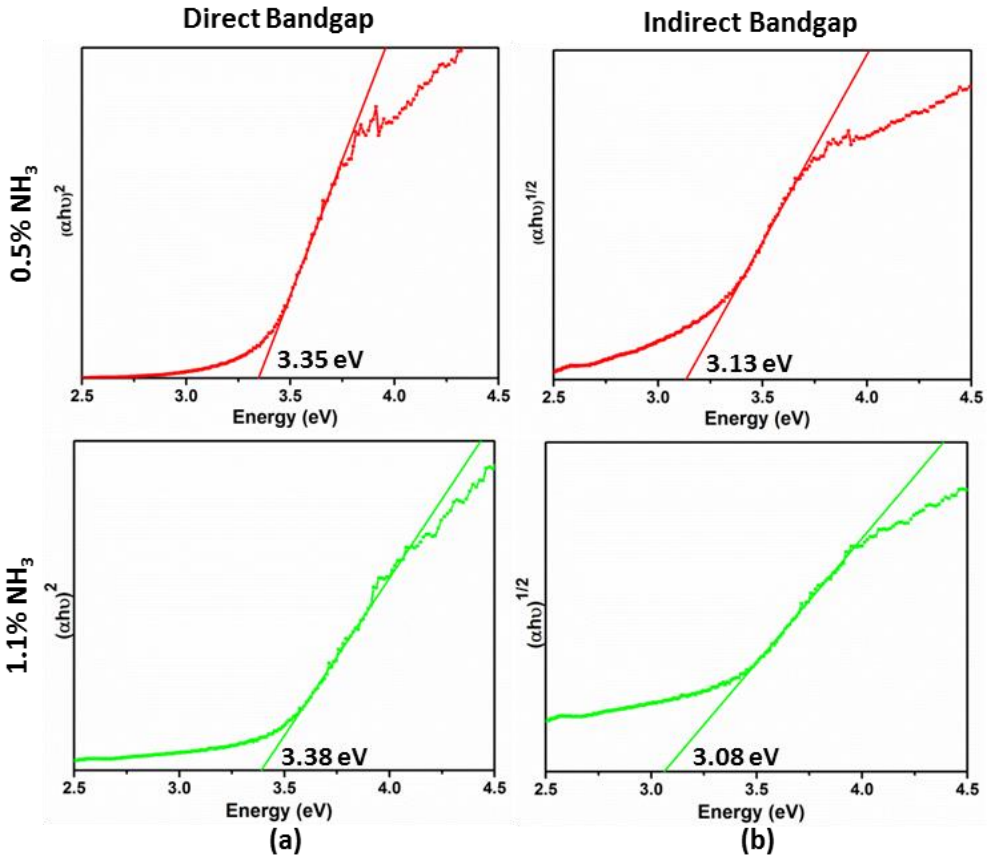

Figure 6. 14: Measured (a) direct and (b) indirect bandgap for samples synthesized at 0.5% NH_3 and 1.1% NH_3.

UV-Vis measurements have been recorded for all samples to analyse the optical behaviour of the materials. Samples were deposited directly onto quartz substrates to record the transmittance (figure 6.14). The sample synthesised at 0.5% NH_3 concentration shows an obvious increase in the absorption compared to the 0.0%NH_3 and absorption is further increased at higher ammonia concentration, i.e. 1.1%NH_3.

Figure 6.15 reports Tauc plots for both direct and indirect bandgap transitions for the samples synthesised at 0.5% NH_3 and 1.1% NH_3. The measured direct bandgap (figure 6.15a) values do not change significantly; these are 3.35 eV and 3.38 eV for samples 0.5% NH_3 and 1.1% NH_3, respectively. Similarly, the indirect bandgap was 3.13 eV and 3.08 eV for sample 0.5% NH_3 and 1.1% NH_3, respectively.

6.5 Conclusion

According to obtained results, N_2 precursor doesn't support pure phase of Zn_2N_3. With ammonia, Zn_2N_3 production is observed with a degree of oxidation. Plasma stability is very strongly influenced by ammonia concentration. Therefore, only one sample (0.5% NH_3) showed repeatable Zn_2N_3 production, where TEM, Raman, XPS and UV-Vis measurements all support the formation of zinc nitride in the sample synthesised at 0.5% NH_3. HRTEM (figure 6.11c) and SAED (figure 6.11d) results showed two planes specifically designated to Zn_2N_3 (220) and (620) planes. XPS supported the presence of both Zn-N as well as Zn-O bonds. The oxidation observed in XPS (figure 6.12d) measurements can be associated with exposure to air after synthesis; where from the TEM results where sample was collected in toluene appears to have prevented oxidation via exposure to air or humidity. Sample 0.5% NH_3 showed both direct and indirect bandgap of 3.35 eV and 3.13 eV (figure 6.15). With vast range of Zn_2N_3 bandgap (1.2 eV- 3.4 eV), Zn_2N_3 shows higher bandgap when ammonia is used in synthesis.[18,28,29] This can be observed because of fair possibility of incorporation of H as an impurity in the crystal structure. Raman (figure 6.13) results support the fact that zinc nitride is produced by showing Zn-N vibration in Raman (only in sample 0.5% NH_3).

6.6 References

1. Galesic, I. & Kolbesen, B. O. Characterization of transition metal nitride formation in rapid thermal processing (RTP). *Fresenius. J. Anal. Chem.* **365,** 199–202 (1999).

2. Nandi, D. K. *et al.* Atomic layer deposited tungsten nitride thin films as a new lithium-ion battery anode. *Phys. Chem. Chem. Phys.* **17,** 17445–17453 (2015).

3. Sinha, S. & Sarkar, S. K. Atomic layer deposition of textured zinc nitride thin films. *RSC Adv.* **4,** 47177–47183 (2014).

4. Ji, W. *et al.* Partially nitrided molybdenum trioxide with promoted performance as an anode material for lithium-ion batteries. *J. Mater. Chem. A* **2,** 699–704 (2014).

5. Quesada-Cabrera, R., Sotelo-Vazquez, C., Darr, J. A. & Parkin, I. P. Critical influence of surface nitrogen species on the activity of N-doped TiO2 thin-films during photodegradation of stearic acid under UV light irradiation. *Appl. Catal. B Environ.* **160-161,** 582–588 (2014).

6. Wang, M. *et al.* N Doping to ZnO Nanorods for Photoelectrochemical Water Splitting under Visible Light: Engineered Impurity Distribution and Terraced Band Structure. *Sci. Rep.* **5,** (2015).

7. Kim, C., Kim, K. & Moon, J. H. Highly N-doped microporous carbon nanospheres with high energy storage and conversion efficiency. *Sci. Rep.* **7,** 25–27 (2017).

8. Mouvier, G. X-Ray Nitrogen Photoelectron Spectroscopy of Oxides Adsorbed on Iron Oxides. **348,** 342–348 (1975).

9. Jain, G. *et al.* Porous zinc oxide nanocrystalline film deposition by atmospheric pressure plasma: Fabrication and energy band estimation; Porous zinc oxide nanocrystalline film deposition by atmospheric pressure plasma: Fabrication and energy band estimation. (2017). doi:10.1002/ppap.201700052

10. Khan, W. S. & Cao, C. Synthesis, growth mechanism and optical characterization of zinc nitride hollow structures. *J. Cryst. Growth* **312,** 1838–

1843 (2010).

11. Taylor, P. N. *et al.* Synthesis of widely tunable and highly luminescent zinc nitride nanocrystals. *J. Mater. Chem. C* **2,** 4379–4382 (2014).

12. Partin, D. E., Williams, D. J. & O'Keeffe, M. The Crystal Structures of Mg3N2and Zn3N2. *J. Solid State Chem.* **132,** 56–59 (1997).

13. Yoo, S.-H., Walsh, A., Scanlon, D. O. & Soon, A. Electronic structure and band alignment of zinc nitride, Zn_3N_2. *RSC Adv.* **4,** 3306–3311 (2014).

14. Futsuhara, M., Yoshioka, K. & Takai, O. Structural, electrical and optical properties of zinc nitride thin films prepared by reactive rf magnetron sputtering. *Thin Solid Films* **322,** 274–281 (1998).

15. Zong, F. *et al.* Structural properties of zinc nitride empty balls. *Mater. Lett.* **60,** 905–908 (2006).

16. Yoo, S.-H., Walsh, A., Scanlon, D. O. & Soon, A. Electronic structure and band alignment of zinc nitride, Zn_3N_2. *RSC Adv.* **4,** 3306–3311 (2014).

17. Taylor, P. N. *et al.* Synthesis of widely tunable and highly luminescent zinc nitride nanocrystals. *J. Mater. Chem. C* **2,** 4379–4382 (2014).

18. Khan, W. S. & Cao, C. Synthesis, growth mechanism and optical characterization of zinc nitride hollow structures. *J. Cryst. Growth* **312,** 1838–1843 (2010).

19. William M. Haynes. *CRC Handbook of Chemistry and Physics (96 ed.),.*

20. Cao, X., Sato, A., Ninomiya, Y. & Yamada, N. Oxygen-doped zinc nitride as a high-mobility nitride-based semiconductor. *J. Phys. Chem. C* **119,** 5327–5333 (2015).

21. Fettkenhauer, C., Clavel, G., Kailasam, K., Antonietti, M. & Dontsova, D. Facile synthesis of new, highly efficient SnO_2 /carbon nitride composite photocatalysts for the hydrogen evolution reaction. *Green Chem.* **17,** 3350–3361 (2015).

22. Rajaambal, S., Mapa, M. & Gopinath, C. S. $In_{1-x}Ga_xN$@ZnO: a rationally

designed and quantum dot integrated material for water splitting and solar harvesting applications. *Dalt. Trans.* **43,** 12546 (2014).

23. Kaschner, A. *et al.* Nitrogen-related local vibrational modes in ZnO:N. *Appl. Phys. Lett.* **80,** 1909–1911 (2002).

24. Xing, G. Z. *et al.* Structural and electrical characteristics of high quality (100) orientated-Zn3N2 thin films grown by radio-frequency magnetron sputtering. *J. Appl. Phys.* **108,** 083710 (2010).

25. Ling, C., Song, Y. & Chang, S. Rapid thermal oxidation of zinc nitride film. *Jpn. J. Appl. Phys.* **06,** 2–7 (2015).

26. Kumari, R., Sahai, A. & Goswami, N. Effect of nitrogen doping on structural and optical properties of ZnO nanoparticles. *Prog. Nat. Sci. Mater. Int.* **25,** 300–309 (2015).

27. Alshammari, A. S. *et al.* Visible-light photocatalysis on C-doped ZnO derived from polymer-assisted pyrolysis. *RSC Adv.* **5,** 27690–27698 (2015).

28. Zong, F. *et al.* Structural properties and photoluminescence of zinc nitride nanowires. *Appl. Phys. Lett.* **87,** 1–3 (2005).

29. Khan, W. S. *et al.* Optical properties and characterization of zinc nitride nanoneedles prepared from ball-milled Zn powders. *Mater. Lett.* **65,** 1264–1267 (2011).

Chapter 7: Conclusion and future work

7.1 Conclusion

Atmospheric pressure plasma showed the versatility of tuning the material properties by changing the material composition and size of zinc-based semiconductors. Different nanostructures of ZnO were produced by gas phase plasma process using pure metallic zinc wire and environmental oxygen.

In one instance a porous ZnO film was produced from the deposition of nanocrystallites. Detailed characterization has confirmed the high purity of porous ZnO. The Fermi level, bandgap energy and energy band alignment has confirmed ZnO electronic structure. Low intrinsic defects, high porosity and easy to deposit synthesis method offer opportunities to use this porous ZnO in dye sensitised solar cell, catalytic studies and solar cells.

The same system was then used to produce ZnO quantum dots (QDs) with strong quantum confinement effects because of the very small average size ~1.9 nm. Surface passivation by hydroxyl groups was also achieved and confirmed by XPS and FTIR. Passivation has satisfied the majority of surface defects and has been considered responsible for removing visible emission. Further, this was corroborated by the shift of the PL intensity because of ionized acceptor exciton complex formation. The strong nature of the UV absorption and emission without any defect contribution makes these hydroxyl-passivated QDs strong candidates in UV based application such as UVB absorber in cosmetics because of the large band gap, UV emitters etc.

In the second part of thesis, ZnO was doped with N and N-C with a liquid-based plasma process. The impact of N-doping was not significant on the bandgap and energy band diagram; however, the emission and electrochemical properties were affected. The bandgap and energy band was significantly changed when N-C co-doping was achieved, with further reduced emission in the visible range. Drastic improvement in the electrochemical nature of ZnO was observed with N-C doping. A high pseudo-capacitive nature of N-C doped ZnO was observed. Also, a detailed characterization of doped ZnO has allowed investigating the location of the dopants. ZnO shows a

solubility limit towards substitutional doping and further doping concentrations are accommodated at interstitial sites in the ZnO lattice.

The hybrid-plasma liquid system was also used in the synthesis of zinc peroxide (ZnO_2). Results have shown the production of H_2O_2 resulting from the reaction of $Zn(OH)_2$ with water leading to ZnO_2.

Another Zn based semiconductor, Zn_2N_3, was synthesised with the gas-phase atmospheric pressure plasma. Again, pure metallic zinc wire was used to synthesis zinc nitride. The choice of the nitrogen precursor played an important role for the synthesis of Zn_2N_3.

The main achievements of this work can be summarized as follows:

- A microplasma-based gas-phase synthesis method was developed and demonstrated for the synthesis of porous ZnO films with pure solid metallic precursor.
- Self-passivated with reduced surface defect density and quantum confined ZnO QDs were produced with stable UV emission. The stability of the UV emission was tested for more than one and half years.
- Microplasma-induced synthesis of doped ZnO was demonstrated. The effect of doping on ZnO structural, chemical and optical properties were studied thoroughly. For the first time, the pseudocapacitive nature of N-doped and N-C doped ZnO was demonstrated.
- The bandgap of ZnO was tailored from 3.23 eV to 2.98 eV with doping. More importantly, doping in ZnO has shifted the absorption edge drastically towards the visible region.
- A detailed study has been performed to investigate dopants location in the ZnO lattice, which has also demonstrated the crucial in-built nature of ZnO towards substitution doping.
- Microplasma-induced synthesis technique has also demonstrated ZnO_2 formation.
- For the first time, a study for the synthesis of Zn_2N_3 with atmospheric pressure plasma was demonstrated which showed the complexity of producing stable Zn_2N_3.

7.2 Future direction of this work

Zn-based semiconductors (e.g. ZnO, doped ZnO, ZnS, ZnO_2 etc) can be used in different applications. The following are possible directions to further study in this work:

a) Studying the use of porous ZnO in different applications, e.g. solar cells, catalytic studies etc. Easy deposition process and high surface area of porous ZnO can show a significant improvement in ZnO uses in these types of applications.
b) Initial results have shown great potential of N-C doped ZnO in energy storage applications. It can be a great opportunity to form a composite material for batteries, e.g. with graphene to improve storage capacity and life time of batteries.
c) Other applications such as degradation of dye molecules and other pollutants in water can be studied.
d) Further work should explore the opportunity of hybrid-plasma liquid system in terms of the very wide range of parameters such as applied current, gas flow rate, electrolyte composition which may lead to a change in size, shape and doping level in ZnO. Eventually, the effect on all these parameters on pseudocapacitive behaviour of doped ZnO can be studied.
e) Zinc Nitride can be a potential candidate in many optoelectronic applications because of wide bandgap tunability. To work in this direction, more study is required towards plasma characterization so to achieve better control over process temperature, stabilty etc. Many parameters can be changed to optimize the process, such as applied power, more combinations of nitrogen precursor gas flow, changing the zinc and nitrogen precursor etc. Also, control of Zn_2N_3 oxidation needs to be improved by tuning the synthesis conditions.